To the Graduate Council:

I am submitting herewith a dissertation written by Subramaniam Shanmugham entitled "Processing and Mechanical Behavior of Nicalon/SiC and Nextel/SiC Composites with Sol-Gel Derived Oxide Interfacial Coatings." I have examined the final copy of this dissertation for form and content and recommend that it be accepted in partial fulfillment of the requirements for the degree of Doctor of Philosophy, with a major in Metallurgical Engineering.

Peter K. Liaw, Major Professor

We have read this dissertation
and recommend its acceptance:

Accepted for the Council:

Associate Vice Chancellor and
Dean of The Graduate School

Processing and Mechanical Behavior of Nicalon/SiC and Nextel/SiC Composites with Sol-Gel Derived Oxide Interfacial Coatings

A Dissertation
Presented for the
Doctor of Philosophy
Degree
The University of Tennessee, Knoxville

Subramaniam Shanmugham
May 1997

Copyright © Subramaniam Shanmugham, 1997

All rights reserved

DEDICATION

This dissertation is dedicated to my parents, Mr. and Mrs. Shanmugham,

who have made me what I am today.

ACKNOWLEDGMENTS

Dissertation is a learning phase, struggle, and test of your patience and perseverance, and "always takes more time than you think." During the dissertation period, many have been patient and understanding, helped, advised, supported, and guided me. I am grateful to my dissertation committee, Drs. P. K. Liaw, T. M. Besmann, C. J. McHargue, J. D. Landes, and A. Bleier, and Mr. D. P. Stinton, for their guidance, encouragement, constructive advises, and criticisms during the course of this work. In particular, I am indebted to Mr. D. P. Stinton, who has always taken time to help, encourage, support, and propel me in the positive direction. Special thanks to Drs. C. J. McHargue and T. M. Besmann for arranging the opportunity to work at the Oak Ridge National Laboratory (ORNL) for the last five years.

I am thankful to Dr. K. L. More and Mr. R. A. Lowden for making the TEM study possible, Mr. D. N. Braski for conducting the Auger work, and Mr. J. J. Henry and J. A. Hurley for performing the matrix infiltration. I am also thankful to Dr. J. E. Spruiell, Mr. N. Miriyala, and Ms. S. P. Maples for all the help they rendered during my last six years of stay at the University of Tennessee. I am grateful to the following ORNL personnel, who have helped me in different phases of my dissertation: Drs. S. T. Misture, O. B. Cavin, M. Paranthaman, Y. Bae, W. Y. Lee, E. Lara-Curzio, E. R. Kupp, R. R. Judkins, P. T. Carlson, P. F. Tortorelli, D. R. Johnson, H. T. Lin, and M. K. Ferber, Mr. W. D. Porter, Mr. J. C. McLaughlin, Mr. K. M. Cooley, Ms. D. Coffey and Ms. R. L. Martin.

I would also like to thank the project sponsor, U. S. Department of Energy, Office of Fossil Energy, Advanced Research and Technology Development Materials Program, under contract DE-AC05-96OR22464 with Lockheed Martin Energy Research Corporation, and under subcontract 11B-99732C-64 to the University of Tennessee.

Finally, I am thankful to my parents, Mr. and Mrs. Shanmugham, wife, Dharma, and sister, Sumathi, for their support and encouragement in all my endeavors.

ABSTRACT

It is well established that the fiber-matrix interface plays a key role in determining the mechanical properties of ceramic matrix composites. Currently, Nicalon-fiber/SiC-matrix composites and Nextel-fiber/SiC-matrix composites owe their good mechanical properties at room temperature to either carbon (C) or boron nitride (BN) interfaces, which provide a weak interfacial bond. However, C and BN interfaces encounter oxidation problems at elevated temperatures resulting in degradation of mechanical properties of these composites in oxidizing environments. Hence, alternative oxidation-resistant interface materials need to be identified and developed.

Recent analytical and finite element modeling studies have indicated that low modulus interfacial coatings may be desirable to reduce residual radial compressive stresses at fiber-matrix interfaces which develop upon cooling from processing to room temperature. Two oxides, mullite and aluminum titanate, were chosen as interface materials for Nicalon/SiC and Nextel/SiC composites based on their relatively low modulus and their good oxidation resistance at elevated temperatures.

Mullite and aluminum titanate precursor sols were developed for coating applications. High temperature X-ray diffraction studies in air identified that mullite crystallizes between 950°C and 1050°C, while aluminum titanate forms between 1200°C and 1400°C. The crystallization temperature of mullite was lowered by 100°C compared to those reported in the literature. Nicalon tows are embrittled during the formation of mullite at 1000°C, and hence, there is a need to protect the fibers by a relatively inert material during the sol-gel oxide processing. The aluminum titanate formation temperature is high and would damage Nicalon and Nextel fibers. However, Nicalon fibers dip-coated in an aluminum titanate sol and heat-treated at 1000°C for up to 10 h in air, forming an alumina-titania (Al_2O_3-TiO_2) mixture, were not embrittled. Based on the non-embrittlement of the fibers, the Al_2O_3-TiO_2 mixture was chosen as an alternative to aluminum titanate for an interface material. Additionally, there is a need to protect the oxide coatings from the HCl attack, a by-product of the SiC matrix deposition reaction.

To protect the fibers and oxides during the processing, a C coating was selected because of its inertness and ease of processing.

To study the effect of protecting the fibers by an inert material during sol-gel oxide coating, oxide/C, and C/oxide/C interfaces were considered for Nicalon/SiC and Nextel/SiC composites. Since composites with C/oxide/C interfaces exhibited higher flexural strengths than composites with oxide/C interfaces in the as-processed condition, C/oxide/C interfaces were studied. Also, Nicalon/SiC composites with C/oxide/C interfaces retained damage-tolerant behavior and substantial amount of their as-processed strengths even after 24 h oxidation at 1000°C in air than Nextel/SiC composites with C/oxide/C interfaces. On these basis, Nicalon/SiC composites with C/oxide/C interfaces were chosen for further investigation. Transmission electron microscopy studies identified that the obtained oxide coatings were very thin (< 0.1 μm), and hence, that the effect of modulus on the mechanical properties could not be investigated in the present study. A control sample of a Nicalon/SiC composite with a thin C (< 0.1 μm) interface was also fabricated.

Nicalon/SiC composites with C and C/oxide/C interfaces were fabricated and flexure tested at room temperature in both as-processed and oxidized conditions. Flexural strengths of the composites with C, and C/oxide/C interfaces decreased with increasing exposure time at 1000°C, but they retained graceful failure even after 500 h oxidation. Composites with C/oxide/C interfaces retained substantial flexural strengths than a composite with a C interface after 200 h oxidation at 500°C. After 200 h oxidation at 750°C, composites with C and C/oxide/C interfaces underwent catastrophic failure and drastic reduction in strengths (> 73%). Nicalon/SiC composites with C/oxide/C interfaces performed poorly at 750°C, so Nicalon/SiC composites with BN/oxide/BN interfaces were fabricated and tested in both as-processed and oxidized conditions. Additionally, a control sample, Nicalon/SiC composite with a BN interface, was fabricated and flexure tested. Composites with BN and BN/Al_2O_3-TiO_2/BN interfaces retained substantial strengths and exhibited graceful failure even after 200 h exposure at 500°C, 750°C, and 1000°C, whereas the composite with a BN/mullite/BN interface failed predominantly in a catastrophic manner after exposure at 750°C and 1000°C.

TABLE OF CONTENTS

CHAPTER 1 INTRODUCTION 1

CHAPTER 2 LITERATURE SURVEY 7

2.1. Introduction 7
2.2. Fiber Reinforcements 8
2.2.1. Discovery of Nicalon 10
2.2.2. Literature Survey for Nicalon Fibers 12
2.2.3. Literature Survey for Nextel Fibers 18
2.3. Matrices and Matrix Processing Techniques 21
2.3.1. Traditional Mixing and Slurry Infiltration Techniques 22
2.3.2. Chemical Synthesis Methods: Sol-Gel and Polymer Infiltration and Pyrolysis 23
2.3.3. Liquid Infiltration Techniques: Melt Infiltration and DIMOX 26
2.3.4. In-situ Chemical Reaction Methods: Reaction Bonding and CVI 28
2.4. Interface and its Significance 34
2.4.1. Composite Fundamentals 35
2.4.1.1. Stress-Strain Behavior 35
2.4.1.2. Energy Balance Approach 39
2.4.1.3. The Short Crack-Fracture Mechanics Approach 42
2.4.1.4. The Local Flaw Model 44
2.4.2. Toughening Mechanisms in CFCCs 44
2.4.3. Residual Stresses 47
2.4.4. Realization of Interface Significance 48
2.4.5. Techniques for Applying Interface Coatings 49
2.5. Literature Survey for Nicalon/SiC Composites 52
2.5.1. Research at Oak Ridge National Laboratory and University of Tennessee 52
2.5.2. Research at Laboratoire des Composites Thermostructuraux, France 63
2.5.3. Research by Other Groups 67
2.6. Literature Survey for Nextel/SiC Composites 71
2.7. Implications and Critical Issues 73
2.8. Sol-Gel Synthesis of Mullite and Aluminum Titanate 75
2.9. Flexure Testing 77

CHAPTER 3 RATIONALE 79

CHAPTER 4 THERMOCHEMICAL ANALYSIS 87

4.1. Processing Conditions 89
4.2. Interface Compatibility with the SiC Matrix 90
4.3. Interface Coating Chemical Stability with the Nicalon Fiber 91

CHAPTER 5 EXPERIMENTAL PROCEDURE 92

5.1. Materials 92
5.2. Development of Sols for Coating Applications 92
5.2.1. Mullite and Aluminosilicate Precursor Sols 92
5.2.2. Aluminum Titanate Precursor Sol 94
5.3. Gel Characterization Studies 95
5.3.1. Differential Scanning Calorimetry 95
5.3.2. High-Temperature X-ray Diffraction 96
5.4. Nicalon Cloth and Tow Coating Studies 97
5.5. Composite Fabrication 98
5.5.1. Preform Fabrication 98
5.5.2. C Coating 98
5.5.3. BN Coating 99
5.5.4. Mullite Coating 99
5.5.5. Al_2O_3-TiO_2 Coating 100
5.5.6. Infiltration of the SiC Matrix 100
5.5.7. Interface Coating Thickness Calculation 102
5.5.8. Fabricated Composites 103
5.6. Flexure Testing 103
5.6.1. Specimen Preparation and Density Measurement 103
5.6.2. Four-Point Bend Testing and Heat Treatment 103
5.7. Microanalysis 105
5.7.1. Scanning Electron Microscopy 105
5.7.2. Transmission Electron Microscopy 105
5.7.3. Auger Electron Spectroscopy 106
5.8. Analytical Modeling 107

CHAPTER 6 RESULTS 108

6.1. Introduction 108

6.2. Sols Development 108
6.2.1. Mullite and Aluminosilicate Precursor Sols 108
6.2.2. Aluminum Titanate Precursor Sol 108
6.3. Gel Characterization Studies 109
6.3.1. Differential Scanning Calorimetry 109
6.3.2. High-Temperature X-ray Diffraction 111
6.4. Nicalon Cloth and Tow Coating Studies 113
6.5. Density of Fabricated Composites 115

6.6. Flexural Strength and Microanalysis of Fabricated Nicalon/SiC Composites 116
6.6.1. Composite with a C Interface (CVI 1077) 117
6.6.2. Composites with Oxide/C Interfaces 119
6.6.2.1. Composite with a Mullite/C Interface (CVI 982) 119
6.6.2.1. Composite with an Al_2O_3-TiO_2/C Interface (CVI 985) 120
6.6.3. Composites with C/mullite/C Interfaces 120
6.6.3.1. CVI 986 121
6.6.3.2. CVI 1033 123
6.6.3.3. CVI 1080 124
6.6.3.4. CVI 1081 124
6.6.4. Composites with C/Al_2O_3-TiO_2/C Interfaces 125
6.6.4.1. CVI 1002 125
6.6.4.2. CVI 1036 127
6.6.4.3. CVI 1066 128
6.6.5. Composite with a BN Interface (CVI 1068) 129
6.6.6. Composite with a BN/Al_2O_3-TiO_2/BN Interface (CVI 1073) .. 131
6.6.7. Composite with a BN/mullite/BN Interface (CVI 1054) 133
6.7. Flexural Strength and Microanalysis of Nextel/SiC Composites 134
6.7.1. Composite with a Mullite/C Interface (CVI 997) 135
6.7.2. Composite with an Al_2O_3-TiO_2/C Interface (CVI 998) 135
6.7.3. Composite with a C/mullite/C Interface (CVI 999) 136
6.7.4. Composite with a C/Al_2O_3-TiO_2/C Interface (CVI 1000) 136

CHAPTER 7 DISCUSSION 138

7.1. Sol and Gel Characterization Studies 138
7.1.1. Mullite and Aluminosilicate 138
7.1.2. Aluminum Titanate 139
7.2. Nicalon Cloth and Tow Coating Studies 140
7.3. Nicalon/SiC Composites with C, Oxide/C, and C/oxide/C Interfaces 140
7.4. Nicalon/SiC Composites with BN, and BN/oxide/BN Interfaces 148
7.5. Nextel/SiC Composites with Oxide/C, and C/oxide/C Interfaces 150

CHAPTER 8 SUMMARY, CONCLUSIONS AND FUTURE WORK 152

8.1. Summary 152
8.2. Conclusions 156
8.3. Future Work 157

REFERENCES 160

APPENDICES 179

APPENDIX A 180

APPENDIX B 201

APPENDIX C 359

APPENDIX D 361

Vita 381

LIST OF TABLES (APPENDIX A)

Table 1. Selected properties of commercially available non-oxide continuous ceramic fibers 181

Table 2. Selected properties of commercially available oxide continuous ceramic fibers 182

Table 3. Ceramic matrices of interest along with processing method(s) 183

Table 4. Properties of the fiber, matrix, and interface materials used for modeling investigation 184

Table 5. List of fabricated Nicalon/SiC composites with C, oxide/C, and C/oxide/C interfaces 185

Table 6. List of fabricated Nicalon/SiC composites with BN and BN/oxide/BN interfaces 186

Table 7. List of fabricated Nextel/SiC composites with oxide/C and C/oxide/C interfaces 187

Table 8. Summary of the number of flexure bars of Nicalon/SiC composites tested at room temperature in both as-processed and oxidized conditions 188

Table 9. Summary of the number of flexure bars of Nextel/SiC composites tested at room temperature in both as-processed and oxidized conditions 189

Table 10. Summary of the Nicalon/SiC composites and Nextel/SiC composites selected for Auger electron spectroscopy studies 190

Table 11. Summary of DSC and high temperature XRD results of mullite crystallization from powders derived from mullite precursor gels 191

Table 12. Summary of DSC and high temperature XRD results of aluminum titanate formation from powders derived from aluminum titanate precursor gels 192

Table 13. Density of fabricated Nicalon/SiC composites with C, oxide/C, and C/oxide/C interfaces along with C coating thicknesses 193

Table 14. Density of fabricated Nicalon/SiC composites with BN and BN/oxide/BN interfaces along with BN coating thicknesses 194

Table 15. Density of fabricated Nextel/SiC composites with oxide/C, and C/oxide/C interfaces along with C coating thicknesses 195

Table 16. Flexural strengths of Nicalon/SiC composites with C, oxide/C, C/oxide/C, BN and BN/oxide/BN interfaces in the as-processed condition 196

Table 17. Comparison of flexural strengths of Nicalon/SiC composites in the as-processed condition and after oxidation at 1000°C in air 197

Table 18. Comparison of flexural strengths of Nicalon/SiC composites in the as-processed condition and after oxidation for 200 h each at 500°C, 750°C, and 1000°C in air 198

Table 19. Interface debonding characteristics of the Nicalon/SiC composites and Nextel/SiC composites based on Auger electron spectroscopy studies 199

Table 20. Comparison of flexural strengths of Nextel/SiC composites in the as-processed condition and after oxidation at 1000°C in air 200

LIST OF FIGURES (APPENDIX B)

Fig. B.2.1. Conversion process of cured PCS into SiC by pyrolysis 202

Fig. B.2.2. Flow diagram for the Nicalon fiber manufacturing process 203

Fig. B.2.3. Tensile strength as a function of temperature of SiC-based and oxide fibers 204

Fig. B.2.4. A schematic of the 3M process for making an alumina fiber 205

Fig. B.2.5. Tensile strength versus temperature for Nextel fibers 206

Fig. B.2.6. Creep rate versus stress for Nextel 720 and other commercially available polycrystalline oxide fibers 207

Fig. B.2.7. Flow diagram of the tape lay-up fabrication of glass matrix composites 208

Fig. B.2.8. Comparison of slurry infiltration with the sol-gel process for making oxide fiber reinforced oxide composites 209

Fig. B.2.9. Schematic flow diagram for making a fiber-reinforced Blackglas ceramic composite by a polymer infiltration and pyrolysis process 210

Fig. B.2.10. Schematic of a melt infiltration process 211

Fig. B.2.11. A schematic of the DIMOX process for making composites 212

Fig. B.2.12. A schematic of the production of SCS-6 fiber reinforced silicon nitride by a reaction bonding process 213

Fig. B.2.13. Five types of chemical vapor infiltration processes 214

Fig. B.2.14. Schematic of the FCVI process 215

Fig. B.2.15. Influence of interfacial bond strength on the failure of a ceramic matrix composite (a) strong interface bond and (b) weak interface bond 216

Fig. B.2.16. (a) Stress-strain relationships for brittle fiber and matrix (b) composite fracture strength vs volume fraction for the matrix/fiber combination in (a) 217

Fig. B.2.17. Stress-strain curve for a "tough" ceramic fiber reinforced ceramic matrix composite....218

Fig. B.2.18. Fracture mechanisms in ceramic matrix composites (the different cases are described in the text)....219

Fig. B.2.19. Failure modes in a high toughness CFCC under tension....220

Fig. B.2.20. Interfacial sliding and fiber debonding in a CFCC....221

Fig. B.2.21. Influence of thermal expansion mismatch on residual stresses (a) $\alpha_f > \alpha_m$ and (b) $\alpha_f < \alpha_m$ 222

Fig. B. 2.22. Comparison of four-point flexure curves of composites with different carbon interface thicknesses 223

Fig. B.2.23. Yoldas' method for making polymeric mullite precursor gel....224

Fig. B.3.1. Schematic illustrating whisker (fiber)/film (interface)/matrix system as well as the interfacial and axial tractions to maintain continuity at the interfaces during cooling 225

Fig. B.3.2. Compressive residual thermal stresses at the fiber/matrix regions in Nicalon/SiC composites 226

Fig. B.3.3. Compressive residual thermal stresses at the fiber/matrix regions in Nextel/SiC composites 227

Fig. B.3.4. Oxide interface concept for a fiber-reinforced ceramic matrix composite....228

Fig. B.4.1. Computed TiO_2/SiC phase diagram for the temperature range of 1000-1200°C....229

Fig. B.4.2. Computed Al_2O_3/Nicalon phase diagram for the temperature range of 1000-1200°C....230

Fig. B.4.3. Computed TiO_2/Nicalon phase diagram for the temperature range of 1000-1200°C....231

Fig. B.4.4. Computed mullite/Nicalon phase diagram for the temperature range of 1000-1200°C....232

Fig. B.5.1. Flow diagram of the synthesis of mullite precursor gel using Yoldas' method....233

Fig. B.5.2. Flow diagram of the synthesis of an aluminum titanate precursor gel.234

Fig. B.5.3. Schematic of a FCVI system 235

Fig. B.5.4. Schematic of the furnace used to densify fibrous preforms by the FCVI process 236

Fig. B.5.5. Procedure for calculating the interface coating thickness 237

Fig. B.6.1. DSC curve of the powder obtained from the mullite precursor gel (MI) using the ASB-TMOS combination showing a mullite crystallization event around 990°C 238

Fig. B.6.2. DSC curve of the powder obtained from the mullite precursor gel (MII) using the ASB-TEOS combination showing a mullite crystallization event around 990°C 239

Fig. B.6.3. DSC curve of the powder obtained from the EI mullite precursor gel in air showing a sharp exothermic event around 990°C suggesting mullite crystallization 240

Fig. B.6.4. DSC curve of the powder obtained from the EI mullite precursor gel in argon showing a sharp exothermic event around 990°C indicating mullite crystallization 241

Fig. B.6.5. DSC curve of the powder obtained from the MEI mullite precursor gel in air showing a sharp exothermic event around 990°C indicating mullite crystallization 242

Fig. B.6.6. DSC curve of the powder obtained from the MEI mullite precursor gel in argon showing an exothermic event around 990°C suggesting mullite crystallization 243

Fig. B.6.7. DSC curve of ATI aluminum titanate precursor gel derived powder indicating aluminum titanate formation around 1360°C 244

Fig. B.6.8. DSC curve of ATII aluminum titanate precursor gel derived powder in air indicating the aluminum titanate formation event occurring around 1370°C 245

Fig. B.6.9. DSC curve of ATII aluminum titanate precursor gel derived powder in argon indicating the aluminum titanate formation event taking place around 1200°C 246

Fig. B.6.10. High temperature XRD patterns indicating that mullite crystallization occurs at 1050°C from the MI mullite precursor gel derived powder 247

Fig. B.6.11. High temperature XRD patterns showing that mullite crystallization takes place at 1050°C from the MII mullite precursor gel 248

Fig. B.6.12. High temperature XRD patterns in air showing that mullite crystallization takes place at 950°C from the EI mullite precursor gel derived powder 249

Fig. B.6.13. High temperature XRD patterns indicating that mullite crystallization occurs at 1000°C in argon from the EI mullite precursor gel derived powder 250

Fig. B.6.14. High temperature XRD patterns in air obtained from MEI mullite precursor gel derived powder showing that mullite crystallization occurs at 950°C 251

Fig. B.6.15. High temperature XRD patterns obtained in argon from MEI mullite precursor gel derived powder suggesting that mullite crystallization takes place at 1000°C 252

Fig. B.6.16. High temperature XRD patterns obtained in air from the ATI aluminum titanate precursor gel derived powder indicating that aluminum titanate forms at 1400°C 253

Fig. B.6.17. High temperature XRD patterns obtained in air from the ATII aluminum titanate precursor gel derived powder indicating that aluminum titanate forms at 1300°C 254

Fig. B.6.18. High temperature XRD patterns obtained in argon from the ATII aluminum titanate precursor gel derived powder suggesting that aluminum titanate forms at 1200°C 255

Fig. B.6.19. Mullite coating on a Nicalon tow heat-treated at 1000°C in air (a) A secondary electron image and (b) An EDX spectrum 256

Fig. B.6.20. Alumina-titania coating on a Nicalon tow heat-treated at 1000°C (a) A secondary electron image and (b) An EDX spectrum 257

Fig. B.6.21. Tensile region of the fracture surface of a CVI 1077 composite (C interface) shows fiber pullout of the order of 300 μm in the as-processed condition 258

Fig. B.6.22. Fracture surface of an in-situ broken CVI 1077 composite in the as-processed condition 259

Fig. B.6.23. Compositional depth profiles obtained on a CVI 1077 composite in the as-processed condition (a) Fiber and (b) Trough 260

Fig. B.6.24. Representative load vs displacement curves for a CVI 1077 composite in the as-processed and oxidized conditions 261

Fig. B.6.25. Fracture surface of a CVI 1077 composite after 200 h oxidation at 750°C 262

Fig. B.6.26. Representative load vs displacement curves of a CVI 1077 composite in the as-processed condition and after oxidation for up to 500 h at 1000°C 263

Fig. B.6.27. Fracture surface of a CVI 1077 composite after 500 h oxidation at 1000°C 264

Fig. B.6.28. Fracture surface of an in-situ broken CVI 1077 sample oxidized for 500 h at 1000°C 265

Fig. B.6.29. Compositional depth profiles obtained on a CVI 1077 composite after 500 h oxidation at 1000°C (a) Fiber and (b) Trough 266

Fig. B.6.30. Fracture surface of a CVI 982 composite (mullite/C interface) (a) As-processed condition and (b) After 24 h oxidation at 1000°C.... 267

Fig. B.6.31. Compositional depth profiles obtained on a CVI 982 composite in the as-processed condition (a) Fiber and (b) Trough 268

Fig. B.6.32. Representative load vs displacement curves of a CVI 982 composite in the as-processed and oxidized conditions 269

Fig. B.6.33. Fracture surface of a CVI 985 composite (Al_2O_3-TiO_2/C interface) (a) As-processed condition and (b) After 24 h oxidation at 1000°C.... 270

Fig. B.6.34. Compositional depth profiles obtained on a CVI 985 composite in the as-processed condition (a) Fiber (b) Trough 271

Fig. B.6.35. Representative load vs displacement curves of a CVI 985 composite in the as-processed and oxidized conditions 272

Fig. B.6.36. Representative load vs displacement curves of a CVI 986 composite (C/mullite/C interface) in the as-processed condition and after oxidation at 1000°C for up to 500 h 273

Fig. B.6.37. Fracture surface of a CVI 986 composite broken in-situ (a) As-processed condition and (b) After 500 h oxidation at 1000°C.. 274

Fig. B.6.38. Compositional depth profiles obtained on a CVI 986 composite in the as-processed condition (a) Fiber and (b) Trough 275

Fig. B.6.39. TEM image of a C/mullite/C interface in the CVI 986 composite. The mullite layer is microcrystalline and is ~ 70 nm thick, while the inner and outer carbon layers are each ~ 20 nm thick 276

Fig. B.6.40. TEM image of a CVI 986 composite shows the absence of a mullite layer in the C/mullite/C interface. Instead of mullite, only voids are observed in between the C layers 277

Fig. B.6.41. Fracture surface of a CVI 986 composite (a) As-processed condition (b) After 24 h oxidation at 1000°C and (c) After 500 h oxidation at 1000°C 278

Fig. B.6.42. Compositional depth profiles obtained on a CVI 986 composite after 500 h oxidation at 1000°C (a) Fiber and (b) Trough 279

Fig. B.6.43. Representative load vs displacement curves of a CVI 1033 composite (C/mullite/C interface) in the as-processed as well as oxidized conditions 280

Fig. B.6.44. Fracture surface of a CVI 1033 composite showing considerable amount of fiber pullout in the as-processed condition 281

Fig. B.6.45. After 200 h oxidation at 1000°C, CVI 1033 composite fracture surface showing that the fiber pullout is confined to the interior of the sample 282

Fig. B.6.46. CVI 1033 composite fracture surface after 200 h oxidation at 500°C showing good fiber pullout 283

Fig. B.6.47. Fracture surface of a CVI 1033 composite after 200 h oxidation at 750°C showing brittle fracture 284

Fig. B.6.48. CVI 1080 composite fracture surface showing good amount of fiber pullout in the as-processed condition 285

Fig. B.6.49. Fracture surface of a CVI 1080 composite after 24 h oxidation at 1000°C showing good amount of fiber pullout 286

Fig. B.6.50. The tensile edge of the fracture surface of a CVI 1080 composite after 24 h oxidation at 1000°C. Note that the embrittlement zone extends ~ 200 μm 287

Fig. B.6.51. Fracture surface of a CVI 1080 composite after 200 h oxidation at 1000°C showing embrittlement near the sample edges 288

Fig. B.6.52. After 500 h oxidation at 1000°C, fracture surface of a CVI 1080 composite showing that the fiber pullout is seen only in the composite interior 289

Fig. B.6.53. Representative load vs displacement curves of a CVI 1080 composite in the as-processed condition and after oxidation for up to 500 h at 1000°C 290

Fig. B.6.54. Fracture surface of a CVI 1081 composite (C/mullite/C interface) showing good amount of fiber pullout in the as-processed condition.. 291

Fig. B.6.55. Near the tensile region of the CVI 1081 composite fracture surface, fiber pullout of the order of ~ 200 μm is observed 292

Fig. B.6.56. Load vs displacement curve for a CVI 1081 composite in the as-processed and oxidized conditions 293

Fig. B.6.57. Fracture surface of a CVI 1081 composite exhibiting brittle fracture after oxidation at 750°C for 200 h in air 294

Fig. B.6.58. Fracture surface of a CVI 1081 composite showing a good amount of fiber pullout even after 200 h oxidation at 500°C in air 295

Fig. B.6.59. CVI 1081 composite exhibiting a fibrous fracture surface with a good amount of fiber pullout even after 200 h oxidation at 1000°C in air 296

Fig. B.6.60. Embrittlement (~200 μm width) occurring near the tensile region in the CVI 1081 composite after oxidation for 200 h at 1000°C in air 297

Fig. B.6.61. Representative load vs displacement curves of the CVI 1002 composite (C/Al_2O_3-TiO_2/C interface) in the as-processed condition and after oxidation for up to 500 h showing graceful failure 298

Fig. B.6.62. TEM image of the CVI 1002 composite showing that the Al_2O_3-TiO_2 layer (~ 30-50 μm thick) is bounded by C layers 299

Fig. B.6.63. The CVI 1002 composite displaying a considerable amount of fiber pullout, with pullout lengths typically > 500 μm, in the as-processed condition 300

Fig. B.6.64. Micrograph showing three fibers (1, 2, 3) and two troughs (4, 5) selected for AES analysis in the CVI 1002 composite 301

Fig. B.6.65. Compositional depth profiles obtained on the CVI 1002 composite in the as-processed condition (a) Fiber and (b) Trough 302

Fig. B.6.66. CVI 1002 fracture surface after oxidation at 1000°C in air (a) 200 h exposure and (b) 500 h exposure. Note that with increasing exposure time at 1000°C, the fiber pullout is confined to the interior of the composite and the regions adjacent to the tensile edge exhibit brittle fracture....303

Fig. B.6.67. After oxidation for 500 h at 1000°C in air, a TEM image showing that C layers are replaced by SiO_2 along with the degradation of the Nicalon fiber surface. However, the Al_2O_3-TiO_2 layer (~30-50 μm thick) is intact..304

Fig. B.6.68. Al_2O_3-TiO_2 layer persisting even after 20 min of Ar sputtering on one fiber in the CVI 1002 composite oxidized for 500 h at 1000°C.....305

Fig. B.6.69. CVI 1036 composite (C/Al_2O_3-TiO_2/C interface) exhibiting good load bearing capacity and graceful failure in the as-processed condition as well as after oxidation for 200 h each at 500°C and 1000°C. Note that the flexure bars exposed to 750°C, however, undergo drastic reduction (79%) in strength....306

Fig. B.6.70. Fracture surface of a CVI 1036 composite in the as-processed condition showing considerable amount of fiber pullout....307

Fig. B.6.71. CVI 1036 composite showing considerable amount of fiber pullout even after 200 h exposure at 500°C in air....308

Fig. B.6.72. After oxidation at 750°C for 200 h in air, the CVI 1036 composite fracture surface showing brittle fracture....309

Fig. B.6.73. CVI 1036 composite fracture surface displaying reduced amount of fiber pullout after 200 h oxidation at 1000°C in air. Note that near the edges of the sample, only brittle fracture is observed....310

Fig. B.6.74. Fracture surface showing the embrittlement zone near the tensile edge (~300 μm) in the CVI 1036 composite after 200 h oxidation at 1000°C....311

Fig. B.6.75. CVI 1066 composite (C/Al_2O_3-TiO_2/C interface) fracture surface in the as-processed condition showing good amount of fiber pullout.....312

Fig. B.6.76. Fracture surface of a CVI 1066 composite showing good amount of fiber pullout even after oxidation for 24 h at 1000°C....313

Fig. B.6.77. CVI 1066 fracture surface after 200 h oxidation at 1000°C showing good amount of fiber pullout. Note that the composite underwent only 14% strength reduction compared to the as-processed condition.....314

Fig. B.6.78. Fracture surface of a CVI 1066 composite, after 200 h oxidation at 1000°C followed by 200 h oxidation at 750°C in air, showing a good amount of fiber pullout 315

Fig. B.6.79. Fracture surface of a CVI 1066 composite (exposed at 750°C for 200 h following 200 h exposure at 1000°C in air) exhibiting an embrittlement zone ~250 μm width near the tensile edge 316

Fig. B.6.80. CVI 1066 composite fracture surface exhibiting a considerable amount of fiber pullout in the interior even after 500 h oxidation at 1000°C in air. However, brittle fracture is occurring near the edges of the sample 317

Fig. B.6.81. CVI 1066 composite fracture surface showing that the embrittlement zone near the tensile edge (~ 300 μm wide) after 500 h oxidation at 1000°C in air 318

Fig. B.6.82. (a) Representative load vs displacement curves of a CVI 1066 composite in the as-processed and after oxidation at 1000°C for up to 500 h in air and (b) Comparison of CVI 1066 and CVI 1036 load vs displacement curve after oxidation at 750°C for 200 h in air. Prior to 750°C oxidation, the CVI 1066 sample was exposed for 200 h at 1000°C in air 319

Fig. B.6.83. Representative load vs displacement curves of a CVI 1068 composite (BN interface) in the as-processed condition and after oxidation at 1000°C for up to 500 h in air 320

Fig. B.6.84. In the as-processed condition, the fracture surface of a CVI 1068 composite showing very little fiber pullout 321

Fig. B.6.85. CVI 1068 composite fracture surface exhibiting predominantly brittle fracture after oxidation at 1000°C for 24 h 322

Fig. B.6.86. Fracture surface of a CVI 1068 composite after 200 h oxidation at 1000°C in air showing brittle fracture 323

Fig. B.6.87. After 500 h oxidation at 1000°C, the fracture surface of a CVI 1068 composite fracture surface showing brittle fracture in the tensile region 324

Fig. B.6.88. Fracture surface of the CVI 1068 composite after oxidation for 200 h at (a) 500°C and (b) 750°C 325

Fig. B.6.89. Representative load vs displacement curves of a composite with a BN interface in the as-processed and after oxidation conditions 326

Fig. B.6.90. Compositional depth profile of a composite with a BN interface in the as-processed condition (a) Fiber and (b) Trough 327

Fig. B.6.91. Compositional depth profiles obtained on a composite with a BN interface after oxidation at 1000°C for 500 h (a) Fiber and (b) Trough 328

Fig. B.6.92. In the as-processed condition, the fracture surface of a composite with a BN/Al_2O_3-TiO_2/BN interface (CVI 1073) showing good amount of fiber pullout 329

Fig. B.6.93. Fracture surface of a CVI 1073 composite after oxidation at 1000°C for 24 h showing brittle fracture with very little fiber pullout 330

Fig. B.6.94. Fracture surface of a CVI 1073 composite after oxidation for 500 h at 1000°C showing good fiber pullout in the compressive region 331

Fig. B.6.95. The tensile region of the fracture surface of a CVI 1073 composite after 500 h oxidation at 1000°C showing fiber pullout 332

Fig. B.6.96. Fracture surface of a CVI 1073 composite after oxidation at 500°C for 200 h 333

Fig. B.6.97. Fracture surface of a CVI 1073 composite after oxidation at 750°C for 200 h 334

Fig. B.6.98. Representative load vs displacement curves of a composite with a BN/Al_2O_3-TiO_2/BN interface in the as-processed condition and after oxidation at 1000°C for up to 500 h 335

Fig. B.6.99. Representative load vs displacement curves of a composite with a BN/Al_2O_3-TiO_2/BN interface in the as-processed condition and after oxidation for 200 h each at 500°C, 750°C, and 1000°C 336

Fig. B.6.100. Compositional depth profiles on a composite with a BN/Al_2O_3-TiO_2/BN interface in the as-processed condition (a) Fiber and (b) Trough 337

Fig. B.6.101. Compositional depth profiles on a composite with a BN/Al_2O_3-TiO_2/BN interface after 500 h oxidation at 1000°C (a) Fiber and (b) Trough 338

Fig. B.6.102. Fracture surface of a CVI 1054 composite (BN/mullite/BN interface) in the as-processed condition 339

Fig. B.6.103. Fracture surface of a CVI 1054 composite exhibiting brittle fracture after 24 h oxidation at 1000°C 340

Fig. B.6.104. Fracture surface of a CVI 1054 composite after oxidation at 1000°C for 200 h 341

Fig. B.6.105. Fracture surface of a CVI 1054 composite after 500 h oxidation at 1000°C 342

Fig. B.6.106. Fracture surface of a CVI 1054 composite after oxidation for 200 h at (a) 500°C and (b) 750°C 343

Fig. B.6.107. Representative load vs displacement curves of a composite with a BN/mullite/BN interface in the as-processed condition and after oxidation for up to 500 h at 1000°C 344

Fig. B.6.108. Representative load vs displacement curves of a composite with a BN/mullite/BN interface in the as-processed and oxidized conditions 345

Fig. B.6.109. Fracture surface of a Nextel/SiC composite with a mullite/C interface (CVI 997) in the as-processed condition 346

Fig. B.6.110. Fracture surface of a CVI 997 composite after oxidation at 1000°C for 24 h 347

Fig. B.6.111. Representative load vs displacement curve of a Nextel/SiC composite with a mullite/C interface 348

Fig. B.6.112. Compositional depth profile obtained on a trough in a Nextel/SiC composite with a mullite/C interface 349

Fig. B.6.113. Fracture surface of a Nextel/SiC composite with an Al_2O_3-TiO_2/C interface (CVI 998) (a) As-processed condition and (b) After oxidation at 1000°C for 24 h 350

Fig. B.6.114. Nextel/SiC composite with an Al_2O_3-TiO_2/C interface (a) Load vs displacement curve and (b) Compositional depth profile on a trough.. 351

Fig. B.6.115. Fracture surface of a Nextel/SiC composite with a C/mullite/C interface (CVI 999) (a) As-processed condition and (b) After 24 h oxidation at 1000°C 352

Fig. B.6.116. Representative load vs displacement curves of a CVI 999 composite. 353

Fig. B.6.117. Compositional depth profiles obtained on a CVI 999 composite (a) Fiber and (b) Trough 354

Fig. B.6.118. Fracture surface of a Nextel/SiC composite with a C/Al_2O_3-TiO_2/C interface (CVI 1000) in the as-processed condition 355

Fig. B.6.119. Representative load vs displacement curves of a composite with a C/Al_2O_3-TiO_2/C interface in the as-processed and oxidized conditions 356

Fig. B.6.120. Fracture surface of a CVI 1000 composite showing brittle fracture after oxidation for 200 h at 1000°C 357

Fig. B.6.121. Compositional depth profile obtained on a CVI 1000 composite in the as-processed condition (a) Fiber and (b) Trough 358

NOMENCLATURE AND ABBREVIATIONS

Nicalon	A Si-C-O fiber, trademark of Nippon Carbon Company
Nextel 440	An Al_2O_3-SiO_2-B_2O_3 fiber, trademark of 3M Company
TMOS	Tetramethoxy silane
TEOS	Tetraethoxy silane
ASB	Aluminum sec-butoxide
C	Carbon
BN	Boron nitride
E	Young's modulus
υ	Poisson's ratio
α	Coefficient of thermal expansion
MI	Mullite sol or gel obtained from ASB/TMOS combination, with the gel dried at 60°
MII	Mullite sol or gel obtained from ASB/TEOS combination, with the gel dried at 60°C
EI	Mullite sol or gel obtained from ASB/TEOS combination, with the gel dried at 110°C
MEI	Mullite sol or gel obtained from ASB/TEOS combination using 2-methoxy ethanol as solvent
ATI	Aluminum titanate sol or gel, with the gel dried at 60°C
ATII	Aluminum titanate sol or gel, with the gel driet at 110°C
DSC	Differential scanning calorimetry
XRD	X-ray diffraction
AES	Auger electron spectroscopy
SEM	Scanning electron microscope

TEM	Transmission electron microscopy
CVI	Chemical vapor infiltration
CFCC	Continuous fiber-reinforced ceramic matrix composite
CMC	Ceramic matrix composite
FCVI	Forced flow-thermal gradient chemical vapor infiltration
ICVI	Isothermal chemical vapor infiltration
MTS	Methyltrichlorosilane
SiC	Silicon carbide
SAM	Scanning Auger Microprobe
In-situ fracture	A portion of the flexure bar broken in-situ for AES study
SiO_2	Silica
Al_2O_3	Alumina
TiO_2	Titania

CHAPTER 1

INTRODUCTION

During the last few decades there has been an increasing demand for high-performance materials for aerospace, military, and heat engine applications [1-4]. These materials are intended to perform for limited or extended service at elevated temperatures. Unfortunately, traditional and advanced metallic alloys do not possess the required attributes, such as thermal stability and good mechanical properties to perform well at those temperatures. Advanced ceramics, such as oxides, carbides, nitrides and borides, possess the desired characteristics and have the potential to extend the performance limits beyond those offered by the conventional metallic materials. Their outstanding properties, such as low density, high chemical stability, high hardness and low wear, high strength and elastic modulus, and high melting point, make them attractive for high-temperature structural applications.

Advanced ceramic materials, however, do not possess any significant stress-relieving mechanisms at low and intermediate temperatures, and are inherently notch-sensitive and brittle, susceptible to thermal shock and have low fracture toughness [3]. Their strength is governed by the catastrophic growth of a single crack developed from a small defect, and these flaws are typically less than 100 μm [5]. The fracture strength is directly dependent on the fracture toughness and inversely related to the defect size.

In order to improve the reliability of ceramics, two approaches have been employed [1]. The first approach involves improving strength by reducing the flaw size in the material. This involves the identification of the sources of the strength-deteriorating

defects followed by developing techniques to process ceramics with reduced frequency and size of defects to obtain uniform and high strengths.

The second approach is concerned with identifying means to improve the toughness or resistance to fracture, and hence some tolerance to flaws. This method includes the introduction of platelets, particles, whiskers, discontinuous fibers and continuous fibers to create barriers to crack propagation [6-15]. Some of the most marked improvements in toughness have been obtained by the reinforcement of continuous fibers in ceramic matrices [11-15]. These materials are termed continuous fiber ceramic matrix composites (CFCCs).

CFCCs have three constituents: fiber, matrix and interface. Ideally, the fibers have high strength, high elastic modulus, good thermal and environmental stability over the entire service temperature regime. A range of oxide and non-oxide ceramic fibers are suitable and have been developed for high-temperature applications.

Potential ceramic matrix materials include silicon carbide, alumina, glass-ceramics, carbon and various glasses. During the matrix selection process, particular attention is paid to the following attributes: chemical and thermal compatibility with fiber, environmental stability, and ease of composite fabrication.

It is well recognized and widely accepted that the interface between the fiber and the matrix plays a key role in determining the composite properties [16-20]. Ideally, the interface is strong enough for axial load transfer and strength in the transverse direction, and yet, weak enough to make an impinging matrix crack to be deflected and enabling the fracture process to occur through several stages: debonding at the interface, crack deflection, fiber slip and pullout and ultimately fiber failure [1, 18].

The eventual deployment of the CFCCs for long-term, elevated-temperature oxidative environment applications will require the following: (1) interface materials that provide the desired weakening of the interfacial bond and possess the chemical stability over the entire regime of use temperatures and (2) chemical compatibility of the fiber/interface/matrix system. Hence, it is essential to develop interface materials having the following features over the entire application temperature regime: weak interfacial bond, thermal and environment stability, low thermal expansion mismatch and chemical stability with the fiber and matrix.

Limitations of the status-quo weak interfaces like carbon and boron nitride in CFCCs are their chemical instability at elevated temperatures in oxidizing environments. Hence, alternative oxidation-resistant interface materials need to be identified and developed. Recent analytical and finite element modeling studies have indicated that low modulus interfacial coatings may be effective in reducing the residual radial stresses at the fiber-matrix interface in systems where the fiber has a lower thermal expansion coefficient than the matrix. Generally, metal oxides exhibit good oxidation resistance at elevated temperatures and possess thermal expansion close to those of Nicalon fiber (Ceramic grade, a trademark of Nippon Carbon Company, Yokohama, Japan), Nextel 440 fiber (a trademark of 3M Co., Minnesota, from Chapter 3 onwards, it would be referred as Nextel), and the SiC matrix. Thermomechanical modeling studies identified that two interface materials, mullite, and aluminum titanate, may be effective in reducing the residual radial stresses and promote good fiber pullout properties of the composite. Oxides could be prepared with high purity at a relatively low temperature by a sol-gel

process. Hence, the sol-gel process was chosen for depositing the oxides in the present study.

The objectives of the present research are:

(1) Synthesize and characterize the mullite and aluminum titanate precursor sols and gels;

(2) Develop procedures for fabricating Nicalon/SiC and Nextel/SiC composites with sol-gel derived oxide interfacial coatings; and

(3) Conduct flexure testing of the fabricated composites at room temperature in both as-processed and oxidized conditions and characterize the resulting fracture surfaces using a scanning electron microscope. On selected as-processed and oxidized samples, perform transmission electron microscopy analysis of the fiber-matrix interfaces and Auger electron spectroscopy analysis for determining the interface debonding characteristics.

In the present study, the effect of sol-gel derived oxide interfacial coatings on the mechanical properties of Nicalon/SiC and Nextel/SiC composites was investigated. However, the difficulty of synthesizing aluminum titanate at temperatures < 1200°C proved to be a problem. On the positive side, Nicalon fibers dip-coated in an aluminum titanate precursor sol and heat-treated at 1000°C in air were not embrittled. On the basis of non-embrittlement of the fibers, alumina-titania was chosen as an alternative to aluminum titanate for the interface material. Thermochemical analyses of the oxides, mullite, alumina, and titania, with Nicalon, SiC, and processing conditions were conducted.

Additionally, mullite deposition by the sol-gel process on Nicalon fibers inevitably embrittled the fibers. To overcome this problem, a thin C layer (< 50 nm) was applied on fibers in some cases prior to the oxide deposition by the sol-gel process.

Given the propensity of the oxides to be attacked by HCl (a by-product of the SiC matrix deposition process), a thin C layer (< 50 nm) was deposited on the oxides prior to the SiC matrix infiltration. Hence, two different interfaces were investigated for Nicalon/SiC and Nextel 440/SiC composites, namely, oxide/C and C/oxide/C interfaces. For Nicalon/SiC composites, additionally, BN/mullite/BN, and BN/Al_2O_3-TiO_2/BN interfaces were studied. Nicalon/SiC composites with C (< 100 nm thick) and BN interfaces served the purpose of control samples and were also fabricated.

Nicalon/SiC composites with C, mullite/C, Al_2O_3-TiO_2/C, C/mullite/C, C/Al_2O_3-TiO_2/C, BN, BN/mullite/BN, and BN/Al_2O_3-TiO_2/BN interfaces were fabricated. The fabricated composites were flexure tested at room temperature in both as-processed and oxidized conditions. Flexure bars were oxidized at 1000°C in air for up to 500 h, and 200 h each at 500°C, and 750°C in air. After flexure testing, the resulting fracture surfaces were examined by a scanning electron microscope (SEM) to understand the fracture behavior. On selected as-processed and oxidized samples, the following studies were conducted: (1) transmission electron microscope (TEM) analysis of the fiber-matrix interfaces and (2) Auger electron spectroscopy (AES) analysis for determining the interface debonding characteristics.

Nextel 440/SiC composites with mullite/C, Al_2O_3-TiO_2/C, C/mullite/C and C/Al_2O_3-TiO_2/C interfaces were fabricated. Flexure testing of the fabricated Nextel 440/SiC composites in the as-processed as well as after oxidation was conducted. The flexure bars were oxidized at 1000°C for up to 200 h in air. The resulting fracture surfaces were examined using a SEM, and the interface debonding characteristics of selected samples were determined by AES.

Additionally, an elastic stress solution for calculating thermal stresses in composites with two film (interface) layers was derived. This stress solution was used to study the effect of two film (interface) layers between the fiber and matrix on the residual radial thermal stresses.

CHAPTER 2

LITERATURE SURVEY

2.1. Introduction

A composite material is defined as a material that consists of a reinforcement material distributed in a matrix material. The reinforcement material can be particles, whiskers, platelets, or continuous fibers. Typically, the composite material has properties that are distinct from each of its constituents. Composites are classified in terms of the matrix material into polymer matrix composites, metal matrix composites or ceramic matrix composites (CMCs). The objective of the fiber reinforcement is different in each case: for polymers, it is to increase stiffness and strength; for metals, it is to prevent plastic deformation particularly creep in addition to the enhancement of stiffness and strength; and for ceramics, it is to improve the toughness [1]. Ceramic matrix composites reinforced with continuous fibers are termed as CFCCs.

CFCCs have three constituents: fiber, matrix and interface. In this Chapter, the various constituents of CFCCs are discussed along with a literature survey for Nicalon/SiC and Nextel/SiC composites. Compilation of fibers along with the literature survey of Nicalon and Nextel fibers is presented first. Following this, the matrix processing techniques are discussed. Then, the interface role is highlighted followed by a literature survey for Nicalon/SiC and Nextel/SiC composites. Then, the pertinent sol-gel synthesis studies of mullite and aluminum titanate are presented followed by a section on flexure testing.

2.2. Fiber Reinforcements

The development of high performance composite materials for both civilian and military applications have been made possible by the availability of ceramic fibers with high modulus and tensile strength, low density, and good chemical and thermal stability. Both oxide and non-oxide ceramic fibers have been developed over the last forty years and are commercially available. These include alumina, mullite, zirconia, boron, carbon, boron nitride and glass fibers.

The oxide fibers, in general, have higher oxidation resistance than non-oxide fibers and that is reflected in their maximum use temperature in oxidizing environments. Among the non-oxide fibers, much research has been done in developing silicon carbide fibers for high temperature applications [22-26]. This is because a protective silica layer is formed on silicon carbide during high temperature oxidation and acts as a barrier to oxidation [27]. Although the oxide fibers have higher oxidation resistance than the non-oxide fibers, they suffer from the disadvantage of lower creep and grain-growth resistance.

Ceramic fibers also have low values of strain to failure. Their elongation to failure is typically less than 2 %. Also, the fiber flexibility is measured as 1/MR, where M is the bending moment and R is the radius of curvature [2]. Thus, fiber flexibility is given by $64/Ed^4$, and hence, is inversely related to Young's modulus, E, and fiber diameter, d. In the case of ceramic fibers, they usually have high E. Hence, a flexible ceramic fiber is possible only with a very thin fiber.

The tensile strength of the ceramic fibers is indirectly dependent on the fiber or filament diameter. As the fiber diameter decreases, the tensile strength increases. This

results from reduced or fewer flaws with the decreasing fiber diameter. Thus, tensile strengths close to theoretical predictions are possible with a reduced fiber size. For example, the tensile strength of whiskers (single crystal, diameter of a few μm, and length of a few mm) approaches the theoretical strength [2].

Ceramic fibers can be either continuous or discontinuous and are commercially available. Continuous ceramic fibers have the following advantages over discontinuous fibers: ease of handling, ability to be aligned and fabricated into intricate shapes in a composite, uniformity of properties in different directions, and less health hazard [2, 27].

Most of the non-oxide and oxide continuous fibers are compiled in Tables 1* and 2, respectively, along with their important mechanical properties [2, 27-31]. However, carbon, SiO_2, and other glass fibers are not included in the compilation. This is because there are many manufacturers for these fibers. The maximum use temperature, although listed in some of the fiber data sheets, is not included. This is because the maximum use temperature of the fiber depends on the matrix with which it is combined, application, and the test condition used. Also for most of the ceramic fibers, the strength decreases with increasing temperature, longer testing time and exposure to an oxidizing environment. From Tables 1 and 2, it is clear that the ceramic fiber diameter ranges from 3 to 140 μm, the tensile strength varies from 1.0 to 7 GPa, the tensile modulus ranges from 76 to 435 GPa, the density varies from 2.3 to 4.2 g/cm^3, and the coefficient of thermal expansion ranges from 1.5 to 8.8 x 10^{-6}/°C.

* All tables are included in Appendix A.

The continuous ceramic fibers are usually produced by one of the following methods: sol-gel, chemical vapor deposition (CVD), slurry-spinning, melt-grown, chemical conversion of precursor fibers, or controlled pyrolysis of polymer precursors. The fiber formation process is critical because it influences the fiber properties and cost. The methods used for processing inorganic fibers with the exception of glass fibers are presented in detail along with extensive references by Bracke et al [32]. Inorganic fibers have been the subject of many articles in the literature, and notable reviews have been published by Weddell [27], Sowman and Johnson [30], Cooke [33], and Chawla [2]. In the next section, the discovery and literature survey for Nicalon fibers is presented. Following this, a literature survey for Nextel fibers is presented.

2.2.1. Discovery of Nicalon

Lot of effort has been expended on developing SiC fibers because of the attractive properties of SiC including high thermal stability, low density, high tensile strength and Young's modulus, good creep resistance and excellent oxidation resistance up to 1800°C [27]. The production of continuous SiC filaments was reported in 1966 by Galasso et al. [34], and subsequently, Yajima et al. [23] synthesized continuous SiC fibers from polycarbosilanes. The production of SiC fibers by the polymer precursor technique could be traced to the concept of producing carbon fibers [35]. During the carbon fiber synthesis from polyacrylonitrile or certain kinds of mesophase pitch, the skeleton of carbon remains after pyrolysis. Similarly, by heating a suitable organometallic polymer, a skeleton comprising of Si and C can be obtained. Utilizing this concept, Yajima et al. [23] succeeded in producing continuous SiC fibers from polycarbosilanes.

Polycarbosilane is a generic term for organosilicon polymers with -Si-C bonds [35]. Yajima et al. [23] obtained polycarbosilane (PCS) from dimethyldichlorosilane as the starting material. First, dodecamethylcyclohexasilane (DMCHS) was obtained from dimethyldichlorosilane by the addition of chips of a lithium wire in a tetrahydrofuran solvent. Subsequently, the DMCHS was ring-cleaved and polymerized in an autoclave around 400°C for 48 h to obtain PCS. Then, the PCS was dissolved in benzene to yield a viscous liquid. The viscous liquid was then stretched by means of a glass rod to result in fibers of 10-20 μm in diameter. From the fibers obtained, benzene was evaporated to result in a brittle fiber made up of polymers with an average molecular weight of 1500. Subsequently, the organosilicon fiber was heat-treated at 1000°C for 2 h in vacuum to obtain a black and metallic luster fiber with a yield of 60 weight %. The resulting fibers were then heat-treated at 1200°C, 1300°C, and 1500°C, respectively, for at least 2 hours in vacuum. They reported that the tensile strength of the fibers after heat treatment at 1200°C, 1300°C, and 1500°C was about 3.43 GPa which was close to that of SiC whiskers. Subsequently, Yajima et al. [24] reported a tensile strength of 3.43 GPa and a Young's modulus of 294 GPa for the above SiC fiber. They also reported that the fiber comprised of ultrafine-grain crystallites of β-SiC with no apparent fiber texture measurable by X-ray diffraction and high-voltage electron microscopy. Nippon Carbon Company commercialized the production of continuous SiC fibers based on Yajima et al.'s process [23] and made Nicalon commercially available in 1979 [36]. Subsequently, Yajima et al. [25] synthesized PCS from polydimethylsilane and conducted a structural study of PCS by infrared spectra, chemical analyses, and nuclear magnetic resonance spectra.

In a series of articles starting in 1978, Hasegawa and co-workers [25, 37-40] reported the synthesis of polycarbosilanes by different procedures, examined their structure, and determined the properties of the resulting silicon carbide fiber. In the 1989 article, Hasegawa [40] summarized that the cured polycarbosilane fibers are converted into the SiC fiber by five stages and is shown in Fig. B.2.1[Δ] . In the first stage, the cross-linking concentration is increased by the dehydration between the silanol groups in the cured PCS fiber [40]. In the second stage, the cured PCS fiber is converted into the inorganic structure by the decomposition of the side chains. During this process, a large gas evolution takes place along with a density increase. In the third stage, there is a gradual increase in the density with increasing temperature, and the inorganic products have an amorphous structure. In the fourth stage, gas evolution occurs by the reaction between the Si-O bonds and the excess carbon along with the crystal growth of β-SiC. In the final stage, the gas evolution continues to occur. Figure B.2.2 is a flow diagram for producing Nicalon fibers [41].

Okamura [35] and Yajima [26] published comprehensive reviews on the production of ceramic fibers from polymer precursors. Okamura [35], in particular, gives a historical development of polycarbosilane from different starting materials.

2.2.2. Literature Survey for Nicalon Fibers

Nicalon has been supplied by Nippon Carbon Company since 1979 and have been available in different grades: standard, ceramic, high volume resistivity (HVR) and low volume resistivity (LVR). Recently, Hi-Nicalon, a silicon carbide fiber with a low oxygen content, has been developed and has been commercially available since 1992 [36].

[Δ] All figures are included in Appendix B.

Mah et al. [42] determined the tensile strength of individual Nicalon fibers after heat treatment at 1200°C, 1300°C, and 1400°C, in three environments: Air, argon and vacuum. They reported that the Nicalon fiber strength degraded at temperatures above 1200°C, and was independent of the test environment, with a drastic tensile strength reduction taking place in vacuum. They attributed this strength reduction of the fibers to the evaporation of CO (identified by secondary ion mass spectrometry, SIMS) and the grain growth of β-SiC. Further, the tensile strength at 1300°C and 1400°C, was higher than at 1200°C in air. They ascribed this increase in strength to the formation of the protective SiO_2 layer on the fiber surface, which suppressed the CO evolution.

Simon and Bunsell [43] studied two types of standard Nicalon fiber, namely, NLP 101 and NLM 102, having some microstructural differences. They conducted tensile tests of single fibers over a temperature range of 24°C to 1300°C, in air and argon for NLP 101 fibers, and in air for NLM 102 fibers. They reported that the drop in strength above 1000°C was higher in NLP 101 fibers than NLM 102 fibers. They observed that the NLP101 fibers had a glassy (amorphous) structure, while the NLM 102 fibers were microcrystalline with a SiC grain radius of 1.7 nm. In a subsequent study, Simon and Bunsell [44] conducted creep testing of the above fiber types and concluded that both the fiber types crept at temperatures above 1000°C.

Researchers at Celanese Research Company conducted thermal stability studies in air, argon, and nitrogen environments on two different grades of Nicalon: standard (NLP 101) and ceramic (NLM 202) [45-47]. The empirical formulae of the standard and ceramic grade fibers were $SiC_{1.1}O_{0.5}$ and $SiC_{1.4}O_{1.3}$, respectively. They reported that both fibers exhibit tensile strength reductions following heat treatment above 1200°C, with the

fiber failure mechanism dependent upon the environment. For example, the grain growth played a dominant role in the strength reduction in argon for NLP-101 fibers. They reported that the SiC fibers were polyphasic on both local and bulk levels. Sawyer et al. [46] observed the presence of heterogeneous local particles, and the bulk fiber chemistry comprised of a mixture of Si-C, Si-O, and Si-X species. The Si-X can contain overlapping species (for example, mixed O-Si-C). Clark et al. [47] reported that the ceramic grade Nicalon had higher degradation resistance and strength retention than the standard grade. They noted that both fibers were microcrystalline with a crystallite size of about 2.5 nm in diameter. The standard grade exhibited considerable grain growth of β-SiC, while the ceramic grade did not exhibit any marked grain growth in argon at elevated temperatures. They inferred that the lower oxygen level resulted in higher thermal stability and better mechanical properties.

Fareed et al. [48] conducted tensile testing, SEM, DSC, thermogravimetric and differential thermal analyses on ceramic grade Nicalon yarn exposed to 600°C, 1000°C and 1300°C, in air and argon. Based on their study, they concluded the following: (1) SiC oxidation occurs at temperatures > 600°C, (2) tensile strength in argon is higher than in air for all the temperatures investigated, (3) thermal exposure at 1300°C results in fiber sintering, and severe surface degradation in air, and argon, and (4) fracture surfaces of fibers exposed to 1300°C are planar, while at temperatures ≤ 1000°C, they show mirror-mist-hackle-crack branching.

Johnson et al. [49] conducted mass-spectrometric vapor pressure studies on ceramic grade Nicalon fibers from 1000°C to 1390°C and SEM studies on the exposed fibers. They reported that the vaporization is kinetically limited with the release of SiO

being predominant. Sawyer et al. [46] reported that the Nicalon fiber surfaces contained high concentrations of Si-O bonding which could be depleted over 90% by heat treating at 1400°C in argon for 12 h. However, Mah et al. [42] reported CO as the major vapor species from Nicalon fibers. Johnson et al. [49] attributed this difference in observation to the inability of the SIMS technique used by Mah et al. [42] to detect condensable species.

Maniette and Oberlin [50] conducted TEM studies on three Nicalon fiber types with some microstructural differences: NLP 001, NLP 101 and NLP 201. In addition, the NLP 201 was heat-treated for 48 h in air at 1300°C. They reported that the Nicalon fiber types were crystalline, the exception being NLP 001, with the SiC crystal size of 2 nm (101), 3 nm (201) and up to 7 nm (201 heat-treated). Laffon et al. [51] studied the structure of Nicalon-based ceramic fibers by several techniques and proposed a model. The Nicalon fiber is comprised of pure β-SiC embedded in a continuum of tetrahedral SiC_xO_y (with $x + y = 4$). Porte and Sartre [52] reported the presence of a silicon oxycarbide phase (SiC_xO_y), in addition to SiC, SiO_2, and C, in Nicalon fibers by a X-ray photoelectron spectroscopy study.

Pysher et al. [53] determined tensile strengths and Young's modulus of ceramic grade Nicalon, and four other ceramic fibers from room temperature to 1400°C in air. Their tensile strength results are summarized in Figure B.2.3, and Nicalon exhibited the highest strength among the five fibers tested at temperatures above 1100°C. They concluded that the internal void formation and oxidation limit the high-temperature use of SiC-based fibers. Kim and Moorhead [54] studied the tensile strength of Nicalon fibers after exposure to the following environments: (1) H_2-H_2O atmospheres for 10 h at

1000°C and 1200°C and (2) air for 2 to 100 h at 800°C to 1400°C. They inferred the following: (1) in H_2-H_2O environments, the most severe reduction in strength occurred in dry H_2 due to the reaction between SiO_2 in the fiber and the H_2 gas, (2) in air, the fiber strengths decreased rapidly between 1 to 5 h exposure, and thereafter, was either increased or decreased at a lower rate, and (3) the beneficial effect of a SiO_2 layer in air was reduced, when it was too thick.

Tan et al. [55] performed a microwave nitrogen plasma treatment on Nicalon fibers and studied the surface chemical changes with X-ray photoelectron spectroscopy and Auger electron spectroscopy. They observed that new functional groups, such as C-N, Si-O-N and Si-N, were introduced on the surface, and the level of nitradation increased with an increase in the applied microwave power. Further, there was no reduction in strength, which inferred that the nitrogen plasma treatment may be an effective pretreatment of SiC fibers. Bleay et al. [56] performed an electron probe microanalysis of a Nicalon fiber and reported that it contained 54.9 wt.% Si, 32.1 wt.% C, and 11.6 wt.% O. Based on their fine structure studies of the X-ray emission bands, they concluded that the Nicalon fiber consisted of 46 vol.% SiC, 34 vol.% silicon oxycarbide and 20 vol.% free carbon. Also, the oxygen content in the oxycarbide region varied with location, with the outermost fiber regions being richer in oxygen. Further, they proposed that the silicon oxycarbide and free carbon formed an amorphous network surrounding the SiC microcrystallites, which were several micrometers in diameter.

Jia et al. [57] conducted tensile creep tests of Nicalon single filaments in argon at 1300°C at stress levels of 300 to 700 MPa. They reported that the fibers exhibited only primary creep and described a rheological model to explain the fiber deformation. For the

test conditions utilized, the thermogravimetric (TGA) and TEM analyses suggested that the Nicalon microstructure was unstable, resulting in a weight loss and SiC grain growth. They attributed the instability to the decomposition of a silicon oxycarbide phase in the fiber, forming SiC and CO as products. Shimoo et al. [58] examined the thermal stability of Nicalon NL400 at 1300°C, 1400°C and 1500°C in argon and oxygen by TGA and XRD. In argon, Nicalon pyrolyzed to crystallize into β-SiC accompanied by SiO and CO evolutions. In oxygen, the pyrolytic reaction of the core was retarded by the oxide film formed around Nicalon. Further, the Nicalon coated with a silica film by an oxidation treatment pyrolyzed very little in an argon atmosphere, due to the suppression of the volatilization of SiO and CO by the silica layer.

The thermal degradation of the Nicalon fibers NLM-202 in an inert gas flow at atmospheric pressure was theoretically investigated by conducting thermodynamic calculations in the Si-C-O-H system, and the results were compared with the TEM studies in the literature [59]. Coustumer et al. [60] determined the surface roughness and observed that the NL-200 Nicalon fiber surface shows periodic roughness around its circumference. They reported that the deepest and the smoothest roughness detectable is around 70 to 100 nm, and 1 to 4 nm, respectively. Belitskus [61] has provided a comprehensive literature review on Nicalon fibers.

Recently, Takeda et al. [62] reported the development of SiC fibers with remarkable thermal stability by reducing the oxygen content. Electron beam irradiation in a helium stream was used for curing the PCS fibers, and then the fibers were pyrolyzed in an inert atmosphere. In a subsequent article [63], they reported the tensile strength and elastic modulus of the fibers to be 2.8 GPa and 270 GPa, respectively. In 1994, Takeda

et al. [64] synthesized SiC fibers with various C/Si atomic ratios and studied the microstructure, thermal stability, oxidation and creep resistance. Among the fibers studied, they concluded that the near stoichiometric SiC fiber exhibited remarkable mechanical and thermal properties. Berger et al. [65] studied the microstructure and thermomechanical stability of a low oxygen (0.5 wt%) Nicalon fiber. They reported that the continuous Si-C-O phase was absent, and the fiber consisted of β-SiC grains of 5-20 nm in diameter and turbostratic aggregates of carbon 2-5 nm in diameter. The Young's modulus was around 300 GPa at room temperature, which remains the same up to 1200°C in air. The reduction in strength even at temperature as low as 800°C is attributed to the oxidation of the carbon-rich surface in the new fiber. Further, SiC is oxidized at elevated temperatures, and above 1200°C, it forms a thick cristobalite layer on the fiber surface, with defects at the glass/ceramic interface.

2.2.3. Literature Survey for Nextel Fibers

Commercially available Nextel fibers are all produced by sol-gel processes. In the sol-gel process of making the oxide fibers, the following steps are involved [2, 61]: Formulation of the sol by mixing appropriate compounds to form a homogeneous solution, concentration of the sol to result in a viscous gel by heating or catalysis, spinning the resultant precursor fiber, and finally, calcination to obtain the oxide fiber. A schematic of producing a Nextel 610 fiber, an alumina fiber, is shown in Figure B.2.4 [2]. The selected properties of the Nextel fibers are summarized in Table 2. Nextel 440 and Nextel 480 ceramic fibers have the same chemical compositions: Al_2O_3-70 wt.%, SiO_2-28 wt.%, and B_2O_3- 2 wt.%. The function of B_2O_3 is to promote densification and mullite formation [30]. The Nextel 480 fiber is essentially a mullite fiber. The Nextel 440

fiber consists of a mixture of Al_2O_3, in eta or gamma form, and amorphous SiO_2, which on heat treatment at temperatures above 1200°C convert to all-mullite fibers. Hence, the maximum use temperature for this fiber is 1200°C.

Holtz et al. [66] conducted tensile strength measurements, of Nextel 312, Nextel 440, and Nextel 480, at room temperature after heat treatments at elevated temperatures in air, hydrogen, and vacuum. All the three fibers exhibited the lowest tensile strength on exposure to hydrogen at temperatures above 1000°C. In addition, they also determined the tensile strength and Young's modulus as a function of test temperature in air for the three fiber types. Among the fibers, the Nextel 480 had the highest tensile modulus at all temperatures with the modulus significantly decreasing above 1000°C. Their tensile strength measurements are summarized in Fig. B.2.5 [66]. Nextel 312, Nextel 440, and Nextel 480 fibers underwent a significant strength reduction above 800°C, 1000°C, and 800°C, respectively. Based on their creep measurements at two stress levels, they ranked the fibers for creep resistance in the following descending order: Nextel 480, Nextel 440, and Nextel 312.

Johnson et al. [67] reported the properties of Nextel 480 ceramic fibers. They conducted room-temperature measurements of tensile strength, and tensile modulus after exposure up to 1400°C in air, vacuum, and hydrogen. They also determined the tensile strength and creep rate (at stress levels of 69 MPa and 138 MPa) at temperatures up to 1300°C in air. They concluded that the Nextel 480 fiber is thermally stable, retains sufficient integrity to withstand fabrication temperatures up to 1300°C, and can be used for structural applications up to 1200°C.

The stability of Nextel 312 fibers in basic, acidic, and neutral environments was detected by photoacoustic Fourier transform infrared spectroscopy [68]. The fibers upon exposure to the above conditions formed boric acid, which converted to B_2O_3 at high temperatures. The formation of B_2O_3 enhanced the surface stability and improved the adhesive properties of the fibers to a polymer matrix.

The effect of high-temperature exposure (900°C, 1100°C, and 1300°C) on the tensile strength of Nextel 610 fibers was examined by Xu et al. [69]. They determined the tensile strength using a two-parameter Weibull distribution and concluded that the grain growth was the main cause for the fiber strength reduction. Also, the defects, such as surface flaws, formed during the high-temperature exposure, which was another reason for the fiber strength degradation. Wilson et al. [70] reported the high-temperature tensile strength and creep properties of Nextel 720 in the temperature range of 1000°C to 1300°C. They observed that Nextel 720 fibers had a creep rate three orders of magnitude less than Nextel 610 fibers, and retained 85% of its room-temperature tensile strength at 1200°C. The remarkable performance of Nextel 720 fibers were ascribed to their unique two-phase microstructure comprising of mosaic and elongated grains of α-alumina and mullite. Figure B.2.6 shows their comparison of strain rate vs stress for Nextel 720 and some selected commercial polycrystalline oxide fibers. Earlier, Wilson et al. [71] had reported that the creep rate of the Nextel 480 fibers (all-mullite fiber) was fifty times less than the Nextel 610 fibers (all-alumina fiber). Their result is consistent with the fact that the diffusivities of Si^{4+} and O^{2-} in mullite is lower in comparison to Al^{3+} and O^{2-} in alumina. Tressler and Di Carlo [72] provide a good review

on the issues related to the current status of creep and stress rupture of advanced ceramic fibers. In the following section, several matrix processing techniques are presented.

2.3. Matrices and Matrix Processing Techniques

Potential ceramic matrix materials include glass and glass-ceramics, oxides, carbides, borides, nitrides, sialons, silicides, intermetallics, and carbon, and some of the important matrices are compiled in Table 3 [2, 61, 73-78]. Glass and glass-ceramics are easy to fabricate to theoretical density and are usually processed by slurry infiltration, sol-gel, or melt infiltration. Ceramic matrices, such as carbides, oxides, borides, nitrides, sialons, and silicon oxycarbides, are difficult to process to full density, and are typically processed by chemical vapor infiltration (CVI), sol-gel, polymer pyrolysis, reaction bonding, directed melt oxidation (DIMOX), or slurry-infiltration.

The desired characteristics of a ceramic matrix material are the following [2, 12, 61, 73, 74]: low density, high toughness, good resistance to creep, fatigue and impact, and ease of fabrication. In addition, they must be chemically inert with the fiber reinforcement during both processing and service, form a mechanical or frictional bond with the reinforcement, should not damage the reinforcement physically, should be chemically, thermally, and environmentally stable, retain strength and modulus at high temperatures, and possess the desired coefficient of thermal expansion. In this section, different methods of processing ceramic matrix composites are presented and will be limited to those used for processing CFCCs.

Processing methods used for producing CFCCs fall in to four categories [2, 61, 74-77]: traditional mixing and slurry infiltration, chemical synthesis, liquid infiltration,

and in-situ chemical reactions. The traditional mixing and slurry infiltration technique is widely used for processing glass and glass-ceramic matrices, and are typically hot-pressed near glass-softening temperatures. Chemical synthesis methods include sol-gel and polymer pyrolysis, and are employed to make matrices of oxides, carbides, oxycarbides, oxynitrides, and nitrides. Liquid infiltration techniques include melt infiltration and directed melt oxidation/nitration and are utilized to make matrices of oxides, nitrides, and intermetallics. Methods that rely on in-situ chemical reactions, such as chemical vapor infiltration, and reaction bonding, are employed for making ceramic matrices including carbon, carbides, borides, nitrides, and oxides.

2.3.1. Traditional Mixing and Slurry Infiltration Techniques

The slurry infiltration method involves the incorporation of fiber reinforcements into an unconsolidated matrix followed by matrix consolidation using hot pressing and is shown schematically in Fig. B.2.7 [73]. A fiber yarn is first passed through a slurry containing matrix powder and additives (carrier liquid, binder, dispersant, etc.). The resulting slurry-impregnated yarn is wound on to a mandrel and dried. The impregnated prepegs are then cut, stacked and densified to form the final composite by hot pressing. If a binder is present, it is burnt-out prior to the hot pressing step. In order to obtain full densification, hot pressing is done near the glass-softening temperature. This will enable the glass to flow readily and fill the interstices between individual fibers within the yarn prepregs. This method is widely used for making glass and glass-ceramics and is well documented by Prewo et al. [73]. They divided the fabrication processes into three types: hot pressing of infiltrated unitapes and fabric lay-ups, hot matrix transfer into woven preforms, and hot injection molding of chopped fiber compounds or preforms. Utilizing

this method, Prewo et al. [73] have fabricated complex-shaped composite articles and composites greater than 98% theoretical density. Some of the composites that have been fabricated by the slurry infiltration technique include Nicalon reinforced with barium-magnesium aluminosilicate (BMAS), barium aluminosilicate (BAS), lithium aluminosilicate (LAS), and calcium aluminosilicate (CAS) matrices.

The slurry infiltration method has the following advantages: ease of fabrication, and ability to make complex shapes. However, it has its limitations [61, 74, 77]: labor-intensive, confined to 1- or 2 dimensional fiber orientations, inhomogeneous in the matrix, expensive, and cannot be used for all refractory matrices of interest. This method is presently confined to glass and glass-ceramic matrices due to the non-availability of fibers resistant to high-temperature degradation or oxidation. In addition, this method has been used for processing the silicon nitride matrix, which densifies by liquid-phase sintering. The slurry infiltration method is described in detail in Chawla [2], Belitskus [61], Prewo et al. [73], Cornie et al. [74], and Warren and Lundberg [77].

2.3.2. Chemical Synthesis Methods: Sol-Gel and Polymer Infiltration and Pyrolysis

Chemical synthesis methods include sol-gel, and polymer infiltration and pyrolysis. Some of the potential advantages realized by using them to process CFCCs include [74, 79]: (1) ability to form homogeneous high-purity single-phase matrices and multiphase matrices with a uniform constituent distribution, (2) lower processing temperatures compared to conventional processing techniques, (3) ease of infiltration and fabricating complex shapes, (4) reduction in damage to reinforcement during processing and (5) low cost. However, both methods have the following disadvantages: large shrinkage during processing, matrix cracking, residual fine pores, and the presence of

carbon and hydroxyl groups after drying, multiple infiltration-cycles, long-processing times and high cost of polymer precursors. Utilizing the polymer pyrolysis method, CFCC matrices including silicon carbide, silicon nitride, silicon oxycarbide, silicon oxynitride, boron nitride, aluminum nitride, and mixture of these materials can be easily prepared. By employing the sol-gel technique, CFCC matrices of oxides, such as mullite, alumina, silica, etc., can be readily processed. There have been instances where polymer pyrolysis and sol-gel methods have been used in combination.

There are two types of sol-gel techniques [79]: colloidal and metal-organic polymerization. In the colloidal process, the surface chemistry is exploited to suspend very fine particles in a solution to obtain a colloidal sol. This sol suspension is then gelled by forming a cross-linked particulate network. Then, the gel material is dried to obtain a porous and amorphous ceramic body, which may then be calcined, and densified by sintering. In the metal-organic polymerization method, the reactivity of metal-organic precursors is utilized, and in particular, metal alkoxides are the widely used precursors. Metal alkoxides are $M(OR)_n$ compounds, where R is an organic group, and n is the valence of the metal M. They are sensitive to moisture, heat and light. Depending upon the matrix requirement, either single or multiple metal alkoxides are polymerized by controlled hydrolysis (hydrolytic polycondensation) to produce a cross-linked gel. This gel may then be dried, calcined, and densified by sintering to produce the desired oxide.

The processing of a CFCC matrix by the sol-gel method involves the formation of fiber gel prepregs followed by a heat treatment and final densification of the matrix by hot pressing [80]. Typically, the fiber gel prepregs are obtained by dipping the yarn in a precursor sol of the desired matrix. There are three methods for forming the fiber gel

prepregs, namely, strand dipping, wet winding, and dry winding. Usually, cracks are formed during drying due to shrinking and can be healed by repeating the impregnation/drying cycles. The prepregs are then calcined in air, usually between 500 to 700°C. The infiltration, drying, and calcination procedure is carried out 4-20 times until a certain volume percentage of matrix (for example, 50%) is attained. Subsequently, the prepregs are hot pressed at a suitable temperature for matrix densification, and to result in the desired composite. Figure B.2.8 is a comparison of the preparation of CFCCs using sol-gel and slurry infiltration methods. Some of the CFCCs fabricated using sol-gel include Tryanno SiC fiber-reinforced zirconia titanate, Nicalon fiber-reinforced aluminum phosphate, and carbon reinforced with matrices of alumina, mullite and SiO_2.

According to Mah et al. [79], the CFCCs can be processed by polymer infiltration and pyrolysis in four steps: (1) polymer infiltration of the reinforcement preform, (2) densification of the polymer impregnated preform, (3) cure of the polymer matrix, and (4) pyrolysis and conversion of the cured polymer into the ceramic matrix. The required properties of ceramic matrix precursor polymers are ease of processing, air stability, high ceramic-conversion yield, and low pyrolysis temperature. The volume contraction during the polymer-ceramic transition is significant, and hence, methods to combat material shrinkage have been developed. These include the development of high ceramic yield polymers as matrix precursors and the usage of matrix material powder as a filler in ceramic precursor polymer. Some of the CFCCs processed using polymer infiltration and pyrolysis include Nicalon/Blackglas, Nextel 440/Blackglas, and Nicalon/Silicon oxynitride composites.

A schematic flow diagram of forming a fiber-reinforced Blackglas ceramic composite is shown in Fig. B.2.9 [81]. As shown in the figure, the ceramic fiber preform is infiltrated with a blackglas resin in a resin-transfer mold to form the fiber-reinforced blackglas polymer composite. In the second stage, the composite is pyrolyzed in nitrogen at 1000°C to obtain a composite with 25 to 30% porosity. Then, the composite is densified by multiple infiltration of the polymer followed by the pyrolysis step. The sol-gel and polymer pyrolysis processes are described in detail by Belitskus [61], Cornie et al. [74], Mah et al. [79], Fitzer and Gadow [80], and Mazdiyasni [82].

2.3.3. Liquid Infiltration Techniques: Melt Infiltration and DIMOX

Liquid infiltration techniques include melt infiltration and DIMOX. Melt infiltration is well developed for metallic systems, but its application for ceramic systems has been limited [74]. It possesses the following advantages [83]: produce fully dense composites with good geometric and dimensional accuracy, easy to process complex net-shape composites in one step, and good matrix homogeneity. However, melt infiltration has its limitations [2, 74]: high processing temperature leads to increased fiber-matrix interactions, ceramic melts have higher viscosities than metal melts leading to low rates and difficulty of infiltrating preforms, and the possibility of matrix cracking on solidification due to the thermal expansion mismatch between the fiber and the matrix. This method has been used for making fluoride and oxide matrices.

Hillig [83] at the General Electric Company has done considerable work on melt infiltration. He discussed the theory, and addressed the issues involved in successfully adapting melt infiltration to produce ceramic matrix composites. The issues include chemical reactivity, viscosity, wetting, and desirable properties of the reinforcement and

the matrix material. A schematic of the pressure infiltration process is shown in Fig. B.2.10 [2] and consists of a radio frequency heated graphite component in a vacuum hot-press to preheat the fiber preform as well as to melt the matrix material. The matrix material is first melted, and wicks into the porous preform by capillary pressure. The matrix then crystallizes upon cooling. Pressure or vacuum applications can aid the infiltration process. Utilizing the melt infiltration method, Hillig and co-workers have synthesized SCS-6 fiber reinforced strontium aluminosilicate matrix composites [84]. The composite exhibited damage-tolerant behavior at both room temperature and 1450°C.

The DIMOX process was discovered by Newkirk and is well developed for producing CFCCs [61, 85]. This method has the following advantages: low cost, low processing temperature for matrix growth, microstructural tailorability, and net-shape processing of complex parts with good dimensional accuracy. However, it has the limitation that the residual metal content can possibly limit the high-temperature performance of the composite. A schematic representation of the DIMOX process to produce a net-shape composite is shown in Fig. B.2.11 [2]. Typically, ceramic matrices, such as oxides, nitrides, borides, carbides, and titanates, can be processed using this method.

Fareed and co-workers at DuPont Lanxide Corporation have synthesized Nicalon fiber-reinforced aluminum oxide composites using this method [86, 87]. First, the Nicalon fabric preform was given a duplex coating of BN and SiC using a CVD method. The SiC layer protects the BN inner layer from oxidation and chemical attack during the matrix processing. BN serves the purpose of providing a weak interface between the fiber and the matrix. Then, the Nicalon preform is brought in contact with a molten

aluminum alloy at high temperatures (900°C to 1100°C). As a result, a three-dimensional interconnected network of α-alumina matrix grows into the preform, originating from the alloy/preform interface. However, in the matrix phase, an interconnected network of microscopic metal channels around few microns in diameter is present. The matrix growth process is sustained by the surface energy driving forces. As a consequence, the molten alloy wicks from the reservoir through the microchannels to the growth front and reacts to form the matrix. This process continues till the reaction front comes in contact with a gas-permeable barrier layer. This layer is normally applied to one or more external surfaces of the preform to enable the formation of a net-shape component. Notable reviews on the DIMOX process have been given by Belitskus [61] and Newkirk et al. [88].

2.3.4. In-situ Chemical Reaction Methods: Reaction Bonding and CVI

In-situ chemical reaction methods include reaction bonding, and chemical vapor infiltration. In the reaction bonding technique, the consolidation and densification of the crystalline ceramic matrices occur after the continuous fiber tows or preforms are slurry infiltrated [61]. Typically, the ceramic matrix of a slurry-infiltrated preform forms by a chemical reaction, which falls into three categories. In the first variation, the slurry-impregnated preform containing particulate materials are reacted with a gas media. In the second type, the reaction occurs due to the infiltration of a molten material into the slurry-impregnated preform containing particulate materials. In the third variation, the slurry-impregnated preform is made up of different types of particulate materials, which can react at elevated temperatures to form the desired matrix. The advantages of the reaction bonding method include [2, 61]: little or no matrix shrinkage; typically volume increase

occurs on reaction, resulting in a reduced porosity or effective filling of the preform pores; large volume fraction of fibers and continuous cloth preforms can be used; and low processing temperatures compared to sintering, which results in the likelihood of less fiber-matrix reaction. However, the method has the limitation of high porosity. Utilizing this technique, ceramic matrices, such as silicon carbide, silicon nitride, aluminum phosphate, and aluminum borates, have been produced.

Bhatt and co-workers at NASA-Lewis Research Center have synthesized and reported the properties of SCS-6 fiber reinforced silicon nitride composites and is outlined in Fig. B.2.12 [89-90]. In the first step, the SCS-6 fibers were wound onto an axially translating mandrel to produce a desired fiber spacing, and coated with a fugitive polymer binder. The fiber mats were then cut from this drum. High-purity silicon powder was attrition-milled to obtain an average particle size of 0.3 μm. This powder was mixed with an organic solvent and polymeric binder to obtain a dough of desired consistency. After this, the dough was rolled to obtain a silicon cloth of proper thickness. The fiber mat and silicon cloth were stacked in an alternate sequence to produce a multilayer preform. Then, the preform was debinderized, and hot pressed for consolidation. Finally, the consolidated preforms were nitrided in a nitridation furnace to transform silicon to silicon nitride.

Chemical vapor deposition is widely used for forming thin coatings of ceramic materials, such as carbon, carbides, borides, oxides, and nitrides [91]. Recently, a specialized form of CVD has been utilized for producing ceramic matrices in CFCCs, and is referred as chemical vapor infiltration [13, 15, 76, 92-97]. The CVI process involves the deposition of a ceramic matrix on the surfaces of a heated porous fibrous

preform from a gaseous precursor. Typically, commencing with a fibrous preform of open porosity of the order of 40-80%, the CVI technique produces CFCCs with a residual porosity in the range of 10-15%. The advantages realized using CVI include [2, 76, 92-94]: low processing temperature compared to the sintering temperature, resulting in relatively undamaged fibers during processing; fabrication of near net-shape parts of complex geometries; considerable flexibility in terms of fibers used and matrices formed; ability to use continuous fibers in pre-conceived beneficial orientations that remain undisturbed due to the absence of external pressure on preforms during CVI densification; and production of CFCCs with good mechanical properties at elevated temperatures. The limitations of the process are long processing times, expensive, and inability to eliminate residual open porosity. A number of ceramic matrices including carbon, oxides, carbides, borides, and nitrides can be processed using CVI techniques.

Bickerdike et al. [98] were the first to use the CVI process for infiltrating carbon into porous graphite bodies. This technique has matured commercially to the extent that 50% of the carbon/carbon composites manufactured are produced by CVI [93]. Jenkin [99] was the first to use the CVI process for fabricating a ceramic fiber-reinforced ceramic composite. He infiltrated chromium carbide into a fibrous alumina preform. The University of Karlsruhe, the University of Bordeaux, Society of European Propulsion, DuPont Lanxide Inc., Oak Ridge National Laboratory and Amercom have been key players in furthering the continued high interest in CVI processing [92]. At present, SiC matrix CVI composites are manufactured on an industrial scale, mainly for space and aeronautical applications [76]. Currently, 3M and DuPont Lanxide Inc. are using the CVI

process to fabricate filters for hot gas clean-up in advanced coal combustion systems [96].

In the CVI process of fabricating CFCCs, the preform made from ceramic fibers is the starting material, and has the shape of the desired final component [76]. The continuous-fiber preform may be 1D (D means dimension), 2D or 3D. Among these, the 2D preforms are widely used. They are made by stacking the ceramic fabrics in close contact with each other within a container (for example, graphite). Then, the preform is loaded into the CVI furnace for matrix deposition. Usually, prior to matrix densification of the fibrous preforms, an interface (for example, carbon or boron nitride) is deposited to enable a weak interface formation between the fiber and the matrix.

In the CVI process, the gaseous reactants infiltrate the porous fiber preform maintained at high temperatures and deposit the matrix material in the pore network of the preform via a standard CVD reaction [93, 97]. As the deposition continues, the CVD coating grows to produce the composite matrix. Typically, the CVI process imposes very little mechanical stress on the fibers, and by selecting a suitable fiber-interface-matrix system along with very little thermal expansion mismatch, a CFCC with minimal residual stresses can be produced.

During CVI, the main objective is to maximize the matrix deposition rate and minimize density gradients [97]. However, there is an intrinsic rivalry between the deposition and the mass transport of the gaseous species. Rapid deposition reactions usually produce severe density gradients, with the result that full densification occurs near the external regions and much lower densities in the interior surfaces. In contrast, very

slow deposition reactions require a long time for densifying the part, resulting in an uneconomical process.

CVI techniques can be classified into five categories based on the following [92]: whether the preform is isothermal or has a thermal gradient, and the way in which the gaseous species contact or flow through the preform. The five categories are summarized in Fig. B.2.13: type I, isothermal; type II, thermal gradient; type III, isothermal-forced flow; type IV, thermal gradient-forced flow; and type V, pulsed flow [93]. Among these, the isothermal CVI (ICVI) is currently the commercial method of choice.

In ICVI, the preform is placed in a hot wall deposition chamber, where the temperature is presumed to be uniform. The ICVI relies only on diffusion for species transport and typically is operated at a reduced pressure of 1 to 10 kPa for controlling the deposition rate. Details of this method are given by Naslain [76] and Besmann [93]. The ICVI process has the following limitations [61, 76, 93]: low densification rate, long processing times, overcoating of the outer surface due to rapid deposition before the infiltration is complete, and periodical removal for machining is required to open diffusion paths from the surface. However, it is commercially viable due to the fact that large number of preforms are infiltrated simultaneously and is applicable to both simple and complex geometries [76].

In order to surmount problems of slow diffusion and restricted permeability, an improved forced flow-thermal gradient (type IV) (FCVI) process has been developed at Oak Ridge National Laboratory (ORNL) [13, 91-94, 100-102]. In this method, alternative flow paths are provided to result in a continued forced flow of the gaseous species through the preform, even though some regions of the preform might have

become impermeable. Earlier, Jenkin [99] utilized a similar method, however, the reagent gas flow stopped (hence the infiltration), when a portion of the preform became impermeable.

The FCVI method employs both a pressure and thermal gradient on the preform (Fig. B.2.14) [91]. In FCVI, the fibrous preforms are confined in a graphite holder. The preform is placed in a reactor where one end is cooled, and the opposite end is heated to result in a thermal gradient across the preform. Typically, the reactant gases are forced through the cool-side of the preform at atmospheric pressure. The reactant gases undergo a surface reaction as they pass through the preform, resulting in the deposition of ceramic matrix and an effluent gas. During the SiC matrix deposition from chlorosilanes, the effluent gas has a poisoning effect on the rate of reaction. This poisoning along with the reactant depletion tends to reduce the deposition rate. However, the temperature of the gases are increased as they travel toward the hot-side of the preform, and this results in increased deposition rates. The deposition is controlled by increasing the temperature to offset reactant depletion and effluent gas buildup.

Routinely, Nicalon/SiC composites are prepared at ORNL, and the SiC matrix is typically deposited from methyltrichlorosilane (MTS) carried in hydrogen. Recent work has established that the SiC formation takes place not by a simple first order process, but via a complex reaction, with the overall reaction written [96]:

$$CH_3SiCl_3(g) \xrightarrow{H_2} SiC(s) + 3HCl(g) \quad (2.1)$$

A considerable amount of effort has been devoted to develop models for the CVI process, which has resulted in a better understanding [96]. These models require that the physical system and chemical behavior are represented. Accurate modeling requires the

simultaneous solution of a number of difficult problems, such as surface deposition, chemical kinetics, and flow. Besmann and co-workers [93, 96], and Naslain [76] have discussed in detail the issues in modeling along with a review of the literature. Modeling the CVI process is a multi-faceted task, and there are several obstacles to portray the CVI process accurately [103]: uncertainty of the chemical kinetics of the system; and limited understanding of the material transport properties of the porous preforms and the chemical reactive flow during ICVI through the porous preforms makes the transport calculations difficult. Among the existing models, the GTCVI developed by Starr [104] has proven to be practical for optimizing the ORNL FCVI process. The advantages of the FCVI process include [76]: significantly reduced processing time of one order of magnitude less than ICVI, and being well suited for thick-wall fiber preforms. However, it is limited to simple geometries. Using FCVI, Nicalon/SiC composites measuring over 12 mm thick has been fabricated within 14 hours. In contrast, a time span of weeks or months is required to process few millimeters thick components using ICVI.

2.4. Interface and its Significance

It is widely accepted that the interface between the fiber and the matrix plays a key role in determining the composite properties [16-20]. A strong interface in a CFCC may promote an effective load transfer between the fiber and the matrix, however, it will not arrest an impinging matrix crack, and the composite is more likely to fail in a brittle manner (Fig. B.2.15 (a) [2]). On the other hand, a weak interface will allow the oncoming matrix crack to be deflected and enable the fracture process to occur through several stages: debonding at the interface, crack deflection, crack bridging, fiber fracture

and fiber slip and pull-out (Fig. B.2.15 (a)) [2, 18]. All the above energy dissipating mechanisms promote improved fracture toughness and imparts a non-catastrophic mode of failure. From the above discussion, it is easy to infer that an optimum interface strength is desirable to maximize strength gains and obtain considerable toughness.

In this section, the stress-strain behavior of a composite is presented first along with the models for predicting critical matrix cracking stresses. Then, the toughening mechanisms in CFCCs are discussed. This is followed by a discussion of the residual thermal stresses that arise during processing in CFCCs. After this section, a literature survey of Nicalon/SiC composites and Nextel/SiC composites is presented.

2.4.1. Composite Fundamentals

2.4.1.1. Stress-Strain Behavior

The theory of fiber reinforcement indicates that significant strengthening is accomplished only if the elastic modulus of the fibers is higher than that of the matrix, and the tensile stresses can be transferred to the fibers [3]. A ceramic fiber has a higher strength and failure strain than a bulk ceramic material. The matrix serves an indirect purpose of holding the fibers intact and providing barriers to crack propagation between individual fibers. The stress transfer to the fibers is accomplished by the plastic or elastic deformation of the matrix.

Consider an unidirectional, long fiber composite subjected to an axial loading [1] in which the strain to failure of the fiber is higher than that of the matrix ($\varepsilon_f < \varepsilon_m$). Under this condition, the stress-strain behavior of the composite can be easily obtained by referring to the individual stress-strain behavior of the fiber and the matrix. As shown in

Fig. B.2.16 (a), at any composite strain, ε_c, prior to matrix fracture, the stresses in the fiber (σ_f) and the matrix (σ_m) are given by:

$$\sigma_f = E_f \varepsilon_c \; ; \qquad and \qquad \sigma_m = E_m \varepsilon_c \quad (2.2)$$

where E_f and E_m are the Young's moduli of the fiber and the matrix, respectively. Up to the fracture strain of the matrix, ε_{mf}, the composite properties including stress (σ_c) and the axial Young's modulus (E_c) can be derived from the rule of mixtures:

$$\sigma_c = \sigma_f V_f + \sigma_m V_m \; ; \qquad and \qquad E_c = E_f V_f + E_m V_m \quad (2.3)$$

where V_f and V_m are the volume fractions of the fiber and the matrix, respectively.

If the fiber volume fraction is very low, the fibers will fracture when the matrix fails, and the composite failure occurs immediately. In this case, the composite fracture stress can be obtained from the above equation. This is applicable to the situation left of the V_t line in Fig. B.2.16 (b). Above the critical or transition volume fraction, $V_f > V_t$, the fibers will sustain the load even after matrix failure, and the final composite fracture stress is given by:

$$\sigma_{cF} = \sigma_{fF} V_f \quad (2.4)$$

where the subscript F refers to the fracture condition.

The matrix withdraws from the fracture surface, when it fails. As a result, the matrix stress will attain its full value, σ_{mF}, at a distance behind the fracture surface. This distance corresponds to a load transfer length that is inversely dependent on the fiber/matrix bond. As a consequence, with a constant or increasing composite load, fracture continues to occur at regular intervals or spacings throughout the entire length of the composite. This phenomenon is referred as multiple fracture. The multiple crack

spacing in the case of a constant interfacial shear stress (frictional bonding), τ, is given by:

$$l_r = \sigma_{mf}\, r\, V_m / (2\tau\, V_f) \quad (2.5)$$

where r is the fiber radius. The model described above ignores the following effects: the presence of fibers on the fracture strain of the matrix, and the scatter in the fiber strength.

When a composite is progressively loaded, the rule of mixtures initially governs the stress-strain relationship of the tensile curve [105]. This is applicable to the linear elastic region of the theoretical stress-strain curve in Fig. B.2.17 [106]. The initial departure from the linearity of the stress-strain curve occurs upon matrix cracking, and the corresponding point is referred as the proportional limit. Matrix cracking arises from preexisting flaws, exemplified by a crack in the matrix with intact bridging fibers over its entire surface. In order for a non-catastrophic mode of failure to occur, the first crack in the matrix should extend indefinitely and break only a small portion of the fibers. With continued loading, matrix cracking continues to occur periodically. The matrix crack spacing is governed by a characteristic stress transfer length associated with the bridging fibers. These cracks split the composite into "blocks" of matrix held together by intact fibers, and this phenomenon is referred as "fiber-bridging" of matrix cracks.

The bridging fibers minimize crack openings, and hence, higher strains are required for matrix crack propagation. The increasing non-linear portion of the stress-strain curve is governed by the fiber properties, as conditioned by frictional interactions of fibers with the matrix "block". The ultimate tensile strength is determined by the fiber bundle failure, and the tail portion of the stress-strain curve influenced by the pullout of the broken fibers. Typically, the above failure mechanism is observed in composite

materials, including CFCCs, reinforced cements, glasses, and glass-ceramics. The described failure mechanism is applicable in cases where the fiber-matrix bonding is weak. On the other hand, if the fiber-matrix bonding is strong then a major portion of the fibers could break in the wake of the first matrix crack as it grows, and the composite will exhibit brittle fracture. The ultimate strength is restricted by the extension of a single dominant crack and is influenced mainly by the fracture resistance curve. The zone of bridging fibers behind the crack tip determines the type of the resistance curve and the steady-state toughness value.

The initial occurrence of matrix cracking is an important event and signifies the onset of permanent damage [107]. This is because, after this point, the fibers can be attacked by the environment via the matrix cracks. Hence, the theoretical prediction of the onset stress for matrix cracking has attained significance and has been the subject of many studies [108-115]. These studies predict the matrix cracking stress for an unidirectional composite subjected to certain conditions and can be divided into three categories: the energy balance approach, the short crack-fracture mechanics method and the local flaw model.

The prominent models in the energy balance approach are the following: Aveston, Cooper and Kelly (ACK) [108], Aveston and Kelly [109] Budiansky, Hutchinson and Evans (BHE) [110], Kuo and Chou [111], and Hsueh [112]. These models consider the state of the composite before crack initiation and after the completion of crack propagation. By balancing the energy changes that occur during these processes, the critical stress required for matrix cracking is evaluated. The short-crack fracture mechanics approach assumes a short starter crack and treats the case of a self-similar

crack propagation as a fracture mechanics problem. The important models in this category are the following: Marshall, Cox and Evans (MCE) [113], McCartney [114], and Chiang, Wang and Chou [115]. The local flaw model approach developed by Wang et al. [116] simulates the matrix cracking phenomenon at its initial condition and depicts it at a local level where the fiber, matrix, interface, and other physical identities of similar dimensions are present.

2.4.1.2. Energy Balance Approach

The critical stress for matrix cracking was first derived by ACK [108] using the energy balance analysis. They considered the case of an unidirectional composite consisting of uniformly spaced fibers in a homogeneous matrix material. The fibers are held in the matrix by either interface bonding or matrix shrinkage due to processing or both. The bridging fibers were allowed to slip through the matrix against friction in the wake of the crack, with the sliding resistance of the interface represented by a constant frictional shear stress, τ. They assumed the long crack to propagate in a stable and self-similar manner across the fibers and set up an equation for the energy balance between the uncracked and cracked composite regions:

$$2\gamma_m V_m + \gamma_{db} + U_s + \Delta U_f = \Delta W + \Delta U_m \quad (2.6)$$

where $\gamma_m V_m$, γ_{db}, U_s, ΔU_f, ΔW, and ΔU_m represent the matrix fracture energy, the work done in debonding the fiber/matrix interface, the energy dissipated due to frictional fiber sliding, the fiber strain energy increment, the work done by the far-field tensile stress, and the strain energy released by the cracked matrix, respectively. By ignoring the interface debonding term, they derived the critical applied stress for matrix cracking, σ_{crit}, as

$$\sigma_{crit} = \left(\frac{12 V_f^{\,2} E_f E_c^{\,2} \gamma_m \tau}{a V_m E_m^{\,2}} \right)^{1/3} \qquad (2.7)$$

where V, E, γ, τ, and a represent the volume fraction, Young's modulus, fracture surface energy, shear stress, and fiber radius, respectively, and the subscripts f, m, and c, represent the fiber, matrix, and composite, respectively.

In a subsequent study, Aveston and Kelly [109] considered a fiber surrounded by a hexagonal matrix as a representative volume element of the composite and utilized a shear lag model to analyze the stress transfer between the fiber and the matrix in the presence of matrix cracking. The stress transfer solutions were computed assuming that the average displacement in the matrix was represented by the displacement in the matrix at a radial distance R from the center of the fiber. The work done by the applied stress during the matrix cracking was then calculated from the stress transfer solutions. They derived the steady-state matrix cracking stress for a bonded interface condition using the energy balance condition as:

$$\sigma_{crit} = \left(\frac{c_f E_f E_c G_m}{a E_m} \right)^{0.5} \left(\frac{E_c}{\ln(R/a) c_m (1+\upsilon_m) E_f} \right)^{0.25} \qquad (2.8)$$

where σ_{crit} is the critical loading stress on the composite for matrix cracking, the subscripts m, f, and c, represent the matrix, fiber, and the composite, respectively, G_m is the energy release rate for matrix cracking ($G_m = 2\gamma_m$), a is the fiber radius, E is the Young's modulus, ν is the Poisson's ratio, and c is the volume fraction.

Subsequently, BHE [110] considered two cases regarding the fiber-matrix interfaces: unbonded fibers bonded to the matrix by initial pressures due to thermal or

other strain mismatches, but vulnerable to frictional slip, and fibers initially under radial tension and weakly bonded to the matrix, but susceptible to debonding by the high stresses near the tip of an oncoming matrix crack. For these two cases, three situations are possible (i) no slip can occur with enough frictional resistance, (ii) unbonded but frictionally constrained slipping fibers, and (iii) if debonding occurs, the debonded areas will open up, and the crack will propagate. The first case is equivalent to that considered by Aveston and Kelly [108] and the BHE expression was similar with the exception that R was replaced by R^*. R^* is the effective radius and is given by:

$$\ln(\frac{R^*}{a}) = -\frac{2\ln(c_f) + c_m(3 - c_f)}{4c_m^2} \qquad (2.9)$$

The critical matrix cracking stress given by BHE [110] for the case of slipping fibers (large slip) was similar to that of the ACK expression [108]. Further, BHE derived a general expression to bridge the gap between the no-slip (situation 1 or Aveston and Kelly [109]) and large-slip (situation 2 - special case or ACK [108]) results. For the case of initially bonded but debonding fibers (situation 3), the matrix cracking stress, σ_{crit}, is given by:

$$\frac{\sigma_{crit}}{\sigma_0} + \frac{E_c \sigma`_m}{E_m \sigma_0} = \left\{ \frac{1 + \frac{4c_f l_d G_d}{c_m a G_m}}{1 + \frac{B^2 l_d}{c_m a}\left(\frac{6E_c}{(1+\nu_m)E_f}\right)^{0.5}} \right\}^{0.5} \qquad (2.10)$$

where B is a function of c_m and c_f, σ_0 is a function of B, c_f, c_m, E_f, E_c, E_m, G_m, a, and ν_m, $\sigma`_m$ is the initial axial stress in the matrix in the unloaded composite, G_d is the critical debonding energy release rate, and l_d is the fiber debond length.

Kuo and Chou [111] derived the critical stress for matrix cracking and obtained closed-form solutions for two limiting situations. The first limiting situation was for perfect interfacial bonding, and the critical matrix cracking stress is:

$$\sigma_{crit} = \left(\frac{4\beta\gamma_m E_c E_f c_f}{3E_m} \right)^{0.5} - E_c(\alpha_c - \alpha_m)\Delta T \qquad (2.11)$$

where β is a function of G_f, G_m, c_m, c_f, E_m, E_f, E_c, and a, α represents the thermal expansion coefficient, and ΔT is the ambient temperature minus the thermal stress-free temperature. The second limiting situation was for complete debonding and frictional sliding, and the critical matrix cracking stress was the ACK expression [108] minus the second term in the above equation.

Recently, Hsueh [112] derived a general expression for the matrix cracking stress bridged by intact fibers, which debond from the matrix and then slip against the matrix in friction for an unidirectional CFCC under tensile loading parallel to the fiber axis:

$$\sigma_{crit}^3 - 3\sigma_d^2\sigma_{crit} + 2\sigma_d^3 = -\frac{6E_f E_c^2 G_m \tau_i}{a c_f c_m E_m^2} \qquad (2.12)$$

where σ_d is the debond stress, and τ_i is the interfacial shear stress. From his general expression of the matrix cracking stress, both the ACK [108] and the MCE [113] expressions can be derived as special cases.

2.4.1.3. The Short Crack-Fracture Mechanics Approach

MCE [113], McCartney [114], and Chiang, Wang and Chou (CWC) [115] considered the case of fiber-bridged cracks having an arbitrary length, with the fiber-matrix interface behavior in the crack wake being similar to the ACK [108] model. However, the length of the crack was dependent on the strength of the unreinforced

matrix unlike the ACK model. The ACK model assumed a crack-size independence of the matrix-cracking stress and is justified for the large crack situation they considered [113].

All the short crack fracture mechanics models considered a single crack propagating self-similarly in mode I in a semi-infinite homogeneous medium and solved it as a fracture mechanics problem [107]. An equivalent crack surface traction was considered to recover the influence of fiber bridging behind the crack, and this enabled the evaluation of the mode-I stress intensity factor, K_I, at the crack tip. The critical condition for crack propagation is obtained by considering the presence of a critical stress intensity factor, K_{IC}, for the composite.

The MCE [113], McCartney [114] and CWC [115] models gave different definitions for K_{IC} with the MCE and McCartney models giving the highest and lowest K_{IC} values, respectively [107]. All the short crack-fracture mechanics models gave similar results as the ACK model [108] for the long crack case. However, the models differed in their long crack definition. The MCE obtained an approximate analytical solution and expressed it in normalized form [113]:

$$\frac{\sigma_{crit}}{\sigma_m} = \frac{1}{3}\left(\frac{c}{c_m}\right)^{-0.5} + \frac{2}{3}\left(\frac{c}{c_m}\right)0.25 \qquad (2.13)$$

where c, c_m, and σ_m represent the crack length, characteristic crack length, and characteristic stress, respectively. The McCartney model [114] gave an expression for the critical matrix cracking stress as:

$$\sigma_{crit} = \sigma_m(\mu_c Y^2)^{-0.33} \qquad (2.14)$$

where σ_m, and Y are the characteristic stress, and a complicated integral equation involving μ_c, respectively.

2.4.1.4. The Local Flaw Model

The local flaw model, developed by Wang et al. [116], is based on the concept that microcracks in the matrix are produced by randomly distributed manufacturing flaws and that the flaws which influence the microcracks are confined in the matrix and in the fiber/matrix interfaces. The model assumes that under tensile loading, there exists a location or region where these flaws can become critical such that they can grow, mutually interact and coalesce. The model considers a local initiator cell comprising of two neighboring fibers separated by a spacing *s*. A flaw of size, *a*, is present in the matrix region between these two fibers, and a pair of interface flaws of size, *2b*, surrounds the matrix flaw. Outside this region, it is assumed that the medium is uniform and possesses the effective properties of the composite. The strain energy release rate criterion of the linear elastic fracture mechanics is utilized to obtain the critical condition for the growth of the matrix crack, namely $G(\varepsilon_c, \Delta T) = 2\gamma_m$. From this, the critically applied composite strain, ε_{cr}, at the growth of the matrix flaw or crack is computed. Then, the critical matrix cracking stress is computed by using $\sigma_{cr} = E_c\varepsilon_{cr}$.

2.4.2. Toughening Mechanisms in CFCCs

In a typical CFCC, the strain to fracture of the matrix, ε_m, is lower than that of the fiber, ε_f. Osmani et al. [117] depicted the different fracture mechanisms that can occur in a 1D CFCC material subjected to a tensile stress (Fig. B.2.18). In the following discussion, R refers to the fracture energy. Figure B.2.18 (a) shows a CFCC subjected to a tensile stress, and the matrix cracking (mode I) occurs first (Fig. B.2.18 (b)). As a

result of the matrix cracking, the fibers are subjected to an overload, and a shear stress occurs at the interface. Outwater and Murphy [118] provided an expression for the critical stress, σ_f^D, in the fibers at the plane of the matrix cracking for the onset of interface debonding:

$$\sigma_f^D = \left(\frac{4E_f G_{IIc}}{r}\right)^{0.5} \quad (2.15)$$

where E_f is the Young's modulus of the fibers, G_{IIC} is the mode II toughness of the fiber-matrix interface, and r is the radius of the fiber. There are four possible situations [117].

Case 1 (Fig. B.2.18 (c)): If $\sigma_f^D > \sigma_f^R$ (where σ_f^R is the fiber strength), the fibers will break without debonding at the interface with the fracture energy, R_1, given by:

$$R_1 = 2(v_f + v_m)\gamma_f \quad (2.16)$$

where v_f, v_m, and γ_f, represent the fiber volume fraction, matrix volume fraction, and the surface energy of the fibers, respectively.

Case 2 (Fig. B.2.18 (d)): If $\sigma_f^D < \sigma_f^R$, the interface debonding precedes fiber fracture. With sustained loading, the debonding continues, and the fibers elongate with the energy dissipation occurring by matrix friction [119]. If the Weibull's modulus of the fibers, m, is high (the fiber strength not distributed), the fibers fracture at the line of the matrix crack (Fig. B.2.18 (e)), and the fracture energy, R_2, being

$$R_2 = R_1 + [v_f r(\sigma_f^R)^3/3E_f\tau] \quad (2.17)$$

where τ is the interface shear friction stress.

Case 3: If m of the fibers is low, the fibers break on both sides of the matrix crack (Fig. B.2.18 (f)). In this situation, the fiber pullout precedes separation, which gives rise to another significant supplementary energy dissipation (Fig. B.2.18 (g)):

$$R_3 = R_2 + V_f \tau L_P^2 / 3r \quad (2.18)$$

where L_p is the pullout length. L_P increases with increasing σ_f^R and r, and decreasing m, and G_{IIc} or τ [119].

Case 4: When the fibers are not parallel to the applied force, the crack propagates parallel to the fibers (Fig. B.2.18(h)) in mode I, II or in a mixed mode. Under this condition, the matrix cracking (γ_m), interface debonding (γ_i), and microcracks and other factors (γ_s) contribute to the fracture energy, R_4:

$$R_4 = 2(\beta_1 \gamma_m + \beta_2 \gamma_i + \beta_3 \gamma_s) \quad (2.19)$$

where β_1, β_2, and β_3 are the weighing factors.

Evans and Marshall [105] provided a classical treatment on the mechanical behavior of CFCCs. CFCCs display important damage mechanisms in mode I, mode II, and mixed mode I/II, and compression. The failure sequence is governed by the applied stress state and the reinforcement type: uniaxial, woven or laminated. The failure processes of an uniaxially reinforced CMC's under tension are shown in Fig. B.2.19 [105]. Figure B.2.20 [106] illustrates the initial debonding of fibers at the crack front and fiber debonding in the crack wake. For crack bridging by the fibers, the interface debonding should take place in preference to fiber failure, as the matrix crack approaches the interface. Under this situation, the shear stress, τ, of the debonded interface plays an important role of controlling the load transfer rate from the fiber to the matrix. For example, a large τ increases the load transfer, with the fiber axial stress decreasing rapidly with the distance from the matrix crack plane. In this situation, the fibers fail at regions near the matrix crack plane, and reduces significantly the pullout contribution to toughness. On the other hand, a small τ enhances the toughness. For the interface

debonding to occur in preference to fiber failure, the following condition must be satisfied [120]:

$$G_{ic}/G_{fc} \leq 0.25 \quad (2.20)$$

where G_{ic} and G_{fc} represent the critical strain energy release rate for the interface and the fiber, respectively. Although direct experimental evidence is lacking, crack interactions with fibers and whiskers seem to support the general features.

2.4.3. Residual Stresses

CFCCs are usually processed at elevated temperatures (> 1000°C). As a result, residual thermal stresses form on cooling from processing to room temperature, if the fiber and the matrix have dissimilar coefficients of thermal expansion. If α_f and α_m represent the coefficients of thermal expansion of the fiber and matrix, respectively, three scenarios are possible for a given fiber/matrix combination [3]: (1) $\alpha_f > \alpha_m$ (2) $\alpha_f < \alpha_m$ and (3) $\alpha_f = \alpha_m$.

If $\alpha_f > \alpha_m$, then the fiber will contract away from the matrix upon cooling in the radial direction. As a result, the possibility of interfacial debonding is increased (Fig. B.2.21 (a)) [106]. If extensive debonding occurs, there is an insufficient load transfer from the matrix to the fiber, and the toughening mechanisms, such as fiber pullout and crack bridging, will be lost. On the other hand, if there is no debonding, the fiber will be in residual tension and could result in a premature fiber failure. If $\alpha_f < \alpha_m$, the matrix will shrink more than the fiber on cooling from the processing temperature (Fig. B.2.21 (b)). This will cause the matrix to compress the fibers in the radial direction, and result in increasing the frictional and chemical bonding at the fiber/matrix interface. If the clamping stress is very high, damage to the fibers may occur resulting in a lower

composite strength. The tensile stress on the matrix balances the compressive stress on the fiber. This tensile stress could cause a premature failure or microcracking around the fiber/matrix interface [105]. If $\alpha_f = \alpha_m$, then there will be no thermal residual stresses at the fiber/matrix interface.

From the above discussion, it could be inferred that $\Delta\alpha$ (α_m - α_f) should be kept at a value slightly > 0 to ascertain some interfacial friction between the fiber and matrix. If $\Delta\alpha < 0$, then debonding of the fibers can occur, resulting in a loss of reinforcement.

Hsueh et al. [21] investigated the effects of interfacial films on thermal stresses in whisker-reinforced (or fiber-reinforced) ceramics. For the case, $\alpha_f < \alpha_m$, compressive clamping stresses would be present and inhibit interface debonding, and/or pullout. If the mismatch in the thermomechanical properties is high enough, it could cause brittle fracture. Based on their analytical model, they proposed that the interface material with a low Young's modulus would reduce the thermal stresses. For interface materials with the same Young's modulus, a material with a higher thermal expansion coefficient will be more effective in reducing the thermal stresses. Their analytical expressions are shown in Appendix C.

2.4.4. Realization of Interface Significance

In the 1980's, researchers at United Technologies Research Center (UTRC) were trying to develop a high strength, high toughness, and low density ceramic matrix composite for use temperature of at least 1000°C [122-125]. Brennan and Prewo [125] identified that the Nicalon fiber reinforced LAS matrix composite would satisfy their application requirements. In a subsequent key article, Brennan [122] demonstrated that a Nicalon-LAS III composite with Nb_2O_5 addition (exhibiting high strength and high

toughness) had a carbon-rich zone of 10 to 40 nm in thickness at the fiber surface, while the Nicalon-LAS I with a TiO_2 addition (displaying low strength and low toughness) was devoid of the carbon-rich layer. It should be noted that the carbon-rich zone formed due to in-situ reactions, and following Brennan's [122] article, the concept of modifying the composite properties by tailoring the interface gained prominence. This concept was also extended to other composite systems, such as Nicalon/SiC and Nextel/SiC.

2.4.5. Techniques for Applying Interface Coatings

Gulden et al. [126] gave some guidelines while considering methods for depositing coatings on ceramic fibers: (1) should produce stable coatings with minimal fiber degradation, (2) must provide non-porous, adherent and uniform coatings, (3) should result in minimal fiber bridging, and (4) must be scaleable to high throughputs. The following techniques have been used for applying coatings on fibers: sol-gel, CVD, polymer precursors, colloidal, in-situ and nitradation. The CVD coatings are usually applied at low pressures and moderate to high temperatures to obtain uniform coatings. However, the CVD method is expensive and may entail corrosive by-products, such as HCl, which may degrade the fibers. Further, all oxides of interest (for example, mullite) cannot be easily obtained. The sol-gel, colloidal or polymeric precursor method are relatively inexpensive than CVD. However, they entail problems, such as non-uniformity, fiber-bridging, and some times may damage the fibers during processing, resulting in poor handleability.

In the sol-gel route, the fibers are first coated by passing through a precursor sol of a desired composition. This is followed by drying or curing, calcination and sintering to produce the desired coating. Shanmugham et al. [127] applied coatings of alumina-

titania, and aluminosilicate with alumina/silica ratios of 3, 1.5 (mullite) and 0.75 on Nicalon fiber tows and cloth. Hay and co-workers [128-130] developed an apparatus for coating continuous fiber monofilaments and tows and applied coatings of carbon, and several oxides (for example, alumina) on different fibers (Nicalon, FP and PRD-166). Villalobos and Speyer [131] obtained predominantly β-spodumene ($LiAlSi_2O_6$) coatings on Nicalon fiber tows.

In the CVD method, the coating is obtained by reacting gaseous mixtures at appropriate temperature and pressure conditions. Caputo et al. [132] applied BN and pyrocarbon (C) coatings on Nicalon fibers. They reported that the BN coating adhered well to the Nicalon fibers and speculated that the bonds between the layer planes of the BN coating should be weaker than bonds between BN and the matrix or the fibers. Their C coating separated from the fibers on cooling to room temperature and speculated that this debonding should allow the fibers to pull out of the matrix. They also stated that the C coatings reduced the possibility of fiber degradation due to the use of propylene and hydrogen as precursors compared to the BN deposition from the BCl_3 precursor. Rice [133] patented the application of BN as a fiber coating for CFCCs. Fernando et al. [134] studied the effect of boron nitride coatings deposited by CVD on the tensile strength of Nextel 480 fiber. They reported that the BN coated fiber had a higher mean tensile strength (2905 MPa) than the uncoated fiber (1766 MPa). Khasgiwale et al. [135] characterized the pseudo-porous SiC/C coatings deposited by CVD on Nextel 440 and Nicalon fibers in the as-received condition and after oxidation at 600°C and 1000°C for 20 h. They reported that the pseudo-porous SiC/C coating on Nicalon fibers was more oxidation resistant than the same coating on Nextel 440 fibers.

In the nitradation method, the coating is obtained by bombarding the surface with a gas. Khasgiwale et al. [136] obtained a BN rich layer on Nextel 312 fibers by a suitable ammonia treatment. They reported that the ammonia treatment of the fibers above 1000°C resulted in the crystallization of the fiber. Based on their high-resolution TEM study, they concluded that the BN coating was amorphous in certain regions and turbostratic in other locations. In the in-situ method, the coating is obtained by means of a reaction between the fiber and the matrix. Brennan [122] reported an in-situ carbon-rich layer of 30-50 nm thickness in a Nicalon/lithium aluminosilicate (LAS)-III matrix composite.

Gulden et al. [126] deposited alumina and yttria coatings by a sol-gel method, silicon carbide and silicon nitride by a polymer route, and boron nitride by a CVD method on both Nicalon and Nextel 480 fibers. Additionally, they deposited silicon carbide by a CVD route on Nicalon fibers. They were able to deposit uniform, smooth and adherent coatings of 0.1 to 0.5 μm in thickness. They inferred that the stoichiometry and adherence of CVD coatings were influenced by the coating conditions. In the case of the sol-gel and polymer methods, the following parameters are vital: sol production conditions and concentration, the degree to which the tow wicks together, the curing rate and time, and the drying rate and time.

In the following section, a literature survey for the Nicalon/SiC composites is presented.

2.5. Literature Survey for Nicalon/SiC Composites

Over the last 12 years, Nicalon/SiC composites have been studied by several research groups [13, 15, 18, 19, 94, 100, 132]. The Oak Ridge National Laboratory in USA, and the Laboratoire des Composites Thermostructuraux in France have been key players in researching Nicalon/SiC composites and made considerable contributions to the development of this system. Recently, the University of Tennessee researchers in collaboration with the Oak Ridge National Laboratory investigators have also made valuable contributions [19, 103, 106, 121, 127, 137-142]. In the following section, the work done at the Oak Ridge National Laboratory and the University of Tennessee is presented together first. This is followed by the research studies conducted by the Laboratoire des Composites Thermostructuraux (LCTS) researchers. Then, the research studies done by other investigators are presented.

2.5.1. Research at Oak Ridge National Laboratory and University of Tennessee

Caputo and Lackey [100] fabricated Nicalon (chopped fibers) reinforced SiC composites by a FCVI process with fiber volume content of 20 to 50% and density of 2.2 g/cm^3 within 6 h. The SiC matrix was mainly β-SiC with small amounts of silicon. Subsequently, Caputo et al. [132] fabricated Nicalon/SiC composites using both chopped and stacked layers of unidirectional Nicalon fibers with a fiber volume content of 40 to 60%. They reported a maximum flexural strength of 330 MPa with a strain of 1.05% for a composite with unidirectional fibers (58 vol.%) and 77% theoretical density (TD). Their fracture surface examination revealed extensive fiber pullout at the tensile fracture surface of the specimen. On the other hand, another composite sample with 45 vol. % of fibers and 72% theoretical density had low flexural strength (100 MPa) and low strain value

(0.2-0.4%). They speculated that these behavioral variations may be processing related. Composites made from chopped fibers (15-25 vol.%) had very low flexural strength (107-175 MPa) and little fiber pullout.

Stinton et al. [143] fabricated Nicalon/SiC composites using chopped fibers, unidirectional fibers, and cloth preforms of Nicalon. The vol.% of the Nicalon fibers were 21.9 and 25.4, 39.5 and 45.5, and 37.9 and 41.6, respectively for chopped, unidirectional, and cloth preforms. Composites with chopped fibers, unidirectional fibers and cloth preforms had flexural strength values ranging from 53 to 177 MPa, 213 to 410 MPa, and 187 to 476 MPa, respectively. Composites with chopped fibers, unidirectional fibers, and cloth preforms had densities ranging from 51.4 to 81%, 68.3 to 77.7%, and 73.3 to 90.3%, respectively, of the TD. They reported that the strain tolerance of the composites ranked in the following descending order: unidirectional, cloth, and chopped fibers. They recognized that the degradation of the SiC fibers occurred at their processing temperature (~1200°C) and initiated efforts to reduce the deposition temperature.

From this point onwards, the composites were all made using Nicalon cloth unless and otherwise specified. Caputo et al. [13] fabricated four Nicalon/SiC composites with a carbon interface of dimensions, 45 mm in diameter and 13 mm thick. The average density of the four specimens ranged from 81.5 to 85.9% of TD. The flexural strength values of the four specimens ranged from 288 to 324 MPa and 123 to 173 MPa, respectively, at room temperature and 1000°C in air, respectively. They attributed the strength degradation with increasing temperature to the oxidation of the carbon interface. Further, the samples tested at 1000°C showed brittle failure. Their loss in strength at high temperature was in sharp contrast to that reported by Lamicq et al. [144] for a similar

material. Lamicq et al. [144] observed that the Nicalon/SiC composite with an unspecified intermediate coating had nearly the same strength from room temperature to 1200°C followed by a progressive decrease with increasing temperature.

Lowden and Stinton [145, 146] and Lowden [147] fabricated Nicalon/SiC composites with various interfacial coatings including silicon, pyrocarbon, boron, silicon carbide, molybdenum and boron nitride. Additionally, a composite was synthesized without any interface, and it had low flexural strength (82 MPa) and displayed brittle fracture. Further, they also studied the effect of varying carbon thickness from 0.03 μm to 0.12 μm. Among the fabricated composites, the composites with boron or carbon interface had high flexural strength (> 300 MPa) and exhibited good fiber pullout characteristics. On the other hand, the composites with a silicon or boron nitride or silicon carbide or molybdenum interface had low flexural strength (< 138 MPa) and displayed brittle fracture or limited fiber pullout. The composite with the thickest carbon coating (0.12 μm) had the highest flexural strength (390 MPa) and displayed extensive fiber pullout, while the composite with the thinnest carbon coating (0.03 μm) had low flexural strength (< 125 MPa) and exhibited brittle failure. Based on their interfacial frictional stress measurements using the indentation method, they reported that the composite with the carbon (0.6 MPa) and boron interface (6.3 MPa) had low frictional stress values.

Lowden and More [148] studied Nicalon/SiC composites with carbon and BN interfaces and with no interface between the fiber and the matrix. Additionally, they investigated the effect of coating thickness of the carbon interface (0.07 to > 0.5 μm) on the mechanical properties as well as the effect of temperature (up to 1200°C in air) on the

flexural strength of composites with carbon (~ 0.2 μm) and BN (~ 0.2 μm) interfaces. The composite without any interface coating exhibited low flexural strength (82 MPa) and high frictional stress (49 MPa) at room temperature. On the other hand, the composite with a boron nitride interface had moderate flexural strength (350 MPa), exhibited fiber pullout, and low frictional stress (6.6 MPa). The composite with a carbon interface thickness of 0.07 μm had moderate flexural strength (344 MPa), limited fiber pullout and moderate frictional stress (11 MPa). Increasing the carbon thickness to 0.17 μm, the composite had high flexural strength (420 MPa), extensive fiber pullout, and low frictional stress (4.3 MPa). A further increase in the carbon thickness to 0.28 μm resulted in a composite with a moderate strength (390 MPa), extensive fiber pullout, and very low frictional stress (0.6 MPa). Composites with carbon interface thickness > 0.5 μm had a flexural strength of 352 MPa and very extensive fiber pullout. The frictional stress was not evaluated for this case. The flexural strength of composites with BN and carbon interfaces increased slightly with temperatures up to 1000°C beyond which the degradation of fiber properties resulted in strength reduction.

Stinton et al. [149] infiltrated Nicalon/SiC composites with carbon interfaces at different hot-face temperatures. They observed that infiltration temperatures < 1200°C resulted in composites with an average flexural strength of 380 MPa and fracture toughness of 23 MPa-$m^{0.5}$, while infiltration temperatures > 1200°C produced composites with an average flexural strength less than 325 MPa. They attributed the decrease in flexural strength with increasing processing temperature to the strength degradation of Nicalon fibers. Roman et al. [150] studied the effects of time and thermal gradient across the preform during the infiltration of Nicalon/SiC composites and

concluded that higher gas flow rates would result in reducing the infiltration time. Radiation induced microstructural and mechanical property changes of Nicalon/SiC composites with carbon interfaces have been studied by Snead et al. [151, 152]. Based on their studies, they concluded that improved radiation resistance can be anticipated in composites fabricated with low oxygen Nicalon fibers.

Lowden et al. [153] investigated boron-doped carbon and boron nitride as interfacial coatings for Nicalon/SiC composites and conducted flexural strength measurements in the following conditions: as-processed and after exposure at 1000°C for 24 h in air. They observed that the carbon to boron ratio in certain concentration regimes (15 to 37.5, and 18 to 36 for propylene- and methane-derived coatings, respectively) resulted in high flexural strengths (> 378 MPa) at room temperature and enhanced oxidation resistance of the composites. Increasing boron levels beyond the above ratios resulted in composites with decreased strengths and toughness. They attributed this behavior to the B_2O_3 formation, which segregated to active oxidation regions and shields them from further oxidation. Composites with a BN interface had high flexural strength (> 389 MPa) and retained considerable post-exposure strength (> 282 MPa), however, they were embrittled by the heat treatment. High-resolution electron microscopy studies revealed that after oxidation, thin layers were formed at the fiber-BN interlayer interface, which consisted of an amorphous region (most likely silica), and a carbon film immediately adjacent to the fiber. The chemical interaction between the fibers and interlayer was attributed to the possible presence of oxygen in the as-deposited BN coating, and was the likely cause for the degradation of strength and toughness of the composite.

Tortorelli et al. [154] conducted thermogravimetric analysis to investigate the reaction kinetics associated with the elevated-temperature oxidation of the carbon or BN interface in Nicalon/SiC composites. Flexure bars of a composite with a carbon interface (~0.36 μm thick) were tested at room temperature after exposure at 950°C in air for 0, 0.25, 0.58, 2, 24, 100, and 800 h. The flexural strength, proportional limit, and the fiber pullout of the composite decreased drastically with increasing exposure time at 950°C. For exposures less than 2 h, some loss of interfacial graphite was observed, while exposures greater than 24 h resulted in the absence of graphite. On the other hand, a composite with a BN interface did not undergo any appreciable weight loss or gain at 950°C and showed better oxidation resistance than the composite with a carbon interface.

Vaidyanathan et al. [155] investigated the effect of fabric lay-up orientation (0/30/60° and 0/45/45°) on the room- and high-temperature (1000°C in air) tensile behavior of Nicalon/SiC composites. Samples tested at 1000°C were given a surface coating of SiC prior to testing. The composite with the 0/30/60° orientation exhibited higher tensile strength (189 MPa) than the 0/45/45° composite (175 MPa), which was ascribed to a more efficient matrix infiltration. Both composites did not show any strength reduction at 1000°C.

Walukas [121] studied the potential of sol-gel derived alumina, zirconia, and titania interfacial coatings for Nicalon/SiC composites. Prior to the infiltration of the SiC matrix, a thin carbon layer was applied on the sol-gel oxide coatings. Additionally, a control sample with a thin C interface (40 nm) was fabricated. Among the fabricated composites with oxide interfaces, the composite with a thin alumina interface exhibited the highest flexural strength (262 MPa) and work of fracture (70 kJ/m^2). This composite

did not undergo any significant reduction in strength (253 MPa) and work of fracture (62 kJ/m^2) after oxidation at 1000°C for 1000 h in air. However, the alumina interface coating formed a mullite layer by a reaction with the fiber and functioned moderately well as an interface coating. On the other hand, composites with titania and zirconia interfaces exhibited low flexure strength (< 198 MPa) and underwent a significant strength reduction (< 121 MPa) along with brittle failure after oxidation at 1000°C for 1000 h in air. The control sample with a C interface had an as-processed flexural strength of 325 MPa and after 1000 h oxidation at 1000°C, the strength decreased to 183 MPa. The fracture surface examination of the oxidized sample by SEM revealed that the fiber pullout was confined to the composite interior, while the sample edges were embrittled. His TEM study identified that after 1000 h oxidation, the C interface was intact in the interior of the composite. Based on his results, he concluded that mullite would be a worthwhile interface candidate to pursue.

Lowden [156] investigated the effect of the coating thickness (0, 0.10, 0.17, 0.26, 0.52 and 0.99 μm) of carbon interfaces on the mechanical properties of Nicalon/SiC composites. Composites with carbon coating thickness > 0.26 μm exhibited composite behavior, while those with < 0.26 μm displayed more brittle behavior. He found that the interfacial shear stress varied inversely with the coating thickness at room temperature. Additionally, flexure strength measurements were conducted on a composite with a carbon interface (~ 0.3 μm) at room temperature after oxidation at 1000°C for 100, 500, and 1000 h in air. Some of the flexure bars were coated with an external SiC surface coating prior to oxidation. Post-exposure room-temperature flexure testing results confirmed the need for a protective external coating, since the strengths of uncoated bars

(no SiC overcoat) degraded within short periods of oxidation (100 h) in air. Longer exposure times resulted in brittle behavior due to the formation of a silica interlayer, which bonds the fiber and the matrix strongly. Subsequently, Miller et al. [141, 142] studied the effect of carbon coating thickness (0 to 1.27 μm) on the flexural strength, shear strength and toughness of Nicalon/SiC composites. Figure B.2.22 summarizes their flexural strength results. Up to the carbon thickness of 0.03 μm, the composite exhibited brittle failure. At an intermediate carbon coating thickness, around 0.13 μm, the composite exhibited high strength and toughness. Beyond a 0.25 μm carbon coating thickness, the flexural strength decreased and leveled off to 275 MPa at a carbon thickness of 0.6 μm. They conducted extensive fractography and developed a micromechanics model to predict the load vs displacement behavior for the composite, which agreed well with their experimental load vs displacement plots. Lara-Curzio et al. [157] studied the interfacial properties of Nicalon/SiC composites as a function of carbon interface thickness (0.03 to 1.2 μm). The effective interfacial frictional stress decreased with increasing carbon thickness from 24.6±9.9 MPa for a 0.03 μm thickness to 3.8±1.4 MPa for a thickness of 1.25 μm.

Lowden et al. [158] investigated the potential of a porous silicon carbide as an interface material for Nicalon/SiC composites. Prior to the porous silicon carbide interface deposition, a thin layer of carbon was applied on the fiber surface. Following the porous SiC deposition, the SiC matrix was infiltrated. Based on their flexural strength measurements at room temperature, in the as-processed condition and after oxidation at 1000°C for 24 h in air, they concluded that the composite with a porous SiC interface retained considerable flexural strength after oxidation than a composite with a carbon

interface. However, the as-fabricated strength of a composite with a porous SiC interface was low (78 to 224 MPa) compared to the composite with a carbon interface (404 MPa).

Beecher et al. [159] conducted thermal conductivity measurements for Nicalon/SiC composites with different carbon interface thicknesses (0.03-0.983 μm). Their results indicated that the thermal conductivity for the composite with a carbon interface was less than that for the composite without any interface. Further, the thermal conductivity increased with increase in the coating thickness of carbon in comparison to the composite with the thinnest carbon coating.

The effect of fiber orientation on the monotonic and fatigue behavior of Nicalon/SiC composites has been studied by Chawla and coworkers [137, 160], and Miriyala [106]. The loading configurations were classified as edge-on and transverse based on whether the loads were applied parallel or normal to the fabric plane, respectively. Chawla [137] observed that the flexural strength in the transverse orientation (350 MPa) was less than that in the edge-on configuration (400 MPa). However, the proportional limit (150 MPa) remained the same in both orientations. The mode of failure was in-plane shear and interlaminar cracking in edge-on and transverse orientations, respectively. The fatigue behavior was dependent on the fabric orientation. The fabric plies were able to slide with respect to each other in the transverse orientation and the specimen underwent a higher bending displacement and did not fail. While in the case of edge-on samples, they were incapable of undergoing large displacements, and if failed within few loading cycles. Further, post-fatigue tests revealed that the transverse samples had higher work of fracture than the edge-on specimens, due to their compliant structure.

Shanmugham et al. [19] performed FEM analysis and reported that a low modulus interfacial coating will be effective in reducing the radial stresses that result from cooling the composite from processing to room temperature. Further, for the interfacial materials with the same modulus, a material with a higher thermal expansion coefficient than those of the fiber and the matrix is more effective in reducing the radial stresses, as compared to a material with a lower thermal expansion coefficient. Their FEM results were similar to the analytical modeling results of Hsueh et al. [21]. Shanmugham et al. [19] fabricated Nicalon/SiC composites with carbon, alumina, and mullite interfacial coatings. A colloidal process was utilized to deposit alumina and mullite interfacial coatings, while a CVD process was used to produce the carbon interfacial coating. They conducted fracture surface studies of flexure bars, as processed and after oxidation at 1000°C for 24 h in air. Composites with carbon and alumina interfacial coatings exhibited brittle fracture after oxidation, while the composite with a mullite interfacial coating retained considerable fiber pullout after oxidation. Their colloidal process, however, resulted in non-uniform coatings and suggested the use of sol-gel methods for obtaining uniform coatings. In a subsequent study, Shanmugham et al. [127] fabricated Nicalon/SiC composites with a mullite interface (50 nm thick) deposited by a sol-gel process. However, the composite exhibited brittle fracture. They attributed this behavior to the degradation of the Nicalon fibers during the sol-gel processing of the mullite interface.

Lin et al. [161] conducted static fatigue tests over a temperature range of 425°C to 1150°C in air on Nicalon/SiC composites with a carbon interface. They reported a fatigue limit of ~100 MPa at temperatures ≤ 950°C which decreased to ~70 MPa at 1150°C.

The lifetime of the composite was greater than 10 h at an applied stress level of ≥ 100 MPa at temperatures ≤ 600°C. For stress levels higher than 100 MPa, the composite had a lifetime of less than 1 h at 950°C. In contrast, the composite with a protective external SiC seal coat increased the lifetime greater than 10 times at 425°C. However, this SiC seal coat had no significant impact on lifetime values at 950°C.

Liaw and coworkers [139, 140, 162-164] utilized ultrasonic techniques to measure the in-plane and through-thickness elastic moduli of Nicalon/SiC composites. The in-plane moduli values were found to be higher than the through-thickness longitudinal moduli. With increasing porosity, both in-plane and through-thickness moduli values decreased significantly. A micromechanics model was developed to predict the microstructural effect on the elastic moduli, and the predicted moduli values were in good agreement with the experimental values. Liaw [140] summarized the work performed by his research group on various aspects of Nicalon/SiC composites: Development of a multi-step FCVI process for reducing the fabrication time [103, 138], modulus measurement [139, 162-164], interface and its effect on properties [19, 141, 142], and fracture and fatigue behavior [106, 137, 160].

Besmann et al. [165] reported the fabrication of Nicalon/SiC composite disks 24.6 cm in diameter and 1.27 cm in thickness. These composites had carbon interfaces and exhibited a flexural strength of 480 MPa and an effective modulus of 240 GPa. Earlier, Besmann et al. [93] wrote an overview of the vapor-phase fabrication process along with various aspects of composites: fiber, matrix and interface. Matlin [103, 138] and coworkers developed a two-step FCVI process that reduced infiltration times for

Nicalon/SiC composites (44.5 cm in diameter and 1.27 cm in thickness) by two-thirds while maintaining final densities around 90%.

2.5.2. Research at Laboratoire des Composites Thermostructuraux, France

Naslain [166] reported that Nicalon/SiC composites were fabricated by an ICVI process in their laboratory and were intended to overcome the oxidation resistance of C/C composites. He gave an overview of the work going on in the fibrous ceramic-ceramic composite materials for transport applications. Naslain [76] discussed the fundamentals of the CVI processing and presented a good summary of the work carried out on Nicalon/SiC composites in France.

Lamon [167] measured interfacial properties of Nicalon/SiC microcomposites with a carbon interface from tensile tests. From the load-displacement curve, properties such as debond length, shear stress, and critical strain energy release rate, were determined. In a subsequent paper, Lamon et al. [168] discussed a microcomposite test procedure for evaluating the constituent properties of CFCCs. Based on their analysis and experimental results on Nicalon/SiC composites with carbon and BN interfaces, they demonstrated that the interfacial sliding resistance can be obtained from the unload/reload hysterisis, after one (or more) matrix crack was produced in the specimen.

Filipuzzi et al. [169] investigated the oxidation behavior of unidirectional Nicalon/SiC composites with a carbon interface using thermogravimetric analysis, optical/electron microscopy, and electrical measurements. They also studied the effect of temperature and carbon interface thickness on the oxidation behavior. Based on their results, they proposed a three stage oxidation process: (1) oxygen reacting with the carbon interface which results in the formation of pores around the fibers; (2) diffusion of

oxygen and carbon oxides along the pores; and (3) oxygen reacting with the pore walls producing the growth of silica layers on both the fibers and matrix. For composites with a thin carbon interface (0.1 μm) heat-treated at temperatures > 1000°C in air, the pores were rapidly sealed by silica. In such cases, the materials displayed a self-healing character with the oxidation damages being limited to the vicinity of the external surface. In contrast, samples exposed for 300 h at 900°C in air formed microcracks due to mechanical stresses resulting from the in-situ SiC/SiO_2 conversion. However, composites with a thick carbon interface (1 μm) did not exhibit any self-healing behavior, since carbon was totally consumed before silica could seal the pores. Subsequently, Filipuzzi and Naslain [170] proposed a model for the oxidation mechanisms and kinetics of Nicalon/SiC composites with a carbon interface. Their model predicted the gaseous species concentration, silica thickness profiles along the pore, the length of carbon consumed by oxidation and the relative weight change. The theoretical prediction of the thermogravimetric curve agreed well with the carbon interface length measurements consumed by oxidation. Based on their modeling results, they concluded that the oxidation resistance of composites with a thin carbon interface (≤ 0.1 μm) was good at temperatures ≥ 1100°C due to self-healing behavior.

Naslain et al. [15] deposited a turbostratic BN (N/B ratio < 1) interface by an ICVI process on Nicalon fibers at ~1000°C. The long infiltration process at 1000°C of the SiC matrix acts as an annealing treatment, with BN attaining near stoichiometry and the oxygen content lowered below 5 at.%. In contrast, the Nicalon fiber undergoes some decomposition resulting in the formation of a SiO_2/C amorphous double layer at the BN/Nicalon interface. The microcracks formed due to the matrix failure was deflected by

the BN/SiO_2 interface, which is the weaker link in the Nicalon/C/SiO_2/BN/SiC matrix sequence.

Prouhet and coworkers [171, 172] investigated Nicalon/SiC composites with different BN interface thicknesses (0.15, 0.5 and 2.7 μm) and characterized the microstructure of the interfacial zones and mechanical behavior through AES/TEM analyses, and tensile tests, respectively. Similar to Naslain et al. [15], they also observed a SiO_2/C double layer in between the Nicalon/BN interface. Among the three materials investigated, the composite with an intermediate BN thickness (0.5 μm) exhibited the highest tensile strength (187 MPa). The discontinuities in the SiO_2/C double layer between the Nicalon/BN interface was attributed as the cause for the premature failure of the sample with the smallest BN thickness (0.15 μm). Following this, Dugne et al. [173] conducted TEM, AES, and SIMS studies of Nicalon/SiC composites with BN interfaces. They attributed the toughness of this composite to the combination of a layered structure interface (BN) and the C/SiO_2 layer resulting from the thermal decomposition of the Nicalon fiber.

Droillard [174] fabricated Nicalon/SiC composites with carbon and multi-layered $(C\text{-}SiC)_n$ interfaces and examined the relationship between the fracture toughness and fiber/matrix interfaces. In some cases, the fibers were treated before infiltration to modify the interfacial mechanisms, and in others, the fibers were in the untreated condition before the interface and matrix infiltration. The R-curve behavior and the fracture toughness for a failure crack was found to be influenced by the process zone produced at the notch or crack tip. The process zone resulted from matrix cracks and the highest strain energy

release rates were obtained for composites, which had strong fiber/matrix interactions producing a high density of matrix cracks.

Rebillat et al. [175] examined the mechanical behavior of the interfaces using single fiber push-out tests in Nicalon/SiC composites with multi-layered $(C\text{-}SiC)_n$ interfaces. They examined composites with both untreated and treated fibers, with the treatment being done to obtain a strong bonding. In the case of composites with untreated fibers, the interfacial characteristics were obtained from the non-linear portion of the stress-displacement curve. The resistance to the interface crack growth and fiber sliding was found to increase with the number of (C-SiC) interfacial sequence. In the case of composites with treated fibers, the push-out curves displayed an upward curvature resulting in different modes of interface cracking. In a subsequent paper, Rebillat et al. [176] studied the interfacial bond strength in Nicalon/C/SiC composite materials using single fiber push-out tests. The interfacial properties were analyzed using techniques including nanoindentation, microindentation with push-out and push-back tests, and finite element modeling. For composites with treated fibers, high toughness was attributed to the lowering of interfacial shear stress.

Naslain [177] discussed the concept of layered interfaces for Nicalon/SiC composites: (1) interface of anisotropic C, BN, Ti_3SiC_2 and phyllosiloxides with layered crystal structures and (2) multi-layered $(C\text{-}SiC)_n$ interface with a layered microstructure. According to him, the interface must accomplish several functions: fiber-matrix load transfer, deflection of the matrix microcracks parallel to the fiber axis, and absorption of the thermal residual stresses arising from thermal expansion mismatch during processing. In addition, the interface must act as a diffusion barrier, and be chemically

compatible with the fiber and matrix, and use environment. Nicalon/SiC composites with multilayer $(C/SiC)_n$ interfaces were developed to overcome the limitation of oxidation of carbon (~500°C). In contrast, Nicalon/SiC composites with BN interfaces encounter oxidation problems due to the oxidation of BN at ~900°C to form B_2O_3.

Lamicq et al. [144] reported the thermomechanical and environmental test results on Nicalon/SiC composites (the interface was not mentioned) fabricated using the ICVI process. The flexural strength increased with increasing temperature up to 1300°C, and then decreased with further increasing the temperature. Their material did not lose any strength (~ 380 MPa at room temperature) even after oxidation at 1100°C for 500 h in air, and the fracture toughness values were as high as 25 MPa-$m^{0.5}$, which remained unchanged up to 1400°C.

2.5.3. Research by Other Groups

Eckel and Bradt [178] determined the strength distribution of reinforcing fibers in a Nicalon/SiC composite. The fiber strengths and the Weibull moduli of the Nicalon fibers in the processed composite was less than the unprocessed Nicalon fibers, indicating that the fiber damage occurred during weaving or during some stage of the manufacturing process. In a subsequent article, Eckel and Bradt [179] reported that the thermal expansion of a Nicalon/SiC composite was 4.45 x 10^{-6}/°C parallel to the fiber orientation direction. The thermal expansion predicted using the rule of mixtures agreed well with their experimental values.

Navarre et al. [180] observed the crack path in a Nicalon/SiC composite using X-ray radiography and SEM. Their X-ray technique was found to be useful in observing the main matrix crack. The effective crack increment was found to be 1/2 the main

matrix crack increment due to crack bridging by the fibers. Hasselman et al. [181] investigated the role of interfacial debonding and matrix cracking in determining the effective thermal diffusivity of Nicalon/SiC composites. The thermal diffusivity values were ~ 20 x 10^6 m^2/s and ~ 9 x 10^6 m^2/s of the composite in air in the direction parallel and perpendicular to the fiber plane, respectively. The thermal diffusivity values of the composites both parallel and perpendicular to the fiber plane decreased with increasing temperature. Based on their experimental results, they concluded that debonding and matrix cracking did not take place on cooling from 1000°C to room temperature, but did occur when heated to 1500°C.

Frety et al. [182] studied the effect of oxidizing Nicalon/SiC composites having carbon interfaces with different thicknesses at 800°C and 1400°C up to 1000 h in air. Long-term oxidation resulted in embrittlement and weakening of composites. The composite heat-treated at 800°C in air underwent strong decrease in strength, while the material heat-treated at 1400°C did not undergo any significant strength reduction. An amorphous silica layer replaced the original carbon layer on oxidation at 800°C. On the other hand, both turbostratic carbon and silica (α-cristobalite) interlayers were observed on samples oxidized at 1400°C. They explained this difference in the interlayers to the rapid oxidation of the silicon carbide at 1400°C, resulting in passive oxidation of the composite, before the carbon interface was completely oxidized.

Yang et al. [183] examined the effect of a 3-D braided structure and a 2-D plain-weave fabric architecture on the mechanical properties of Nicalon/SiC composites. The flexural strength of the 3-D and 2-D materials were 692 MPa and 326 MPa, respectively at room temperature. On heat treatment at 1200°C for 100 h, the flexural strength of the

3-D and 2-D materials decreased and were 345 MPa and 170 MPa, respectively. The fracture toughness value of the 3-D material (29.8 MPa-$m^{0.5}$) was higher than that of the 2-D composite (16.2 MPa-$m^{0.5}$). Based on the flexural strength, fracture toughness and damage tolerance results, they concluded that the 3-D braided Nicalon/SiC composite was superior to the 2-D woven laminate composite. In a subsequent study, Yang et al. [184] examined the thermal shock, thermal aging, thermal cycling, and impact behavior of 3-D braided and 2-D woven laminate composites. They concluded that the 3-D braided composite showed better thermomechanical durability than the 2-D woven composite after thermal exposure at elevated temperatures. This variation in performance was attributed to the difference in the fiber distribution, matrix porosity and interlaminar shear strength.

Henager and Jones [185] conducted subcritical crack growth measurements on Nicalon/SiC composites with carbon and BN interfaces. They determined the velocities of effective elastic cracks as a function of the applied stress intensity in both argon and argon plus 2000 ppm oxygen at 1100°C. The crack velocity (V) was found to depend weakly on the applied stress intensity (K) in the V-K diagrams over a range of applied stress intensity values, and this region was termed as the stage-II regime. Following this stage was a stage-III regime, which was only observed at higher stress intensity values. They also developed a 2D micromechanics model for predicting the time dependence of observed crack-bridging events.

Singh et al. [186] studied the effect of carbon coating thicknesses (ranging from 0 to 1.25 μm) on the mechanical properties of Nicalon/SiC composites. The ultimate strength and the work of fracture was evaluated from the four-point bend testing, while

the retained in-situ fiber strength in the fractured composites were determined by fractographic techniques. They observed that the retained in-situ fiber strength, ultimate strength, and work-of-fracture of the composites increased with increasing the carbon thickness, and attained the maximum at a coating thickness of 0.3 μm. However, a further increase in the carbon thickness did not improve the mechanical properties of either the fibers or the composites. Subsequently, Singh et al. [187] reported the ultimate strength, work of fracture, and retained in-situ fiber strength for a Nicalon/SiC composite with a 0.3 μm carbon interface from room temperature to 1300°C. Prior to testing at elevated temperatures, the samples were coated with an external overcoat of SiC (35 μm thick). The ultimate strength values increased with increasing temperature up to 800°C, attaining a peak value of 460 MPa compared to 370 MPa at room temperature. With further increasing temperature, the strength dropped to 280 MPa at 1300°C. They attributed this decrease in strength to the degradation of in-situ fiber strengths.

Kmetz et al. [188] reported a tensile strength of 277 MPa for a Nicalon/SiC composite with a BN interface with the occurrence of extensive fiber pullout and crack bridging. In contrast, a Nicalon/SiC composite without any interface had a low tensile strength (70 MPa) and displayed brittle fracture. Tensile strength measurements conducted on composites heat-treated at 1050°C for 50 h in air or at 1100°C for 70 h did not show any significant strength reduction. The XRD analysis indicated an amorphous BN interface, and the AES study confirmed that the slippage occurred in the BN interface material.

Kerans [20] observed that for obtaining composites with good damage-tolerant behavior, a relatively weak bond and low friction must exist between the fiber and the

matrix. In order for the matrix crack to be deflected around the fiber, the fiber-matrix interface must debond along with some amount of sliding of the fiber. The post-fracture sliding of the fiber is governed by the residual stress, coefficient of friction, interfacial fracture topography and wear properties. Kerans [20] noted that interfacial fracture topography is important, with the fracture surface roughness playing a more important role than the thermal residual stresses in accounting for final friction. Based on his interfacial topography modeling study of Nicalon/SiC composites with a C interface, he concluded that the role of the major portion of the C interface in composites is elastic. Hence, he suggested that a very thin layer of a weak interface, such as C or BN, is enough for interface debonding to occur provided a sufficient compliance is accomplished by a thicker, oxidation-resistant coating.

2.6. Literature Survey for Nextel/SiC Composites

Veltri et al. [189] reported the fabrication of Nextel 440/SiC composites using methyldichlorosilane precursor and a thermal gradient CVI process in a low-pressure reactor environment. Additionally, they fabricated Nicalon/SiC composites. The Nicalon/SiC composite had a maximum flexural strength of 450 MPa, while the Nextel/SiC composite had a maximum flexural strength of 140 MPa. This strength difference was ascribed to the fact that the Nextel/SiC was a 2D composite, while the Nicalon/SiC was a 1D composite. Further, the Nextel/SiC composite exhibited brittle fracture, whereas the Nicalon/SiC composite showed fiber pullout characteristics.

Wetherhold and Popp [190] determined the bending and tensile moduli of Nextel 312/SiC composites in two orthogonal directions utilizing flexure and uniaxial tensile

testing, respectively. The tensile moduli was found to be higher than the bending moduli. They attributed this difference to the lack of mid-plane symmetry of the woven form.

Weaver et al. [191] fabricated Nextel/SiC composites with three different Nextel fibers (Nextel 312, Nextel 440, and Nextel 550) and a carbon interface. Additionally, Nextel 440/SiC composites with boron-doped carbon and BN interfaces, and a Nextel 312/SiC composite with a BN interface were manufactured. Among the composites with a carbon interface, there was not any significant difference in room-temperature flexural strength (192 to 222 MPa). However, after oxidation at 1000°C in air for 100 h, the Nextel 440/SiC composite had the highest strength (173 MPa). The Nextel 312/SiC composite had a brittle fracture after oxidation, while the other two composites had some amount of fiber pullout. In contrast, samples of similar composition exhibited no significant change in flexural strength on heat treatment at 1000°C for 100 h in argon, and showed a considerable amount of fiber pullout. In the case of composites with a BN interface, the Nextel 440/SiC composite had a higher flexural strength (340 MPa) than the Nextel 312/SiC composite (300 MPa). Even after oxidation at 1000°C in air for 100 h, they did not show any significant strength reduction. The Nextel 440/SiC composite with a boron-doped carbon interface (0.05 μm thick) had a flexural strength of 250 MPa and 114 MPa in the as-processed condition and after oxidation in air, respectively. They concluded that the Nextel/SiC composites with the BN interface had a better oxidation resistance than composites with carbon or boron-doped carbon interfaces.

Vaidyanathan et al. [192] compared the mechanical behavior of Nextel 312/SiC composites with that of Nicalon/SiC composites. In both cases, carbon was the interface layer. The Nextel 312/SiC composite had a tensile strength of 112 MPa, while the

Nicalon/SiC composite had a higher tensile strength of 189 MPa. This difference was attributed to the lower tensile strength of the Nextel fiber in comparison to the Nicalon fiber. Fracture surface examination studies revealed that fiber pullout and fiber bridging contributed to composite toughening. Tortorelli et al. [193] investigated the oxidation reactions (in air) associated with exposing Nextel/SiC composites with carbon and BN interfaces using thermogravimetric analysis. In the case of composites with a carbon interface, they underwent rapid net weight losses followed by monotonic weight gains. This trend was attributed to the sequential reactions associated with the oxidation of carbon and the formation of SiO_2 on the SiC. In contrast, the composites with a BN interface did not show any weight loss and exhibited improved oxidation resistance. Post-exposure flexure testing of oxidized Nextel 312/SiC composites with a carbon interface underwent rapid decrease in first matrix cracking stress and strength. This behavior can be partly ascribed to the loss of the carbon coating followed by a gradual deterioration of the pullout amounts in the fracture surface that is associated with the SiO_2 formation. In the following section, the sol-gel synthesis of mullite and aluminum titanate reported in the literature is presented.

2.7. Implications and Critical Issues

It is evident from the research investigations presented that interface plays a crucial role in determining the properties of Nicalon/SiC and Nextel/SiC composites. Currently, these composites owe their mechanical properties to either C or BN interfaces, which provide a weak interfacial bond [18-20]. However, composites with C or BN interfaces encounter oxidation problems at elevated temperatures resulting in degradation

of mechanical properties [177]. In the case of Nicalon/SiC composites with C interfaces, drastic reduction in mechanical properties have been observed at temperatures ≥ 800°C [153, 154, 156, 182]. This degradation is attributed to the oxidation of the C layer followed by the subsequent formation of SiO_2 at these elevated temperatures [156, 182]. In the case of Nicalon/SiC composites with BN interfaces, substantial amount of as-processed strength is retained even after exposure at temperatures ≥ 1000°C but with loss in toughness [153, 154, 171]. The reduction in toughness is attributed to the formation of SiO_2/C amorphous double layer at the Nicalon/BN interface either during the processing or after oxidation for short periods (24 h) at 1000°C [15, 153, 173].

To overcome the limitations of C and BN interfaces, several interface materials such as silicon, boron, molybdenum, boron-doped C, alumina, zirconia, titania, multilayered $(C\text{-}SiC)_n$ and porous silicon carbide have been investigated for Nicalon/SiC composites [121, 145-147, 153, 174, 177]. Among them, composites with alumina (modified to mullite), and porous SiC interface have shown the most promising behavior after oxidation [121, 194]. The investigation of Walukas [121] identified that composites with thin alumina (< 50 nm) interfaces retained considerable strength (253 MPa) even after 1000 h oxidation at 1000°C, but the alumina was converted to mullite. Besmann et al. [194] have shown that composites with porous or poorly consolidated SiC interface to be oxidation-resistant even after 100 h oxidation at 1000°C. Composites with multilayered $(C\text{-}SiC)_n$ interfaces have exhibited good mechanical properties at room temperature, however, high temperature mechanical properties are yet to be reported [174].

Researchers have also debated the importance of residual stresses and fiber roughness during the debonding and post-fracture sliding of the fiber to obtain composites with good toughness [19-21, 195, 196]. Kerans and coworkers [20, 196] have indicated that roughness might play a major role during fiber sliding, and concluded that a thin C layer may be sufficient for debonding purpose but a thick compliant layer is required for sliding purpose. On the other hand, Hsueh et al. [21] has indicated that residual stresses might play an important role for debonding to occur, and concluded that a low modulus interfacial coating is required.

Based on the above discussion, the eventual deployment of Nicalon/SiC composites for long-term, elevated-temperature oxidizing environment applications will require the following: (1) interface materials that provide the desired weakening of the interfacial bond and possess the chemical stability over the entire use temperature regime and (2) chemical and thermomechanical compatibility of the fiber/interface/matrix system. Hence, it is essential to develop oxidation-resistant interface materials having the following attributes over the entire application temperature regime: weak interfacial bond, thermal and environmental stability, good thermomechanical, and chemical stability with the fiber and the matrix.

2.8. Sol-Gel Synthesis of Mullite and Aluminum Titanate

Sacks et al. [197] gave a good summary of the chemical precursor combinations and processes utilized by several researchers for synthesizing mullite ($3Al_2O_3.2SiO_2$) gels, precipitates, and powders. The sol-gel methods utilize colloidal suspensions, soluble salts and metal-organic compounds as precursor materials with each involving

different homogeneity and ultra-structure in their pre-ceramic gels [198]. Among these starting materials, a high degree of homogeneity along with a good oxide network is achieved only with metalorganic precursors (alkoxides).

Yoldas [198] reported the synthesis of mullite precursor gels by hydrolytic poycondensation of silicon alkoxide with aluminum alkoxide, colloidal alumina and aluminum nitrate. Among the three processing routes investigated, only the polymeric method involving polycondensation of silicon alkoxide with aluminum alkoxide produced 100% mullite crystallization at 1050°C. Yoldas' polymeric method for synthesizing mullite precursor gel is summarized in Fig. B.2.23. First, a clear, stable polyorganoaluminum solution is formed by the hydrolysis of aluminum sec-butoxide (ASB) with 0.5-1.0 mol water in dry ethanol. Following this, tetramethoxy silane in appropriate amounts to obtain the stoichiometric mullite composition is added. Subsequently, a water-HCl-methanol mixture is added to the above mixture. This mixture gelled immediately, and after 5-10 minutes, it forms a water-like clear liquid. This mullite precursor sol can be utilized for coating applications. Then, an appropriate amount of water in methanol is added for a complete hydrolytic condensation to occur, and a mullite precursor gel is formed within few minutes.

Huling and Messing [199] reported the crystallization of molecular aluminosilicate gels from an aluminum nitrate nonhydrate-tetraethoxy silane molecular sol. It was observed that if the segregation of the transition alumina-yielding species took place during gelation, the epitaxial nucleation of spinel occurred at 980°C. However, if the alumina segregation is avoided, tetragonal mullite (t-mullite) crystallizes at 980°C. On the other hand, if the molecular gels are synthesized and heated to avoid phase

separation, then o-mulllite (orthorhombic mullite) forms directly from the gel at 700°C. Chakravorty and Ghosh [200] and Li and Thomson [201] have also reported the synthesis of mullite using sol-gel methods.

Aluminum titanate has a good potential for thermal shock applications due to its low thermal expansion [202]. It has low modulus due to its extensive microcracking tendency. Prasadarao [202] reported the synthesis of aluminum titanate by two different methods: a monophasic gel formation by co-hydrolysis and polycondensation reactions of chelated ASB and titanium iso-propoxide and a diphasic gel formation from boehmite and anatase. The effect of seeding agents, such as magnesium oxide, and iron oxide, on the crystallization and densification of aluminum titanate obtained from monophasic and diphasic gels were examined. In the presence of iron oxide and MgO, the β-Al_2TiO_5 formed at 1250°C and 1450°C, respectively. In the following section, the merits and demerits of flexure testing are discussed.

2.9. Flexure Testing

Flexure or bend testing is less involved, rapid, relatively inexpensive, and needs less material for testing in comparison to tensile testing [106, 121]. In flexure testing, a simple beam specimen is placed in either a three- or four-point bend test fixture and loaded to fracture. Generally, the four-point bend testing is preferred since a greater amount of material is under high stress. The maximum stress in the sample is calculated using the simple beam theory. The U. S. Army published MIL-STD-1942A [203] "Flexure Strength of High Performance Ceramics at Ambient Temperature" in 1990 and

permitted several specimen-fixture combinations since they believed that no one specimen would meet all the requirements of the engineering ceramic community.

The application of flexure testing to ceramics and ceramic matrix composites, however, has some limitations. Many ceramics at high temperatures in flexure tests exhibit characteristics, such as shifting of the neutral axis or higher creep resistance in compression [106]. The shifting of the neutral axis occurs due to a decrease in moduli at a lower strain in tension than in compression. In addition, the stress distribution is not uniform within the ceramic sample in bend tests, and the maximum stress occurs only at the representative surface volume of the bar. Also, ceramics are surface-flaw sensitive and do not have the same tensile and compressive moduli, which the bend theory assumes to be equal. Typically, the bend test gives higher strength than that of the tensile test. This difference can be ascribed to a non-uniform stress distribution in a flexure bar, anisotropy of the fiber architecture, variation in tensile and compressive behavior, and low interlaminar shear strength. However, flexure testing has its merits: it offers qualitatively similar results to tensile testing regarding trends and damage development provided the failure mode is tensile. It is also useful for materials-development purposes and can measure the stress at which the first matrix cracking occurs.

In the case of four-point bend testing, the flexure strength, σ_f, can be computed using the formula:

$$\sigma_f = \frac{3P(L-a)}{2bh^2} \quad (2.21)$$

where P is the failure load, L and a are the outer and inner span lengths of the fixture, respectively, and b and h are the width and thickness of the sample, respectively.

CHAPTER 3

RATIONALE

According to Hsueh et al. [21], composites which display extensive fiber pullout have fiber/matrix combinations, such that negligible radial compressive clamping or even tensile stresses are developed on the fibers, and hence, have low interfacial shear stresses. They considered the case of a single fiber (whisker) surrounded by an infinite matrix, with an interface material (film) in between the fiber and the matrix. Their schematic is shown in Fig. B.3.1. σ_a and σ_b represent the stresses that are developed at the fiber/interface and the interface/matrix regions, respectively. Further, they reported that compressive clamping stresses are present, if the fiber has a lower thermal expansion coefficient than the matrix. For this case, interfacial coating material with a low Young's modulus will reduce the thermomechanical stresses. Using Hsueh et al's [21] model, Walukas [121] conducted a thermomechancial compatibility study of Nicalon/SiC composites with the following oxides as interfaces: alumina, titania, zirconia, mullite, zircon, and cordierite. These oxides have moduli ranging from 117-386 GPa, and have coefficient of thermal expansion in the order of 3.7-8.8 x 10^{-6}/°C. Based on this study, Walukas [121] concluded that the above oxides start lowering the compressive stresses at the fiber-matrix interface significantly only if they are greater than 0.3 μm in thickness. Hence, in the present study an interface coating thickness of 0.5 μm was considered.

Two composite systems, namely, Nicalon/SiC, and Nextel 440/SiC, are under consideration. In the case of a Nicalon/SiC composite, the Nicalon fiber has a lower thermal expansion coefficient (3.9 x 10^{-6}/°C) than the SiC matrix (5.5 x 10^{-6}/°C). While,

for the Nextel 440/SiC composite case, the Nextel 440 fiber has a thermal expansion coefficient (5.3 x 10^{-6}/°C) very close to that of the SiC matrix. Hsueh et al's [21] model was utilized to investigate the influence of interface material properties on the residual thermal stresses that would develop for these two composite systems on cooling from the processing to room temperature. For this investigation, a 1000°C differential was considered between the processing and room temperatures. The material properties utilized for the modeling investigation are reported in Table 4. The interface materials are denoted by the notation E*xyz*. The letter E refers to the interface material and *x, y, and z* take values corresponding to the interface materials' Young's modulus, Poisson's ratio, and coefficient of thermal expansion, respectively. The Young's modulus of 20 GPa, 140 GPa, and 400 GPa of an interface material corresponds to a *x* value of 1, 2 and 3, respectively. The Poisson's ratio value of 0.1 and 0.3 of an interface material corresponds to a *y* value of 1, and 2, respectively. The coefficients of thermal expansion of 1 x 10^{-6}/°C and 10 x 10^{-6}/°C of an interface material correspond to *z* values of 1 and 2, respectively. As is evident from the above notation, an interface material E221 has the following properties: Young's modulus of 140 GPa, Poisson's ratio of 0.3, and coefficient of thermal expansion of 1 x 10^{-6}/°C. Figures B.3.2 and B.3.3 show the thermal residual radial stresses that would develop on the Nicalon/SiC composite and Nextel 440/SiC composite, respectively.

For the case of a Nicalon/SiC composite without an interface, a compressive residual thermal radial stress of 232 MPa would be developed (using Hsueh et al.'s model). From Fig. B.3.2, it is clear for interface materials with low thermal expansion coefficients (1 x 10^{-6}/°C) and low Poisson's ratio (0.1), an interface material with a low

Young's modulus (E111: 20 MPa) is more effective in reducing the radial clamping stresses than an interface material with a high Young's modulus (E311: 400 MPa). Further, for interface materials with similar Young's moduli and Poisson's ratios, an interfacial material with a higher thermal expansion coefficient (E112: 10 x 10^{-6}/°C) reduces the radial clamping stresses much more than a material with a lower thermal expansion coefficient (E111: 1 x 10^{-6}/°C). It should also be noted that an interface material with a moderate Young's modulus and a higher thermal expansion coefficient (E212) would produce a lower residual radial stress state between the fiber and the matrix than an interface material with a low thermal expansion coefficient and a low Young's modulus (E111). Hence, both low modulus and moderate Young's modulus interface materials can reduce the radial thermal stresses, provided they have appropriate thermal expansion coefficients.

In the case of low thermal expansion coefficient (1 x 10^{-6}/°C) interface materials with similar Young's moduli, an interface material with a low Poisson's ratio (E211: 0.1) will reduce the radial clamping stresses much more than a material with a high Poisson's ratio (E221: 0.3). While for high thermal expansion coefficient (10 x 10^{-6}/°C) interface materials with similar Young's moduli, an interface material with a high Poisson's ratio (E322: 0.3) is more effective in reducing the radial clamping stresses than a material with a low Poisson's ratio (E312: 0.1). Based on the modeling results for Nicalon/SiC composites, it could be concluded that an interface material with low modulus, high thermal expansion coefficient, and high Poisson's ratio (E122) will be the most effective in reducing the radial thermal stresses among all the combinations studied. Such an interface material could result in extensive fiber pullout and low interfacial shear stresses.

In the case of a Nextel 440/SiC composite without an interface, a very small compressive residual thermal radial stress of 29 MPa would be developed (using Hsueh et al.'s model). From Fig. B.3.3, it is evident that the introduction of an interface material with a high coefficient of thermal expansion between the fiber and the matrix results in the formation of a residual tensile radial stress at least in one or both of the following regions: fiber/interface or interface/matrix. For interface materials with low thermal expansion coefficients (1 x 10^{-6}/°C), and low Poisson's ratios (0.1), increasing the Young's modulus results in increasing the residual compressive radial stresses in the interface/matrix region (see E111, E211, E311). Further, for interface materials with low thermal expansion coefficients and similar Young's moduli, increasing the Poisson's ratio results in the radial stresses (averaging the fiber/interface and interface/matrix regions) tending towards being compressive.

For interface materials with high thermal expansion coefficients (10 x 10^{-6}/°C), and low Poisson's ratios (0.1), increasing the Young's modulus results in increasing the residual tensile radial stress at the interface/matrix region (E112, E212, E312 in Fig. B.3.3). Further for interface materials with high thermal expansion coefficients and similar Young's moduli, increasing the Poisson's ratio results in increasing the residual tensile radial thermal stresses. Based on the modeling studies for Nextel 440/SiC composites, it could be concluded that the introduction of an interface material with a high coefficient of thermal expansion results in the formation of a residual tensile radial stress at least in one or both of the regions: fiber/interface or interface/matrix. For this situation, an introduction of an interface material should aid extensive fiber pullout and promote low interfacial shear stresses between the fiber and the matrix.

From the above discussion, it could be concluded that a low or moderate Young's modulus interface material could aid in reducing the residual compressive radial stresses in Nicalon/SiC composites. While in the case of Nextel/SiC composites, the introduction of an interface material with a low or moderate Young's modulus and high coefficient of thermal expansion could result in changing the radial stresses from a compressive to a tensile state. Such an interface material should promote extensive fiber pullout and result in low interfacial shear stresses between the fiber and the matrix.

From the thermomechanical stand point of view, a low or moderate Young's modulus interface material would be favorable in reducing the residual compressive radial stresses for Nicalon/SiC and Nextel 440/SiC composites. From the oxidation viewpoint, metal oxides have good oxidation resistance at elevated temperatures, and hence can be good interface materials, provided they have good chemical compatibility with the fiber and the matrix. Two metal oxides, mullite (E = 140 GPa) and aluminum titanate (E = 20 GPa), were chosen as interface materials based on the thermomechanical modeling study conducted using Hsueh et al's [21] model. Based on Walukas [121] work, the oxide coatings are effective in reducing the compressive radial stresses only if they are > 0.3 μm thick.

Thermodynamic modeling studies indicated that mullite was phase stable with SiC (See Chapter 4). Although mullite coatings can be obtained at 1000°C in air by a sol-gel process (See Section 6.3.2), during the process of the deposition of mullite on Nicalon fibers, the fibers were embrittled (See Section 6.4). Additionally, a Nicalon/SiC composite fabricated with a thin mullite coating (~ 50 nm) exhibited catastrophic failure, and a silica layer was observed between the mullite interface and Nicalon fiber [127].

Hence, the need to protect Nicalon fibers during the sol-gel processing of mullite was recognized.

Thermodynamic modeling studies conducted by Besmann [204] indicated that aluminum titanate was not phase stable with SiC in the considered temperature range (1000°C-1600°C). High temperature X-ray diffraction studies indicated that aluminum titanate forms only at temperature ≥ 1300°C in air from the powders derived via the sol-gel process (See Section 6.3.2). The formation temperature is very high and would degrade Nicalon fibers. On the other hand, when Nicalon fibers were dip-coated in the aluminum titanate sol and heat-treated at 1000°C in air for up to 10 h, the fibers were not embrittled (See Section 6.4). At 1000°C, only an alumina-titania mixture is formed on the fibers. Based on the non-embrittlement of Nicalon fibers by the alumina-titania coating, alumina-titania was considered as the interface material alternative to aluminum titanate. Although the calculated modulus of alumina-titania coating is high, alumina-titania was chosen for further consideration based on non-embrittlement of Nicalon fibers.

TEM analyses identified that the applied mullite and alumina-titania coatings were less than 0.1 μm (See Section 6.6). Earlier, Walukas [121] indicated that the oxide coatings of alumina, titania, and mullite are not effective in reducing the compressive residual radial stresses till their coating thickness was greater than 0.3 μm. Hence, the effect of the modulus of the interface materials on the composite properties could not be studied in the present investigation. Hence, the present study is concerned with investigating the effect of sol-gel derived oxide interfacial coatings on the mechanical properties of Nicalon/SiC and Nextel/SiC composites.

In order to avoid the damage to the fibers during the sol-gel processing of the oxide, there is a need to apply a thin carbon coating (inner carbon layer) prior to the deposition of an oxide coating. Thermodynamic modeling studies performed by Walukas [121] indicated that the oxide coatings of alumina, titania, and zirconia would be attacked by HCl, a by-product of the SiC matrix formation reaction. It was surmised that a thin carbon coating (outer carbon layer) deposited on the oxide coating prior to the SiC matrix infiltration may help prevent the HCl attack. Hence, a multilayer interface concept was developed in order to prevent the damage of the fiber or the coating during the sol-gel and CVI processing.

In order to obtain a better understanding of the type of interfaces that would be appropriate to pursue, Nicalon/SiC and Nextel/SiC composites with the following interfaces were considered: An oxide/C interface (no inner carbon layer) and a C/oxide/C interface. The composite with an oxide/C interface would identify the degradation of Nicalon or Nextel fibers, if any, that might occur during the sol-gel processing of the oxide. This is because, the oxide coating is directly applied on the fibers in this case. The composite with a C/oxide/C interface is likely to have better mechanical properties than a composite with a C/oxide interface, since the likelihood of the fiber degradation taking place during the sol-gel processing of the oxide is reduced due to an inner carbon layer. A schematic of a composite with a C/oxide/C interface is shown in Fig. B.3.4 and is termed as a composite with an oxide interface concept.

As described in the Doctoral Dissertation Proposal earlier, the C/oxide/C interface proved to be effective in promoting good mechanical properties of the composite than the oxide/C interface. Further, Nicalon/SiC composites with C/oxide/C interfaces retained a

considerable amount of their as-processed flexural strengths even after 24 h oxidation at 1000°C in air than Nextel/SiC composites with C/oxide/C interfaces. On this basis, Nicalon/SiC composites with C/oxide/C interfaces were fabricated for oxidation studies. Also, Nicalon/SiC composites with C/mullite/C (CVI 986, CVI # refers to the identification of the composite) and C/Al_2O_3-TiO_2/C (CVI 1002) interfaces retained graceful failure even after 500 h oxidation at 1000°C. This was the first time that Nicalon/SiC composites with C/oxide/C interfaces were fabricated. Hence, it was vital to ensure that the flexural strengths as well as the graceful failure of these composites are reproducible. For this purpose, a composite with a C/mullite/C interface (CVI 1080) and a composite with a C/Al_2O_3-TiO_2/C (CVI 1066) were fabricated. Further, a control sample of Nicalon/SiC composite with a thin C (~ 0.04 μm) interface was fabricated and tested.

Additionally, Nicalon/SiC composites with C/oxide/C interfaces were fabricated and evaluated for their flexural strengths and composite behavior after oxidation for 200 h each at 500°C, 750°C, and 1000°C. Since, Nicalon/SiC composites with C/oxide/C interfaces underwent a drastic reduction in strength at 750°C in air (Section 6.6), Nicalon/SiC composites with BN/oxide/BN interfaces were fabricated for oxidation studies. The experimental procedure and results of composites with C, oxide/C, C/oxide/C, BN, and BN/oxide/BN interfaces are reported in the following sections.

CHAPTER 4

THERMOCHEMICAL ANALYSIS

Besmann et al. [194] outlined the characteristics that an interface material should possess in a composite. Apart from meeting the mechanical and physical requirements, ideally the interface should satisfy the thermochemical compatibility stipulation. This mandates that the interface be oxidation-resistant and thermochemically stable with respect to the fiber, matrix, processing and service conditions. The status-quo interfaces, C and BN, promote good mechanical properties for Nicalon/SiC composites at room temperature. However, after oxidation at 1000°C in air, the chemical degradation of the fiber, interface or both have been reported in these composites [148, 153]. For example, C protects the Nicalon fiber during the processing of the SiC matrix and promotes a weak interface at room temperature resulting in composites with good strength and toughness [148, 156]. Electron microprobe studies have shown that such composites exposed to air even for limited time periods (100 h) lose their carbon interface coating due to oxidation [156]. Longer exposure times of 1000 h in air result in a brittle composite, and the TEM study identified that the carbon interface is replaced by an amorphous SiO_2 layer throughout the composite . Lowden [156] summarized that the carbon oxidizes first and once it is removed along the entire fiber length, the SiO_2 layer grows from both sides due to the oxidation of the Nicalon fiber and the SiC matrix. Hence, in the quest of a suitable interface material, the chemical compatibility of the interface with the fiber and matrix during processing as well as service is imperative.

Chemical reactions take place rapidly at high temperatures with the equilibrium attained in a very short time. Thus, the chemical behavior of a fiber/interface/matrix system at elevated temperatures need to be analyzed by thermochemical stability studies. The development of thermodynamic computer programs, such as SOLGASMIX-PV, CHEMSAGE, and Thermo-Calc, have made it easier to conduct thermodynamic equilibrium calculations [205-207]. These programs compute the equilibrium based on the method of minimizing the global Gibbs free energy for any given set of conditions.

All the equilibrium computations were performed using the Thermo-Calc program. Thermo-Calc is a thermodynamic software developed by the Royal Institute of Technology in Stockholm, Sweden [207] and contains a fairly comprehensive and a database validated by many European research centers. There are seven modules connected to the Thermo-Calc system including database, tabulation, post processor, thermodynamic, parrot, system utility, and user written application modules.

For performing an equilibrium calculation along with the post processing of data, three steps are involved. The first step involves a database selection and retrieval of the necessary data. This includes selecting the Scientific Group Thermodata Europe (SGTE) substance database, system (elements) definition, and retrieval of the data of the various phases involved in the calculation from the database. The second step involves the equilibrium computation. During this stage, the number of moles of the elements, pressure and temperature conditions are specified so that the degree of freedom is zero. Then, the equilibrium is computed. If necessary, the equilibrium calculations are then performed over the needed temperature range in increments. The third step involves the post processing of the computed data and involves either tabulation or plotting. For our

case, the number of moles of different phases involved versus the temperature was plotted.

In the present case, the fiber was Nicalon (ceramic grade) and the matrix was SiC. The interface materials considered were Al_2O_3, TiO_2, and mullite. The interface material should be chemically compatible with the fiber and matrix during processing and service conditions. If not, protection by means of an inert layer can be explored.

4.1. Processing Conditions

The SiC matrix is deposited by the decomposition of methyltricholorosilane (MTS) in the presence of hydrogen into SiC and HCl and is described in detail in Sections 2.3.4 and 5.5.6. Earlier, Walukas [121] conducted a thermochemical stability study during the densification of the composite with varying MTS/oxide ratios at 1200°C. He reported that mullite, Al_2O_3, and TiO_2 were vulnerable to a chloride species attack with the metals in the oxides completely chlorinated beyond a certain value of MTS/oxide ratios. For example, the MTS/oxide ratio was ~4/1 for Al_2O_3 to be completely chlorinated. His experimental study identified that C served the purpose of protecting Al_2O_3 and TiO_2 well during the SiC matrix deposition process. Based on the work of Walukas [121], it was decided that a thin carbon layer (< 50 nm) would be deposited on mullite and an Al_2O_3-TiO_2 mixture prior to the deposition of the SiC matrix. Such a carbon layer would protect the oxide coating from being attacked by the HCl during the processing of the matrix.

4.2. Interface Compatibility with the SiC Matrix

A portion of the phase diagram was calculated for the following systems: Al_2O_3/SiC, TiO_2/SiC, and mullite/SiC. Equilibrium computations were conducted for a 0.101 MPa pressure and a temperature range of 1000°C-1200°C. The temperatures were chosen to cover the regime, at which the composites were processed, and the long-term oxidation treatment at 1000°C. A very small amount of 0.1 mol of Ar was added during each equilibrium computation along with a 100 mol total contribution from SiC and the chosen oxide.

Initially, the equilibrium was computed for 95 mols of SiC and 5 mols of oxide at 1000°C. After this, the temperature was incremented in 50°C intervals up to 1200°C along with the equilibrium computation. Then, the molar amounts of oxide and SiC were increased and decreased, respectively, in steps of 5 mols. Whenever a phase transformation took place, the computations were conducted in 1 mol increments to better delineate the phase boundary.

The mullite/SiC and Al_2O_3/SiC systems were phase stable with each other for the temperatures and concentrations at which the equilibrium computations were conducted. However, the TiO_2/SiC system was not stable and the calculated portion of the TiO_2/SiC phase diagram is shown in Fig. B.4.1. Since the deposited oxide coatings are thin (< 0.15 μm) with respect to the SiC matrix, the regions of higher molar concentrations of SiC attain significance. In the region of SiC molar concentrations > 50%, TiO_2 is not stable and all the titanium is present in the form of TiC. In this regime, TiC, SiC, and SiO_2 coexist with each other.

4.3. Interface Coating Chemical Stability with the Nicalon Fiber

Ceramic grade Nicalon (NL 202) has a composition (wt.%) of 58% Si, 31% C, and 11% O, which corresponds to 1.249 mols of C and 0.333 mols of O for every mol of Si. Portions of the pseudo-phase diagrams were computed for Al_2O_3/Nicalon, TiO_2/Nicalon and mullite/Nicalon in a procedure similar to the oxide/SiC phase diagrams. After the equilibrium computation of 95 mols of Si with corresponding C and O molar amounts and 5 mols of the chosen oxide, the oxide mols and Si mols were increased and decreased, respectively, by 5 mols in increments across the diagram.

The computed portions of the Al_2O_3/Nicalon, TiO_2/Nicalon and mullite/Nicalon phase diagrams are summarized in Fig. B.4.2, B.4.3, and B.4.4, respectively. The calculated phase diagrams are approximate, and in certain regions appear to violate the phase rule. For example, two four-phase regions are next to each other in Fig. B.4.2. Since the calculations were made in a coarse, incremental nature, the three-phase regime comprising of mullite, C, and SiC did not coexist in the computations.

For the case of the Al_2O_3/Nicalon system (Fig. B.4.2), it was found that for Al_2O_3 molar concentrations < 25%, Al_2O_3 reacts with SiO_2 in the Nicalon fiber to form mullite. On the other hand, the mullite/Nicalon system (Fig. B. 4.4) seems to be stable with mullite, C, SiC, and SiO_2 prevailing throughout the temperatures and concentrations at which the equilibrium calculations were conducted. The TiO_2/Nicalon phase diagram (Fig. B. 4.3) was observed to be similar to that of the TiO_2/SiC phase diagram. For TiO_2 molar concentrations < 46%, all the titanium is present in the form of TiC.

CHAPTER 5

EXPERIMENTAL PROCEDURE

5.1. Materials

Composites were fabricated using plain weave ceramic grade Nicalon (NLM-202) or Nextel 440 cloth as reinforcements. C coating was deposited using 99.96% pure propylene (Matheson Gas Products, Atlanta, GA), and 99.99% pure argon (Liquid Air Co., Knoxville, TN). BN coating was deposited using BCl_3 (BOC Gases, Pheonix, AZ), NH_3 (Air Liquide, Morrisville, PA), and hydrogen gas (Liquid Air Co., Knoxville, TN). The following sol-gel precursors were obtained from Johnson Matthey, Ward Hill, MA: aluminum sec-butoxide (ASB, $AlO(C_4H_9)_3$), titanium (IV) ethoxide (TEOD, $Ti(C_2H_5O)_4$), tetramethoxysilane (TMOS, $Si(CH_3O)_4$), and tetraethoxysilane (TEOS, $Si(C_2H_5O)_4$). 200 proof ethanol (C_2H_5OH) and 2-methoxy ethanol were obtained from Aaper Chemical Company, Shelbyville, KY, and Aldrich Chemical Company, Milwaukee, WI, respectively. The SiC matrix was deposited using 99.97% pure methyltrichlorosilane (MTS, CH_3SiCl_3, PCR, Inc., Gainesville, FL) and ultra high purity hydrogen gas (Liquid Air Co., Knoxville, TN).

5.2. Development of Sols for Coating Applications

5.2.1. Mullite and Aluminosilicate Precursor Sols

The procedure used in this work for the preparation of the polymeric mullite precursor sol has been slightly modified from that of Yoldas [198]: The mullite sol has a lower molar concentration; the amount of water added for hydrolysis during the stages of

sol formation and gelation is different; and no acid catalyst is employed during the formation of the mullite precursor sol.

105 g ethanol was added to 1.5 g water in a flask. To this mixture, 30.8 g ASB was added, and the solution was shaken to form a white slurry. This white slurry converted to a clear, water-like liquid within 12 h when kept at 55°C, and is termed as the polymeric alumina precursor sol. It was observed that the addition of 2-4 drops of concentrated HCl prior to the pouring of ASB quickens the clearing up process of the white slurry. It should be noted that the addition of Con. HCl is not mandatory for obtaining a clear alumina precursor sol.

Two mullite precursor sols were obtained, as described below. To about 60 cm^3 alumina precursor sol, either 2.23 cm^3 TMOS or 3.35 cm^3 TEOS was added. Then, 0.27 cm^3 water mixed with 50 cm^3 ethanol was added to produce a clear, water-like liquid and is referred to as the polymeric mullite precursor sol. The mullite precursor sol obtained from the ASB/TMOS formulation and the ASB/TEOS combination are termed as MI and MII, respectively. For gelation studies, 2.71 cm^3 water in 25 cm^3 ethanol was then poured into each of the mullite sols (MI and MII) and gelled at 60°C. This gel was dried at 60°C for 168 h. The process procedure is summarized in Fig. B.5.1. Additionally, polymeric aluminosilicate precursor sols with final alumina/silica ratios of 0.75 and 3 were synthesized using the ASB/TEOS combination.

Since the coatings obtained on the Nicalon and Nextel preforms were dried at 110°C to form the oxide precursor coating, gelation studies were also conducted on gels dried at 110°C as summarized below. To about 80 cm^3 alumina precursor sol, 4.47 cm^3 TEOS was added. Then, 0.7 cm^3 water mixed with 60 cm^3 ethanol was added to form

initially a clear sol, which gelled within 5 min. This gel then formed a clear sol after 2 h. To this sol, 2 cm^3 water mixed with 60 cm^3 ethanol was added. This mullite precursor sol mixture, termed as EI, then gelled for the final time within 16 h. The mullite precursor gel was then dried at 110°C for 168 h. It was later observed, as summarized in section , that this ethanol-based mullite precursor sols did not produce an uniform coating. Consequently, a 2-methoxy ethanol-based mullite precursor sol was developed.

For gelation studies, to about 10 cm^3 alumina precursor sol, 0.55 cm^3 TEOS was added. Then, 0.5 cm^3 water mixed with 10 cm^3 2-methoxy ethanol was added to form a mullite precursor gel instantly. This gel then formed a clear sol, which is a water like liquid within 2 h. Then, this mullite precursor sol, termed as MEI, gelled again for the final time within 16 h. This mullite precursor gel was then dried at 110°C for 168 h.

The following recipe was used for preparing the ethanol-based mullite precursor sol for interface coating applications in Nicalon/SiC composites: alumina sol-80 cm^3, TEOS-4.47 cm^3, distilled water-0.7 cm^3, and ethanol-80 cm^3. This sol gelled initially within 5 min and then cleared again within 2 h. This clear mullite precursor sol was then used for coating purposes.

For coating the Nicalon preforms with the 2-methoxy ethanol-based mullite precursor sol, the following recipe was utilized: alumina sol-80 cm^3, TEOS-4.47 cm^3, distilled water-2 cm^3, and 2-methoxy ethanol-80 cm^3. This sol gelled instantly and cleared within 16 h. This clear mullite precursor sol was then used for coating purposes.

5.2.2. Aluminum Titanate Precursor Sol

For synthesizing the aluminum titanate precursor sol, 10 cm^3 titanium ethoxide was first dissolved in 40 cm^3 2-methoxyethanol. 23.62 cm^3 of the above mixture was

then poured into 60 cm^3 of alumina precursor sol. Next, 0.27 cm^3 water in 50 cm^3 ethanol was added to produce a polymeric aluminum titanate precursor sol. For gelation studies, 3.25 cm^3 water in 25 cm^3 ethanol was poured into the aluminum titanate sol and gelled at 60°C. This aluminum titanate gel termed as ATI was then dried at 60°C for 168 h. The process procedure is summarized in Fig. B.5.2.

Since the aluminum titanate coatings obtained on the Nicalon and Nextel preforms were dried at 110°C to form the oxide precursor coating, gelation studies were also conducted on the aluminum titanate precursor gel dried at 110°C as summarized below. First, 10 cm^3 titanium ethoxide was dissolved in 40 cm^3 2-methoxyethanol. To about 80 cm^3 alumina precursor sol, 25.76 cm^3 of the above mixture was poured. Then, 0.8 cm^3 water in 60 cm^3 ethanol was added to form a clear sol within few minutes. To this clear sol, 3.8 cm^3 water in 60 cm^3 ethanol is added to form an aluminum titanate precursor gel instantly. This precursor gel is termed as ATII. The following recipe was used for preparing the aluminum titanate precursor sol for interface coating applications in Nicalon/SiC composites: alumina sol-80 cm^3, TEOD in 2-methoxyethanol-25.76 cm^3, distilled water-1 cm^3, and ethanol-100 cm^3.

5.3. Gel Characterization Studies

5.3.1. Differential Scanning Calorimetry

Differential scanning calorimetry (Stanton Redcroft DSC 1500) runs were conducted in a Pt crucible with sapphire (45 mg) as the reference material, and about 40-50 mg of the precursor powder obtained from the gel as the test sample. The DSC furnace was ramped at 20°C/min between 20°C and 1450°C for all the mullite precursor

powders. For the MI and MII mullite precursor powders, the DSC runs were conducted in air. Whereas for the EI and MEI mullite precursor powders, the DSC runs were performed in both air and argon. For the ATI aluminum titanate precursor powder, the DSC furnace was ramped at 20°C/min between 20°C and 1450°C, and the measurement was conducted in air. Whereas for the ATII aluminum titanate precursor powder, the DSC furnace was ramped at 20°C/min between 20°C and 1500°C, with the measurements conducted in both air and argon.

5.3.2. High Temperature X-ray Diffraction

High temperature XRD patterns were obtained using a Scintag PAD X θ/θ diffractometer equipped with a Cu X-ray tube, a Buehler high-temperature furnace and an mBraum position-sensitive detector. A type-S thermocouple spot welded to the bottom surface of the heating strip enables the temperature measurement of the sample. The Pt/Rh strip as well as a Pt/Rh surrounding strip were used to heat the powder samples. About 50 mg of the mullite or aluminum titanate precursor gel was crushed into a fine powder using a ceramic mortar and pestle. To this ground powder, a few drops of ethanol was added to form a slurry. This slurry was then spread evenly on the Pt/Rh heating strip. The ethanol evaporated after few minutes leaving behind a thin film of the sample on the strip. A calibrated Micristar temperature controller ensured that the selected heating/cooling rates were maintained, with the strip temperature within ± 1°C.

The XRD patterns were collected in a dynamic air (100 cm^3/min) or argon atmosphere over the scan range of 20° to 70° 2θ at 5°/min at several temperatures up to 1350°C for the mullite precursor gel and 1450°C or 1500°C for the aluminum titanate precursor gel. For the mullite precursor powders, the XRD patterns were obtained at

27°C, 700°C, 750°C, 800°C, 900°C, 950°C, 1000°C, 1050°C, 1100°C, 1200°C, and 1350°C during heating, and at 50°C during cooling. Heating rates were 50°C/min up to 1100°C, and 20°C/min above 1100°C. The cooling rate was 100°C/min. For the MI and MII precursor powders, the XRD patterns were collected in air. Whereas for the EI and MEI mullite precursor powders, the XRD patterns were collected in both air and argon. For the ATI aluminum titanate precursor powder, the XRD patterns were obtained in air at 27°C, 500°C, 600°C, 700°C, 800°C, 900°C, 950°C, 1000°C, 1050°C, 1100°C, 1200°C, 1300°C, 1350°C, 1400°C, and 1450°C, during heating, and at 50°C during cooling. Heating rates were 50°C/min up to 1000°C, and 20°C/min above 1100°C. The cooling rate was 100°C/min. Whereas for the ATII aluminum titanate precursor powder, the XRD patterns were collected in both air and argon utilizing the same temperature cycle, with an additional data collection step at 1500°C during heating. The obtained XRD patterns were identified by comparing with the International Centre for Diffraction Data (ICDD) patterns of mullite, α-alumina, titania, and aluminum titanate.

5.4. Nicalon Cloth and Tow Coating Studies

Nicalon cloths (6.35 mm in diameter) were dipped in mullite sols (MII) of concentration ranging from 1 to 4.87 wt.%, and heat treated at 1000°C for 1 h in air. Following this, the samples were examined using a scanning electron microscope to determine the coating characteristics. Nicalon tows, 150 cm long, were withdrawn from the 3 wt.% mullite (both MI and MII) precursor sols, and aluminum titanate precursor sols at the rate of 37 mm/min. The coated tows were then heated in air at 1000°C for 1h or 10 h in air. In addition, Nicalon tows were dip-coated in the synthesized polymeric

aluminosilicate sols having different alumina/silica ratios and heat-treated at 1000°C for 1 h in air. X-ray diffraction patterns were obtained on Nicalon cloths dipcoated in mullite precursor sol and aluminum titanate precursor sol, dried at 110°C, and heat-treated at 1000°C for 1 h in air.

5.5. Composite Fabrication

5.5.1. Preform Fabrication

The fibrous preforms of Nicalon or Nextel were prepared by stacking multiple layers of the corresponding cloth (45 mm in diameter) in a 0°/30°/60° sequence within the cavity of a graphite holder (12.5 mm in thickness). The preform was compressed by hand and held within the holder by a graphite lid. In the case of a Nicalon preform, there were 50 layers of Nicalon cloth, while only 45 layers of Nextel cloth were in a Nextel preform.

5.5.2. C Coating

C coating was deposited under isothermal and reduced pressure conditions on the Nicalon/Nextel fibrous preform or on the oxide layer within the FCVI furnace as follows:

Temperature : 1100°C

Pressure : ~ 1-2 kPa

Gas flows : 25 cm^3/min propylene, 500 cm^3/min argon

A control Nicalon/SiC composite sample was fabricated with only a thin C interface coating. For this case, the C layer was deposited for 30 min using the above conditions. Thin CVD carbon coatings were deposited for 15 min in some cases on the fibrous preform (inner carbon layer) prior to the oxide deposition by the sol-gel route.

The objective of applying the inner carbon layer is to protect the fibrous preform during the formation of the sol-gel oxide. The carbon coatings were deposited for 15 min on the sol-gel oxide (outer carbon layer) in all cases prior to the SiC matrix infiltration. The purpose of the outer carbon layer is to prevent the oxide coatings from being attacked by the corrosive CVD environments.

5.5.3. BN Coating

BN coating layers were deposited either on the Nicalon preform or on the oxide layer using a forced-flow, isothermal CVI method as follows:

Temperature : 1100°C

Pressure : 5 kPa

Gas flows : 25 cm^3/min BCl_3, 25 cm^3/min NH_3, and 500 cm^3/min H_2

A control Nicalon/SiC composite was fabricated with only a BN interface coating. For this case, the BN coating layer was deposited for 1 h. Earlier, Lowden et al [153] reported that a deposition time of 1 h, using the above reagents and flow parameters, produced a 0.2 μm BN coating thickness. Two other Nicalon/SiC composites were fabricated with BN coating layers being a part of the interface: BN/ Al_2O_3-TiO_2/BN and BN/mullite/BN. For the above two samples, the inner BN layer was deposited directly on the fibrous preform for 30 min, and the outer BN layer was deposited on the oxide coating for 30 min.

5.5.4. Mullite Coating

Mullite coating was obtained either directly on the Nicalon or Nextel preforms or on the carbon-coated Nicalon or Nextel preforms using the following procedure. The mullite precursor coatings were obtained by vacuum infiltration of the mullite precursor

sol (ethanol or 2-methoxy ethanol based) followed by drying at 110°C in air. This step was repeated 3-4 times till a desired final coating thickness of 200-300 nm was obtained (determined by weight gain). Then the mullite precursor-coated preforms were heat treated in argon at 1050°C for 1 h to obtain the mullite coatings.

5.5.5. Al_2O_3-TiO_2 Coating

Al_2O_3-TiO_2 coating was obtained either directly on the Nicalon or Nextel preforms or on the carbon-coated Nicalon or Nextel preforms using the following procedure. The Al_2O_3-TiO_2 precursor coatings were obtained by vacuum infiltration of the aluminum titanate precursor sol followed by drying at 110°C in air. This step was repeated 3-4 times till a desired final coating thickness of 200-300 nm was obtained (determined from a weight gain). Then, the Al_2O_3-TiO_2 precursor-coated preforms were heat-treated in argon at 1050°C for 1 h to obtain the alumina-titania coatings.

5.5.6. Infiltration of the SiC Matrix

The SiC matrix was infiltrated using a FCVI process developed at Oak Ridge National Laboratory [28, 91-94, 100]. A schematic of an FCVI system is shown in Fig. B.5.3 [208]. The following portion is adapted from the articles of Lowden et al. [208], Stinton et al. [91] and Walukas [121]. In brief, the furnace is cylindrical in shape and is heated resistively. The water-cooled injector and the graphite preform holder are the critical components of the infiltration system and is shown in Fig. B.5.4.

The water-cooled injector is made up of several concentric metal tubes. These tubes are connected to form separate gas and water passages. The graphite preform holder is placed on the top of the water-cooled surface and is gripped in place by an outer perimeter lip and a cylindrical graphite chamber. In addition, the chamber performs the

function of isolating the heating element from the reactant gases. Since the preform holder is in contact with the water-cooled injector, it helps to cool the bottom and side surfaces of the preform. As a result, a steep temperature gradient is created within the preform.

The MTS exists as a liquid at room temperature, and hence, hydrogen gas is passed through a reservoir of liquid MTS to carry MTS vapor into the reaction chamber. The reactant gases, hydrogen and MTS, enter the chamber through the cool portion of the preform. As the gases pass through the preform, the reaction rate for the SiC matrix deposition is lower near the cooler surfaces and increases as it approaches the hotter surfaces. The reactant gases are depleted due to the matrix deposition in the cooler regions, hence the infiltration in the hotter volumes is reduced. Near the cooler regions, deposition rate is lowered due to the lower temperature, whereas for the volume near the heated surface, the depletion of the reactants results in slower infiltration. As the densification continues, thermal conductivity is increased while the thermal gradient is decreased. As the permeability of the densified regions is reduced, the reactant gases are forced to flow through the more porous regions in the preform. With time, temperatures across the preform increases and this along with the changes in the permeability, alters the deposition conditions resulting in more efficient infiltration of the coarser porosity. The infiltration is completed, when the pressure drop across the preform reaches 70-140 kPa due to decreased permeability. At this stage, the furnace shuts off automatically, and the gas flows are stopped. The process parameters used for the SiC infiltration of the Nicalon and Nextel preforms are as follows: top surface temperature of 1200°C; MTS

flow of 0.3 cm^3/min and hydrogen flow of 500 cm^3/min; and exhaust pressure of 101 kPa. Typically, the SiC matrix infiltration was completed within 20 hours.

5.5.7. Interface Coating Thickness Calculation

In order to calculate the coating thickness of the interface, weight measurements of the sample were carried out at different stages of the coating process. The weight of the graphite holder with the lid was first measured. Then, the weight of the preforms with the graphite holder was measured and recorded. If the carbon coating was applied directly on the preform, there would be a net weight loss at this stage, due to the removal of the sizing from the preform. The sample with the carbon coating was cooled, and its weight was recorded. Then, the weight of the sample after the oxide deposition prior to heat treatment was recorded. After the heat treatment at 1050°C to obtain the desired oxide coating, the sample was cooled, and its weight was recorded. Then, a carbon coating was deposited on the sample, and the weight was recorded after cooling the sample. The outer carbon coating thickness can be calculated accurately, since there is no loss of volatiles at this stage. By making the assumption that the sample would have the same weight gain of carbon in the initial stage (inner layer) as it did in the final stage (outer layer), the initial carbon coating thickness can be computed. Once the inner carbon thickness is determined, the oxide coating thickness can be computed from the net weight gain of the oxide. Finally, the sample's weight is measured after the SiC infiltration to calculate the net weight gain of SiC. The interface coating thickness calculation procedure is summarized in Fig. B.5.5.

5.5.8. Fabricated Composites

Table 5 lists the fabricated Nicalon/SiC composites with C, oxide/C, and C/oxide/C interfaces along with the CVI#, reagents used to deposit the oxide coatings, and the C deposition times. CVI 1077 is the control Nicalon/SiC sample with a C interface coating. CVI 982 and CVI 985 are Nicalon/SiC composites with an oxide/C interface. The remaining composites in Table 5 are composites with C/oxide/C interfaces. Table 6 is a compilation of the fabricated Nicalon/SiC composites with BN and BN/oxide/BN interfaces along with their CVI#, reagents used to deposit the oxide coatings, and the BN deposition times. CVI 1073 is the control Nicalon/SiC sample with a BN interface. Table 7 summarizes the fabricated Nextel/SiC composites with oxide/C and C/oxide/C interfaces along with the CVI#, reagents used for oxide deposition, and the C deposition times.

5.6. Flexure Testing

5.6.1. Specimen Preparation and Density Measurement

The graphite holder and the lid were removed from the composite samples using a lathe. After this, the cylindrical sample was ground on both sides, and 24 flexure bars of dimensions ~ 2.5 x 3.0 x > 33 mm were obtained by cutting. The geometrical density of each of the flexure bars was determined from the weight and dimension measurements of the bar.

5.6.2. Four-Point Bend Testing and Heat Treatment

The flexural strength of the composite bars were determined at room temperature in both as-processed and after oxidation in air up to 1000°C. The flexure strength

measurements were conducted using a testing machine manufactured by Applied Testing System. The flexure testing machine is connected, and its operation is computer controlled. The flexural strength was determined using a four-point bend test fixture (with 30 or 20 mm outer span and 10 mm inner span) on an Applied Testing System machine equipped with a 4375 N load cell. The specimen was placed in the fixture and loaded during the downward motion of the crosshead. The crosshead speed utilized was 2.54 mm/min.

Table 8 summarizes the flexure test conditions of Nicalon/SiC composites with C, BN, oxide/C, C/oxide/C and BN/oxide/BN interfaces. As is evident from Table 8, the bars were bend-tested at room temperature in the as-processed (AP) condition and after post-oxidation in air in one of the following conditions: 24 h, 200 h, or 500 h at 1000°C, 200 h at 500°C or 750°C, and 200 h at 1000°C in air followed by a heat treatment for 200 h at 750°C. The number of bars tested in each of the above conditions are listed in the table.

Table 9 summarizes the flexural test conditions of Nextel/SiC composites with oxide/C and C/oxide/C interfaces. As shown in Table 9, 12 flexure bars of each of the fabricated composites were tested at room temperature in the as-processed condition. With the exception of a Nextel/SiC composite with a C/Al_2O_3-TiO_2/C interface, 12 flexure bars of each of the fabricated composites were tested at room temperature after post-oxidation at 1000°C for 24 h in air. For the case of Nextel/SiC composite with a C/Al_2O_3-TiO_2/C interface, 6 flexure bars were each tested at room temperature after post-oxidation at 1000°C in air for 24 h and 200 h, respectively.

5.7. Microanalysis

5.7.1. Scanning Electron Microscopy

After flexure testing, samples which did not completely fracture were separated by hand for fracture surface investigation. The fracture surfaces of the tested bars were examined using a Hitachi S-800 SEM equipped with an energy dispersive X-ray system. The images were captured as a digital image on a computer using an Adobe Photoshop software. During the microscopy study, more attention was given to the tensile region of the broken flexure bar. At least one flexure bar of each of the fabricated composites were examined in the SEM under every flexure tested condition.

5.7.2. Transmission Electron Microscopy

The fiber-matrix interfaces in Nicalon/SiC composites with C/mullite/C (CVI 986) and C/alumina-titania/C (CVI 1002) interfacial coatings were analyzed using transmission electron microscopy (TEM) in the as-processed condition. Additionally, the CVI 1002 sample oxidized at 1000°C for 500 h in air was studied.

Portions of the fractured specimens, 2.5 mm thick, were initially cut using a diamond blade so that several fiber bundle cross-sections were visible. Then, the samples were ground using a 6 μm embedded diamond disc to a thickness of 125 μm. Next, the samples were polished with 1 μm and dimpled to a center thickness of 25 μm. Finally, the samples were ion-milled to electron transparency using argon ions.

High resolution images of composite interfaces were obtained at 200 kV using a Hitachi HF-2000 cold field emission gun microscope, which is equipped with a Noran/4 Π EDX system. EDS patterns were obtained on the fiber-matrix interfaces and were used to identify the coatings.

5.7.3. Auger Electron Spectroscopy

Table 10 lists the Nicalon/SiC and Nextel/SiC composites analyzed using a PHI Electronics 660 Scanning Auger Microprobe (SAM) system at a low accelerating voltage of 2 kV and a beam current of 10 nA. To study the fiber-matrix interfaces of the above composites, notched sample bars (2.5 x 3 x 15 mm) were impact-fractured in situ and the fresh fracture surfaces were analyzed. The in-situ fractures and analyses were performed with a chamber pressure less than 9×10^{-9} Pa.

After the in-situ fracture of the specimens, suitable regions with troughs and fibers were selected. For the AES analysis, three fibers and two troughs were picked. Troughs are regions, where the fibers have been pulled out and impressions of fibers are left behind. To obtain the composition depth profiles, the samples were sputtered with 3.5 kV argon ions at a specimen tilt angle of 30°. Earlier, Braski et al. [209] reported that the sputtered material removal rate was 20 nm/min for SiO_2 and 15 nm/min for SiC based on calibration experiments conducted on these materials. Since the sputtering rate of oxides, carbides, and nitrides don't vary that much, a 15 nm/min removal rate was applied for all materials during this study. The depth profiles were obtained up to a maximum of 25 min. The sensitivity factor at 2 kV is 0.35 for both Si1 (~76-85 ev) and Si2 (~90-95 ev), as determined with a NIST SiC standard (112b) under the experimental conditions. All other sensitivity factors used were those given by the PHI software. After the depth profiles were obtained, usually the matrix composition was determined.

5.8. Analytical Modeling

An elastic stress solution for thermal stresses in ceramic matrix composites with a two layer interface, where the fiber volume fraction is low, was derived, and the details along with the results are given in Appendix D.

CHAPTER 6

RESULTS

6.1. Introduction

In this Chapter, the results of the sol and gel characterization studies are first summarized. This is followed by a discussion of the Nicalon cloth and tow studies. Then, the density, flexure testing and microanalysis results of Nicalon/SiC and Nextel/SiC composites are presented.

6.2. Sols Development

6.2.1. Mullite and Aluminosilicate Precursor Sols

The mullite precursor sols, MI, MII, EI, and MEI, were obtained as described in Section 5.2.1. These sols were transparent and formed a clear, water-like liquid. After the above sols were gelled, the gels were off-white in color, and translucent. These gels, after drying at 60°C or 110°C looked like tiny crystals, which were off-white in color, with most of them translucent, and some transparent. The polymeric aluminosilicate precursor sols (alumina/silica ratios of 0.75 and 3) and gels also exhibited characteristics similar to that of the above mullite precursor sols.

6.2.2. Aluminum Titanate Precursor Sol

The aluminum titanate precursor sols, ATI, and ATII, were obtained as described in Section 5.2.2. These sols were transparent and formed a clear, water-like liquid. After the above sols were gelled, the gels were off-white in color, and translucent. These gels,

after drying at 60°C or 110°C, looked like tiny crystals, which were brownish-yellow in color, with most of them translucent, and some transparent.

6.3. Gel Characterization Studies

6.3.1. Differential Scanning Calorimetry

The dried mullite precursor gels, MI, MII, EI, and MEI, and the dried aluminum titanate precursor gels, ATI and ATII, were obtained and grounded into a fine powder, and the DSC study was conducted as described in Section 5.3.1. All the mullite precursor powders were white in color, while the aluminum titanate precursor powders were yellow in color.

The DSC curves obtained in air from the powders derived from the mullite precursor gels, MI, and MII, are shown in Figs. B.6.1 and B.6.2, respectively. The above two DSC curves show an initial endothermic peak around 150°C corresponding to a water loss followed by two broad exothermic peaks between 220°C and 640°C. These exothermic peaks represent the organics being burnt out from the powders. This is then followed by a sharp exothermic peak around 990°C in both curves, indicating the mullite crystallization event. Thus, the mullite crystallization temperature is independent of whether the mullite precursor powder is obtained from the TMOS/ASB (MI) or the TEOS/ASB (MII) combination. Beyond the 990°C exothermic peak in both the DSC curves, no other event is observed up to 1450°C. The color of the powders were usually white after the DSC runs.

The DSC curves obtained from the powders derived from the mullite precursor gel, EI, in air and argon are shown in Figs. B.6.3. and B.6.4, respectively. As shown in

Fig. B.6.3, the EI powder exhibits a mullite crystallization temperature around 990°C, which is similar to that of the MI and MII mullite precursor powders (Figs. B.6.1 and B.6.2). The EI powder, however, in argon do not exhibit any exothermic event(s) between 150°C and 650°C (Fig. B.6.4). As shown in Fig. B.6.4, the water loss event is prolonged up to 350°C, but the mullite crystallization event takes place at 990°C.

The DSC curves obtained from the powders derived from the mullite precursor gel, MEI, in air and argon are shown in Figs. B.6.5. and B.6.6, respectively. From the above figures, it is observed that the mullite crystallization event takes place at 990°C in both air and argon. The water loss event, however, is prolonged in argon (Fig. B.6.6) up to ~ 450°C in comparison to air (Fig. B. 6.5). After the DSC runs, the powder colors were observed to be white in air and black in argon.

The DSC curve obtained from the aluminum titanate precursor gel, ATI, in air is shown in Fig. B.6.7. This curve shows an endothermic event between 20°C and 360°C, which corresponds to a water loss. This is followed by three exothermic peaks below 710°C, which indicates the organics burnout. After this, there are two exothermic peaks between 780°C and 920°C, which signifies titania crystallization. This is followed by another exothermic peak at 990°C, which indicates alumina crystallization. Finally, there is an endothermic event occurring around 1360°C, which corresponds to aluminum titanate formation. After the DSC run, the powder was yellow in color.

The DSC curves obtained from the powders derived from the aluminum titanate precursor gel, ATII, in air and argon are shown in Figs. B.6.8. and B.6.9, respectively. The DSC curve in air for ATII (Fig. B.6.8) is similar to that of the ATI powder (Fig. B.6.7), with the aluminum titanate formation occurring around 1370°C. However, the

DSC curve in argon (Fig. B.6.9) shows two endothermic peaks (1180°C and 1420°C) and the alumina crystallization event is advanced to 920°C. These two endothermic peaks indicate that the aluminum titanate formation may occur as early as 1180°C, and is fully completed by 1420°C. After the DSC runs, the powder colors were observed to be yellow in air and black in argon.

6.3.2. High Temperature X-ray Diffraction

The high temperature XRD patterns were obtained on powders derived from MI, MII, EI, MEI, ATI, and ATII gels, as described in Section 5.3.2. High temperature XRD patterns obtained in air from the powders derived from the MI and MII gels are shown in Figs. B.6.10 and B.6.11, respectively. From Fig. B.6.10, it is evident that at room temperature there are three peaks corresponding to the substrate Pt-Rh, and these peaks are present in the XRD patterns at all temperatures. From room temperature up to 1000°C, only the substrate peaks are present. At around 1050°C, peaks corresponding to mullite are present in addition to the substrate peaks and match well with the standard ICDD pattern for mullite. These mullite peaks continue to be present till 1350°C and are quenched to room temperature. Similar evolution of the mullite peaks is observed from the powder derived from the MII gel (Fig. B.6.11). This suggests that the mullite crystallization temperature is the same for both the TMOS/ASB (MI) and the TEOS/ASB (MII) derived mullite precursor powders.

High temperature XRD patterns obtained for the mullite precursor powder, EI, in air, and argon, are shown in Figs. B.6.12 and B.6.13, respectively. As is evident from Fig. B.6.12, there are five substrate peaks present at room temperature and continue to be present at all temperatures. Up to 900°C, only the substrate peaks are present. In

addition to the substrate peaks, mullite peaks appear at 950°C and match well with the ICDD pattern. These mullite peaks continue to be present till 1350°C and are quenched to room temperature. After the XRD run in air, the mullite powder is white in color In argon, however, the appearance of mullite peaks is delayed till 1000°C (Fig. B.6.13) as compared to 950°C in air (Fig. B.6.12). After the XRD run in argon, the mullite powder is black in color.

High temperature XRD patterns obtained for the mullite precursor powder, MEI, in air, and argon, are shown in Figs. B.6.14, and B.6.15, respectively. From Fig. B.6.14, it is seen that the five substrate peaks are present up to 800°C. Although the mullite peaks seem to appear as early as 900°C, the peaks are fully developed at 950°C. Beyond 950°C, mullite peaks are present till 1350°C and is quenched to room temperature. After the XRD run in air, the mullite powder is white in color. In contrast, the mullite peaks are observed only at 1000°C in argon (Fig. B.6.15), with mullite being black in color on cooling to room temperature.

High temperature XRD patterns collected in air from the aluminum titanate precursor powder, ATI, are shown in Fig. B.6.16. It is evident from Fig. B.6.16, only the three substrate peaks are present at room temperature, and up to 800°C. Titania peaks are observed at 900°C in addition to the substrate peaks, which match well with the ICDD pattern. At 1000°C, alumina peaks appear in addition to the substrate and titania peaks. No other event is observed till 1400°C. Aluminum titanate peaks appear at 1400°C along with some residual amounts of alumina and titania. After the run, the powder is yellow in color.

High temperature XRD patterns obtained for the aluminum titanate precursor powder, ATII, in air, and argon, are shown in Figs. B.6.17, and B.6.18, respectively. As shown in Fig. B.6.17, there are five substrate peaks at room temperature and persist at all temperatures of data collection. Up to 700°C, only the substrate peaks are present. At 800°C, titania peaks start to appear and at 900°C, alumina peaks along with titania peaks are present. Aluminum titanate peaks emerge at 1300°C, with small amounts of titania and alumina still present. These peaks continue to be present till 1500°C, and are quenched to room temperature. The color of the powder after the XRD run in air is yellow. In contrast, the emergence of titania and alumina peaks in argon is delayed till 900°C, and 950°C, respectively (Fig. B.6.18). But the aluminum titanate peaks appear as early as 1200°C, and are fully developed by 1300°C. After the XRD run in argon, the powder is black in color. Table 11 summarizes the mullite crystallization temperature as indicated by the DSC curves and high temperature XRD patterns. Table 12 summarizes the aluminum titanate formation temperature as indicated by the DSC curves and high temperature XRD patterns.

6.4. Nicalon Cloth and Tow Coating Studies

Mullite coatings were obtained on Nicalon cloth by dip-coating in sols of different wt.% yield of mullite. These studies indicate that more uniform coatings were obtained at 1 to 3 wt.% yield of oxide coating sol than from the 5 wt.% oxide yield sol. The room-temperature XRD pattern of a Nicalon cloth dip-coated in mullite sol and heat treated at 1050°C in air for 30 minutes indicated that mullite is formed. Coated Nicalon tows were used to determine whether Nicalon is damaged during sol-gel processing. Nicalon tows

were dip-coated in mullite sol (MII) at various withdrawal rates, and it was found that a slow withdrawal rate (3.7 cm/min) resulted in thin (100 nm or less) and much more uniform coatings than other withdrawal rates (> 3.7 cm/min). Figure B.6.19 shows a secondary electron image of a mullite coating on a Nicalon tow heat treated at 1000°C along with an energy dispersive X-ray (EDS) spectrum. EDS analyses indicate that the relative intensity of aluminum to silicon peaks varied from one region to another in the tow.

Nicalon tows coated with a mullite (MI) sol (alumina/silica ratio = 1.5) and heat treated at 1000°C for 1 h in air had poor handleability and the coated tows were embrittled. Poor handleability refers to the crumbling of the Nicalon tow by a mere finger touch upon cooling. In contrast, Nicalon tows coated with a mullite sol obtained from the ASB/TEOS (MII) formulation and similarly heat-treated had better handleability. However, longer heating times (10 h) in air resulted in poor handleability.

The tows dip-coated in an aluminosilicate precursor sol with a lower alumina/silica ratio of 0.75 and heat treated at 1000°C in air were less handleable than those dip-coated in a mullite sol (MII). On the other hand, the tows dip-coated in an aluminosilicate precursor sol with a high alumina/silica ratio of 3 had good handleability. At the present time, we have not made any quantitative measurement of the strength of the fibers after coating.

Figure B.6.20 shows a secondary electron image of Nicalon tows coated with the aluminum titanate precursor sol and heat treated at 1000°C for 1 h in air. It should be noted that only an alumina and titania mixture would form on Nicalon under this condition. The coated Nicalon tows had good handleability, and this persisted even after

longer heating times (10 h) in air. Since the alumina-titania mixture did not damage the fiber tows, it was decided that alumina-titania coating would be pursued as an interface coating.

6.5. Density of Fabricated Composites

Nicalon/SiC and Nextel/SiC composites were fabricated as described in Section 5.5. After this, 24 flexure bars (~2.5 x 3.0 x >33 mm) were obtained from each composite and their density measured according to the procedure described in Section 5.6.1. Table 13 summarizes the measured densities of Nicalon/SiC composites with C, oxide/C, and C/oxide/C interfaces along with the coating thickness. As listed in Table 13, these composites had average densities ranging from 2.32 ± 0.12 g/cm^3 to 2.52 ± 0.06 g/cm^3, which is approximately 79-86% of the theoretical density.

As mentioned earlier, Nicalon/SiC composite with a C interface layer is the control sample. The C layer thickness in the sample is ~ 0.043 μm (measured by weight gain). In case of composites with oxide/C interfaces, the outer C thickness is less than 0.033 μm. Composites with C/oxide/C interfaces typically had inner C layer thickness less than 0.032 μm, while the outer C layer is less than 0.031 μm thick.

Table 14 summarizes the measured densities of Nicalon/SiC composites with BN, and BN/oxide/BN interfaces along with the coating thickness. It is evident from Table 14, the composites had average densities ranging from 2.39 ± 0.18 g/cm^3 to 2.46 ± 0.1 g/cm^3, which is approximately 81-85% of the theoretical density. The control sample, Nicalon/SiC with a BN interface, had a BN thickness of 0.282 μm. The inner and outer BN coating thicknesses in composites with BN/oxide/BN interfaces were similar.

Table 15 lists the measured densities of Nextel/SiC composites with oxide/C, and C/oxide/C interfaces along with the coating thickness. As listed in Table 15, these composites had average densities ranging from 2.69 ± 0.11 g/cm^3 to 2.77 ± 0.05 g/cm^3, which is approximately 85-89% of the theoretical density. The inner C coating thickness is less than 0.024 μm, while the outer C coating thickness is less than 0.023 μm.

6.6. Flexural Strength and Microanalysis of Fabricated Nicalon/SiC Composites

As described in Section 5.6.2, flexural strength measurements were conducted at room temperature in the as-processed condition. Flexural strength measurements, in the as-processed condition, of the fabricated Nicalon/SiC composites with C, oxide/C, C/oxide/C, BN, and BN/oxide/BN interfaces are summarized in Table 16.

The control sample, composite with a C interface (CVI 1077), had a flexural strength of 311±74 MPa. Composites with oxide/C interfaces (CVI 982 and CVI 985) are those in which either mullite or alumina-titania layer is directly deposited on the fiber followed by a C layer prior to the matrix deposition. These composites exhibited average flexural strengths < 123 MPa, which is relatively low. Composites with C/oxide/C interfaces (CVI 986 and CVI 1002), where both the fibers and the oxides are protected during processing, had flexural strengths averaging > 245 MPa.

Composites with C/mullite/C (CVI 1033, CVI 1080, and CVI 1081) and C/Al_2O_3-TiO_2/C (CVI 1036 and CVI 1066) were fabricated to examine the repeatability of the processing conditions to obtain good flexural strengths. From the flexural strength data of the above composites in Table 16, it is evident that average strengths > 245 MPa is attainable and that the process repeatability is good. Among the fabricated composites

with C, oxide/C, and C/oxide/C interfaces, CVI 1080 (C/mullite/C) had the highest flexural strength.

The control sample, the composite with a BN interface, had an average flexural strength of 274±52 MPa. Composites with BN/mullite/BN and BN/ Al_2O_3-TiO_2/BN interfaces had average flexural strengths of 244±115 and 266±128 MPa, respectively. These standard deviations are high, and suggest that there is not good process control of the interface layers deposition.

As described in Section 5.6.2, Nicalon/SiC composites were oxidized in air up to 1000°C for time periods up to 500 h. Table 17 summarizes the flexural strength results, comparing samples exposed to 1000°C in air up to 500 h with samples in the as-processed condition. Table 18 summarizes the flexural strength results, comparing samples exposed for 200 h at 500°C, 750°C, and 1000°C in air with samples in the as-processed condition. Table 19 summarizes the interface debonding characteristics results of the composites investigated using AES analyses.

6.6.1. Composite with a C interface (CVI 1077)

In the as-processed condition, composite with a C interface had an average flexural strength of 311±74 MPa. Fracture surface analysis of the sample by SEM indicates that the fiber pullout in the tensile region of the sample is limited to 300 μm (Fig. B.6.21). Regions containing fiber pullout adjacent to brittle fracture are also observed. AES analysis of the in-situ fracture surface indicates that there is good amount of fiber pullout in certain regions (Fig. B.6.22). The composition depth profiles were generated for both fibers and troughs. Figures B.6.23 (a) and (b) show a composition depth profile on a fiber and a trough, respectively. C is observed on fiber as

well as the trough after in-situ fracture indicating that the interface debonding occurs within the C layer (Fig. B.6.23). Further, the interface debonding is such that most of the C layer is on the fiber. Based on the AES composition depth profile analysis, the C layer thickness is estimated to be < 90 nm.

As is evident from Table 18, there is greater than 27% flexural strength reduction in the oxidized composite with a C interface compared to the as-processed condition. Among the oxidized samples, the samples oxidized at 750°C underwent the maximum strength reduction to 67±9 MPa from the as-processed condition. Figure B.6.24 shows the load vs displacement curve of representative samples oxidized for 200 h at 500°C, 750°C, and 1000°C along with the as-processed sample. With the exception of samples oxidized at 750°C, the other samples failed in a graceful manner at 500°C and 1000°C (Fig. B.6.24). From the SEM fracture micrographs of the fracture surface in Fig. B.6.25, it is evident that there is a good amount of fiber pullout after oxidation at 750°C. Only, limited amount of fiber pullout is observed at 500°C and 1000°C.

As shown in Table 17, composite with a C interface displayed the maximum percentage decrease in strength in the first 24 h of oxidation (23%) to 238±43 MPa. The flexural strength did not change noticeably even after 500 h oxidation, since the standard deviations of measurements make the flexural strengths overlap with each other. Figure B.6.26 shows the load vs displacement curve of samples oxidized at 1000°C for 24 h, 200 h, and 500 h along with the as-processed sample. It is evident that these samples exhibited graceful failure even after 500 h oxidation at 1000°C (Fig. B.6.26). Figure B.6.27 shows a fracture surface of the composite after 500 h oxidation at 1000°C, and it

shows good amount of fiber pullout in the composite interior. However, brittle fracture is observed near the edges, and extends ~ 500 μm.

The in-situ fracture surface of the composite oxidized for 500 h at 1000°C is shown in Fig. B.6.28. Fiber pullout regions are observed in a majority of the sample. The composition depth profiles were obtained on both fiber and trough regions (Fig. B.6.29). As shown in Fig. B.6.29, C is observed in both fiber and trough regions indicating that the C interface is retained in the interior of the composite even after oxidation, and debonding occurs within the C interface.

6.6.2. Composites with Oxide/C Interfaces

6.6.2.1. Composite with a mullite/C Interface (CVI 982)

The composite with a mullite/C interface had an average flexural strength of 64±8 MPa in the as-processed condition, which is very low (Table 16). Fracture surface examination by SEM shows that this composite exhibits brittle fracture (Fig. B.6.30 (a)). The in-situ fracture surface also shows brittle fracture. Composition depth profiles generated on the fiber and trough are shown in Fig. B.6.31. Al_2O_3 and SiO_2 are observed on the fiber surface, while C is seen on the trough. This suggests that the interface debonding occurred at the mullite/C boundary, with the mullite region going with the fiber. Mullite and C coatings were each < 60 nm in thickness. Also, the mullite thickness changed from one fiber to another indicating that there is non-uniformity in deposition. On the other hand, there was a good repeatability of C coating thickness in the analyzed trough regions.

After oxidation for 24 h at 1000°C, the flexural strength did not change much (Table 17). As shown in Fig. B.6.30 (b), the SEM fracture surface micrograph indicates

brittle fracture. Figure B.6.32 shows the load vs displacement curve of samples oxidized at 1000°C for 24 h along with the as-processed sample, and both samples exhibit brittle fracture.

6.6.2.2. Composite with an Al_2O_3-TiO_2/C Interface (CVI 985)

In the as-processed condition, composite with an Al_2O_3-TiO_2/C interface had an average flexural strength of 122±29 MPa (Table 16). SEM analysis of the fracture surface indicates predominantly brittle fracture, with limited amount of fiber pullout (Fig. B.6.33). Composition depth profiles obtained on the fiber and trough are shown in Fig. B.6.34. After in-situ fracture, Al_2O_3-TiO_2 is observed on the fiber, while C is seen on the matrix. C thickness was ~ 60 nm, while the Al_2O_3-TiO_2 layer thickness was < 105 nm on one fiber and >150 nm thick on the other two fibers. The Al_2O_3-TiO_2 layer thickness varied from one region to another, thus suggesting the non-uniformity of the deposition process.

After oxidation for 24 h at 1000°C, the flexural strength did not change much (Table 17). As shown in Fig. B.6.33 (b), the micrograph of the fracture surface indicates predominantly brittle fracture. Figure B.6.35 shows the load vs displacement curve of samples oxidized at 1000°C for 24 h along with the as-processed sample, and both samples exhibit some amount of graceful fracture.

6.6.3. Composites with C/mullite/C Interfaces

As mentioned earlier in Section 5.5.8, CVI 986 and CVI 1033 are composites with C/mullite/C interfaces. In these composites, the mullite interface coatings were obtained from a TMOS/ASB combination in an ethanol based mullite precursor sol. CVI 1080 and CVI 1081 are also composites with C/mullite/C interfaces. In both the

composites, the mullite interface coatings were obtained from the TMOS/ASB combination in a 2-methoxy ethanol based mullite precursor sol. CVI 1080 and CVI 1081 composites were fabricated with C/mullite/C interfaces, with mullite applied from the 2-methoxy ethanol based mullite precursor sol. These composites were fabricated to improve the uniformity of the mullite coatings in the composite.

6.6.3.1. CVI 986

In the as-processed composite, this material had an average flexural strength of 268±52 MPa (Table 16) and the load vs displacement curve shows good composite behavior (Fig. B.6.36). Figure B.6.37 (a) is a SEM micograph of a fracture surface of a sample broken in-situ for AES analysis, and displays a good amount of fiber pullout. Representative composition depth profiles obtained on the fiber and trough are shown in Fig. B.6.38. Analysis of these depth profiles indicate that the interface debonding occurs at either inside C/mullite boundary or outer mullite/C boundary. In most cases, debonding occurred at the outer mullite/C boundary. For this situation, C is seen on the trough, and the mullite interface is observed on the fiber. Rough estimates of the interface thickness by AES analysis is as follows: Inner C ~ 30 nm, mullite ~ 30-60 nm, and outer C ~ 30 nm.

TEM analysis conducted on the as-processed sample indicated that the mullite coating is non-uniform. Mullite is observed only in few interfaces while in most fiber-matrix interfaces, mullite was not observed. While in others, the mullite interface was almost like a matrix. Figure B.6.39 is a TEM micrograph shows a fiber-matrix interface, where mullite is observed. Figure B.6.40 presents an interface, where mullite is not

present. From the TEM study, it is evident that the mullite coating was non-uniform in the area of study.

As mentioned earlier, samples of CVI 986 were oxidized up to 500 h at 1000°C in air. For the first 24 h of oxidation, the flexural strength was 260±61 MPa, which is the same as that in the as-processed condition. However, the flexural strength decreased with longer exposure times at 1000°C attaining values of 200±47 MPa and 184±28 MPa, after 200 h, and 500 h, respectively. Figure B.6.36 summarizes the load vs displacement curves of the CVI 986 samples in the as-processed condition as well after the oxidation at 1000°C up to 500 h in air. It is evident from the load vs displacement curves that the material exhibits good composite behavior even after 500 h oxidation at 1000°C.

Figure B.6.41 (a), (b), and (c) shows the fracture surface of a CVI 986 samples in the as-processed condition, and after oxidation at 1000°C for 24 h, and 500 h, respectively. In the as-processed condition, the fracture surface shows a considerable amount of fiber pullout. However, with increasing exposure time at 1000°C, the fiber pullout amounts were reduced. It should be noted that after oxidation for 500 h, the fiber pullout is confined to the inside of the sample. Along the outer edges of the sample, brittle fracture was the predominant mode of failure and very little fiber pullout is seen.

Figure B. 6.37 (b) is a SEM micrograph of an in-situ fractured AES sample after 500 h oxidation at 1000°C, and it shows that the fiber pullout is limited to the interior of the sample. AES composition profiles were obtained on the fibers and troughs of this sample. Figure B. 6.42 is a representative profile obtained on a fiber and trough. As is evident from the figure, Al_2O_3 and SiO_2 are seen on the fiber. On the trough, C is observed along with SiO_2. This indicates that the preferred site for debonding is the

mullite/C interface, although in some cases debonding is observed within the mullite layer (mullite being observed on both fiber and matrix).

6.6.3.2. CVI 1033

As mentioned earlier, this composite with a C/mullite/C interface was tested at room temperature in the as-processed condition as well as after oxidation for 200 h each at 500°C, 750°C, and 1000°C in air. In the as-processed condition, this material had a flexural strength of 310±29 MPa and the load vs displacement curve shows a graceful failure (Fig. B.6.43). This composite was fabricated to demonstrate the ability to reproduce the properties displayed by CVI 986. Figure B.6.44 is a SEM image of the fracture surface in the as-processed condition, and it shows a considerable amount of fiber pullout. After 200 h oxidation at 1000°C in air, this material exhibits reduced flexural strength (199±34 MPa). The fracture surface examination reveals that the fiber pullout is restricted to the interior of the composite, while the outer edges exhibited predominantly brittle fracture (Fig. B.6.45).

This material after 200 h oxidation at 500°C in air exhibited flexural strength of 293±27 MPa, which is similar to that in the as-processed condition. The load vs displacement curve (Fig. B.6.43) exhibits a graceful failure, and the SEM micrograph of the fracture surface indicates a good amount of fiber pullout (Fig. B.6.46).

When the composite was subjected to 750°C for 200 h in air, the samples exhibited a drastic reduction in strength to 44±20 MPa, and the material exhibited brittle fracture (Fig. B.6.47). This behavior is also evident from the load vs displacement curve (Fig. B.6.43), which shows brittle fracture.

6.6.3.3. CVI 1080

This composite had a flexural strength of 320±24 MPa in the as-processed condition, and the fracture surface exhibited a good amount of fiber pullout (Fig. B.6.48). After oxidation at 1000°C for 24 h in air, the flexural strength reduced to 238±54 MPa, and the material still exhibited a considerable amount of fiber pullout (Fig. B.6.49). However, brittle fracture was observed near the tensile surface edge with good amount of fiber pullout occurring after that (Fig. B.6.50).

Even after 200 h oxidation at 1000°C in air, the flexural strength (239±39 MPa) did not change from the 24 h oxidation value. The fracture surface examination revealed that the material still sustained good amount of fiber pullout, with the fiber pullout confined to the interior of the sample (Fig. B.6.51). Near the edges, however, brittle fracture was observed. After oxidation for 500 h at 1000°C in air, the composite underwent further reduction in strength to 193±27 MPa. However, the fracture surface of the material displayed a good amount of fiber pullout and up to 300 μm, the edges displayed brittle fracture (Fig. B. 6.52). Figure B.6.53 is a summary of the load vs displacement curve of the samples prior to and after oxidation for up to 500 h at 1000°C in air. The material displayed a graceful failure at all conditions of testing (Fig. B.6.53)

6.6.3.4. CVI 1081

In the as-processed condition, the fracture surface was fibrous in appearance exhibiting a considerable amount of fiber pullout (Fig. B.6.54), and very close to the tensile surface, fiber pullout of the order of 150 μm is observed (Fig. B.6.55). The composite had a flexural strength of 253±38 MPa in the as-processed condition. As mentioned earlier, this composite was oxidized for 200 h each at 500°C, 750°C, and

1000°C. Similar to the CVI 1033 composite, this composite underwent a drastic reduction in strength at 750°C to 67±21 MPa and the load vs displacement curve shows brittle fracture (Fig. B.6.56). The fracture surface had a shiny appearance and showed little fiber pullout (Fig. B.6.57). However, the flexural strength value after oxidation at 500°C (306±127 MPa) and 1000°C (239±80 MPa) in air did not change much from the as-processed strength. Fracture surfaces of samples oxidized at 500°C and 1000°C are fibrous in appearance, and are presented in Figs. B.6.58 and B.6.59, respectively. Both the samples exhibit a good amount of fiber pullout even after 200 h oxidation. However, brittle fracture is observed near the tensile edge of the sample oxidized at 1000°C (Fig. B.6.60). Figure B.6.56 summarizes the load vs displacement curve of the samples in the as-processed as well as after oxidation at conditions mentioned earlier. Except for the sample oxidized at 750°C, all other samples exhibited a graceful failure.

6.6.4. Composites with C/Al_2O_3-TiO_2/C Interfaces

As mentioned earlier in Section 5.5.8, composites CVI 1002, CVI 1036, and CVI 1066 are composites with C/Al_2O_3-TiO_2/C interfaces.

6.6.4.1. CVI 1002

In the as-processed condition, this composite had an average flexural strength of 255±35 MPa and the load vs displacement curve exhibits good composite behavior (Fig. B.6.61). Figure B.6.62 is a TEM micrograph of a C/Al_2O_3-TiO_2/C interface in the composite. The C layer on the fiber is ~ 30 nm in thickness, while the C layer adjacent to the matrix is ~ 30 nm. Between the C layers is the Al_2O_3-TiO_2 interface, which is also ~ 30-50 nm in thickness. The Al_2O_3-TiO_2 interface bounded by C layers appear to be uniform in the area of TEM study and both Al_2O_3 and TiO_2 are crystalline. Figure B.6.63

is a fracture surface of a composite with a C/Al_2O_3-TiO_2/C interface, and it has a fibrous appearance. This sample displayed a considerable amount of fiber pullout, with typical fiber pullout lengths > 500 μm.

Figure B.6.64 shows three fibers, and two troughs which were considered for the AES study. Composition depth profiles were obtained on the fiber and trough, and one such profile is shown in Fig. B.6.65. As shown in Fig. B.6.65 (a), Al, Ti, and C were observed on the fiber, while C was seen on the trough. It shows that in this case, the interface debonding occurred at the Al_2O_3-TiO_2/C interface. The Al_2O_3-TiO_2 coating thickness for this case was estimated to be ~ 50 nm. On analyzing the studied regions, it could be inferred that the interface debonding could occur either at the outer Al_2O_3-TiO_2/C boundary or in the C/Al_2O_3-TiO_2 interface. In the other two fibers studied, Al_2O_3 and TiO_2 were observed but with different coating thicknesses. This indicates that there is a possibility that the Al_2O_3-TiO_2 interface coating thickness may vary from one part of the sample to another.

As pointed out earlier, flexure bars of CVI 1002 were oxidized up to 500 h in air at 1000°C. After 24 h oxidation, the flexural strength reduced to 189±45 MPa, and there was not much variation in flexural strength (217±35 MPa) up to 200 h. After 500 h oxidation, the flexural strength was further decreased to 159±20 MPa. Figure B.6.66 (a) and (b) show the fracture surfaces of samples oxidized for 200 h, and 500 h at 1000°C in air, respectively. It is evident from the above micrographs, the fiber pullout becomes more and more confined to the interior of the sample with increasing exposure time at 1000°C. It should be noted that along the outer edges, only brittle fracture is observed.

Figure B.6.67 shows a TEM image of a sample oxidized for 500 h at 1000°C in air. As shown in the figure, Al_2O_3-TiO_2 is observed bounded by SiO_2 layers. In the as-processed condition, Al_2O_3-TiO_2 is bounded by C layers (Fig. B.6.62). After oxidation, the C layers adjacent to both the fiber and matrix are oxidized and are replaced by the SiO_2 layer. It should be noted that in the oxidized condition, the SiO_2 layer adjacent to the fiber surface is ~60-80 nm thick. In the as-processed condition, C was ~30 nm thick. So the additional 30-50 nm of SiO_2 is likely due to the degradation of the fiber. The AES analysis identified that the SiO_2 layer was observed along with Al_2O_3-TiO_2 on the fiber, although in one case C was seen. After the trough depth profiles were obtained, during the process of analysis it became evident that the troughs selected were portions of the fiber below. Also, Al_2O_3-TiO_2 persisted on one fiber even after 20 min of sputtering (~300 nm depth Fig. B.6.68), while on the other fiber Al_2O_3-TiO_2 was ~105 nm. Based on the fibers studied during the analysis, it could be inferred that the debonding occurred at the Al_2O_3-TiO_2/C boundary.

6.6.4.2. CVI 1036

In the as-processed condition, this composite had an average flexural strength of 246±12 MPa and the load vs displacement curve exhibits good composite behavior (Fig. B.6.69). Figure B.6.70 is a SEM micrograph of a fracture surface showing a considerable amount of fiber pullout, with typical fiber pullout lengths > 300 μm. This composite did not exhibit a significant decrease in flexural strength (225±33 MPa) even after 200 h oxidation at 500°C in air, compared to the as-processed condition. Fracture surface examination revealed that this material exhibited a significant amount of fiber pullout, with fiber pullout lengths ~ 250 μm or more (Fig. B.6.71). However, when this

composite was subjected to oxidation at 750°C in air for 200 h, it underwent drastic reduction in strength to 50±9 MPa. Figure B.6.72 is a fracture surface of a composite after oxidation at 750°C, which shows predominantly brittle fracture and is shiny in appearance. Figure B.6.73 shows a fracture surface of a composite after oxidation at 1000°C in air for 200 h, and the flexural strength is reduced by 44% from the as-processed condition to 139±42 MPa. After this oxidative exposure, the fiber pullout is restricted to the interior of the composite and the edges exhibit brittle fracture (Fig. B.6.74). The embrittlement region near the edges extend to ~200 μm. Figure B.6.69 summarizes the load vs displacement curve in the as-processed as well as post-oxidized conditions. With the exception of the sample oxidized at 750°C in air, all other samples in Fig. B.6.69 show non-catastrophic failure behavior and the same amount of displacement to failure.

6.6.4.3. CVI 1066

In the as-processed condition, this composite had a flexural strength of 298±23 MPa. Figure B.6.75 is a SEM micrograph of a fracture surface, which has a fibrous appearance and shows a considerable amount of fiber pullout. Even after oxidation at 1000°C for 24 h in air, this composite exhibited a flexural strength of 314±29 MPa, and the fracture surface had a fibrous appearance and displayed a substantial amount of fiber pullout (Fig. B.6.76).

When four flexure bars were tested after oxidation at 1000°C for 200 h in air, the composite flexural strength was reduced only by 14% to 257±6 MPa. The fracture surface examination revealed that this composite exhibited a good amount of fiber pullout (Fig. B.6.77). This promising trend prompted us to subject the remaining 2 flexure bars

(after 200 h oxidation at 1000°C in air) to oxidation at 200 h at 750°C in air. After the oxidation treatment at 750°C in air, the flexural strength of the two bars were 252 MPa and 102 MPa, and they exhibited a good amount of fiber pullout (Fig. B.6.78). Fracture surface examination showed that this composite retained a considerable amount of pullout in the interior, with some amount of embrittlement near the tensile edge (Fig. B.6.79). Thus, the flexural bars which were preoxidized at 1000°C prior to exposure at 750°C retained considerable strength compared to CVI 1036 bars which were oxidized at 750°C in air for 200 h directly and had very low flexural strength (50±9 MPa).

This composite retained considerable flexural strength (234±52 MPa) even after 500 h oxidation at 1000°C in air. This is only a 21% flexural strength loss compared to the as-processed condition (298±23 MPa). The fracture surface is fibrous in appearance, and displayed a considerable amount of fiber pullout (Fig. B.6.80). However, near the edges (~ 300 μm) brittle fracture is observed (Fig. B.6.81). Figure B.6.82 (a) summarizes the load vs displacement curve in the as-processed as well as oxidized conditions. As is evident from Fig. B.6.82 (a), the samples exhibit graceful failure even after 500 h oxidation at 1000°C in air. Figure B.6.83 (b) contrasts the behavior of a CVI 1066 sample (oxidized for 200 h at 1000°C followed by 200 h exposure at 750°C) with a CVI 1036 sample (oxidized for 200 h at 750°C). It is evident from Fig. B.6.83 (b), prior exposure to 1000°C of the CVI 1066 sample markedly increases the load bearing capacity and the sample shows graceful failure even after 200 h oxidation at 750°C.

6.6.5. Composite with a BN Interface (CVI 1068)

In the as-processed condition, the composite with a BN interface had a flexural strength of 274±52 MPa. As shown in Fig. B.6.83, the load vs displacement curve of the

composite in the as-processed condition had a large load drop and held the load at a lower level. The fracture surface shows predominantly a brittle fracture with very little fiber pullout (Fig. B.6.84). After oxidation for 24 h at 1000°C in air, the composite had a flexural strength of 198±86 MPa, and the fracture surface displayed brittle fracture (Fig. B.6.85). Further oxidation at 1000°C for 200 h resulted in a flexural strength of 177±87 MPa, and the fracture surface showed brittle fracture (Fig. B.6.86). This sample retained considerable strength (232±116 MPa) even after 500 h oxidation, and the fracture surface exhibited very little fiber pullout (Fig. B.6.87). Additionally, BN samples were oxidized for 200 h each at 500°C and 750°C in air. The composite flexural strength was 246±131 MPa and 211±97 MPa after post oxidation at 500°C and 750°C, respectively. Fracture surface examination of these samples showed that they exhibited brittle fracture. Figure B.6.88 is a fracture surface obtained after 500°C oxidation exposure and shows brittle fracture. As is evident from Tables 17 and 18, there is a considerable scatter in the flexural strength of the composite with a BN interface. This suggests that there may not be good process control of BN deposition compared to C deposition.

Figure B.6.83 shows the load vs displacement curve of BN samples in the as-processed condition and after oxidation at 1000°C up to 500 h. It is evident that even after 500 h oxidation, composite behavior is exhibited but with a large load drop. Figure B.6.89 compares the load vs displacement curves after oxidation at 500°C, 750°C, and 1000°C with the as-processed condition. It is evident from this figure that the composite behavior is retained, but there is a significant load drop at all temperatures.

Composition depth profiles were obtained on fibers and troughs after in-situ fracture of the composite with a BN interface. As is evident from Fig. B.6.90, BN is

observed on both fiber and trough after in-situ fracture. This shows that the debonding occurred within the BN interface. From Fig. B.6.90, it is clear that the BN is gone in both fiber and trough after 15 min of sputtering. This was the case in all the examined troughs and fibers, and there was good consistency in the results. Thus, the BN coating thickness is estimated to be slightly greater than 300 nm but definitely less than 450 nm. After oxidation for 500 h at 1000°C in air, composition depth profiles were also obtained after in-situ fracture. It is evident from Fig. B.6.91, that BN is observed on both fiber and trough after in-situ fracture, and thus, the debonding occurs within the BN layer. It is also evident that the BN is present only up to 7 min (105 nm) and 4 min (60 nm) of sputtering time on fiber and trough, respectively. This shows that the total BN coating thickness is slightly greater than 165 nm.

6.6.6. Composite with a BN/Al_2O_3-TiO_2/BN Interface (CVI 1073)

In the as-processed condition, this composite had a flexural strength of 266±128 MPa. Figure B.6.92 is a SEM micrograph of the as-processed sample after fracture and is fibrous in appearance and shows a good amount of fiber pullout. After oxidation for 24 h at 1000°C in air, the composite flexural strength was reduced to 156±57 MPa. The fracture surface examination revealed that the fiber pullout was reduced substantially, and near the tensile edge, only brittle fracture is seen (Fig. B.6.93). Further oxidation to 200 h and 500 h at 1000°C resulted in flexural strength recovering to 241±96 MPa and 253±88 MPa, respectively. SEM examination of these fracture surfaces identified that there was slightly greater amount of fiber pullouts compared to the sample after 24 h oxidation at 1000°C. Figure B.6.94 shows a fracture surface of the sample after 500 h oxidation at 1000°C in air. This sample exhibits a reasonable amount of fiber pullout in both tensile

and compressive regions. Figure B.6.95 is a SEM micrograph of the same sample near the tensile edge, and it shows good amount of fiber pullout.

The samples flexure tested at room temperature after oxidation for 200 h each at 500°C and 750°C had flexural strength of 151±56 MPa and 315±147 MPa, respectively. The fracture surfaces of the sample after oxidation at 500°C and 750°C are shown in Figs. B.6.96 and B.6.97. As is evident from these micrographs, there is more amount of fiber pullout after oxidation at 750°C than at 500°C.

Figure B.6.98 shows the load vs displacement curve of samples in the as-processed condition and after oxidation at 1000°C up to 500 h in air. From Fig. B.6.98, it is clear that all samples, with the exception of samples oxidized for 24 h at 1000°C in air, exhibit a graceful failure but with large load drops. The sample oxidized for 24 h at 1000°C in air exhibits brittle behavior and also has lower flexural strength values compared to the other conditions of testing.

Figure B.6.99 shows the load vs displacement curve of samples in the as-processed condition and after oxidation for 200 h each at 500°C, 750°C, and 1000°C, respectively. From the above figure, it is evident that the samples exhibit a graceful failure along with large load drops. Of particular significance is the sample oxidized at 500°C, which demonstrates low load bearing capacity, compared to others and also exhibits the lowest flexural strength (151±56 MPa).

As summarized in Tables 17 and 18, the flexural strength of this composite at all conditions of testing show substantial amount of scatter. Although, there appears to be a loss in the flexural strength after oxidation at 500°C for 200 h, and initial exposure at

1000°C for 24 h in air, there is still uncertainty involved in the uniformity of both BN and Al_2O_3-TiO_2 coating processes.

Compositional depth profiles were obtained on fibers and troughs after in-situ fracture of the composite in the as-processed condition. As is evident from Fig. B.6.100, only BN is observed on the fiber, while BN as well as Al_2O_3-TiO_2 is seen on the trough. Further, the BN on the fiber is ~150 nm thick , TiO_2 on the trough is ~120 nm thick, and BN on the trough is ~225 nm thick. The AES analysis indicated that the BN layer as well as Al_2O_3-TiO_2 thickness varied in the troughs, while the BN on the fiber was relatively uniform in thickness. Compositional depth profiles were also obtained on fibers and troughs of the in-situ fractured sample, which was oxidized for 500 h at 1000°C in air. As is evident from Fig. B.6.101, BN is observed on both fiber and trough regions. Except for one trough, where Al_2O_3 is observed and ~ 30 nm thick, Al_2O_3-TiO_2 is not seen in the other trough. The BN coating thickness is estimated to be ~300 nm thick including both fiber and trough sides. From the AES analysis, it could be inferred that BN and Al_2O_3-TiO_2 layers were not uniform and further process development needs to be done.

6.6.7. Composite with a BN/mullite/BN Interface (CVI 1054)

In the as-processed condition, this composite had a flexural strength of 244±115 MPa. Figure B.6.102 shows a fracture surface of the as-processed sample, and after oxidation for 24 h at 1000°C in air, the flexural strength reduced significantly to 75±20 MPa. The fracture surface of this oxidized sample reveals that it exhibits brittle fracture (Fig. B.6.103). Further oxidation to 200 h at 1000°C resulted in an improvement of flexural strength to 171±77 MPa, and the fracture surface exhibits a limited amount of

fiber pullout in the tensile region (Fig. B.6.104). After oxidation for 500 h at 1000°C in air, this composite had a flexural strength of 137±76 MPa. Fracture surface examination shows that a limited amount of fiber pullout occurs in the compressive region, while brittle fracture takes place in the tensile region (Fig. B.6.105).

The samples flexure tested after oxidation for 200 h each at 500°C and 750°C in air had flexural strength of 197±154 MPa and 193±97 MPa, respectively. Fracture surface examination of these samples indicate predominantly brittle fracture. Figure B.6.106 shows a fracture surface of a sample oxidized at 500°C for 200 h near the tensile edge and it exhibits brittle fracture. There is a considerable amount of scatter in the flexural strength in the as-processed as well as oxidized conditions (except at 1000°C for 24 h in air). This scatter in data suggests that there is not good process control of the coatings.

Figure B.6.107 shows the load vs displacement curve in the as-processed as well as after oxidation at 1000°C for up to 500 h in air. With the exception of the as-processed sample, all other samples exhibit predominantly brittle fracture. Figure B.6.108 shows the load vs displacement curve in the as-processed as well as after oxidation for 200 h each at 500°C, 750°C, and 1000°C. It is evident from this figure that samples in the as-processed and after oxidation at 500°C shows graceful failure, while samples oxidized at 750°C and 1000°C demonstrate predominantly brittle fracture.

6.7. Flexural Strength and Microanalysis of Nextel/SiC Composites

The flexural strength results of Nextel/SiC composites in both as-processed and oxidized conditions are summarized in Table 20. Composites with C/oxide/C interfaces

exhibited higher strengths than composites with oxide/C interfaces in the as-processed condition. However, after oxidation, composites with C/oxide/C interfaces underwent drastic reduction in strengths.

6.7.1. Composite with a Mullite/C Interface (CVI 997)

In the as-processed condition, this composite had a flexural strength of 126±12 MPa. Fracture surface examination of the as-processed sample identified that the material underwent brittle fracture (Fig.6.109). Oxidation at 1000°C for 24 h resulted in a flexural strength of 101±11 MPa and the material continued to exhibit brittle fracture (Fig. B.6.110). The load vs displacement curve in Fig. B.6.111 shows that the material exhibits a catastrophic failure.

Compositional depth profile analysis were obtained in the as-processed sample on fibers and troughs. Figure B.6.112 shows the depth profile obtained on the trough, and indicates that C is present on the trough after in-situ fracture and is ~ 30 nm thick. Since the fiber is an aluminosilicate fiber with little boria additions, the depth of mullite coatings could not be ascertained. The only inference that could be made is that the interface debonding occurred at the mullite/C interface.

6.7.2. Composite with an Al_2O_3-TiO_2/C Interface (CVI 998)

The composite had a flexural strength of 107±18 MPa in the as-processed condition and after oxidation for 24 h at 1000°C retained a strength of 99±15 MPa. Fracture surface examinations of both samples indicated brittle fracture with little fiber pullout. Figure B.6.113 (a) and (b) shows the fracture surface of the samples in the as-processed condition and after oxidation at 1000°C for 24 h, respectively. The load vs displacement curve shows brittle failure (Fig. B.6.114 (a)). AES analysis of the as-

processed sample indicates that the interface debonding takes place at either Nextel/Al_2O_3-TiO_2 or Al_2O_3-TiO_2/C interface. In the former case, C as well as Al_2O_3-TiO_2 is observed on the trough (Fig. B.6.114 (b)). While in the latter case, Al_2O_3-TiO_2 is observed on the fiber. The compositional depth profile analysis estimates the Al_2O_3-TiO_2 layer to be ~150 nm and C to be ~30 nm.

6.7.3. Composite with a C/mullite/C Interface (CVI 999)

The composite had a flexural strength of 204±34 MPa in the as-processed condition and after oxidation for 24 h at 1000°C underwent a drastic reduction in strength to 94±16 MPa. In the as-processed condition, the fracture surface displays a considerable amount of fiber pullout (Fig. B.6.115 (a)), and the load vs displacement curve indicates graceful failure (Fig. B.6.116). After oxidation, however, a catastrophic fracture is observed in the load vs displacement curve (Fig. B.6.116), and the fracture surface shows brittle fracture (Fig. B.6.115 (b)). Compositional depth profile analysis of the as-processed sample indicates that the interface debonding occurs at the C/mullite interface. Due to this debonding, C is observed on the fiber, while the mullite layer as well as the outer C layer is seen on the trough. Figure B.6.117 shows the composition depth profile on the trough and fiber. Further, the coating thickness is estimated to be as follows: inner C: 50 nm, mullite: ~50 nm, and outer C:~30 nm.

6.7.4. Composite with a C/Al_2O_3-TiO_2/C Interface (CVI 1000)

In the as-processed condition, this composite had a flexural strength of 234±31 MPa and had good composite behavior (Fig. B.6.118). After oxidation at 1000°C for 24 h, the composite exhibited a graceful failure (Fig. B.6.119) but with a reduced flexural strength (119±27 MPa). Further oxidation at 1000°C for 200 h resulted in a flexural

strength of 97±16 MPa and brittle fracture (Fig. B.6.120). AES analysis revealed that the interface debonding occurred at the Al_2O_3-TiO_2/C interface in the as-processed condition. As a result, C is observed on the trough, while the Al_2O_3-TiO_2 followed by a C layer is seen on the fiber (Fig. B.6.121). The coating thickness based on the AES analysis is as follows: inner C: ~50 nm, Al_2O_3-TiO_2: ~50 nm, and outer C: ~50 nm. Figure B.6.119 summarizes the load vs displacement curve of the samples in the as-processed condition as well as the oxidized conditions. In the as-processed condition as well as after 24 h oxidation at 1000°C, the composite exhibited a graceful failure. Whereas, after oxidation for 200 h at 1000°C in air, the composite displayed brittle fracture.

CHAPTER 7

DISCUSSION

7.1. Sol and Gel Characterization Studies

7.1.1. Mullite and Aluminosilicate

The mullite precursor sol, MI, was prepared using the TMOS/ASB precursor combination as used by Yoldas [198]. Similar to Yoldas' observations, the DSC curve of this mullite precursor powder in air (obtained on gelling and drying at 60°C in air) showed a sharp exothermic peak at 990°C. A high temperature XRD study identified that the mullite crystallizes at 1050°C in air and matches Yoldas' [198] study. Although the mullite precursor sol and gel (dried at 60°C), MII, was prepared from the TEOS/ASB combination, the DSC and high temperature XRD characteristics were similar to that of the MI mullite precursor powder. Thus, the mullite crystallization temperature appears to be independent of the mullite precursor combination (TEOS/ASB or TMOS/ASB) from which mullite is obtained.

The mullite precursor gels, EI, and MEI, were prepared from the TEOS/ASB combination but with ethanol, and 2-methoxy ethanol based solvents, respectively. These gels were dried at 110°C in air unlike the MII gel (dried at 60°C). The DSC curves of EI and MEI in air were similar to that of MII in air, and showed two broad exothermic peaks below 700°C and a sharp exothermic peak at 990°C in air. The DSC curves of EI and MEI in argon, however, did not exhibit any broad exothermic peaks below 700°C in argon. The high temperature XRD patterns of EI and MEI in air indicated that mullite crystallization takes place at 950°C. This mullite crystallization temperature of 950°C is

.100°C lower than that reported by Yoldas [198]. To the best knowledge of the author, no one has reported the mullite crystallization at 950°C from the alkoxide-based precursor gels. Earlier, Shanmugham [210] had shown that mullite could be obtained at 750°C in air, provided the mullite precursor sol is directly converted to a powder at 110°C. The author believes that the low temperature chemistry (drying temperature) plays a vital role in influencing the crystallization temperature. However, detailed experiments are required to substantiate this belief. The high temperature XRD patterns of EI and MEI in argon indicated that mullite crystallizes at 1000°C. Thus, the mullite crystallization occurrence is delayed by 50°C in argon than in air.

7.1.2. Aluminum Titanate

The aluminum titanate precursor gels, ATI, and ATII, were both obtained from the ASB/TEOD precursor combination but were dried at 60°C and 110°C, respectively. A high temperature XRD study identified that aluminum titanate forms at 1400°C and 1300°C in air from ATI and ATII, respectively, along with residual amounts of alumina and titania. Earlier, Prasadarao [202] observed that aluminum titanate forms at 1250°C in air along with a residual alumina from an ASB/titanium isopropoxide gel derived powder. Thus, the aluminum titanate formation temperature in the present study is higher than that reported in the literature and may be attributed to the different precursors along with the procedure used to form the aluminum titanate precursor sol. The high temperature XRD study of the ATII gel in argon indicated that the aluminum titanate peaks appear as early as 1200°C and is fully developed by 1300°C. This concurs well with the DSC curve (Fig. B.6.9), which shows an endothermic peak as early as 1200°C

indicating the formation of aluminum titanate. Hence, aluminum titanate forms at a lower temperature in argon than that in air.

7.2. Nicalon Cloth and Tow Coating Studies

Nicalon tows coated in a mullite sol (MI and MII) and an aluminosilicate sol (alumina/silica ratio of 0.75) and heat-treated at 1000°C for up to 10 h in air were embrittled. Earlier, Hay [211] observed that the mullite coatings obtained above 800°C in air using the sol-gel approach on Nicalon fibers severely degraded and embrittled the fibers. However, he was unable to isolate the factor responsible for this degradation. On the other hand, when the Nicalon tows were protected by a C layer followed by the application of mullite coating by a sol-gel method, the fibers were not embrittled even at 1300°C in air [211]. In contrast, Nicalon tows dipcoated in an aluminum titanate and an aluminosilicate sol (alumina/silica ratio of 3) and heat-treated at 1000°C for up to 10 h in air were not embrittled. It should be noted that no quantitative measurement of the strength of the fibers before and after the deposition of oxide coatings was done.

7.3. Nicalon/SiC Composites with C, Oxide/C, and C/oxide/C Interfaces

Thermomechanical calculations conducted by Walukas [121] indicated that the oxides, alumina, titania, and mullite, offer no significant reduction in compressive radial stresses as an interface coating till they were > 0.3 μm in thickness. Since the oxide coatings obtained in this study were too thin, the effect of modulus on composite behavior could not be studied. Thermochemical analysis indicated that mullite and alumina coatings may be phase stable with the SiC matrix, while the titania coating might

react with the SiC matrix. Based on the work of Walukas [121], the above oxides are prone to the HCl attack (a by-product of the SiC matrix deposition reaction), and hence, in the present study, the oxides were protected by a C layer prior to matrix deposition. Although the thermochemical calculations indicated that alumina and titania coatings may interact with the Nicalon fiber, the non-embrittlement of the fibers during the alumina-titania coating deposition process prompted us to deposit alumina-titania coatings directly on the fibers. Thermochemical calculations indicated that mullite may be stable with the Nicalon fiber, however, the fibers were embrittled during the mullite deposition by a sol-gel process. Hence, composites with oxide/C interfaces were fabricated to explore the extent of damage the oxide coatings could inflict on the composite properties.

In the as-processed condition, the control composite containing a graphite interface exhibited a considerable flexural strength (311±74 MPa), and the estimated C thickness based on a weight gain measurement is ~ 0.04 μm. This strength value is comparable to the flexural strengths of 325±8 MPa and 343±15 MPa obtained by Walukas [121] and Lowden [156] for a Nicalon/SiC composite with a graphite interface of 0.04 μm, and 0.10 μm thickness, respectively. While Lowden [156] reported a limited amount of fiber pullout and brittle failure, a graceful failure as well as a substantial amount of fiber pullout was seen in the fabricated sample, which is similar to the study of Walukas [121]. AES analysis identified that the interface debonding occurred within the C layer.

The Nicalon/SiC composite with a mullite/C interface exhibited very low flexural strength (64±8 MPa) and brittle fracture in the as-processed condition. This low flexural strength may be attributed to the Nicalon fibers embrittlement during the processing of

the mullite on the fiber, as observed in this study as well as Hay's work [211]. On the other hand, the Nicalon/SiC composite with an Al_2O_3-TiO_2/C interface exhibited a flexural strength of 122±29 MPa and a graceful failure in the as-processed condition. This increase in strength compared to a composite with a mullite/C interface may be ascribed to the non-embrittlement of Nicalon fibers on the application of an Al_2O_3-TiO_2 coating by the sol-gel method.

Composites with C/oxide/C interfaces, where the fiber is protected by a C layer prior to the application of the oxide coating, exhibited a graceful failure, good fiber pullout, and flexural strengths (>245 MPa) 3.8 times higher than that of a composite with a mullite/C interface in the as-processed condition. Earlier, Hay [211] observed that the protection of Nicalon fibers by a C layer prior to the application of mullite by the sol-gel method helps in preventing the fiber embrittlement and increases spoolability even at 1300°C in air. Thus, the increase in strength of these composites may partly be attributed to the ability of the C layers to protect the fibers during the processing of the oxide as well as the prevention of the HCl attack on the oxide coatings during the SiC matrix deposition. The TEM micrograph of a Nicalon/SiC composite with a C/Al_2O_3-TiO_2/C interface shows that the Al_2O_3-TiO_2 interface is intact and bounded by C layers in the as-processed condition (Fig. B.6.62). AES analysis indicated that the interface debonding occurred preferentially at the oxide/C interface. This is the first time that composites with C/oxide/C interfaces have been fabricated, and hence, the flexural strength values of these composites could not be compared with that in the literature.

Since the C/oxide/C interfaces has been accomplished for the first time, there are two processing issues to be addressed. The first issue is the uniformity of the oxide

coatings. As indicated by the AES as well as the TEM results of the composites with C/oxide/C interfaces, oxide coatings were not uniform in all areas of study. Although most of the regions may have oxide coatings, there is still a good possibility that certain regions in the sample may not have oxide coatings. Further, the coatings may be of different thickness in different regions. Since the oxide coatings were very thin, it was very difficult to detect these coatings with the S-800 SEM utilized in this study. Second, there is the issue of the reproducibility of the flexural strength and graceful failure results before and after oxidation. As is seen in Table 16, average flexural strengths > 245 MPa are observed in composites with C/oxide/C interfaces in the as-processed condition, which suggests that there is a good reproducibility. The attainment of a graceful failure behavior even after 500 h oxidation at 1000°C in these composites indicate that the repeatability of the process to reproduce non-catastrophic behavior is reasonable, although there is some amount of flexural strength scatter (Table 17).

The effectiveness of C as an interface material in Nicalon/SiC composites at elevated temperatures is limited by its poor oxidation resistance. The oxidation of the C interface and the subsequent silica formation in these composites at 1000°C in air is well understood [18, 156, 170, 177, 208]. First, the oxygen reacts with the C interface near the exposed fiber ends and results in the formation of an annular pore around each fiber [156]. The diffusion of oxygen along the pore must occur for further oxidation of the C interface. During this diffusion process, oxygen can also interact with the Nicalon fiber and the SiC matrix to form silica scales. For C interface thickness > 0.1 μm, the silica formation process is very slow, and the C interface is depleted along the entire fiber length. This is followed by the growth of a silica layer on both fiber and the matrix

surfaces, which eventually grow and bonds them together. Thus, the amorphous silica layer replaces the carbon completely at the fiber-matrix interface and causes a strongly bonded interface. This tightly bonded interface results in a drastic reduction of flexural strength along with brittle fracture, with very little fiber pullout. Lowden [156] reported that composite with a 0.3 μm thick C interface underwent a drastic reduction (> 60%) in flexural strength within 100 h at 1000°C in air, but exhibited a graceful failure. Longer exposure time to 1000 h resulted in a brittle failure, and amorphous SiO_2 replaced the C interface throughout the sample.

Lowden and Stinton [146] reported that a Nicalon/SiC composite with a C coating thickness of 0.03 μm underwent a brittle fracture in the as-processed condition and exhibited a low flexural strength of 108±13 MPa. However, they did not conduct any oxidation study on the composite. In contrast, when the C thickness was increased to 0.1 μm, the flexural strength increased to 343±15 MPa, but the material exhibited a catastrophic failure [156] in the as-processed condition. Filipuzzi et al [169, 170] conducted experimental and modeling studies of the oxidation of the Nicalon/SiC composite with a C interface. They observed that if the C interface thickness is < 0.1 μm and at temperatures ≥ 1100°C, the composite exhibits self-healing behavior. The self-healing behavior means that the silica forms rapidly and seals the annular pore quickly, with the oxidation of C confined very near to the surface. This passive oxidation can help restrict the further oxidation of the C layer in the interior. Walukas [121] reported that C interface coatings of 0.04 μm were retained in the interior of the composite even after 1000 h oxidation at 1000°C, but with a 42% reduction in strength to 183±12 MPa. Further, the fracture surface examination identified that the embrittlement was confined to

the external surface (300-600 μm), and the central regions exhibited a good amount of fiber pullout.

In the present study, the Nicalon/SiC composite with a C interface exhibited graceful failure, but the flexural strength was reduced by ~31% after oxidation for 500 h at 1000°C in air. Similar to the work of Walukas [121], a substantial amount of fiber pullout was observed in the interior, while the regions near the edges were embrittled. TheAES analysis identified that the C layer is retained in the interior even after long term oxidation and the interface debonding continued to occur within the C layer.

Composites with C/oxide/C interfaces also retained a graceful failure after 500 h oxidation at 1000°C, but the extent of flexural strength reduction had a range of 21-39% of the as-processed strength. The reduction in the flexural strength was minimum for the CVI 1066 (C/Al_2O_3-TiO_2/C interface) composite and maximum for the CVI 1080 (C/mullite/C interface) composite. The fracture surfaces of the oxidized samples indicated that the embrittlement was confined to the external edges, while the interior of the composite exhibited a substantial amount of fiber pullout. This behavior is similar to the composite with a C interface. A TEM study of the composite with a C/Al_2O_3-TiO_2/C interface (CVI 1002) oxidized for 500 h at 1000°C in air indicated that the Al_2O_3-TiO_2 layer was intact, while the C layers were replaced by SiO_2 layers. Thus, the new interface was a SiO_2/Al_2O_3-TiO_2/SiO_2 layer. The SiO_2 thickness on the fiber was ~60-80 nm, which is 50 nm thicker than the initial C layer. Thus, the surface of the Nicalon fiber seems to have degraded. The AES analysis of the oxidized CVI 1002 (C/Al_2O_3-TiO_2/C interface) and CVI 986 (C/mullite/C interface) samples indicated that C as well as SiO_2 was observed in the troughs. Thus, there is uncertainty involved in the extent of SiO_2

replacement of the C layers in the oxidized samples. It is possible that the passive oxidation could have limited the replacement of C by SiO_2 to the embrittlement zone, and C might have been retained in the interior as the C/Al_2O_3-TiO_2/C interface. However, the interface debonding after oxidation tends to occur preferentially at the oxide/C (or SiO_2) boundary. The degradation of the fiber along with the interface to SiO_2/Al_2O_3-TiO_2/SiO_2 might have attributed to the observed decrease in flexural strength. There is also the possibility that C interface layers could have been retained in the interior of the sample, and the C/Al_2O_3-TiO_2/C interface could have been intact even after oxidation and might have contributed to the strength and fiber pullout characteristics of the composite.

The composite with a C interface underwent a 35% reduction in flexural strength to 200±45 MPa after 200 h oxidation at 500°C in air, but retained graceful failure. Tortorelli [212] conducted a thermogravimentric study of a Nicalon/SiC with a C interface at 425°C in air and reported the occurrence of the oxidation of the C layer. Subsequently, Lara-Curzio et al. [213] reported that an amorphous SiO_2 layer is formed on a Nicalon fiber (but not on the SiC matrix side) even at 425°C in air along with the recession of the C layer based on their TEM study. Hence, the observed reduction in strength in this study may be attributed to a partial degradation of the C interface. In contrast, composites with C/oxide/C interfaces (CVI 1036, CVI 1033, and CVI 1081) exhibited a decrease in strength up to 11% after 200 h oxidation at 500°C in air. It can be speculated that the oxidation of the C layer as well as the formation of the amorphous SiO_2 layer may be confined only to the Nicalon side, and thus, might have limited the extent of damage to strength.

The composite with a C interface underwent a drastic reduction (78%) in flexural strength to 67±9 MPa after 200 h exposure at 750°C in air. Further, the flexure bars underwent a catastrophic failure. Earlier, Frety et al. [182] reported that the composite with a C interface (0.03-0.07 μm thick) underwent a 65% reduction in strength along with a brittle fracture within 100 h exposure at 800°C in air. Their TEM analyses showed that the C was replaced by an amorphous SiO_2 layer at the fiber-matrix interfaces, and they attributed the embrittlement of the composite to the SiO_2 layer. They also proposed that the silica formation at 800°C is very low, and thus, the onset of passive oxidation is delayed. During this time, oxygen could penetrate into the interior of the sample and cause a massive oxidation of the C layer. Finally, SiO_2 grows and fills the gap at the fiber-matrix interfaces. Evidence of the SiO_2 formation on the Nicalon fiber with the recession of the C interface at temperatures as low as 425°C in a Nicalon/SiC composite has been reported by Lara-Curzio et al. [213]. Similar to the work of Frety et al. [182], it is likely that the massive oxidation of the C layer followed by the SiO_2 growth might have occurred at 750°C in the present study. Thus, the drastic reduction in the strength of the composite may be attributed to the degradation of the C interface.

Composites with C/mullite/C (CVI 1033 and CVI 1081) and C/Al_2O_3-TiO_2/C (CVI 1036) interfaces also underwent a catastrophic failure and a significant reduction (>73%) in flexural strength from the as-processed condition. The complete embrittlement of the fracture surfaces as well as the catastrophic failure in the load vs displacement curves seem to suggest that the C layers might have been replaced by amorphous SiO_2 layers and coexist with the mullite or Al_2O_3-TiO_2 layer. Thus, the drastic reduction in strength may be due to the presence of SiO_2/mullite/SiO_2 or

SiO_2/Al_2O_3-TiO_2/SiO_2 interfaces. However, the strength of the material (CVI 1066: 15% in one sample and 65% in other) as well as a non-catastrophic failure was not significantly affected provided the samples are exposed first at 1000°C for 200 h in air followed by oxidation for 200 h at 750°C in air. It is likely that the passive oxidation of the material might have occurred quickly at 1000°C, and thus, might have limited the extent of the C oxidation during the 750°C treatment. This behavior is similar to that observed by Frety et al. [182], who reported a significant retention of strength in the Nicalon/SiC composite after 100 h at 800°C following a 100 h exposure at 1400°C in air.

7.4. Nicalon/SiC Composites with BN, and BN/oxide/BN Interfaces

Lowden et al. [153] reported that a Nicalon/SiC composite with a BN interface (0.2 μm thick) had a flexural strength of 417±68 MPa but underwent a 31% strength reduction after 24 h oxidation at 1000°C. The decrease in strength was attributed to the decomposition of the fiber and chemical changes (the formation of a C/SiO_2 layer between the Nicalon and BN layer) occurring at the Nicalon/BN interface. However, the composite fabricated in the present study with a BN interface had a lower flexural strength of 274±52 MPa (0.28 μm). Composites with BN, BN/mullite/BN, and BN/Al_2O_3-TiO_2/BN interfaces had similar flexural strength values (244-274 MPa) in the as-processed condition. As is evident from Tables 17 and 18, there is a considerable amount of scatter in the flexural strength values in the as-processed and oxidized conditions. This scatter in flexural strength seems to indicate that there is not good control in processing BN, mullite, and Al_2O_3-TiO_2 layers in these composites. AES analyses conducted on BN and BN/Al_2O_3-TiO_2/BN interfaces indicated that the BN layers as well

as the Al_2O_3-TiO_2 interface layers were non-uniform, and their thickness varied from one area to another in the composite. Hence, the scatter in strength may be attributed to the non-uniformity of these coatings in the composites.

The composite with a BN interface retained flexural strength values comparable to that of the as-processed condition even after 500 h oxidation at 1000°C, and exhibited non-catastrophic behavior. In contrast, the composite with a BN/mullite/BN interface underwent a significant reduction (69%) in flexural strength during the first 24 h oxidation at 1000°C in air, and then recovered to exhibit only a 43% reduction in flexural strength after 500 h oxidation. This composite, however, exhibited predominantly catastrophic failure. The composite with a BN/Al_2O_3-TiO_2/BN interface exhibited a noticeable decrease in flexural strength during the first 24 h oxidation, but regained after that to exhibit strength values similar to the as-processed condition even after 500 h oxidation at 1000°C in air. Similar to the composite with a BN interface, this composite exhibited a non-catastrophic failure.

The composite with a BN interface did not undergo any noticeable flexural strength changes with oxidation temperature (500°C, 750°C, and 1000°C). In contrast, composites with BN/Al_2O_3-TiO_2/BN and BN/mullite/BN interfaces underwent a significant decrease in flexural strengths during the first 24 h oxidation at 1000°C. Additionally, the composite with a BN/Al_2O_3-TiO_2/BN interface underwent a significant decrease (43%) in flexural strength value after 200 h exposure at 500°C. Composites with BN and BN/Al_2O_3-TiO_2/BN interfaces continued to exhibit a non-catastrophic failure at all conditions of testing, while the composite with a mullite interface exhibited a predominantly catastrophic failure after exposure to 750°C and 1000°C.

7.5. Nextel/SiC composites with Oxide/C and C/oxide/C Interfaces

Weaver et al. [191] reported that a Nextel 312/SiC composite with a 0.12 μm thick C interface had a flexural strength of 222±21 MPa in the as-processed condition but underwent a 74% strength degradation after 100 h exposure at 1000°C in air. In contrast, the Nextel 440/SiC composite with a 0.22 μm thick C interface underwent only a 22% strength decrease to 173±28 MPa after similar oxidation. In the present study, composites with oxide/C interfaces (CVI 997 and CVI 998) exhibited flexural strengths less than 130 MPa and brittle fracture in the as-processed condition. It can be speculated that the brittle fracture may either be due to the strong bonding of the oxides on the fiber or the fiber embrittlement during the sol-gel processing of the oxides. Based on the AES analysis, the C and Al_2O_3-TiO_2 layer thicknesses were estimated to be ~30 nm and ~150 nm, respectively, while the mullite coating thickness could not be ascertained since the Nextel 440 fibers were aluminosilicate fibers. The interface debonding seems to occur at the oxide/C interfaces. After oxidation for 24 h at 1000°C in air, they continued to exhibit flexural strengths comparable to the as-processed condition along with brittle fracture.

In contrast, composites with C/oxide/C interfaces (CVI 999 and CVI 1000) exhibited flexural strengths > 200 MPa and non-catastrophic failure in the as-processed condition. These strengths are comparable to the flexural strength values exhibited by a composite with a C interface (0.22 μm thick) in the work of Weaver et al. [191]. Further, the increase in the strength of composites with C/oxide/C interfaces compared to those with oxide/C interfaces may be attributed to the ability of the C interface to protect the fibers during the sol-gel processing of oxides. AES analysis indicated that the debonding

occurred at the C/mullite boundary in the composite with a C/mullite/C interface. In contrast, the debonding occurred at the Al_2O_3-TiO_2/C interface in the composite with a C/Al_2O_3-TiO_2/C interface. The inner and outer C thicknesses were each ~50 nm. The mullite coating as well as the Al_2O_3-TiO_2 coating was each 50 nm in thickness. After oxidation for 24 h at 1000°C in air, a composite with a C/mullite/C interface exhibited a ~53% strength reduction and displayed brittle fracture. The composite with a C/Al_2O_3-TiO_2/C interface after comparable oxidation underwent a 49% strength reduction, but exhibited non-catastrophic failure. However, oxidation for 200 h at 1000°C in air resulted in a catastrophic failure of this composite.

CHAPTER 8

SUMMARY, CONCLUSIONS AND FUTURE WORK

8.1. Summary

Polymeric mullite and aluminum titanate precursor sols were developed for coating applications. A high temperature XRD study identified that for powders derived from the mullite gels dried at 60°C in air, the mullite crystallization occurred at 1050°C in air. In contrast, the mullite precursor powders obtained from the mullite gels dried at 110°C in air, the mullite crystallization takes place at 950°C in air. This mullite crystallization temperature of 950°C is 100°C lower than that reported by Yoldas [195]. The author believes that the drying temperature may have an effect on the mullite crystallization temperature, however a detailed study is required to substantiate this belief. The mullite crystallization temperature is delayed till 1000°C in argon. A high temperature XRD study indicated that aluminum titanate forms at 1300°C and 1200°C in air, and argon, respectively, from the powder derived from the aluminum titanate gel dried at 110°C in air. For gels dried at 60°C in air, aluminum titanate formed at 1400°C in air. Since aluminum titanate forms at temperatures higher than 1200°C, it would damage Nicalon and Nextel fibers.

During the process of the mullite deposition at 1000°C for 1 h in air by a sol-gel method on Nicalon fiber tows, the fibers were embrittled. On the other hand, Nicalon tows dipcoated in an aluminum titanate precursor sol and heat-treated at 1000°C for up to 10 h in air were not embrittled. Only an alumina-titania mixture is formed on Nicalon

fibers at this temperature, and since the fibers had good handleability, it was decided to pursue the alumina-titania coating as an interface coating alternative to aluminum titanate.

Thermomechanical compatibility studies indicated that an interface material with a low or moderate Young's modulus would be effective in reducing the residual compressive radial stresses in Nicalon/SiC and Nextel/SiC composites. Since the oxide coatings obtained in this study were too thin (< 150 nm), the effect of modulus of the interface materials on the composite behavior could not be studied. Based on the thermochemical analysis study, the need for the protection of the oxide coatings from the HCl attack (a by-product of the SiC matrix deposition process) was recognized. For this purpose, an outer C layer was deposited on the oxide coating prior to the SiC matrix deposition. In order to study the effect of protecting the fibers by an inert material during the sol-gel oxide processing, oxide/C and C/oxide/C interfaces were considered for Nicalon/SiC and Nextel/SiC composites.

Nicalon/SiC composites with C, and C/oxide/C interfaces exhibited higher flexural strengths than Nicalon/SiC composites with oxide/C interfaces in both the as-processed condition and after oxidation at 1000°C for 24 h in air. With the exception of the composite with a mullite/C interface, all other composites displayed non-catastrophic failure in the as-processed condition. Among the composites fabricated, the composite with a C/mullite/C interface (CVI 1080) had the highest flexural strength (320±24 MPa) in the as-processed condition. In the case of composites with oxide/C and C/oxide/C interfaces, the AES analysis indicated that the interface debonding occurred preferentially at the oxide/C boundary. While in the composite with a C interface, debonding occurred within the C layer, and the C layer is < 90 nm based on AES results. A TEM study

conducted on a composite with a C/Al_2O_3-TiO_2/C interface (CVI 1002) indicated that the inner and outer C thicknesses were each ~30 nm, while the Al_2O_3-TiO_2 interface was 30-50 nm thick. The TEM study indicated that the interface coatings were uniform. However, a TEM study identified that the mullite coatings were non-uniform in the composite with a C/mullite/C interface (CVI 986).

Flexural strengths of Nicalon/SiC composites with C and C/oxide/C interfaces decreased with increasing exposure time at 1000°C in air and retained a graceful or non-catastrophic failure even after 500 h oxidation. The composite with a C interface displayed a graceful failure and exhibited a 31% flexural strength reduction to 214±68 MPa after 500 h oxidation at 1000°C in air, while composites with C/oxide/C interfaces underwent a 21-39% strength reduction under comparable oxidation conditions. Among the composites fabricated, the composite with a C/Al_2O_3-TiO_2/C interface (CVI 1066) had the highest flexural strength (234±52 MPa) after 500 h oxidation at 1000°C. A TEM study conducted on a composite with a C/Al_2O_3-TiO_2/C interface (CVI 1002) after 500 h oxidation indicated that the C layers were replaced by SiO_2 layers, while the Al_2O_3-TiO_2 layer remained unaffected. Further, there was a surface degradation of the Nicalon fibers and resulted in an additional 50 nm of SiO_2 formation on the fiber. Hence, the reduction in strength of C/oxide/C interfaces could be attributed to the degradation of the fiber as well as the interface to SiO_2/Al_2O_3-TiO_2/SiO_2. An AES analysis of the oxidized composites with C/mullite/C and C/Al_2O_3-TiO_2/C interfaces indicated that C as well as SiO_2 was observed in the troughs, thus, there is uncertainty involved in the extent of the SiO_2 replacement of the C layers in the oxidized samples.

The Nicalon/SiC composite with a C interface retained a graceful failure, but was susceptible to oxidation at 500°C in air, and underwent a 35% strength reduction to 200±45 MPa after 200 h exposure from the as-processed condition. In contrast, flexural strengths of composites with C/oxide/C interfaces were not significantly affected by a 200 h exposure at 500°C in air and retained a graceful failure. For example, flexural strengths of composites with C/mullite/C (CVI 1033) and C/Al_2O_3-TiO_2/C (CVI 1036) interfaces were reduced only by 5% and 11%, respectively, from the as-processed condition.

Nicalon/SiC composites with C and C/oxide/C interfaces underwent catastrophic failure as well as a drastic reduction in flexural strengths (> 73%) after 200 h oxidation at 750°C in air. As shown in a composite with a C/Al_2O_3-TiO_2/C interface (CVI 1066), the extent of damage at 750°C for 200 h in air could be limited by first exposing the composite at 1000°C for 200 h in air followed by 750°C oxidation. In one sample, the flexural strength was reduced only by 15% to 252 MPa after the above exposure.

Nicalon/SiC composites with BN, BN/mullite/BN and BN/Al_2O_3-TiO_2/BN interfaces had similar flexural strengths (244-274 MPa) in the as-processed condition. Composites with BN and BN/Al_2O_3-TiO_2/BN interfaces exhibited a graceful failure even after oxidation at 500°C, 750°C, and 1000°C, while the composite with a BN/mullite/BN interface displayed a predominantly catastrophic failure after exposure at 750°C and 1000°C. The composite with a BN/Al_2O_3-TiO_2/BN interface as well as the composite with a BN/mullite/BN interface showed a significant decrease (> 43%) in strength after an initial exposure at 1000°C for 24 h in air. However, they recovered their strength values with further exposure time at 1000°C. For example, the composite with a BN/Al_2O_3-TiO_2/BN interface had a flexural strength of 253±88 MPa after 500 h oxidation at 1000°C

in air. The composite with a BN/Al_2O_3-TiO_2/BN interface was also sensitive to oxidation at 500°C in air, and underwent a 43% decrease in strength.

Nextel/SiC composites with C/oxide/C interfaces displayed a non-catastrophic failure and exhibited higher flexural strengths than Nextel/SiC composites with oxide/C interfaces in the as-processed condition. In the as-processed condition, the interface debonding in composites, with the exception of a composite with a C/mullite/C interface, occurred at the oxide/C boundary. While in the composite with a C/mullite/C interface, it occurred at the C/mullite boundary. Among the fabricated Nextel/SiC composites, composite with a C/Al_2O_3-TiO_2/C interface had the highest flexural strength (234 MPa) in the as-processed condition. After 24 h oxidation at 1000°C in air, only the composite with a C/Al_2O_3-TiO_2/C interface retained graceful failure but with reduced strength (119±27 MPa). Longer exposure at 1000°C to 200 h in air resulted in a catastrophic failure of this composite.

8.2 Conclusions

The effect of modulus on composite properties could not be investigated, since the obtained oxide coatings were thin. Thin C and C/oxide/C interfaces were effective in promoting damage-tolerant behavior of Nicalon/SiC composites at room temperature and at 1000°C. Nicalon/SiC composites with thin C and C/oxide/C interfaces may not be suitable for long-term application at 750°C in air, since they undergo drastic reduction in strengths and fail in a catastrophic manner. Efforts to replace thin C and C/oxide/C interfaces with BN and BN/oxide/BN interfaces have met some initial success. Nicalon/SiC composites with BN and BN/Al_2O_3-TiO_2/BN interfaces retain damage-

tolerant behavior even after oxidation up to 1000°C in air, and hence, BN and BN/Al_2O_3-TiO_2/BN may have potential as interface materials. Oxide/C and C/oxide/C interfaces did not work for Nextel/SiC composites at 1000°C, since composites with these interfaces exhibit catastrophic failure.

8.3. Future Work

The crystallization temperature of mullite was lowered by 100°C in the present study from that reported in the literature. The author believes that the initial drying temperature may affect the crystallization temperature. Hence, a study involving the synthesis of the mullite precursor sol and gel, and drying at different initial temperatures (for example, 25°C, 60°C, and 110°C) followed by a high temperature XRD study of the derived mullite precursor powders would be worthwhile. Such a study could aid in understanding the effect of drying conditions on the mullite crystallization temperature.

Composites with thin C and C/oxide/C interfaces fabricated in the present study retained damage-tolerant behavior even after 500 h static oxidation at 1000°C in air, but with reduced flexural strengths. However, the performance of these composites may be different in stressed oxidation at 950°C or 1000°C in air. Initial testing of four bars each of composites with C/Al_2O_3-TiO_2/C and C/mullite/C interfaces in stressed oxidation (100 MPa) at 950°C in air was conducted by Lin [214]. Based on the limited testing, it was found that the composite with a C/Al_2O_3-TiO_2/C interface survived for 20 h, while the composite with a C/mullite/C interface as well as the composite with a 0.3 μm thick C interface failed within 10 min. However, the composite with a thin C interface was not

included in the above testing. Hence, composites with thin C and C/Al_2O_3-TiO_2/C interfaces may be fabricated and tested in stressed oxidation at 950°C.

In the present study, composites with BN and BN/Al_2O_3-TiO_2/BN interfaces have exhibited damage-tolerant behavior even after static oxidation up to 1000°C. A follow up study of composites with BN and BN/Al_2O_3-TiO_2/BN interfaces in stressed oxidation between 500°C and 1200°C would be worthwhile.

The present study as well as others reported in the literature have recognized the intermediate temperature effect (600-900°C) on composite mechanical properties. There are two issues at this intermediate temperature. First is the issue of the degradation of Nicalon fibers. This issue could at least be overcome by utilizing Hi-Nicalon fibers, which have very low oxygen contents. Second is the issue of finding an alternate material for the C interface. Although BN may perform well at this intermediate temperature range, it is not a solution for the interface since it is plagued by problems, such as sensitivity to moisture or water vapor attack. Therefore, a material which is phase stable with both the fiber and the matrix along with the ability to retain its structural and chemical integrity at all temperatures is required. Although mullite is phase stable with SiC, and Nicalon fiber, the difficulty of processing it on the fiber without embrittling it is a major challenge. Hence, mullite deposition by a process, such as CVD or combustion CVD, may be utilized and should be tried on Nicalon fibers, and the effect of such deposition on fiber properties should be studied. TiN, suggested by Stinton [215], may also be tried as an alternative to the existing C interface.

TEM analyses was not conducted on Nicalon/SiC composites oxidized at 500°C and 750°C in air. Carrying out of such a study would be beneficial to understanding the effect of such oxidation on the interface modification.

REFERENCES

REFERENCES

1. R. Warren, "Overview," pp. 1-11, and "Fundamental aspects of the Properties of Ceramic-Matrix Composites, " pp.65-113 in Ceramic Matrix Composites, Edited by R. Warren, Chapman and Hall, 1990.

2. K. K. Chawla, Ceramic Matrix Composites, Chapman and Hall, London, 1993.

3. I. W. Donald and P. W. McMillan, "Review-Ceramic Matrix Composites," J. Mater. Sci.,11, 949-72 (1976).

4. M. Karnitz, D. F. Craig, and S. L. Richlen, "Continuous Fiber Ceramic Composite Program," Am. Ceram. Soc. Bull., 70 [3], 430-35 (1991).

5. D. B. Marshall and J. E. Ritter, "Reliability of Advanced Structural Ceramics and Ceramic Matrix Composites," Am. Ceram. Soc. Bull., 66 [2], 309-17 (1987).

6. C. H. McMurtry, W. D. G. Boecker, S. G. Seshadri, and J. S. Fanghi, "Microstructure and Material Properties of SiC-TiB_2 Particulate Composites," Am. Ceram. Soc. Bull., 66 [2], 325-29 (1987).

7. P. F. Becher and G. C. Wei, "Toughening Behavior in SiC-Whisker-Reinforced Alumina," Mater. Sci. Eng., A107, 257-61 (1989).

8. R. Ruh, K. S. Mazdiyasni, and M. G. Mendiratta, "Mechanical and Microstructural Characterization of Mullite and Mullite-SiC-Whisker and ZrO_2-Toughened-Mullite-SiC-Whisker Composites," J. Am. Ceram. Soc., 71 [6], 503-12 (1988).

9. N. Claussen and G. Petzow, "Whisker -Reinforced Zirconia-Toughened Ceramics," pp 649-62 in Tailoring Multiphase and Composite Ceramics, Vol. 20, Edited by R. E. Tressler, G. L. Messing, C. G. Pantano, and R. E. Newnham, Plenum Press, New York, 1986.

10. H. Kodama, T. Suzuki, H. Sakamoto, and T. Miyoshi, "Toughening of Silicon Nitride Matrix Composites by the Addition of Both Silicon Carbide Whiskers and Silicon Carbide Particles," J. Am. Ceram. Soc., 73 [3], 678-83 (1990).

11. D. B. Marshall and A. G. Evans, "Failure Mechanisms in Ceramic-Fiber/Ceramic Matrix Composites," J. Am. Ceram. Soc., 68 [5], 225-31 (1985).

12. T. Mah, M. G. Mendiratta, A. P. Katz, and K. S. Mazdiyasni, "Recent Developments in Fiber-Reinforced High Temperature Ceramic Composites," Am. Ceram. Soc. Bull., 66 [2], 304-8 (1987).

13. A. J. Caputo, D. P. Stinton, R. A. Lowden, and T. M. Besmann, "Fiber-Reinforced SiC Composites with Improved Mechanical Properties," Am. Ceram. Soc. Bull., 66 [2], 368-72 (1987).

14. K. M. Prewo and J. J. Brennan, "Silicon Carbide Fiber Reinforced Glass Ceramic Matrix Composites Exhibiting High Strength and Toughness," J. Mat. Sci., 17, 2371-83 (1982).

15. R. Naslain, O. Dugne, A. Guette, J. Sevely, C. Robin-Brosse, J. P. Rocher, and J. Cotteret, "Boron Nitride Interphase in Ceramic Matrix Composites," J. Am. Ceram. Soc., 74 [10], 2482-88 (1991).

16. J. J. Brennan, "Interfacial Characteristics of Glass-Ceramic Matrix/SiC Fiber Composites," J. de Physique, Colloque C5 Suppl., 10 [49], 791-809 (1988).

17. M. K. Brun and R. N. Singh, "Effect of Thermal Expansion Mismatch and Fiber Coating on the Fiber/Matrix Interfacial Shear Stress in Ceramic Matrix Composites," Adv. Ceram. Mat., 3 [5], 506-9 (1988).

18. R. A. Lowden, "Fiber Coatings and the Mechanical Properties of Fiber-Reinforced Ceramic Composites," pp 619-30 in Ceramic Transactions, Vol. 19, Advanced Composite Materials, Edited by M. D. Sacks, The American Ceramic Society Inc., Westerville, Ohio, 1991.

19. S. Shanmugham, D. P. Stinton, F. Rebillat, A. Bleier, T. M. Besmann, E. Lara-Curzio, and P. K. Liaw, "Oxidation-Resistant Interfacial Coatings for Continuous Fiber Ceramic Composites," Ceram. Eng. Sci. Proc., 16 [4], 389-99 (1995).

20. R. J. Kerans, "The Role of Coating Compliance and Fiber/Matrix Interfacial Topography on Debonding in Ceramic Composites," Scripta Metall. et Mater., 32 [4], 505-9 (1995).

21. C. H. Hsueh, P. F. Becher, and P. Angelini, "Effects of Interfacial Films on Thermal Stresses in Whisker-Reinforced Ceramics," J. Am. Ceram. Soc., 71 [11], 929-33 (1988).

22. W. C. Miller, Encyclopedia of Textiles, Fibers, and Nonwoven Fabrics; pp. 438-50. Edited by M. Grayson, Wiley, New York, 1984.

23. S. Yajima, J. Hayashi, and M. Omori, "Continuous Silicon Carbide Fiber of High Tensile Strength," Chem. Lett., 7, 69 (1975).

24. S. Yajima, K. Okamura, J. Hayashi, and M. Omori, "Synthesis of Continuous SiC Fibers with High Tensile Strength," J. Am. Ceram. Soc., 59 [7-8], 324-27 (1976).

25. S. Yajima, Y. Hasegawa, J. Hayashi, and M. Iimura, "Synthesis of Continuous Silicon carbide Fiber with High Tensile Strength and High Young's Modulus," J. Mat. Sci., 13, 2569-76 (1978).

26. S. Yajima, "Silicon Carbide Fibers," pp. 201-37 in Handbook of Composites, Edited by W. Watt and B. V. Perov, North-Holland, Amsterdam, Netherlands, 1985.

27. J. K. Weddell, "Continuous Ceramic Fibers," J. Text. Inst., 81 [4], 333-59 (1990).

28. Information from fiber data sheet and personal communication from Technical Personnel of: 3M, Textron, BP, Nippon Carbon, Ube Industries, ICI, Tonen, Dow Corning, MER, Saphikon, Mitsui Mining, and Sumitomo Chemical.

29. T. L. Tompkins, "Ceramic Oxide Fibers: Building Blocks for New Applications," Ceramic Industry, April, 1995.

30. H. G. Sowman and D. D. Johnson, "Oxide Fibers from Chemical Ceramic Process," pp. 122-140 in Fiber Reinforced Ceramic Composites: Materials, Processing and Technology, Edited by K. S. Mazdiyasni, Noyes Publications, New Jersey, 1990.

31. J. Persh, "New Department of Defense Initiatives in Composite Materials and Structures," Ceram. Eng. Sci. Proc., 9 [7-8], 529-40 (1988).

32. P. Bracke, H. Schurmans and J. Verhoest, Inorganic Fibers and Composite Materials, Pergamon Press, New York, 1984.

33. T. F. Cooke, "Inorganic Fibers - A Literature Review," J. Am. Ceram. Soc., 74 [12], 2959-78 (1991).

34. F. Galasso, M. Basche, and D. Kuehl, "Preparation, Structure and Properties of Continuous Silicon Carbide Filaments," J. Appl. Phys. Lett., 9 [1], 37-39 (1966).

35 K. Okamura, "Ceramic Fibers from Polymer Precursors," Composites, 18 [2], 107-20 (1987).

36. M. Takeda, J. Sakamoto, A. Saeki, Y. Imai, and H. Ichikawa, "High Performance Silicon Carbide Fiber Hi-Nicalon for Ceramic Matrix Composites," Ceram. Eng. Sci. Proc., 16 [4], 37-44 (1995).

37. Y. Hasegawa, M. Iimura, and S. Yajima, "Synthesis of Continuous Silicon Carbide Fiber, Part 2, Conversion of Polycarbosilane Fibers into Silicon Carbide Fibers," J. Mater. Sci., 15, 720-28 (1980).

38. Y. Hasegawa and K. Okamura, "Synthesis of Continuous Silicon Carbide Fiber, Part 3, Pyrolysis of Polycarbosilane and Structure of the Products," J. Mater. Sci., 18, 3633-48 (1983).

39. Y. Hasegawa and K. Okamura, "Synthesis of Continuous Silicon Carbide Fiber, Part 4, The Structure of Polycarbosilane as the Precursor," J. Mater. Sci., 21, 321-28 (1986).

40. Y. Hasegawa, "Synthesis of Continuous Silicon Carbide Fiber, Part 6, Pyrolysis of Polycarbosilane and Structure of SiC Fibre," J. Mater. Sci., 24, 1177-90 (1989).

41. R. Warren and C. H. Andersson, "Silicon Carbide Fibers and their Potential for Use in Composite Materials, Part 1," Composites, 15 [1], 16-24 (1984).

42. T. Mah, N. L. Hecht, D. E. McCullum, R. Hoenigman, H. M. Kim, A. P. Katz, and H. A. Lipsitt, "Thermal Stability of SiC Fibres (Nicalon)," J. Mater. Sci., 19, 1191-201 (1984).

43. G. Simon and A. R. Bunsell, "Mechanical and Structural Characterization of the Nicalon Silicon Carbide Fiber," J. Mater. Sci., 19, 3649-57 (1984).

44. G. Simon and A. R. Bunsell, "Creep Behavior and Structural Characterization at high Temperatures of Nicalon Silicon Carbide Fibers," J. Mater. Sci., 19, 3658-70 (1984).

45. T. J. Clark, M. Jaffe, J. Rabe, and N. R. Langley, "Thermal Stability Characterization of SiC Ceramic Fibers: I, Mechanical Property and Chemical Structure Effects," Ceram. Eng. Sci. Proc., 6 [7-8], 901-13 (1985).

46. L. C. Sawyer, R. T. Chen, F. Haimbach IV, P. J. Harget, E. R. Prack and M. Jaffe, "Thermal Stability Characterization of SiC Ceramic Fibers: II, Fractography and Structure," Ceram. Eng. Sci. Proc., 6 [7-8], 914-30 (1985).

47. T. J. Clark, R. M. Arons, J. B. Stamatoff and J. Rabe, "Thermal Degradation of Nicalon SiC Fibers," Ceram. Eng. Sci. Proc., 6 [7-8], 576-87 (1985).

48. A. S. Fareed, P. Fang, M. J. Koczak, and F. M. Ko, "Thermomechanical Properties of SiC Yarn," Am. Ceram. Soc. Bull., 66 [2], 353-58 (1987).

49. S. M. Johnson, R. D. Brittain, R. H. Lamoreaux, and D. J. Rowcliffe, "Degradation Mechanisms of Silicon Carbide Fibers," J. Am. Ceram. Soc., 71 [3], C132-C35 (1988).

50. Y. Maniette and A. Oberlin, "TEM Characterization of some crude or air heat-treated SiC Nicalon Fibres," J. Mater. Sci., 24, 3361-70 (1989).

51. C. Laffon, A. M. Flank, P. Lagarde, M. Laridjani, R. Hagege, P. Olry, J. Cotteret, J. Dixmier, J. L. Miquel, H. Hommel, and A. P. Legrand, "Study of Nicalon-based Ceramic Fibres and Powders by EXAFS spectrometry, X-ray Diffractometry and some additional methods," J. Mater. Sci., 24, 1503-12 (1989).

52. L. Porte and A. Sartre, "Evidence for a Silcon Oxycarbide Phase in the Nicalon Silicon Carbide Fibre, J. Mater. Sci., 24, 271-75 (1989).

53. D. J. Pysher, K. C. Goretta, R. S. Hodder, and R. E. Tressler, "Strength of Ceramic Fibers at Elevated Temperatures," J. Am. Ceram. Soc., 72 [2], 284-88 (1989).

54. H. E. Kim and A. J. Moorhead, "Strength of Nicalon Silicon Carbide Fibers Exposed to High-Temperature Gaseous Environments," J. Am. Ceram. Soc., 74 [3], 666-69 (1991).

55. B. J. Tan, Y. Xiao, S. L. Suib, and F. S. Galasso, "Effect of Microwave Nitrogen Plasma Treatment on Nicalon Fibers," Chem. Mater., 3, 652-60 (1991).

56. S. M. Bleay, A. R. Chapman, G. Love, and V. D. Scott, "Electron Microprobe Analysis of Nicalon Fibers," J. Mater. Sci., 27, 5389-96 (1992).

57. N. Jia, R. Bodet and R. E. Tressler, "Effects of Microstructural Instability on the Creep Behavior of Si-C-O (Nicalon) Fibers in Argon," J. Am. Ceram. Soc., 76 [12], 3051-60 (1993).

58. T. Shimoo, H. Chen, and K. Okamura, "High-Temperature Stability of Nicalon under Ar or O_2 atmosphere," J. Mater. Sci., 29, 456-63 (1994).

59. C. Vahlas, P. Rocabois, and C. Bernard, "Thermal Degradation Mechanisms of Nicalon Fibre: A Thermodynamic Simulation," J. Mater. Sci., 29, 5839-46 (1994).

60. P. L. Coustumer, M. Monthioux, and J. -F. Despres, "Surface Roughness of Nicalon Fibre," J. Mater. Sci., 13, 1645-46 (1994).

61. D. Belitskus, Fiber and Whisker Reinforced Ceramics for Structural Applications, Marcel Dekker, New York, 1993.

62. M. Takeda, Y. Imai, H. Ichikawa, T. Ishikawa, T. Seguchi, and K. Okamura, "Properties of the Low Oxygen Content SiC Fiber on High Temperature Heat Treatment," Ceram. Eng. Sci. Proc., 12 [7-8], 1007-18 (1991).

63. M. Takeda, Y. Imai, H. Ichikawa, T. Ishikawa, N. Kasai, T. Seguchi, and K. Okamura, "Thermal Stability of the Low Oxygen Silicon Carbide Fibers Derived from Polycarbosilane," Ceram. Eng. Sci. Proc., 13 [7-8], 209-17 (1992).

64. M. Takeda, J. Sakamoto, Y. Imai, H. Ichikawa, and T. Ishikawa, "Properties of Stoichiometric SiC Fiber Derived from Polycarbosilane," Ceram. Eng. Sci. Proc., 15 [4], 133-41 (1994).

65. M. H. Berger, N. Hocet, and A. R. Bunsell, "Microstructure and Thermo-Mechanical Stability of a Low-Oxygen Nicalon Fibres," J. Microscopy, 177 [3], 230-41 (1995).

66. A. R. Holtz and M. F. Grether, "High Temperature Properties of three Nextel Ceramic Fibers" Presented at the 32nd International SAMPE Symposium and Exhibition, Anaheim, California, April 6-9, 1987.

67. D. D. Johnson, A. R. Holtz, and M. F. Grether, "Properties of Nextel 480 Ceramic Fibers," Ceram. Eng. Sci. Proc., 8 [7-8], 744-54 (1987).

68. A. M. Tiefenthaler and M. W. Urban, "Stability of Nextel Fibers in Aqueous Environments Detected by Photoacoustic Fourier Transform Infrared Spectroscopy," Composites, 20, 585-88 (1989).

69. Z. R. Xu, K. K. Chawla, and X. Li, "Effect of High Temperature Exposure on the Tensile Strength of Alumina Fiber Nextel 610," Mater. Sci. Eng., A171, 249-56 (1993).

70. D. M. Wilson, S. L. Lieder and D. C. Lueneburg, "Microstructure and High Temperature Properties of Nextel 720 Fibers," Ceram. Eng. Sci. Proc., 16 [5], 1005-14 (1995).

71. D. M. Wilson, S. L. Lieder and D. C. Lueneburg, "High Temperature Properties of Nextel 610 and Alumina-Based Nanocomposite Fibers," Ceram. Eng. Sci. Proc., 14 [7-8], 609-21 (1993).

72. R. E. Tressler and J. A. Di Carlo, "High Temperature Mechanical Properties of Advanced Ceramic Fibers," pp. 33-49 in High Temperature Ceramic Matrix Composites, Edited by R. Naslain, J. Lamon, and D. Doumeingts, Woodhead Publishing Limited, September 1993.

73. K. M. Prewo, J. J. Brennan, and G. K. Layden, "Fiber Reinforced Glasses and Glass Ceramics for High Performance Applications," Am. Ceram. Soc. Bull., 65 [2], 305-13 (1986).

74. J. A. Cornie, Y-M. Chiang, D. R. Uhlmann, A. Mortensen, and J. M. Collins, "Processing of Metal and Ceramic Matrix Composites," Am. Ceram. Soc. Bull., 65 [2], 293-304 (1986).

75. L. J. Schioler and J. J. Stiglich, "Ceramic Matrix Composites: A Literature Review," Am. Ceram. Soc. Bull., 65 [2], 289-92 (1986).

76. R. Naslain, "CVI Composites," pp. 199-244 in Ceramic Matrix Composites, Edited by R. Warren, Chapman and Hall, 1990.

77. R. Warren and R. Lundberg, "Principles of Preparation of Ceramic Composites," pp. 35-63 in Ceramic Matrix Composites, Edited by R. Warren, Chapman and Hall, 1990.

78. Engineered Materials Handbook, Vol. 4, Ceramics and Glasses, Samuel J. Schneider, Technical Chairman, ASM International, 1987.

79. T. Mah, Y. F. Yu, E. E. Hermes, and K. S. Mazdiyasni, "Ceramic Fiber Reinforced Metal-organic Precursor Matrix Composites," pp. 278-310 in Fiber Reinforced Ceramic Composites: Materials, Processing and Technology, Edited by K. S. Mazdiyasni, Noyes Publications, New Jersey, 1990.

80. E. Fitzer and R. Gadow, "Fiber Reinforced Ceramics via the Sol/Gel Process" pp. 589-601 in Tailoring Multiphase and Composite Ceramics, Vol. 20, Edited by R. E. Tressler, G. L. Messing, C. G. Pantano, and R. E. Newnham, Plenum Press, New York, 1986.

81. Gateway Materials Technology, Inc., Illinois, USA, Technical Brochure, 1995.

82. K. S. Mazdiyasni, "Ceramic Composite Matrices from Metal-organic Precursors," Mater. Sci. Eng., A144, 83-90 (1991).

83. W. B. Hillig, "Melt Infiltration Approach to Ceramic Matrix Composites," J. Am. Ceram. Soc., 71 [2], C96-9 (1988).

84. M. K. Brun, W. B. Hillig, and H. C. McGuigan, "High Temperature Mechanical Properties of a Continuous Fiber-Reinforced Composite made by Melt Infiltration," Ceram. Eng. Sci. Proc., 10 [7-8], 611-21 (1989).

85. L. D. Maloney, "Makeway for 'Engineered Ceramics'," Design New, 45 [5], 64-71 (1989).

86. A. S. Fareed, D. J. Landini, T. A. Johnson, A. N. Patel, and P. A. Craig, "High Temperature Ceramic Matrix Composites by the Directed Metal Oxidation Process," SME Paper EM92-216, 1-21 (1992).

87. A. S. Fareed, G. H. Schiroky, and C. R. Kennedy, "Development of BN/SiC Duplex Fiber Coatings for Fiber-Reinforced Alumina Matrix Composites Fabricated by Directed Metal Oxidation," Ceram. Eng. Sci. Proc., 14 [9-10], 794-801 (1993).

88. M. S. Newkirk, H. D. Lesher, D. R. White, C. R. Kennedy, A. W. Urquhart, and T. D. Claar, "Preparation of Lanxide Ceramic Matrix Composites: Matrix Formation by the Direct Oxidation of Molten Metals," Ceram. Eng. Sci. Proc., 8 [7-8], 879-885 (1987).

89. R. T. Bhatt, "Properties of Silicon Carbide Fiber-Reinforced Silicon Nitride Matrix Composites," NASA Technical Memorandum 101356, NASA-Lewis Research Center, Cleveland, Ohio (1988).

90. R. T. Bhatt and J. D. Kiser, "Matrix Density Effects on the Mechanical Properties of SiC/RBSN Composites," NASA Technical Memorandum 103098, NASA-Lewis Research Center, Cleveland, Ohio (1990).

91. D. P. Stinton, T. M. Besmann, R. A. Lowden, and B. W. Sheldon, "Vapor Deposition," pp. 215-223 in Engineered Materials Handbook, Vol. 4, Ceramics and Glasses, Samuel J. Schneider, Technical Chairman, ASM International, 1987.

92. W. J. Lackey and T. L. Starr, "Fabrication of Fiber-Reinforced Ceramic Composites by Chemical Vapor Infiltration: Processing, Structure and Properties," pp. 397-450 in Fiber Reinforced Ceramic Composites: Materials, Processing and Technology, Edited by K. S. Mazdiyasni, Noyes Publications, New Jersey, 1990.

93. T. M. Besmann, B. W. Sheldon, R. A. Lowden and D. P. Stinton, "Vapor-Phase Fabrication and Properties of Continuous-Filament Ceramic Composites," Science, 253, 1104-9 (1991).

94. D. P. Stinton, T. M. Besmann, and R. A. Lowden, "Advanced Ceramics by Chemical Vapor Deposition Techniques," Am. Ceram. Bull., 67 [2], 350-5 (1988).

95. R. Naslain, "Ten Years of Research on Fiber-Reinforced Ceramics," Ind. Ceram., 813, 98 (1987).

96. T. M. Besmann, "CVI Processing of Ceramic Matrix Composites," pp. 1-12 in High-Temperature Ceramic Matrix Composites II: Manufacturing and Materials Development, Edited by A. G. Evans and R. Naslain, The American Ceramic Society Inc., Westerville, Ohio, 1995.

97. T. M. Besmann, R. A. Lowden, and D. P. Stinton, pp. 215-29 in High Temperature Ceramic Matrix Composites, Edited by R. Naslain, J. Lamon, and D. Doumeingts, Woodhead Publishing Limited, September 1993.

98. R. L. Bickerdike, A. R. G. Brown, G. Hughes, and H. Ranson, "The Deposition of Pyrolytic Carbon in the Pores of Bonded and Unbonded Carbon Powders," pp. 575-83 in Proc. Fifth Conf. Carbon, Vol. I, Edited by S. Mrosowski, M. C. Studebaker, and P. L. Walker, Pergamon Press, New York,1962.

99. W. C. Jenkin, "Method of Depositing Metals and Metallic Compounds Throughout the Pores of a Porous Body," U.S. Patent 3,160,517, Dec. 8, 1964.

100. A. J. Caputo and W. J. Lackey, "Fabrication of Fiber-Reinforced Ceramic Composites by Chemical Vapor Infiltration," ORNL/TM-9235, Tennessee, October (1984).

101. T. M. Besmann, R. A. Lowden, D. P. Stinton, and T. L. Starr, "A Method for Rapid Chemical Vapor Infiltration of Ceramic Composites," J. de Physique, Colloque C5 Suppl., 5 [50], 229-39 (1989).

102. R. A. Lowden, A. J. Caputo, D. P. Stinton, T. M. Besmann, and M. D. Morris, "Effects of Infiltration Conditions on the Properties of SiC/Nicalon Composites," ORNL/TM-10403, Oak Ridge National Laboratory, Oak Ridge, May (1987).

103. W. M. Matlin, "Development of a Two-Step, Forced Chemical Vapor Infiltration Process," Masters Thesis, The University of Tennessee, Knoxville, Tennessee, August 1995.

104. T. L. Starr, "Modeling of Chemical Vapor Infiltration," ORNL/Sub/856-55901/01, Oak Ridge National Laboratory, Oak Ridge, Tennessee, February (1989).

105. A. G. Evans and D. B. Marshall, "The Mechanical Behavior of Ceramic Matrix Composites," Acta. Metall., 37, 2567-2583 (1989).

106. N. Miriyala, "Fabric Orientation Effects on the Monotonic and Fatigue Behavior of CFCCs," Doctoral Dissertation Proposal, The University of Tennessee, Knoxville, Tennessee, December 1995.

107. P. Karandikar and T-W. Chou, "Structural Properties of Ceramic Matrix Composites," pp. 355-429 in Handbook on Continuous Fiber-Reinfoced Ceramic Matrix Composites, Edited by R. L. Lehman, S. K. El-Rahaiby, and J. B. Wachtman, The American Ceramic Society, Ohio, December 1995.

108. J. Aveston, G. A. Cooper, and A. Kelly, "Single and Multiple Fracture," The Properties of Fiber Composites, National Physics Laboratory Conference Proceedings, IPC Science and Technology Press Ltd., 15-26, November 1971.

109. J. Aveston and A. Kelly, "Theory of Multiple Fracture of Fibrous Composites," J. Mater. Sci., 8 [3], 352-62 (1973).

110. B. Budiansky, J. W. Hutchinson, and A. G. Evans, "Matrix Fracture in Fiber Reinforced Ceramics," J. Mech. Phys. Sol., 34[2], 167-89 (1986).

111. W. S. Kuo and T. W. Chou, "Modeling of the Thermomechanical Behavior of Glass Matrix Composites," pp. 311-18 in Metal and Ceramic Matrix Composites: Processing, Modeling and Characterization, Edited by R. B. Bhagat, P. Kumar, and A. M. Ritter, The Minerals, Metals and Materials Society, Pennsylvania, 1990.

112. C. H. Hsueh, "Matrix Cracking with Frictional Bonding Fibers in Continuous Fibre Ceramic Composites," J. Mater. Sci., 30, 4793-800 (1995).

113. D. Marshall, B. Cox, and A. G. Evans, "The Mechanics of Matrix Cracking in Brittle-Matrix Fiber-Reinforced Composites," Acta Metall., 33 [11], 2013-21 (1985).

114. L. N. McCartney, "Mechanics of Matrix Cracking in Brittle-Matrix Fiber-Reinforced Composites," Proc. R. Soc. Lond., A-409 [1837], 329-50 (1987).

115. Y-C. Chiang, A. S. D. Wang, and T-W. Chou, "On Matrix Cracking in Fiber Reinforced Ceramics," J. Mech. Phy. Solids, 41 [7], 2237-54 (1993).

116. A. S. D. Wang, X. G. Huang, and M. W. Barsoum, "Matrix Crack Initiation in Ceramic Matrix Composites Part II: Models and Simulation Results," Comp. Sci. Tech., 44 [3], 271-82 (1992).

117. H. Osmani, D. Rouby, G. Fantozzi, and J. M. Lequertier, "Toughness, Microstructure and Interface Characteristics for Ceramic Matrix Composites," Comp. Sci. Tech., 37, 191-206 (1990).

118. J. D. Outwater and L. C. Murphy, "On the Fracture Energy of Unidirectional Laminates," pp. 17 in Proceedings of the 24th Annual Technical Conference of Composites, The Society of Plastics Industry, Inc., New York, 1969.

119. J. K. Wells and P. W. R. Beaumont, "Debonding and Pull-Out Processes in Fibrous Composites," J. Mater. Sci., 20, 1275-84 (1985).

120. M. Y. He and J. W. Hutchinson, "Crack Deflection at an Interface Between Dissimilar Elastic Materials," Intl. J. Solids Structures, 25 [9], 1053-67 (1989).

121. D. M. Walukas, "A Study of the Mechanical Properties and Oxidation Resistance of Nicalon/SiC Composites with Sol-Gel Derived Oxide Interfacial Coatings," Masters Thesis, The University of Tennessee, Knoxville, Tennessee, May 1993.

122. J. J. Brennan, "Interfacial Characterization of Glass and Glass-Ceramic Matrix/Nicalon SiC fiber Composites." pp. 549-60 in Tailoring Multiphase and Composite Ceramics, Proceedings of the Twenty-First University Conference on Ceramic Science, University Park, Pennsylvania, Plenum Press, New York, 1986.

123. K. M. Prewo and J. J. Brennan, "High Strength Silicon Carbide Fiber-Reinforced Glass Matrix Composites," J. Mater. Sci., 15, 463-8 (1980).

124. K. M. Prewo and J. J. Brennan, "Silicon Carbide Yarn Reinforced Glass Matrix Composites," J. Mater. Sci., 17, 1201-6 (1982).

125. J. J. Brennan and K. M. Prewo, "Silicon Carbide Fiber-Reinforced Glass-Ceramic Matrix Composites Exhibiting High Strength and Toughness," J. Mater. Sci., 17, 2371-83 (1982).

126. T. D. Gulden, D. A. Hazlebeck, K. P. Norton, and H. H. Streckert, "Ceramic Fiber Coating by Gas-Phase and Liquid-Phase Processes," Ceram. Eng. Sci. Proc., 11 [9-10], 1539-53 (1990).

127. S. Shanmugham, P. K. Liaw, D. P. Stinton, T. M. Besmann, K. L. More, A. Bleier, W. D. Porter, and S. T. Misture, "Development of Sol-Gel Derived Coatings for Nicalon/SiC Composites," To be Published in Ceram. Eng. Sci. Proc. (1996).

128. R. S. Hay and E. E. Hermes, "Sol-Gel Coatings on Continuous Ceramic Fibers," Ceram. Eng. Sci. Proc., 11 [9-10], 1526-38 (1990).

129. R. S. Hay, "Sol-Gel Coating of Fiber Tows," Ceram. Eng. Sci. Proc., 12 [7-8], 064-74 (1991).

130. R. S. Hay, M. D. Petry, K. A. Keller, M. K. Cinibulk, and J. R. Welch, "Carbon and Oxide Coatings on Continuous Ceramic Fibers," pp. 377-82 in Ceramic Matrix Composites-Advanced High-Temperature Structural Materials, Edited by R. A. Lowden, M. K. Ferber, J. R. Hellmann, K. K. Chawla, and S. G. DiPietro, Materials Research Society Symposium Proceedings, Vol. 365, Pennsylvania, 1995.

131. G. R. Villalobos and R. F. Speyer, "Glass-Ceramic Sol-Gel Coating of Ceramic Fibers," Ceram. Eng. Sci. Proc., 15 [5], 731-42 (1994).

132. A. J. Caputo, W. J. Lackey, and D. P. Stinton, "Development of a New, Faster-Process for the Fabrication of Ceramic Fiber-Reinforced Ceramic Composites by Chemical Vapor Infiltration," Ceram. Eng. Sci. Proc., 6 [7-8], 694-706 (1985).

133. R. W. Rice, "BN Coating of Ceramic Fibers for Ceramic Fiber Composites," US Patent 4,642,271, Feb. 10, 1987.

134. J. A. Fernando, K. K. Chawla, M. K. Ferber, and D. Coffey, "Effect of Boron Nitride Coating on the Tensile Strength of Nextel 480 Fiber," Mater. Sci. Eng., A154, 103-8 (1992).

135. N. R. Khasgiwale, E. P. Butler, L. Tsakalakos, D. A. Hensley, W. R. Cannon, S. C. Danforth, and S. T. Gonczy, "Characterization of Pseudo-Porous SiC/C Coatings on Nextel 440 and Nicalon Fibers," pp. 395-400 in Ceramic Matrix Composites-Advanced High-Temperature Structural Materials, Edited by R. A. Lowden, M. K. Ferber, J. R. Hellmann, K. K. Chawla, and S. G. DiPietro, Materials Research Society Symposium Proceedings, Vol. 365, Pennsylvania, 1995.

136. N. R. Khasgiwale, E. P. Butler, L. Tsakalakos, D. A. Hensley, W. R. Cannon, S. C. Danforth, and S. T. Gonczy, "Characterization of BN Rich Layer on Ammonia Treated Nextel 312 Fibers," pp. 389-94 in Ceramic Matrix Composites-Advanced High-Temperature Structural Materials, Edited by R. A. Lowden, M. K. Ferber, J. R. Hellmann, K. K. Chawla, and S. G. DiPietro, Materials Research Society Symposium Proceedings, Vol. 365, Pennsylvania, 1995.

137. N. Chawla, "Effect of Fiber Fabric Orientation on the Mechanical Behavior of Continuous Fiber Ceramic Composites," Masters Thesis, The University of Tennessee, Knoxville, Tennessee, December 1994.

138. W. M. Matlin, D. P. Stinton, and T. M. Besmann, "Development of a Two-Step, Forced Chemical Vapor Infiltration Process," pp. 119-24 in High Temperature Ceramic-Matrix Composites II: Manufacturing and Materials Development, Ceramic Transactions, Vol. 58, The American Ceramic Society, Ohio, 1995.

139. P. K. Liaw, D. K. Hsu, N. Yu, N. Miriyala, V. Saini, and H. Jeong, "Investigation of Metal and Ceramic-Matrix Composites Moduli: Experiment and Theory," Acta. Mater., 44 [5], 2101-13 (1996).

140. P. K. Liaw, "Fiber-Reinforced CMCs: Processing, Mechanical Behavior and Modeling," JOM, 38-44, October 1995.

141. J. H. Miller, R. A. Lowden and P.K. Liaw, "Effects of Fiber Coating Thickness on Fracture Behavior of Continuous Woven Fabric-Reinforced Ceramic Composites," Submitted to J. Am. Ceram. Soc.

142. J. H. Miller, R. A. Lowden and P.K. Liaw, "Fiber Coatings and the Fracture Behavior of Continuous Fiber Ceramic Composite," pp. 403-10 in Ceramic Matrix Composites-Advanced High-Temperature Structural Materials, Materials Research Society Symposium Proceedings, Vol. 365, Edited by R. A. Lowden, M. K. Ferber, J. R. Hellmann, K. K. Chawla, and S. G. DiPietro, Materials Research Society, Pennsylvania, 1995.

143. D. P. Stinton, A. J. Caputo, and R. A. Lowden, "Synthesis of Fiber-Reinforced SiC Composites by Chemical Vapor Infiltration," Am. Ceram. Soc. Bull., 65 [2], 347-50 (1986).

144. P. J. Lamicq, G. A. Bernhart, M. M. Dauchier, and J. G. Mace, "SiC/SiC Composite Ceramics," Am. Ceram. Soc. Bull., 65 [2], 336-38 (1986).

145. R. A. Lowden and D. P. Stinton, "The Influence of the Fiber-Matrix Bond on the Mechanical Behavior of Nicalon/SiC Composites," ORNL/TM-10667, Oak Ridge National Laboratory, Oak Ridge, Tennessee, December 1987.

146. R. A. Lowden and D. P. Stinton, "Interface Modification in Nicalon/SiC Composites," Ceram. Eng. Sci. Proc., 9 [7-8], 705-22 (1988).

147. R. A. Lowden, "Characterization and Control of the Fiber-Matrix Interface in Ceramic Matrix Composites," ORNL/TM-11039, Oak Ridge National Laboratory, Oak Ridge, Tennessee, March 1989.

148. R. A. Lowden and K. L. More, "The Effect of Fiber Coatings on Interfacial Shear Strength and the Mechanical Behavior of Ceramic Composites," pp. 205-14 in Tailored Interfaces in Composite Materials, MRS Symposium Proceedings, Vol. 170, Edited by C. G. Pantano and E. J. H. Chin, Materials Research Society, Pennsylvania, 1990.

149. D. P. Stinton, R. A. Lowden and R. H. Krabill, "Mechanical Property Characterization of Fiber-Reinforced SiC Matrix Composites," ORNL/TM-11524, Oak Ridge National Laboratory, Oak Ridge, Tennessee, April 1990.

150. Y. G. Roman, D. P. Stinton, and T. M. Besmann, "Development of High Density Fiber Reinforced Silicon Carbide FCVI Composites," Journal De Physique IV, Colloque C2, Suppl. au Journal de Physique II, Vol. 1, C2-689-95, September 1991.

151. L. L. Snead, S. J. Zinkle and D. Steiner, "Radiation Induced Microstructure and Mechanical Property Evolution of SiC/C/SiC Composite Materials," J. Nucl. Mater., 191-94, 560-65 (1992).

152. L. L. Snead, M. Osborne, and K. L. More, "Effects of Radiation on SiC-Based Nicalon Fibers," J. Mater. Res., 10 [3], 736-47 (1995).

153. R. A. Lowden, O. J. Schwarz, and K. L. More, "Improved Fiber Coatings for Nicalon/SiC Composites," Ceram. Eng. Sci. Proc., 14 [7-8], 375-84 (1993).

154. P. F. Tortorelli, S. Nijhawan, L. Riester, and R. A. Lowden, "Influence of Fiber Coatings on the Oxidation of Fiber Reinforced SiC Composites," Ceram. Eng. Sci. Proc., 14 [7-8], 358-66 (1993).

155. K. R. Vaidyanathan, J. Sankar, A. D. Kelkar, D. P. Stinton, and M. H. Headinger, "Investigation of Mechanical Properties of Chemically Vapor Infiltrated Ceramic Matrix Composites under Pure Tension," Ceram. Eng. Sci. Proc., 14 [9-10], 1016-27 (1993).

156. R. A. Lowden,"Fiber Coatings and the Mechanical Properties of a Continuous Fiber-Reinforced SiC Matrix Composite," pp. 157-71 in Designing Ceramic Interfaces II Understanding and Tailoring Interfaces for Coating, Composite, and Joining Applications, Proceedings of the Second European Colloquium, Edited by S. D. Peteves, Commision of the European Communities, Netherlands, 1993.

157. E. Lara-Curzio, M. K. Ferber, and R. A. Lowden, "The Effect of Fiber Coating Thickness on the Interfacial Properties of a Continuous Fiber Ceramic Matrix Composite," Ceram. Eng. Sci. Proc., 15 [5], 989-1000 (1995).

158. R. A. Lowden, O. J. Schwarz, and D. P. Stinton, "Development of Oxidation-Resistant Interface Coatings," pp. 105-116 in Proceedings of the Eight Annual Conference on Fossil Energy Materials, Edited by R. R. Judkins, May 1994.

159. S. C. Beecher, R. B. Dinwiddie, and R. A. Lowden, "The Thermal Conductivity of Carbon Coated Silicon Carbide Fibers Embedded in a Silicon Carbide Matrix," pp. 324-34 in Thermal Conductivity, Vol. 22, Edited by T. W. Tong, Technomic Publishing Co., Inc., Pennsylvania, 1994.

160. N. Chawla, P. K. Liaw, E. Lara-Curzio, R. A. Lowden, and M. K. Ferber, "Effect of Fiber Fabric Orientation on the Monotonic and Fatigue Behavior of a Continuous Fiber Ceramic Composite," pp. 291-304 in High Performance Composites: Commonalty of Phenomena, Edited by K. K. Chawla, P. K. Liaw, and S. G. Fishman, The Minerals, Metals and Materials Society, Pennsylvania, 1994.

161. H-T. Lin, P. F. Becher, and P. F. Tortorelli, "Elevated Temperature Static Fatigue of a Nicalon Fiber-Reinforced SiC Composite," pp. 435-40 in Ceramic Matrix Composites-Advanced High-Temperature Structural Materials, Materials Research Society Symposium Proceedings, Vol. 365, Edited by R. A. Lowden, M. K. Ferber, J. R. Hellmann, K. K. Chawla, and S. G. DiPietro, Materials Research Society, Pennsylvania, 1995.

162. P. K. Liaw, N. Yu, D. K. Hsu, N. Miriyala, V. Saini, L. L. Snead, C. J. McHargue, and R. A. Lowden, "Moduli Determination of Continuous Fiber Ceramic Composites," J. Nucl. Mater., 219, 93-100 (1995).

163. D. K. Hsu, P. K. Liaw, N. Yu, V. Saini, N. Miriyala, L. L. Snead, R. A. Lowden, and C. J. McHargue, "Nondestructive Characterization of Woven Fabric Ceramic Composites," pp. 203-8 in Ceramic Matrix Composites-Advanced High-Temperature Structural Materials, Materials Research Society Symposium Proceedings, Vol. 365, Edited by R. A. Lowden, M. K. Ferber, J. R. Hellmann, K. K. Chawla, and S. G. DiPietro, Materials Research Society, Pennsylvania, 1995.

164. P. K. Liaw, N. Miriyala, X. Mao, W. Cao, D. K. Hsu, "Elastic Stiffness Constants of Woven Fabric Reinforced Ceramic Composites: Experiment and Theory," Submitted to J. Comp. Mater.

165. T. M. Besmann, J. C. McLaughlin, and H-T. Lin, "Fabrication of Ceramic Composites: Forced CVI," J. Nucl. Mater., 219, 31-5 (1995).

166. R. Naslain, "Fibrous Ceramic-Ceramic Composite Materials for Transport Applications," pp. 99-115 in Advanced Materials Research and Developments for Transport Composites, MRS-Europe Proceedings, Edited by P. Lamicq, W. J. G. Bunk, and J. G. Wurm, Avenue de Hoggar, France, 1985.

167. J. Lamon, "Influence of Fiber/Matrix Interfacial Properties on the Mechanical Behavior and Reliability of Ceramic Matrix Composites," pp. 63-87 in Designing Ceramic Interfaces II Understanding and Tailoring Interfaces for Coating, Composite, and Joining Applications, Proceedings of the Second European Colloquium, Edited by S. D. Peteves, Commision of the European Communities, 1993.

168. J. Lamon, F. Rebillat, and A. G. Evans, "Microcomposite Test Procedure for Evaluating the Interface Properties of Ceramic Matrix Composites," J. Am. Ceram. Soc., 78 [2], 401-5 (1995).

169. L. Filipuzzi, G. Camus, R. Naslain, and J. Thebault, "Oxidation Mechanisms and Kinetics of 1D-SiC/C/SiC Composite Materials:I, An Experimental Approach," J. Am. Ceram. Soc., 77[2], 459-66 (1994).

170. L. Filipuzzi and R. Naslain, "Oxidation Mechanisms and Kinetics of 1D-SiC/C/SiC Composite Materials:II, Modeling," J. Am. Ceram. Soc., 77[2], 467-80 (1994).

171. S. Prouhet, G. Camus, C. Labrugere, A. Guette, R. Naslain and J. Rey, "Turbostratic Boron Nitride as Interphase Material in SiC/SiC Ceramic Matrix Composites," pp. 557-72 in Designing Ceramic Interfaces II Understanding and Tailoring Interfaces for Coating, Composite, and Joining Applications, Proceedings of the Second European Colloquium, Edited by S. D. Peteves, Commision of the European Communities, 1993.

172. S. Prouhet, G. Camus, C. Labrugere, A. Guette, and E. Martin, "Mechanical Characterization of Si-C(O) Fiber/SiC (CVI) Matrix Composites with a BN-Interphase," J. Am. Ceram. Soc., 77 [3], 649-56 (1994).

173. O. Dugne, S. Prouhet, A. Guette, R. Naslain, R. Fourmeaux, Y. Khin, J. Sevely, J. P. Rocher, and J. Cotteret, "Interface Characterization by TEM, AES, and SIMS in Tough SiC (ex-PCS) Fibre-SiC (CVI) Matrix Composites with a BN Interphase," J. Mater. Sc., 28, 3409-22 (1993).

174. C. Droillard, "Elaboration et caractérisation de composites à interphases séquencées PyC/SiC," Ph. D Thesis, No 913, University of Bordeaux, France, June 1993.

175. F. Rebillat, J. Lamon, R. Naslain, E. Lara-Curzio, M. K. Ferber, and T. M. Besmann, "Damage Modes in Multilayered Interphases in SiC/SiC CVI-Composites," To be published.

176. F. Rebillat, J. Lamon, R. Naslain, E. Lara-Curzio, M. K. Ferber, and T. M. Besmann, "Interfacial Bond Strength in SiC/C/SiC Composite Materials as Studied by Single Fiber Push-Out Tests," To be published.

177. R. Naslain, "The Concept of Layered Interphases in SiC/SiC," pp. 23-40 in High-Temperature Ceramic Matrix Composites II: Manufacturing and Materials Development, Ceramic Transactions, Vol. 58, Edited by A. G. Evans and R. Naslain, The American Ceramic Society, Ohio, 1995.

178. A. J. Eckel and R. C. Bradt, "Strength Distribution of Reinforcing Fibers in a Nicalon Fiber/Chemically Vapor Infiltrated Silicon Carbide Matrix Composite," J. Am. Ceram. Soc., 72 [3], 455-58 (1989).

179. A. J. Eckel and R. C. Bradt, "Thermal Expansion of Laminated, Woven, Continuous Ceramic Fiber/Chemical-Vapor-Infiltrated Silicon Carbide Matrix Composite," J. Am. Ceram. Soc., 73 [5], 1334-38 (1990).

180. G. Navarre, J. C. Rouais, and D. Rouby, "Observation of Crack Path in a SiC-SiC Fibre Composite by X-ray Radiography and SEM," J. Mater. Sci. Let., 9, 636-38 (1990).

181. D. P. Hasselman, A. Venkateswaran, M. Yu, and H. Tawil, "Role of Interfacial Debonding and Matrix Cracking in the Effective Thermal Diffusivity of SiC Fibre-Reinforced Chemical Vapor Deposited SiC Matrix Composites," J. Mater. Sci. Let., 10, 1037-42 (1991).

182. N. Frety, R. Molins, and M. Boussuge, "Oxidizing Ageing Effects on SiC-SiC Composites," J. Mater. Sci., 27, 5084-90 (1992).

183. J. M. Yang, W. Lin, C. J. Shih, W. Kai, S. M. Jeng, and C. V. Burkland, "Mechanical Behavior of Chemical Vapor Infiltration-Processed Two- and Three-Dimensional Nicalon/SiC Composites," J. Mater. Sci., 26, 2954-60 (1991).

184. J. M. Yang, E. Ditmars, W. Lin, and T. Huynh, "Thermomechanical Durability of CVI-Processed Two-Dimensionally Woven and Three-Dimensionally Braided SiC Fibre-Reinforced SiC Composites," J.Mater. Sci., 29, 5491-97 (1994).

185. C. H. Henager, Jr. and R. H. Jones, "Subcritical Crack Growth in CVI Silicon Carbide Reinforced with Nicalon Fibers: Experiment and Model," J. Am. Ceram. Soc., 77 [9], 2381-94 (1994).

186. J. P. Singh, D. Singh, and R. A. Lowden, "Effect of Fiber Coating on Mechanical Properties of Nicalon Fibers and Nicalon-Fiber/SiC Matrix Composites," Ceram. Eng. Sci. Proc., 15 [4], 456-64 (1994).

187. D. Singh, J. P. Singh, and M. J. Wheeler, "Mechanical Behavior of SiC(f)/SiC Composites and Correlation to In Situ Fiber Strength at Room and Elevated Temperatures," J. Am. Ceram. Soc., 79 [3], 591-96 (1996).

188. M. A. Kmetz, J. M. Laliberte, W. S. Willis, S. L. Suib and F. S. Galasso, "Synthesis, Characterization, and Tensile Strength of CVI SiC/BN/SiC Composites," Ceram. Eng. Sci. Proc., 12 [9-10], 2161-74 (1991).

189. R. D. Veltri, D. A. Condit, and F. S. Galasso, "Chemical Vapor Deposited SiC Matrix Composites," J. Am. Ceram. Soc., 72 [3], 478-80 (1989).

190. R. C. Wetherhold and G. J. Popp, "Mechanical Characterization of a Woven Ceramic Fibre/Ceramic Matrix Composite," J. Mater. Sci. Lett., 9, 1187-89 (1990).

191. B. L. Weaver, R. A. Lowden, J. C. McLaughlin, D. P. Stinton, T. M. Besmann, and O. J. Schwarz, "Nextel/SiC Composites Fabricated using Forced Chemical Vapor Infiltration," Ceram. Eng. Sci. Proc., 11 [7-8], 1008-15 (1993).

192. K. R. Vaidyanathan, J. Sankar, A. D. Kelkar, and B. L. Weaver, "Mechanical Properties of Nextel 312 Fiber-Reinforced SiC Matrix Composites in Tension," Ceram. Eng. Sci. Proc., 15 [4], 251-61 (1994).

193. P. F. Tortorelli, C. A. Wijayawardhana, L. Riester, and R. A. Lowden, "Oxidation Effects on Nextel-Reinforced SiC," Ceram. Eng. Sci. Proc., 15 [4], 262-271 (1994).

194. T. M. Besmann, S. Shanmugham, E. R. Kupp, and D. P. Stinton, "Approach to Inherently Stable Interfaces for Ceramic Matrix Composites," pp. 371-80 in Proceedings of the American Society for Composites-Eleventh Technical Conference, Atlanta, GA, Oct. 7-9, 1996.

195. R. J. Kerans, "Issues in the Control of Fiber-Matrix Interface Properties in Ceramic Composites," Scripta Metall. et Mater., 31 [8], 1079-84 (1994).

196. P. D. Jero, R. J. Kerans, and T. A. Parthasarathy, "Effect of Interfacial Roughness on the Frictional Stress Measured Using Pushout Tests," J. Am. Ceram. Soc., 74 [11], 2793-801 (1991).

197. M. D. Sacks, H. W. Lee, and J. A. Pask, pp. 167- in Mullite and Mullite Matrix Composites, Ceramic Transactions, Vol. 6, Edited by S. Somiya, R. F. Davis, and J. A. Pask, The American Ceramic Society, Ohio, 1990.

198. B. E. Yoldas, "Effect of Ultrastructure on Crystallization of Mullite," J. Mater. Sci., 27, 6667-72 (1992).

199. J. C. Huling and G. L. Messing, "Chemistry-Crystallization Relations in Molecular Mullite Gels," J. Non-Crystalline Solids, 147-148, 213-21 (1992).

200. A. K. Chakravorty and D. K. Ghosh, "Synthesis and 980°C Phase Development of Some Mullite Gels," J. Am. Ceram. Soc., 71 [11], 978-87 (1988).

201. D. X. Li and W. J. Thomson, "Kinetic Mechanisms for Mullite Formation from Sol-Gel Precursors," J. Mater. Res., 5 [9], 1963-69 (1990).

202. A. V. Prasadarao, U. Selvaraj, S. Komarneni, A. S. Bhalla, and R. Roy, "Enhanced Densification by Seeding of Sol-Gel-Derived Aluminum Titanate," J. Am. Ceram. Soc., 75 [6], 1529-33 (1992).

203. MIL-STD-1942A, "Flexural Strength of High Performance Ceramics at Ambient Temperature," U.S. Army Materials Technology Laboratory, Watertown, Massachussets, 1990.

204. Besmann, Unpublished work

205. T. M. Besmann, "SOLGASMIX-PV, a Computer Program to Calculate Equilibrium Relationships on Complex Chemical System," ORNL/TM-5775, Oak Ridge National Laboratory, Oak Ridge, TN, April 1977.

206. G. Eriksson and K. Hack, "CHEMSAGE-A Computer Program for the Calculation of Complex Chemical Equilibria," Metall. Trans., 21 B, 1013-23 (1990).

207. B. Jansson, M. Schalin, M. Selleby, and B. Sundman, "The Thermo-Calc Database System Users' Guide," Royal Institute of Technology, November 1993.

208. R. A. Lowden, T. M. Besmann, and D. P. Stinton, "Ceramic Matrix Composites Fabrication and Processing: Chemical Vapor Infiltration," pp. 205-68 in Handbook on Continuous Fiber-Reinfoced Ceramic Matrix Composites, Edited by R. L.Lehman, S. K. El-Rahaiby, and J. B. Wachtman, The American Ceramic Society, Ohio, December 1995.

209. D. N. Braski and K. B. Alexander, "Auger Electron Spectroscopy Analysis of SiC-Whisker Surfaces and SiC-Whisker/Alumina Interfaces," J. Mater. Res., 10 [4], 1016-23 (1995).

210. S. Shanmugham, D. P. Stinton, T. M. Besmann, W. D. Porter, P. K. Liaw, A. Bleier and S. T. Misture, 98th Annual American Ceramics Society Meeting, Indianapolis, April 15, 1996

211. R. S. Hay, D. Petry, and E. Boakye, "Fiber Strength with Coatings from Sols and Solutions, Ceram. Eng. Sci. Proc., 17 [4], 43-52 (1996).

212. P. F. Tortorelli, K. L. More, E. Lara-Curzio, and H. T. Lin, "2.4.2, Environmental Effects," in Continuous Fiber Ceramic Composite Program, Task 2 Supporting Technologies, Bimonthly Progress Report, August-September 1996, M. Rawlins, R. A. Lowden, and M. A. Karnitz, Editors, pp. 59-60.

213. E. Lara-Curzio, P. F. Tortorelli, and K. L. More, "Stress-Rupture of Nicalon/SiC at Intermediate Temperatures," Ceram. Eng. Sci. Proc. (1997, in press).

214. H. T. Lin, Unpublished work.

215. Stinton, Personal communication.

APPENDICES

APPENDIX A

Table 1. Selected properties of commercially available non-oxide continuous ceramic fibers [2, 27-30]

Trade Name	Manufacturer	Composition	Diameter (μm)	Density (g/cm^3)	Tensile Strength (GPa)	Tensile Modulus (GPa)	CTE^ x 10^{-6} (/°C)	ETF^^ (%)	Filaments per yarn or tow	Availability and color	Process Type
SCS-6	Textron	β-SiC on C core	140	3	3.5-7	400	2.3	1	Monofilament	Commercial, Black	CVD
Sigma	BP	β-SiC+α SiC on W core	100	3.4	3.4-4.1	400-410	-	0.8	Monofilament	Commercial	CVD
Nicalon (Ceramic grade)	Nippon Carbon	β-SiC + amorphous mixture of Si, C, and O	15	2.55	3.0	192	3.9	1.5	500	Commercial, Black	Pyrolysis of polymer precursor
Nicalon (HVR grade)	Nippon Carbon	β-SiC + amorphous mixture of Si, C, and O	15	2.32	2.93	186	3.9	1.6	500	Commercial, Black	Pyrolysis of polymer precursor
Hi-Nicalon	Nippon Carbon	β-SiC + amorphous Si+C+O	14	2.74	2.8	270	-	1.0	500	Commercial, Black	Pyrolysis of polymer precursor
Tyranno (S grade)	Ube Industries	Amorphous Si+Ti+O+C	8.5, 11.0	2.35	3.2	170	3.1	1.9	800 and 1600	Commercial, Black	Pyrolysis of polymer precursor
MERX	MER	30-100% β-SiC+C	4-8	3	1-4.5	340-410	-	-	1000-12000	Limited, Greenish black	Chemical conversion of carbon
HPZ	Dow Corning	Amorphous Si+C+O+N	10	2.35	2.1-2.4	140-175	3	1	200-800	Discontinued	Pyrolysis of polymer precursor
MPDZ	Dow Corning	β-SiC + C+O+N	10-15	2.3	1.7-2.1	175-210	-	-	-	Discontinued	Pyrolysis of polymer precursor
MPS	Dow Corning	β/α SiC +O	10-15	2.6-2.7	1.0-1.4	175	-	-	-	Discontinued	Pyrolysis of polymer precursor
Tonen	Tonen	Amorphous Si+N+B	10	2.5	2.5	250	1.5	-	-	-	Pyrolysis of polymer precursor
Textron	Textron	B on W core	100 and 140	2.57	3.6	400	4.5	1	Monofilament	Commercial	CVD

^CTE - Coefficient of thermal expansion, temperature range not specified ^^ETF - Elongation to failure - indicates data not available to the author

Table 2. Selected properties of commercially available oxide continuous ceramic fibers [2, 27-31]

Trade Name	Manufacturer	Composition (wt.%)	Diameter (μm)	Density (g/cm^3)	Tensile Strength (GPa)	Tensile Modulus (GPa)	CTE^ x 10^{-6} (/°C)	ETF^^ (%)	Filaments per yarn or tow	Availability and color	Process Type
Saphikon	Saphikon	Al_2O_3 - 100%	125	3.97	2.1-3.4	386-435	7.9-8.8	11.5 ‖ to c axis	Monofilament	Commercial, Translucent	Melt grown
Fiber FP	Du Pont	Al_2O_3 > 99%	20	3.9	1.4	380	6.8	0.4	200	Discontinued, White	Slurry-spun
Almax	Mitsui Mining	Al_2O_3 > 99%	15	3.6	1.8	320	-	0.5	1000	Commercial, White	Slurry-spun
Nextel 610	3M	Al_2O_3 > 99% Fe_2O_3 - 0.4-0.7% SiO_2 - 0.2-0.3%	12	3.88	1.9	373	7.9	-	-	Commercial,	Sol-gel
Safimax	ICI	Al_2O_3 - 95% SiO_2 - 5%	3	3.3	2	300	-	-	Blanket	White	-
Altex	Sumitomo Chemical	Al_2O_3 - 85% SiO_2 - 15%	10, 15	3.3	1.8	210	8.8	0.8	500 and 1000	Commercial, White	Sol-gel
Nextel 720	3M	Al_2O_3 - 85% SiO_2 - 15%	12	3.4	2.1	260	6.0	-	-	Commercial,	Sol-gel
Nextel 550	3M	Al_2O_3 - 73% SiO_2 - 27%	12	3.03	2.0	193	5.3	-	-	Commercial,	Sol-gel
Nextel 440	3M	Al_2O_3 - 73% SiO_2 - 28% B_2O_3 - 2%	10-12	3.05	2.0	190	5.3	-	-	Commercial, Pink	Sol-gel
Nextel 312	3M	Al_2O_3 - 64% SiO_2 - 24% B_2O_3 - 14%	10-12	2.7	1.7	150	3	-	-	Commercial, White	Sol-gel
PRD-166	Du Pont	Al_2O_3 - 80% ZrO_2 - 20%	20	4.2	2.07	380	9	0.6	-	Discontinued, White	Slurry-spun
Nextel Z-11	3M	ZrO_2 - 68% SiO_2 - 32%	14	3.7	1.3	76	-	-	-	-	Sol-gel

^CTE - Coefficient of thermal expansion, temperature range not specified ^^ETF - Elongation to failure - indicates data not available to the author

Table 3. Ceramic matrices of interest along with processing method(s) [2, 61, 73-78]

Matrix	Processing Method
7740 Borosilicate glass	Slurry infiltration and hot pressing
1723 Aluminosilicate glass	Slurry infiltration and hot pressing
7930 High silica glass	Slurry infiltration and hot pressing
LAS-I glass-ceramic	Slurry infiltration and hot pressing
LAS-II glass-ceramic	Slurry infiltration and hot pressing
LAS-III glass-ceramic	Slurry infiltration and hot pressing
MAS glass-ceramic	Slurry infiltration and hot pressing
BMAS glass-ceramic	Slurry infiltration and hot pressing
Ternary mullite	Slurry infiltration and hot pressing
Hexacelsian	Slurry infiltration and hot pressing
Silicon carbide	Chemical vapor infiltration, reaction bonding, directed metal oxidation, polymer pyrolysis
Silicon nitride	Chemical vapor infiltration, reaction bonding, directed metal oxidation, polymer pyrolysis
Titanium carbide	Chemical vapor infiltration
Titanium diboride	Chemical vapor infiltration
Aluminum nitride	Polymer pyrolysis, directed metal oxidation, chemical vapor infiltration
Blackglas	Polymer pyrolysis
Alumina	Sol-gel, directed metal oxidation
Mullite	Sol-gel
Silica	Sol-gel
Calcium difluoride	Melt infiltration
Strontium aluminosilicate	Melt infiltration
Zirconia	Sol-gel, chemical vapor infiltration

Table 4. Properties of the fiber, matrix, and interface materials used for modeling investigation

Material	Young's modulus, E (GPa)	Poisson's ratio, ν	Coefficient of thermal expansion, α (x 10^{-6}/°C)
Nicalon* fiber	190	0.12	3.9
Nextel 440** fiber	190	0.12	5.3
SiC matrix	400	0.3	5.5
E111 interface***	20	0.1	1
E112 interface	20	0.1	10
E211 interface	140	0.1	1
E212 interface	140	0.1	10
E311 interface	400	0.1	1
E312 interface	400	0.1	10
E121 interface	20	0.3	1
E122 interface	20	0.3	10
E221 interface	140	0.3	1
E222 interface	140	0.3	10
E321 interface	400	0.3	1
E322 interface	400	0.3	10

* Nicalon diameter = 15 μm ** Nextel 440 diameter = 12 μm *** Interface thickness = 0.5 μm

Table 5. List of fabricated Nicalon/SiC composites with C, oxide/C, and C/oxide/C interfaces

CVI #	Interface	Sol used for oxide deposition	C deposition time
CVI 1077	C	-	30 min
CVI 982	Mullite/C	EBMPS*	OC[¶]: 15 min
CVI 986	C/mullite/C	EBMPS	IC[‡]: 15 min OC: 15 min
CVI 1033	C/mullite/C	EBMPS	IC: 15 min OC: 15 min
CVI 1080	C/mullite/C	MEBMPS**	IC: 15 min OC: 15 min
CVI 1081	C/mullite/C	MEBMPS	IC: 15 min OC: 15 min
CVI 985	Al_2O_3-TiO_2/C	ATS[a]	IC: 15 min OC: 15 min
CVI 1002	C/Al_2O_3-TiO_2/C	ATS	IC: 15 min OC: 15 min
CVI 1036	C/Al_2O_3-TiO_2/C	ATS	IC: 15 min OC: 15 min
CVI 1066	C/Al_2O_3-TiO_2/C	ATS	IC: 15 min OC: 15 min

* Ethanol based mullite precursor sol
** 2-methoxy ethanol based mullite precursor sol
[a] Aluminum titanate precursor sol
[¶] Outer C layer
[‡] Inner C layer

Table 6. List of fabricated Nicalon/SiC composites with BN and BN/oxide/BN interfaces

CVI #	Interface	Sol used for oxide deposition	BN deposition time
CVI 1068	BN	-	60 min
CVI 1073	BN/Al_2O_3-TiO_2/BN	ATS[a]	IBN[¶]: 30 min OBN[‡]: 30 min
CVI 1054	BN/mullite/BN	EBMPS*	IBN: 30 min OBN: 30 min

[a] Aluminum titanate precursor sol
* Ethanol based mullite precursor sol
[¶] Inner BN layer
[‡] Outer BN layer

Table 7. List of fabricated Nextel/SiC composites with oxide/C and C/oxide/C interfaces

CVI #	Interface	Sol used for oxide deposition	C deposition time
CVI 997	Mullite/C	EBMPS*	OC‡: 15 min
CVI 998	Al_2O_3-TiO_2/C	ATS[a]	OC: 15 min
CVI 999	C/mullite/C	EBMPS	IC¶: 15 min OC: 15 min
CVI 1000	C/Al_2O_3-TiO_2/C	ATS	IC: 15 min OC: 15 min

* Ethanol based mullite precursor sol
[a] Aluminum titanate precursor sol
‡ Outer C layer
¶ Inner C layer

Table 8. Summary of the number of flexure bars of Nicalon/SiC composites tested at room temperature in both as-processed and oxidized conditions

CVI #	Interface	# of flexure bars in the as-processed condition	# of flexure bars oxidized at 1000°C in air			# of flexure bars oxidized for 200 h in air at		# of flexure bars oxidized at 1000°C for 200 h followed by 750°C for 200 h in air
			24 h	200 h	500 h	500°C	750°C	
1077	C	4	4	4	4	4	4	-
982	Mullite/C	12	12	-	-	-	-	-
985	Al_2O_3-TiO_2/C	12	12	-	-	-	-	-
986	C/mullite/C	12	6	3	3	-	-	-
1033	C/mullite/C	5	-	5	-	5	5	-
1080	C/mullite/C	6	6	6	6	-	-	-
1081	C/mullite/C	6	-	6	-	6	6	-
1002	C/Al_2O_3-TiO_2/C	12	6	3	3	-	-	-
1036	C/Al_2O_3-TiO_2/C	6	-	6	-	6	6	-
1066	C/Al_2O_3-TiO_2/C	6	6	4	6	-	-	2
1068	BN	4	4	4	4	4	4	-
1073	BN/Al_2O_3-TiO_2/BN	4	4	4	4	4	4	-
1054	BN/mullite/BN	4	4	4	4	4	4	-

Table 9. Summary of the number of flexure bars of Nextel/SiC composites tested at room temperature in both as-processed and oxidized conditions

CVI #	Interface	# of flexure bars in the as-processed condition	# of flexure bars oxidized at 1000°C in air	
			24 h	200 h
997	Mullite/C	12	12	-
998	Al_2O_3-TiO_2/C	12	12	-
999	C/mullite/C	12	12	-
1000	C/Al_2O_3-TiO_2/C	12	6	6

Table 10. Summary of the Nicalon/SiC composites and Nextel/SiC composites selected for Auger electron spectroscopy studies

CVI #	Composite	Interface	# of bars in the as-processed condition	# of bars in the oxidized condition (500 h at 1000°C in air)
1077	Nicalon/SiC	C	1	1
982	Nicalon/SiC	Mullite/C	1	-
985	Nicalon/SiC	Al_2O_3-TiO_2/C	1	-
986	Nicalon/SiC	C/mullite/C	1	1
1002	Nicalon/SiC	C/Al_2O_3-TiO_2/C	1	1
1068	Nicalon/SiC	BN	1	1
1073	Nicalon/SiC	BN/Al_2O_3-TiO_2/BN	1	1
997	Nextel/SiC	Mullite/C	1	-
998	Nextel/SiC	Al_2O_3-TiO_2/C	1	-
999	Nextel/SiC	C/mullite/C	1	-
1000	Nextel/SiC	C/Al_2O_3-TiO_2/C	1	-

Table 11. Summary of DSC and high temperature XRD results of mullite crystallization from powders derived from mullite precursor gels

Mullite precursor gel	Drying temperature in air for 168 h to obtain the mullite precursor powder	Test atmosphere	Sharp exothermic event occurrence temperature in the DSC run suggesting mullite crystallization	Mullite crystallization temperature in high temperature XRD study	Color of the powder after the DSC and high temperature XRD runs
MI	60°C	Air	~ 990°C	1050°C	White
MII	60°C	Air	~ 990°C	1050°C	White
EI	110°C	Air	~ 990°C	950°C	White
EII	110°C	Argon	~ 990°C	1000°C	Black
MEI	110°C	Air	~ 990°C	950°C	White
MEI	110°C	Argon	~ 990°C	1000°C	Black

Table 12. Summary of DSC and high temperature XRD results of aluminum titanate formation from powders derived from aluminum titanate precursor gels

Aluminum titanate precursor gel	Drying temperature in air for 168 h to obtain the aluminum titanate precursor powder	Test atmosphere	Endothermic event occurrence temperature in the DSC run indicating the aluminum titanate formation	Aluminum titanate formation* temperature in high temperature XRD study	Color of the powder after the DSC and high temperature XRD runs
ATI	60°C	Air	~ 1360°C	1400°C	Yellow
ATII	110°C	Air	~ 1370°C	1300°C	Yellow
ATII	110°C	Argon	~ 1200°C	1200°C	Black

* Residual amounts of alumina and titania are also present

Table 13. Density of fabricated Nicalon/SiC composites with C, oxide/C, and C/oxide/C interfaces along with C coating thicknesses

CVI#	Interface	Density (g/cm^3)	Inner C layer thickness* (nm)	Outer C layer thickness* (nm)
1077	C	2.36±0.14	43**	-
982	Mullite/C	2.33±0.06	-	11
985	Al_2O_3-TiO_2/C	2.41±0.05	-	33
986	C/mullite/C	2.47±0.06	22	21
1033	C/mullite/C	2.52±0.06	32	31
1080	C/mullite/C	2.40±0.11	22	21
1081	C/mullite/C	2.32±0.11	26	25
1002	C/Al_2O_3-TiO_2/C	2.46±0.06	28	27
1036	C/Al_2O_3-TiO_2/C	2.46±0.08	18	18
1066	C/Al_2O_3-TiO_2/C	2.45±0.07	16	16

* thickness measurements based on weight gain
** control sample where the total C thickness was 43 nm

Table 14. Density of fabricated Nicalon/SiC composites with BN and BN/oxide/BN interfaces along with BN coating thicknesses

CVI#	Interface	Density (g/cm^3)	Inner BN layer thickness* (nm)	Outer BN layer thickness* (nm)
1068	BN	2.46±0.10	282**	-
1073	BN/Al_2O_3-TiO_2/BN	2.39±0.18	113	109
1054	BN/mullite/BN	2.41±0.17	121	116

* thickness measurements based on weight gain
** control sample where the total BN thickness was 282 nm

Table 15. Density of fabricated Nextel/SiC composites with oxide/C, and C/oxide/C interfaces along with C coating thicknesses

CVI#	Interface	Density (g/cm^3)	Inner C layer thickness* (nm)	Outer C layer thickness* (nm)
997	Mullite/C	2.77±0.05	-	17
998	Al_2O_3-TiO_2/C	2.69±0.11	-	10
999	C/mullite/C	2.79±0.08	24	23
1000	C/Al_2O_3-TiO_2/C	2.70±0.09	22	21

* thickness measurements based on weight gain

Table 16. Flexural strengths of Nicalon/SiC composites with C, oxide/C, C/oxide/C, BN and BN/oxide/BN interfaces in the as-processed condition

CVI#	Interface	Flexural strength (MPa)	Graceful or catastrophic failure*
1077	C	311±74	Graceful
982	Mullite/C	64±8	Catastrophic
985	Al_2O_3-TiO_2/C	122±29	Graceful
986	C/mullite/C	268±52	Graceful
1033	C/mullite/C	310±29	Graceful
1080	C/mullite/C	320±24	Graceful
1081	C/mullite/C	253±38	Graceful
1002	C/Al_2O_3-TiO_2/C	255±35	Graceful
1036	C/Al_2O_3-TiO_2/C	246±12	Graceful
1066	C/Al_2O_3-TiO_2/C	298±23	Graceful
1068	BN	274±52	Graceful
1073	BN/ Al_2O_3-TiO_2/BN	266±128	Graceful
1054	BN/mullite/BN	244±115	Graceful

* Typical load vs displacement curve behavior in the as-processed condition

Table 17. Comparison of flexural strengths of Nicalon/SiC composites in the as-processed condition and after oxidation at 1000°C in air

CVI#	Interface	Flexural strength (MPa)			
			Oxidation at 1000°C in air		
		As-processed	24 h	200 h	500 h
1077*	C	311±74	238±43	224±62	214±68
982$^{\Delta}$	Mullite/C	64±8	80±9	-	-
985$^{\kappa}$	Al_2O_3-TiO_2/C	122±29	112±24	-	-
986*	C/mullite/C	268±52	260±61	200±47	184±28
1080*	C/mullite/C	320±24	238±54	239±39	193±27
1002*	C/Al_2O_3-TiO_2/C	255±35	189±45	217±35	159±20
1066*	C/Al_2O_3-TiO_2/C	298±23	314±29	257±64	234±52
1068*	BN	274±52	198±86	177±87	232±116
1073*	BN/Al_2O_3-TiO_2/BN	266±128	156±57	241±96	253±88
1054**	BN/mullite/BN	244±115	75±20	171±77	137±76

* Typical load vs displacement curve shows graceful failure even after 500 h oxidation at 1000°C
$^{\Delta}$ Typical load vs displacement curve shows catastrophic failure in both as-processed and oxidized conditions
$^{\kappa}$ Typical load vs displacement curve shows graceful failure after oxidation for 24 h at 1000°C
** Typical load vs displacement curve shows predominantly catastrophic failure after 500 h oxidation at 1000°C

Table 18. Comparison of flexural strengths of Nicalon/SiC composites in the as-processed condition and after oxidation for 200 h each at 500°C, 750°C, and 1000°C in air

CVI#	Interface	Flexural strength (MPa)			
			Oxidation for 200 h in air		
		As-processed	500°C	750°C	1000°C
1077	C	311±74	200±45	67±9	224±62
1033	C/mullite/C	310±29	293±27	44±20	199±34
1081	C/mullite/C	253±38	306±127	67±21	239±80
1036	C/Al_2O_3-TiO_2/C	246±12	225±33	50±9	139±42
1068	BN	274±52	246±131	211±97	177±87
1073	BN/Al_2O_3-TiO_2/BN	266±128	151±56	315±147	241±96
1054	BN/mullite/BN	244±115	197±154	193±97	171±77

Table 19. Interface debonding characteristics of the Nicalon/SiC composites and Nextel/SiC composites based on Auger electron spectroscopy studies

CVI #	Composite	Interface	As-processed condition	After oxidation for 500 h at 1000°C in air
1077	Nicalon/SiC	C	Within the C layer	Within the C layer
982	Nicalon/SiC	Mullite/C	Mullite/C boundary	-
985	Nicalon/SiC	Al_2O_3-TiO_2/C	Al_2O_3-TiO_2/C boundary	-
986	Nicalon/SiC	C/mullite/C	C/mullite or mullite/C boundary	Mullite/C (SiO_2) boundary
1002	Nicalon/SiC	C/Al_2O_3-TiO_2/C	C/Al_2O_3-TiO_2 or Al_2O_3-TiO_2/C boundary	Al_2O_3-TiO_2/C boundary
1068	Nicalon/SiC	BN	Within the BN layer	Within the BN layer
1073	Nicalon/SiC	BN/Al_2O_3-TiO_2/BN	BN/Al_2O_3-TiO_2 boundary	-
997	Nextel/SiC	Mullite/C	Mullite/C boundary	-
998	Nextel/SiC	Al_2O_3-TiO_2/C	Nextel/Al_2O_3-TiO_2 or Al_2O_3-TiO_2/C boundary	-
999	Nextel/SiC	C/mullite/C	C/mullite boundary	-
1000	Nextel/SiC	C/Al_2O_3-TiO_2/C	Al_2O_3-TiO_2/C boundary	-

Table 20. Comparison of flexural strengths of Nextel/SiC composites in the as-processed condition and after oxidation at 1000°C in air

CVI#	Interface	Density (g/cm^3)	Flexure Strength (MPa)		
			As Processed	Oxidized at 1000°C in air 24 h	200 h
997*	Mullite/C	2.77±0.05	126±12	101±11	-
998*	Al_2O_3-TiO_2/C	2.69±0.11	107±18	99±15	-
999*	C/mullite/C	2.79±0.08	204±34	94±16	-
1000**	C/ Al_2O_3-TiO_2/C	2.70±0.09	234±31	119±27	97±16

* Typical load vs displacement curve shows catastrophic failure after oxidation for 24 h at 1000°C
** Typical load vs displacement curve shows graceful failure after oxidation for 24 h at 1000°C, but catastrophic failure after oxidation for 200 h at 1000°C

APPENDIX B

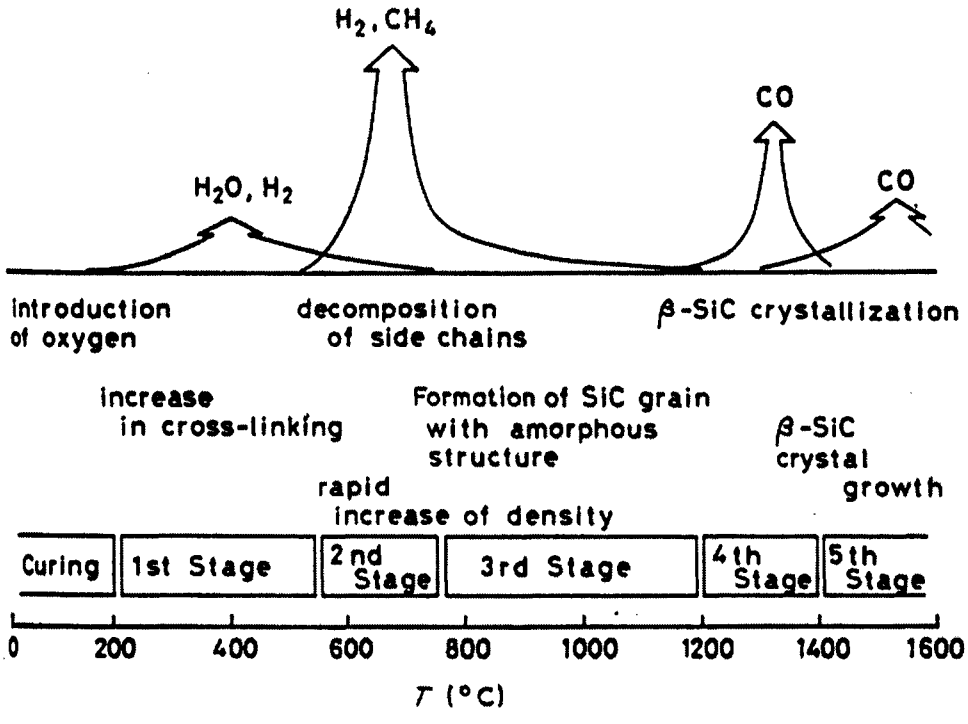


Fig. B.2.1. Conversion process of cured PCS into SiC by pyrolysis

SOURCE Y. Hasegawa, "Synthesis of Continuous Silicon Carbide Fiber, Part 6, Pyrolysis of Polycarbosilane and Structure of SiC Fibre," J. Mater. Sci., 24, 1177-90 (1989).

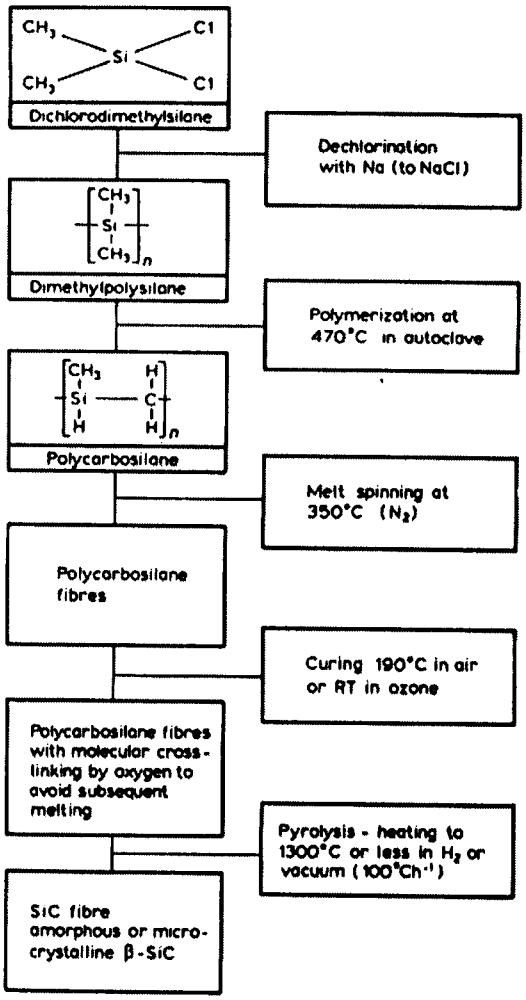


Fig. B.2.2. Flow diagram for the Nicalon fiber manufacturing process

SOURCE Y. Hasegawa, M. Iimura, and S. Yajima, "Synthesis of Continuous Silicon Carbide Fiber, Part 2, Conversion of Polycarbosilane Fibers into Silicon Carbide Fibers," J. Mater. Sci., 15, 720-28 (1980).

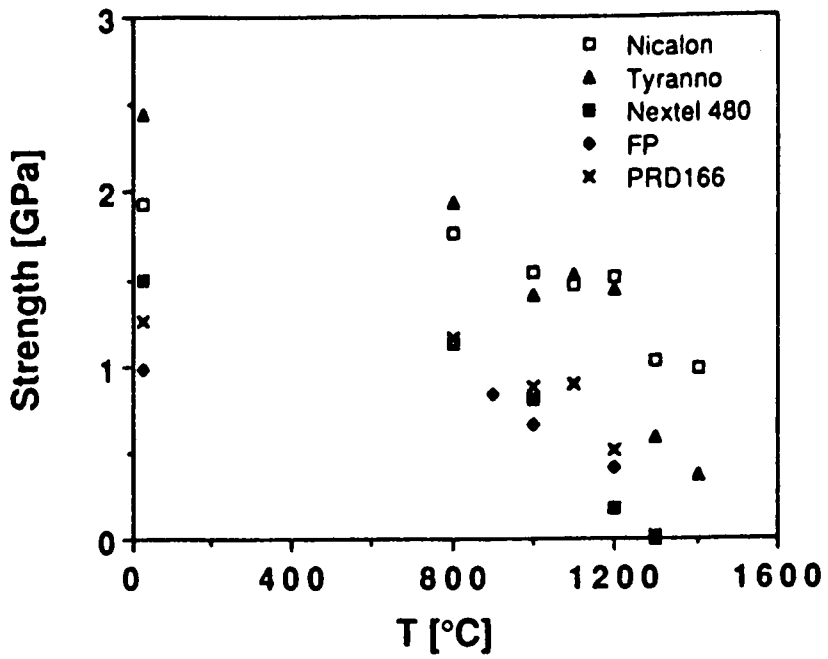


Fig. B.2.3. Tensile strength as a function of temperature of SiC-based and oxide fibers.

SOURCE D. J. Pysher, K. C. Goretta, R. S. Hodder, and R. E. Tressler, "Strength of Ceramic Fibers at Elevated Temperatures," J. Am. Ceram. Soc., 72 [2], 284-88 (1989).

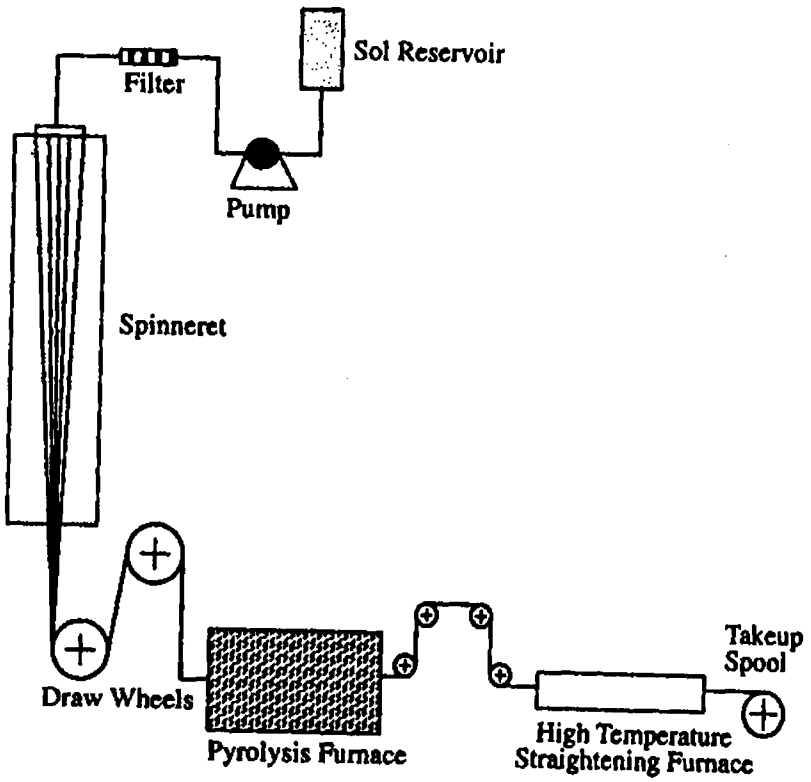


Fig. B.2.4. A schematic of the 3M process for making an alumina fiber

SOURCE K. K. Chawla, Ceramic Matrix Composites, Chapman and Hall, London, 1993.

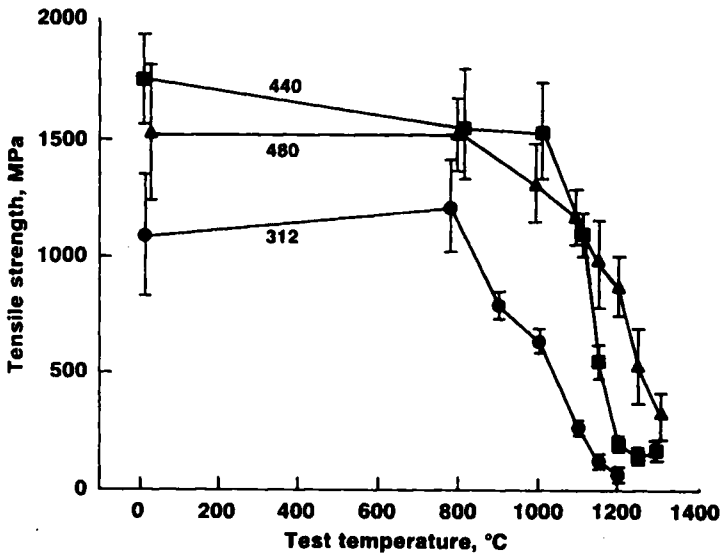


Fig. B.2.5. Tensile strength versus temperature for Nextel fibers

SOURCE A. R. Holtz and M. F. Grether, "High Temperature Properties of three Nextel Ceramic Fibers" Presented at the 32nd International SAMPE Symposium and Exhibition, Anaheim, California, April 6-9, 1987.

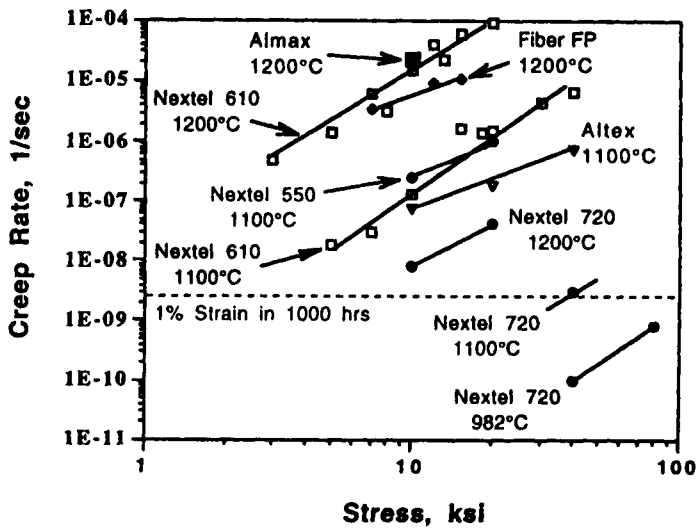


Fig. B.2.6. Creep rate versus stress for Nextel 720 and other commercially available polycrystalline oxide fibers (10 ksi = 69 MPa)

SOURCE D. M. Wilson, S. L. Lieder and D. C. Lueneburg, "Microstructure and High Temperature Properties of Nextel 720 Fibers," Ceram. Eng. Sci. Proc., 16 [5], 1005-14 (1995).

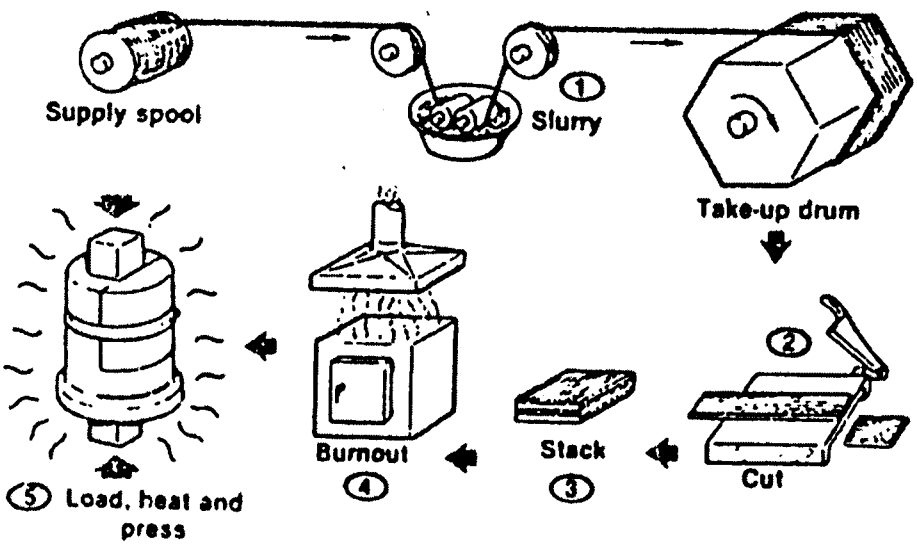


Fig. B.2.7. Flow diagram of the tape lay-up fabrication of glass matrix composites

SOURCE K. M. Prewo, J. J. Brennan, and G. K. Layden, "Fiber Reinforced Glasses and Glass Ceramics for High Performance Applications," Am. Ceram. Soc. Bull., 65 [2], 305-13 (1986).

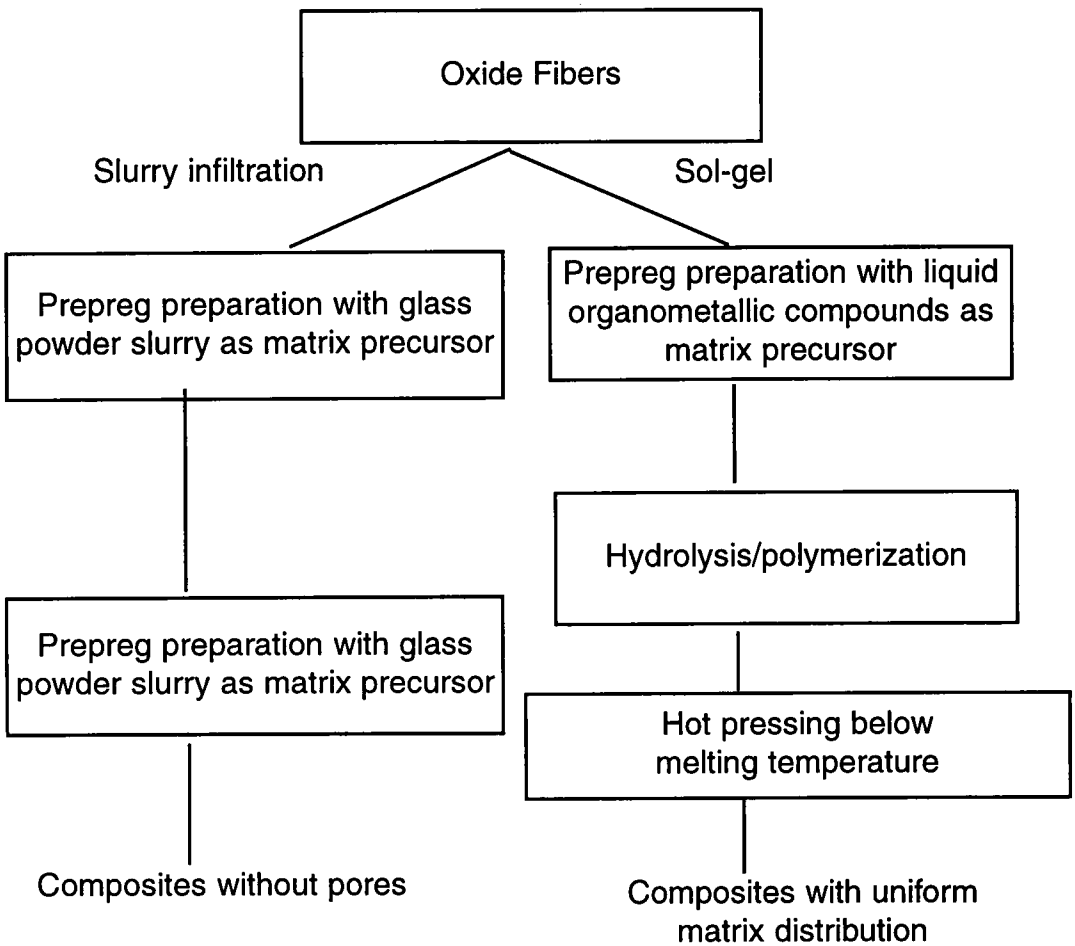


Fig. B.2.8. Comparison of slurry infiltration with the sol-gel process for making oxide fiber reinforced oxide composites

SOURCE E. Fitzer and R. Gadow, "Fiber Reinforced Ceramics via the Sol/Gel Process" pp. 589-601 in Tailoring Multiphase and Composite Ceramics, Vol. 20, Edited by R. E. Tressler, G. L. Messing, C. G. Pantano, and R. E. Newnham, Plenum Press, New York, 1986.

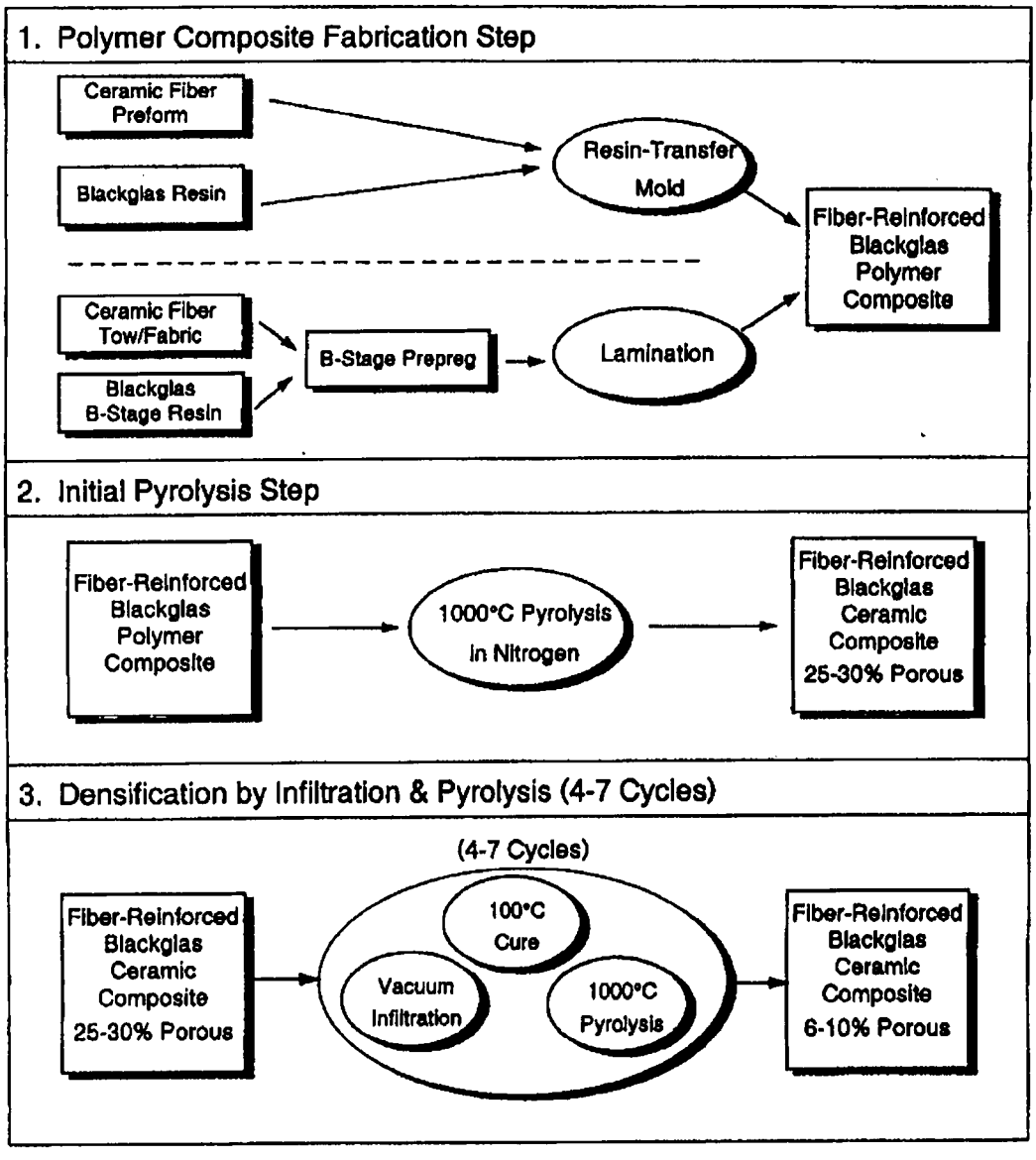


Fig. B.2.9. Schematic flow diagram for making a fiber-reinforced Blackglas ceramic composite by a polymer infiltration and pyrolysis process

SOURCE Gateway Materials Technology, Inc., Illinois, USA, Technical Brochure, 1995.

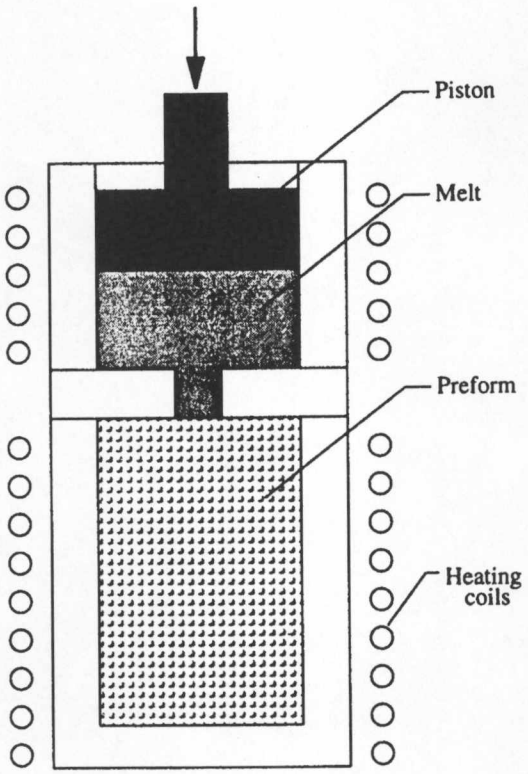


Fig. B.2.10. Schematic of a melt infiltration process

SOURCE K. K. Chawla, Ceramic Matrix Composites, Chapman and Hall, London, 1993.

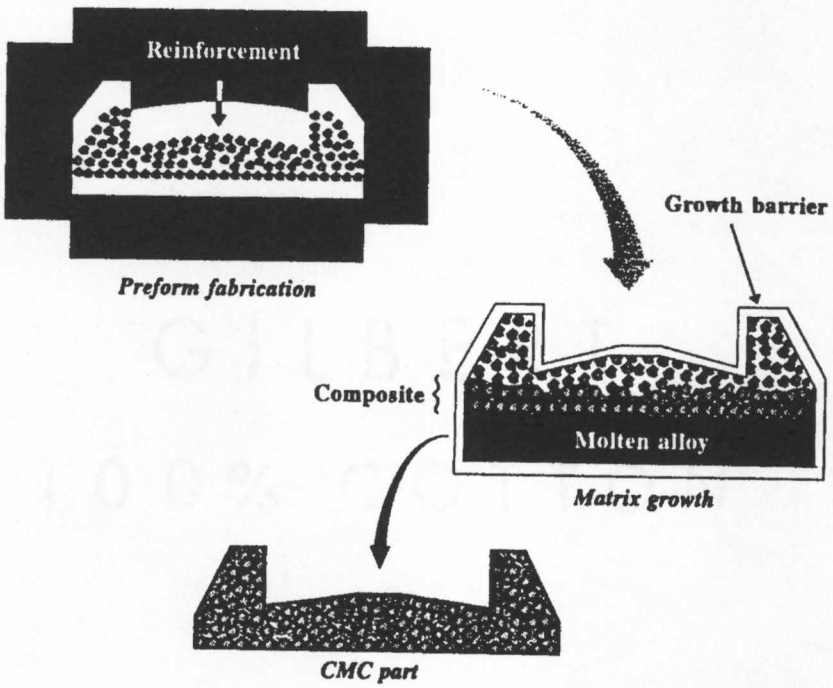


Fig. B.2.11. A schematic of the DIMOX process for making composites

SOURCE K. K. Chawla, Ceramic Matrix Composites, Chapman and Hall, London, 1993.

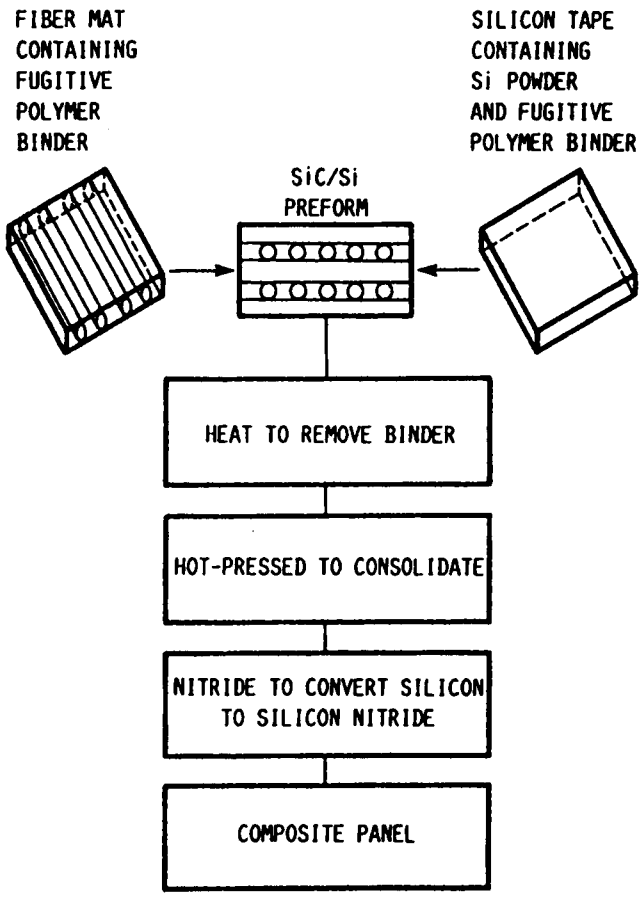


Fig. B.2.12. A schematic of the production of a SCS-6 fiber reinforced silicon nitride by a reaction bonding process

SOURCE R. T. Bhatt, "Properties of Silicon Carbide Fiber-Reinforced Silicon Nitride Matrix Composites," NASA Technical Memorandum 101356, NASA-Lewis Research Center, Cleveland, Ohio (1988).

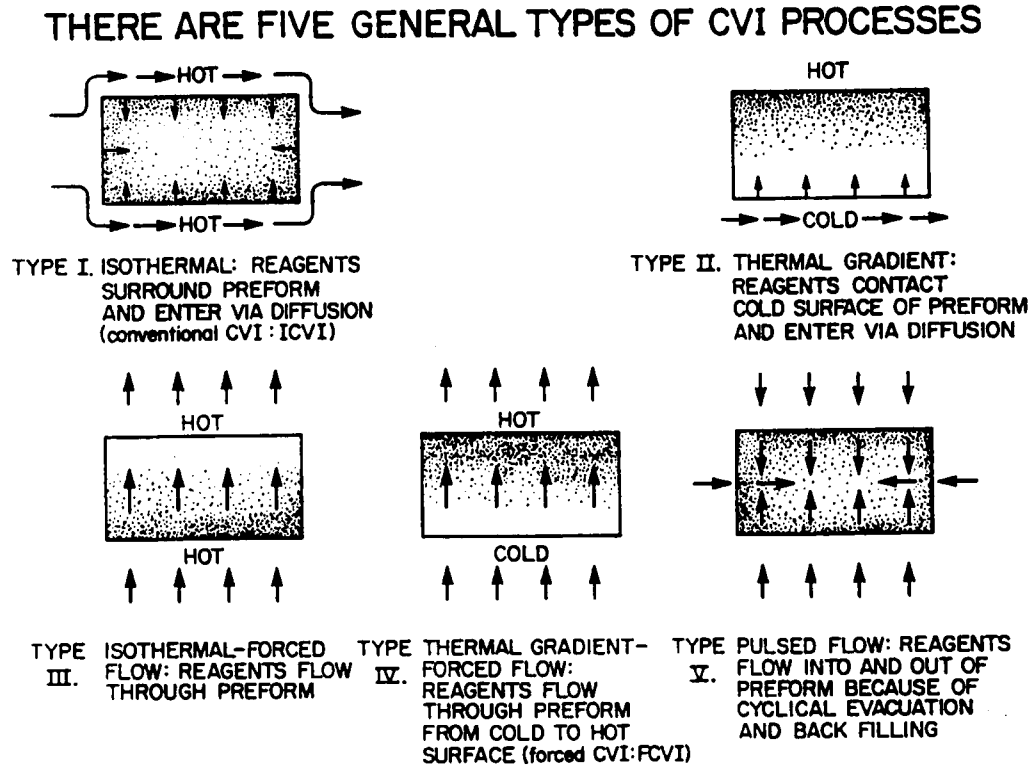


Fig. B.2.13. Five types of chemical vapor infiltration processes

SOURCE T. M. Besmann, B. W. Sheldon, R. A. Lowden and D. P. Stinton, "Vapor-Phase Fabrication and Properties of Continuous-Filament Ceramic Composites," Science, 253, 1104-9 (1991).

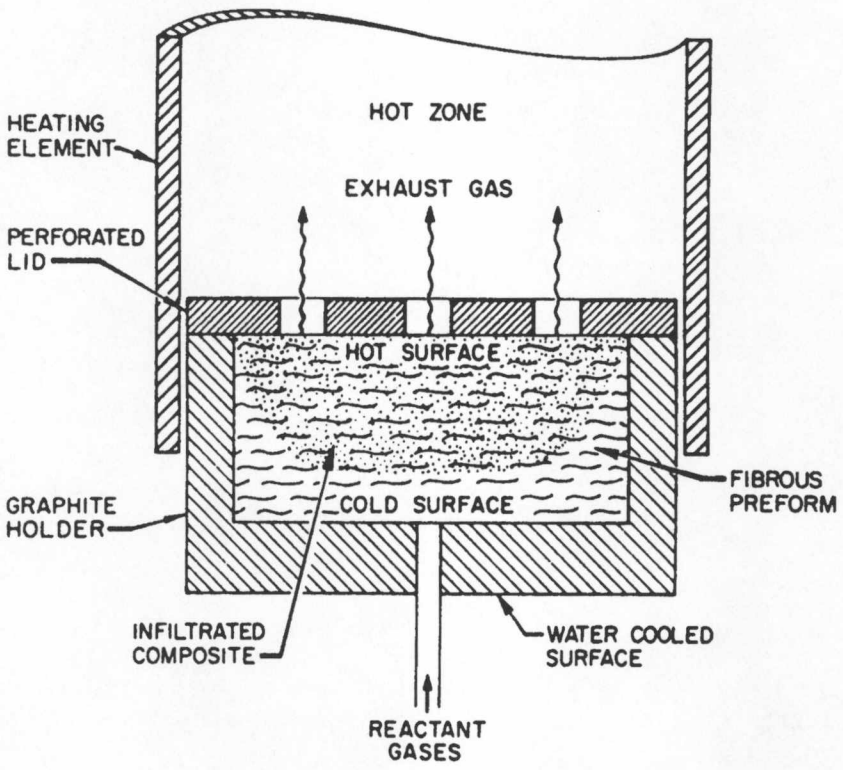


Fig. B.2.14. Schematic of the FCVI process

SOURCE D. P. Stinton, T. M. Besmann, R. A. Lowden, and B. W. Sheldon, "Vapor Deposition," pp. 215-223 in Engineered Materials Handbook, Vol. 4, Ceramics and Glasses, Samuel J. Schneider, Technical Chairman, ASM International, 1987.

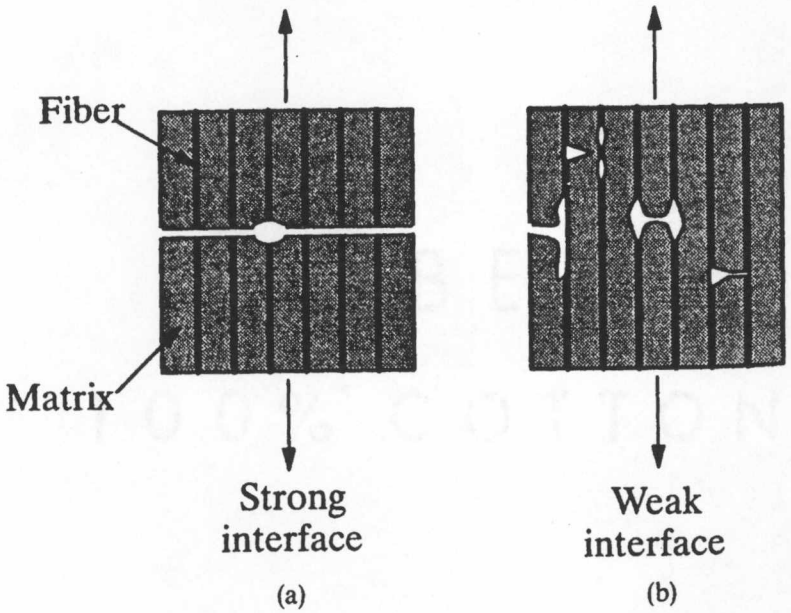


Fig. B.2.15. Influence of interfacial bond strength on the failure of a ceramic matrix composite (a) strong interface bond and (b) weak interface bond

SOURCE K. K. Chawla, Ceramic Matrix Composites, Chapman and Hall, London, 1993.

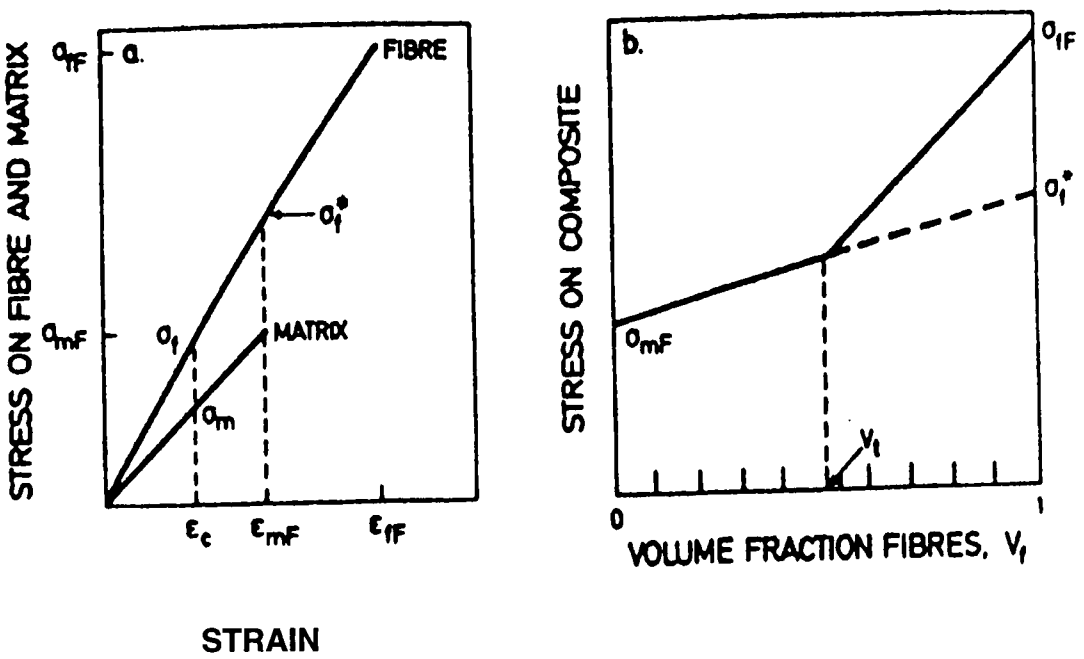


Fig. B.2.16. (a) Stress-strain relationships for brittle fiber and matrix and (b) composite fracture strength vs volume fraction for the matrix/fiber combination in (a)

SOURCE R. Warren, "Fundamental aspects of the Properties of Ceramic-Matrix Composites, " pp.65-113 in Ceramic Matrix Composites, Edited by R. Warren, Chapman and Hall, 1990.

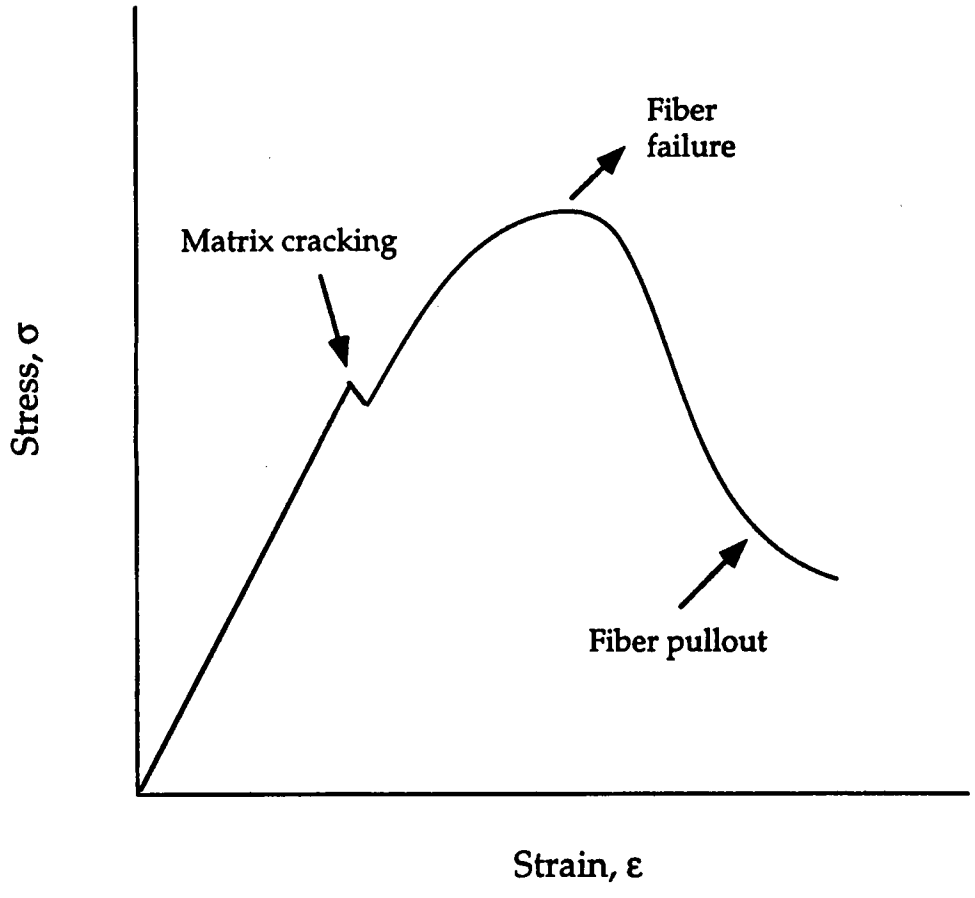


Fig. B.2.17. Stress-strain curve for a "tough" ceramic fiber reinforced ceramic matrix composite

SOURCE N. Miriyala, "Fabric Orientation Effects on the Monotonic and Fatigue Behavior of CFCCs," Doctoral Dissertation Proposal, The University of Tennessee, Knoxville, Tennessee, December 1995.

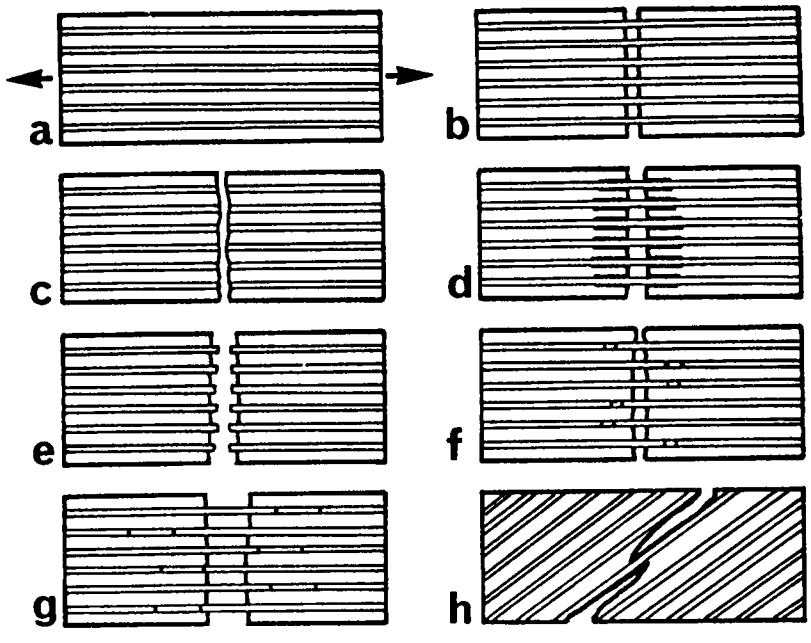


Fig. B.2.18. Fracture mechanisms in ceramic matrix composites (the different cases are described in the text)

SOURCE H. Osmani, D. Rouby, G. Fantozzi, and J. M. Lequertier, "Toughness, Microstructure and Interface Characteristics for Ceramic Matrix Composites," Comp. Sci. Tech., 37, 191-206 (1990).

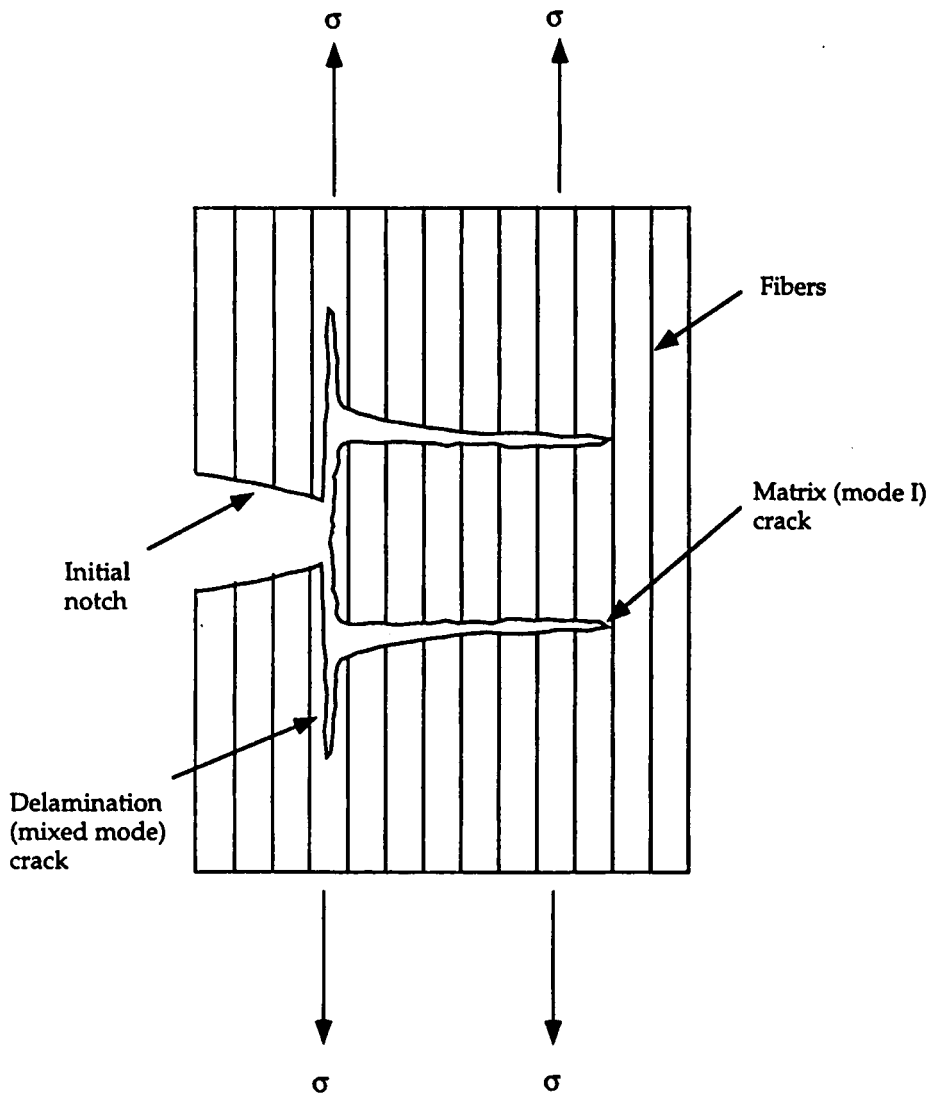


Fig. B.2.19. Failure modes in a high toughness CFCC under tension

SOURCE A. G. Evans and D. B. Marshall, "The Mechanical Behavior of Ceramic Matrix Composites," Acta. Metall., 37, 2567-2583 (1989) and N. Miriyala, "Fabric Orientation Effects on the Monotonic and Fatigue Behavior of CFCCs," Doctoral Dissertation Proposal, The University of Tennessee, Knoxville, Tennessee, December 1995.

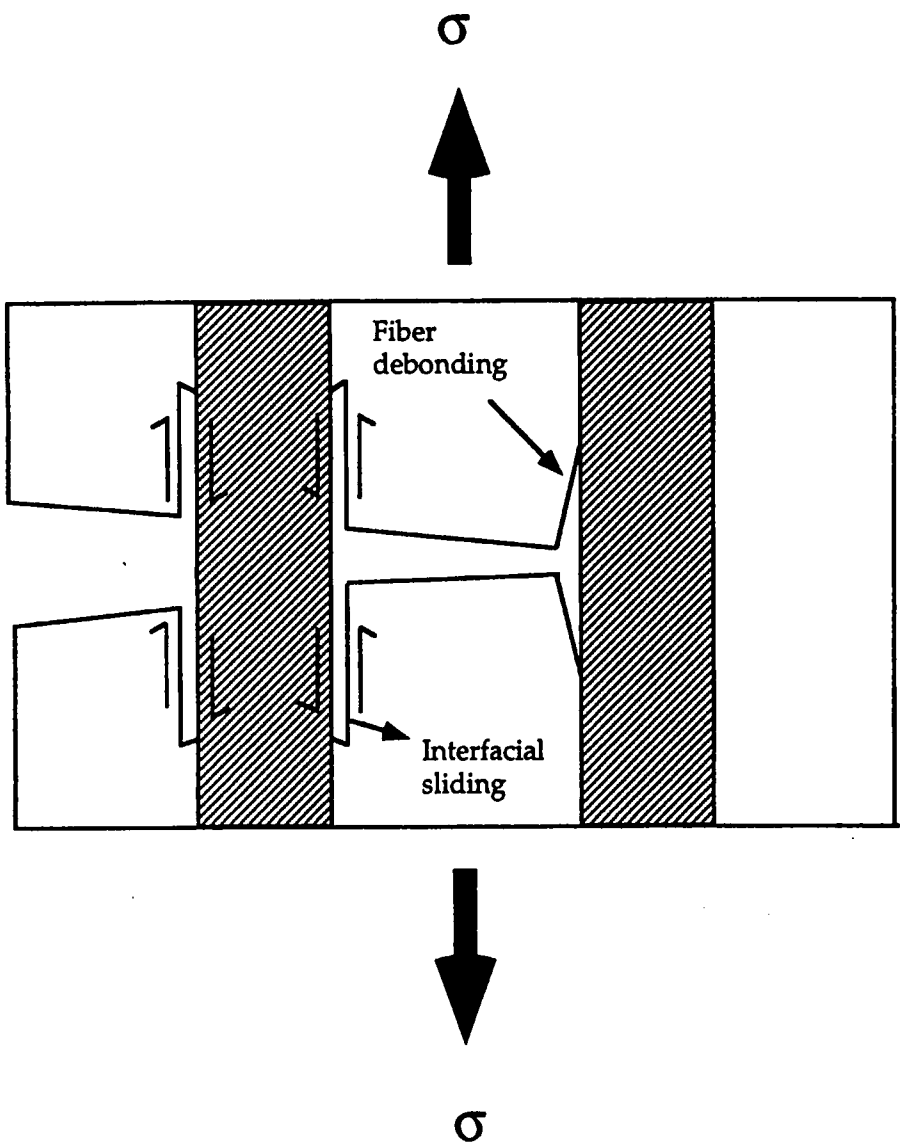


Fig. B.2.20. Interfacial sliding and fiber debonding in a CFCC

SOURCE A. G. Evans and D. B. Marshall, "The Mechanical Behavior of Ceramic Matrix Composites," Acta. Metall., 37, 2567-2583 (1989) and N. Miriyala, "Fabric Orientation Effects on the Monotonic and Fatigue Behavior of CFCCs," Doctoral Dissertation Proposal, The University of Tennessee, Knoxville, Tennessee, December 1995.

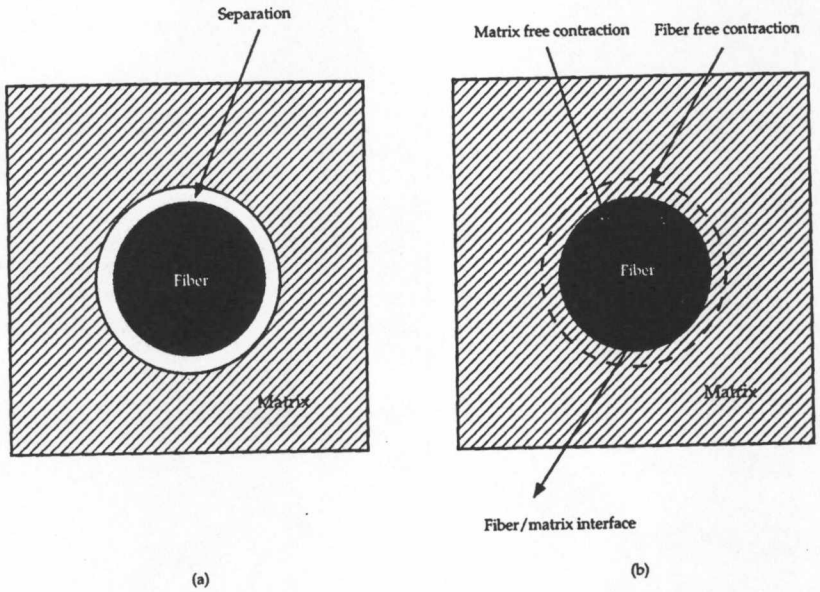


Fig. B.2.21. Influence of thermal expansion mismatch on residual stresses (a) $\alpha_f > \alpha_m$ and (b) $\alpha_f < \alpha_m$

SOURCE N. Miriyala, "Fabric Orientation Effects on the Monotonic and Fatigue Behavior of CFCCs," Doctoral Dissertation Proposal, The University of Tennessee, Knoxville, Tennessee, December 1995.

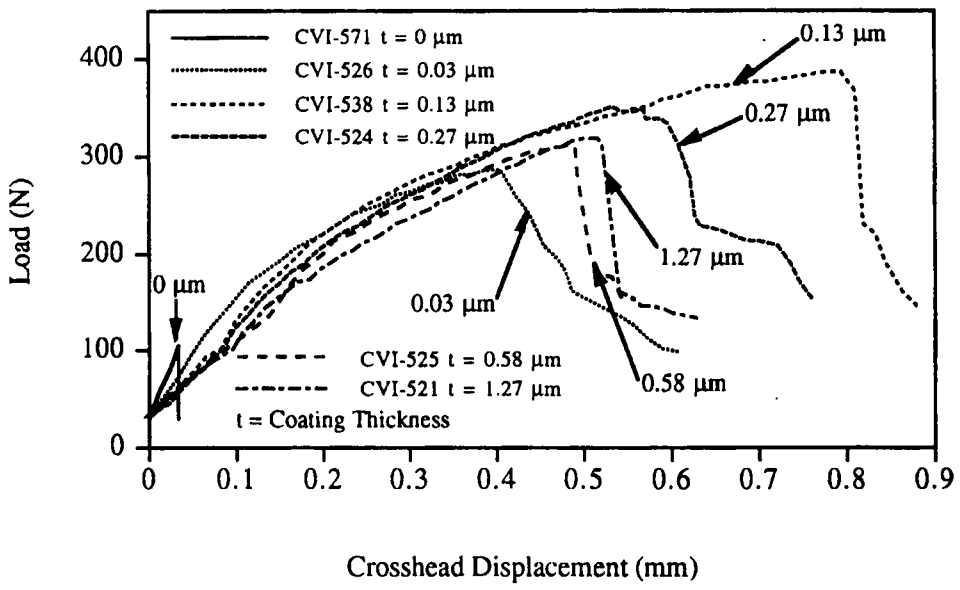


Fig. B.2.22. Comparison of four-point flexure curves of composites with different carbon interface thicknesses

SOURCE J. H. Miller, R. A. Lowden and P.K. Liaw, "Effects of Fiber Coating Thickness on Fracture Behavior of Continuous Woven Fabric-Reinforced Ceramic Composites," Submitted to J. Am. Ceram. Soc.

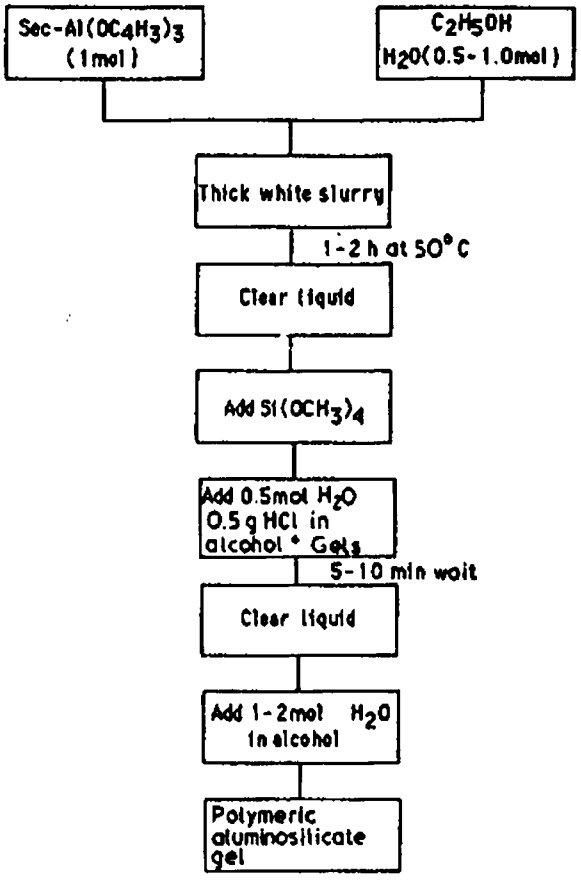


Fig. B.2.23. Yoldas' method for making a polymeric mullite precursor gel

SOURCE B. E. Yoldas, "Effect of Ultrastructure on Crystallization of Mullite,"J. Mater. Sci., 27, 6667-72 (1992).

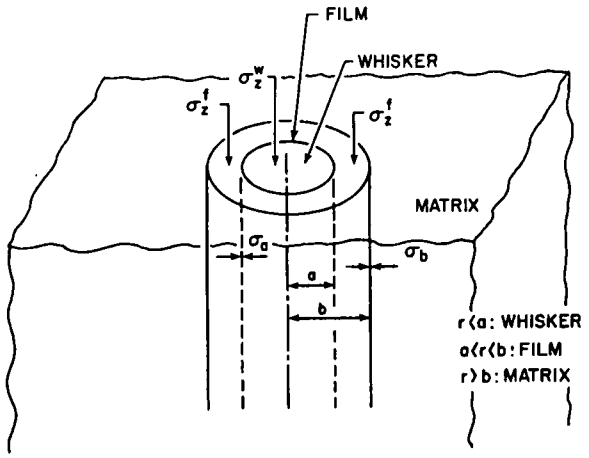


Fig. B.3.1. Schematic illustrating whisker (fiber)/film (interface)/matrix system as well as the interfacial and axial tractions to maintain continuity at the interfaces during cooling

SOURCE C. H. Hsueh, P. F. Becher, and P. Angelini, "Effects of Interfacial Films on Thermal Stresses in Whisker-Reinforced Ceramics," J. Am. Ceram. Soc., 71 [11], 929-33 (1988).

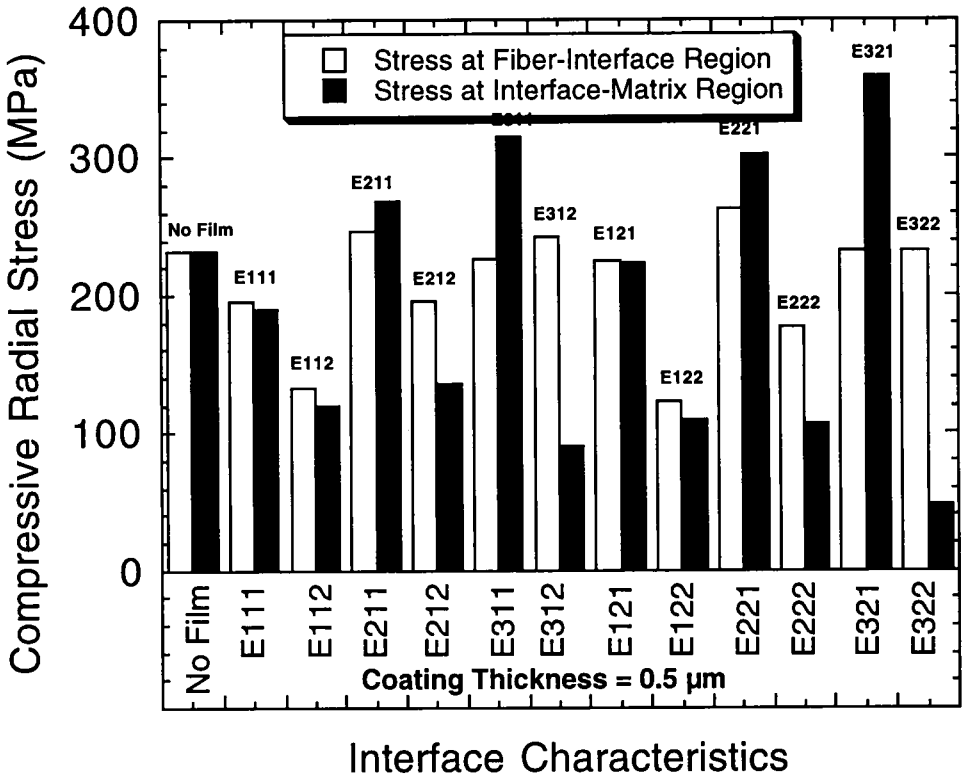


Fig. B.3.2. Compressive residual thermal stresses at the fiber/matrix regions in Nicalon/SiC composites

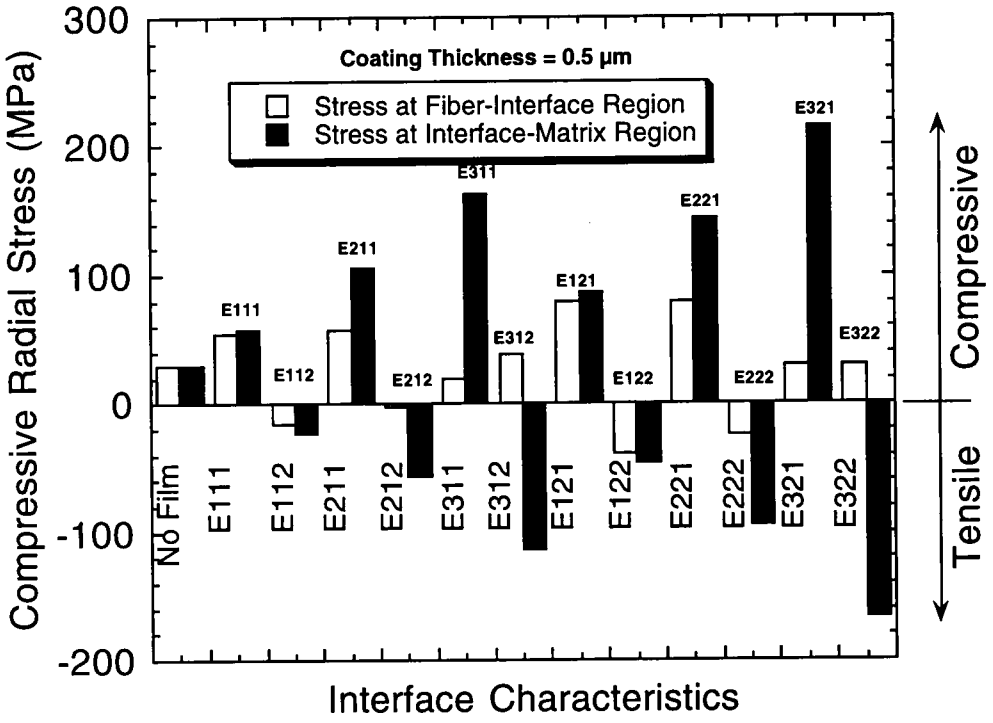
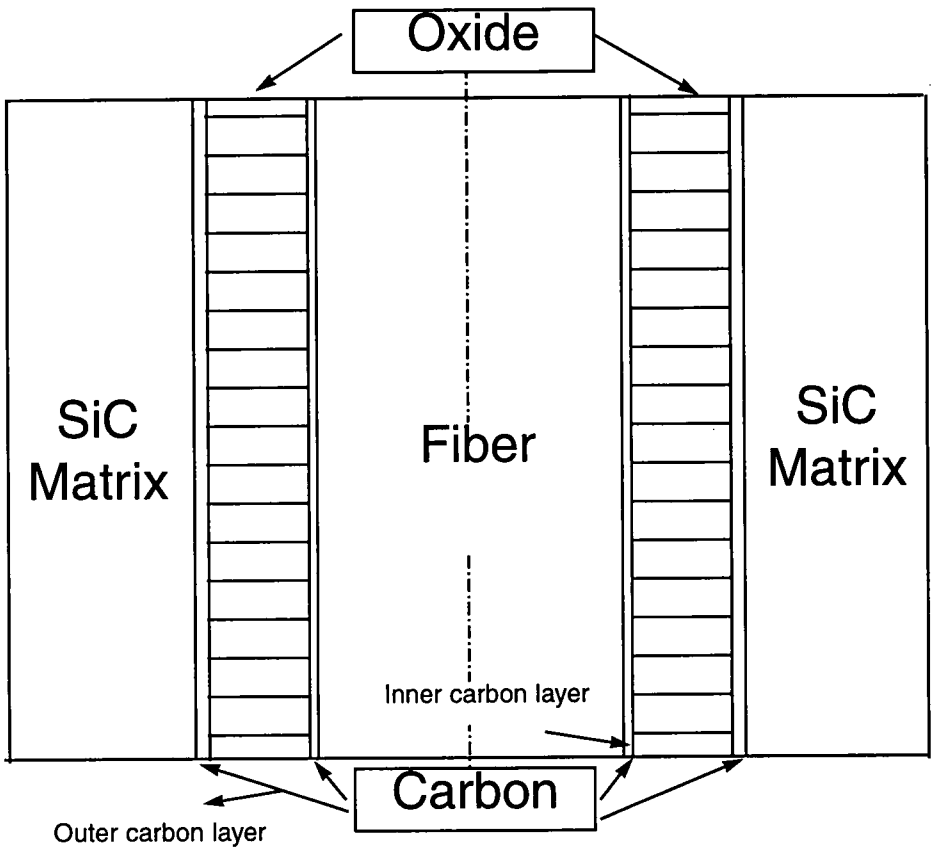


Fig. B.3.3. Compressive residual thermal stresses at the fiber/matrix interface regions in Nextel/SiC composites



Inner Carbon Layer - Protects the fiber during the sol-gel processing of the oxide
Outer Carbon Layer - Protects the oxide coating from HCl attack during the chemical vapor infiltration processing of the SiC Matrix

Fig. B.3.4. Oxide interface concept for a fiber-reinforced ceramic matrix composite

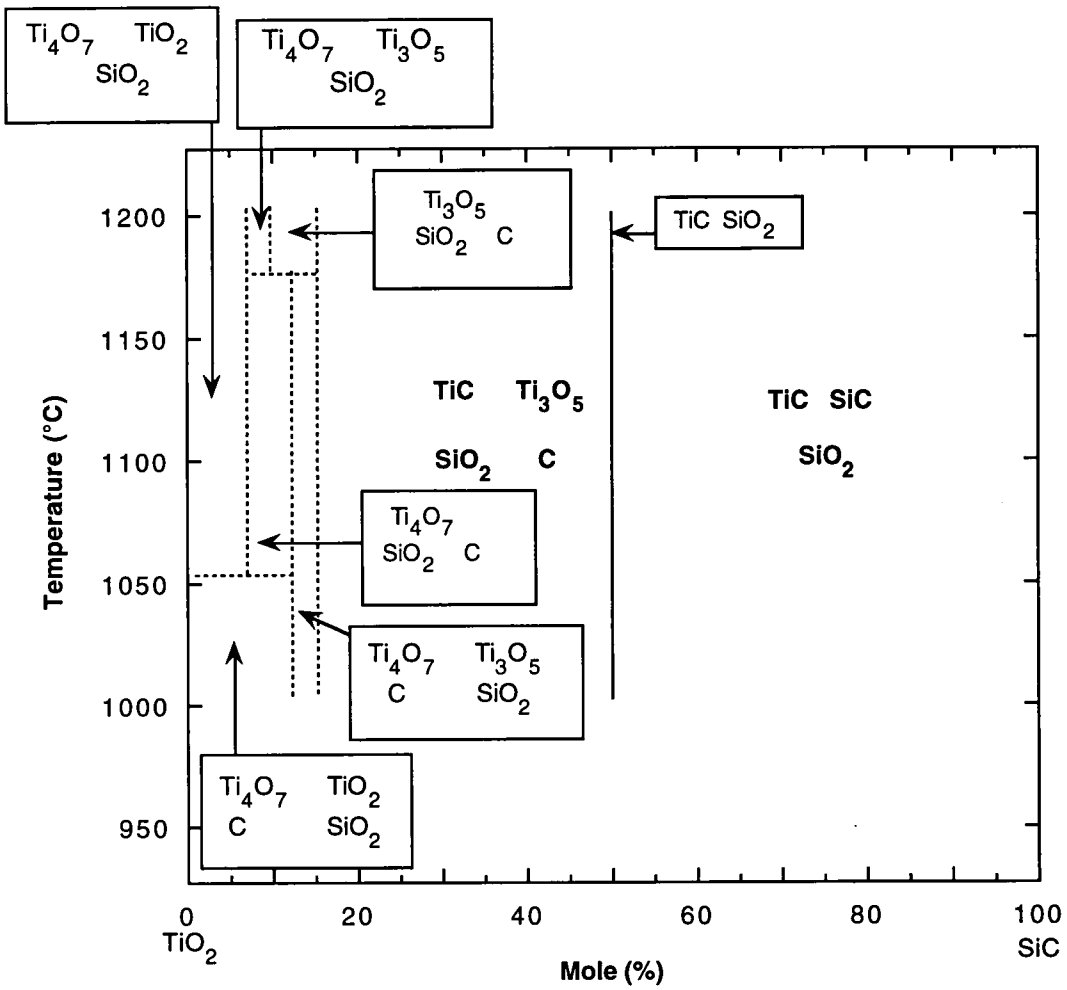


Fig. B.4.1. Computed TiO_2/SiC phase diagram for the temperature range of 1000-1200°C

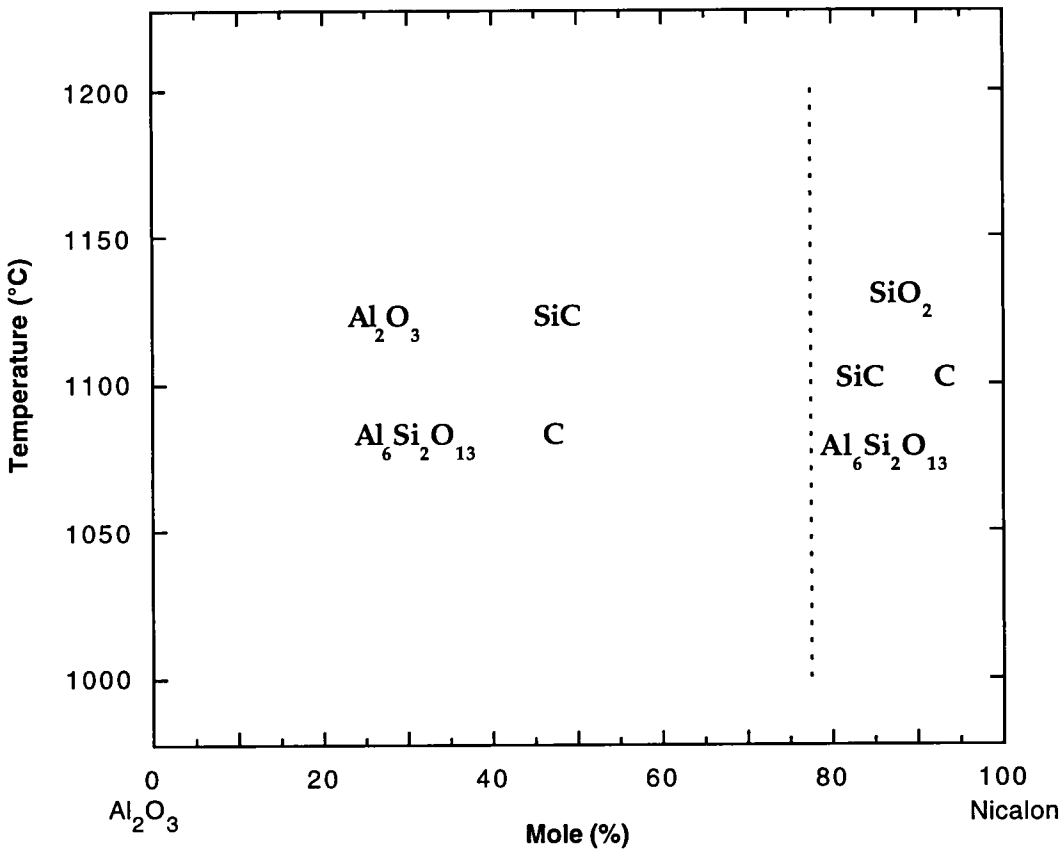


Fig. B.4.2. Computed Al_2O_3/Nicalon phase diagram for the temperature range of 1000-1200°C

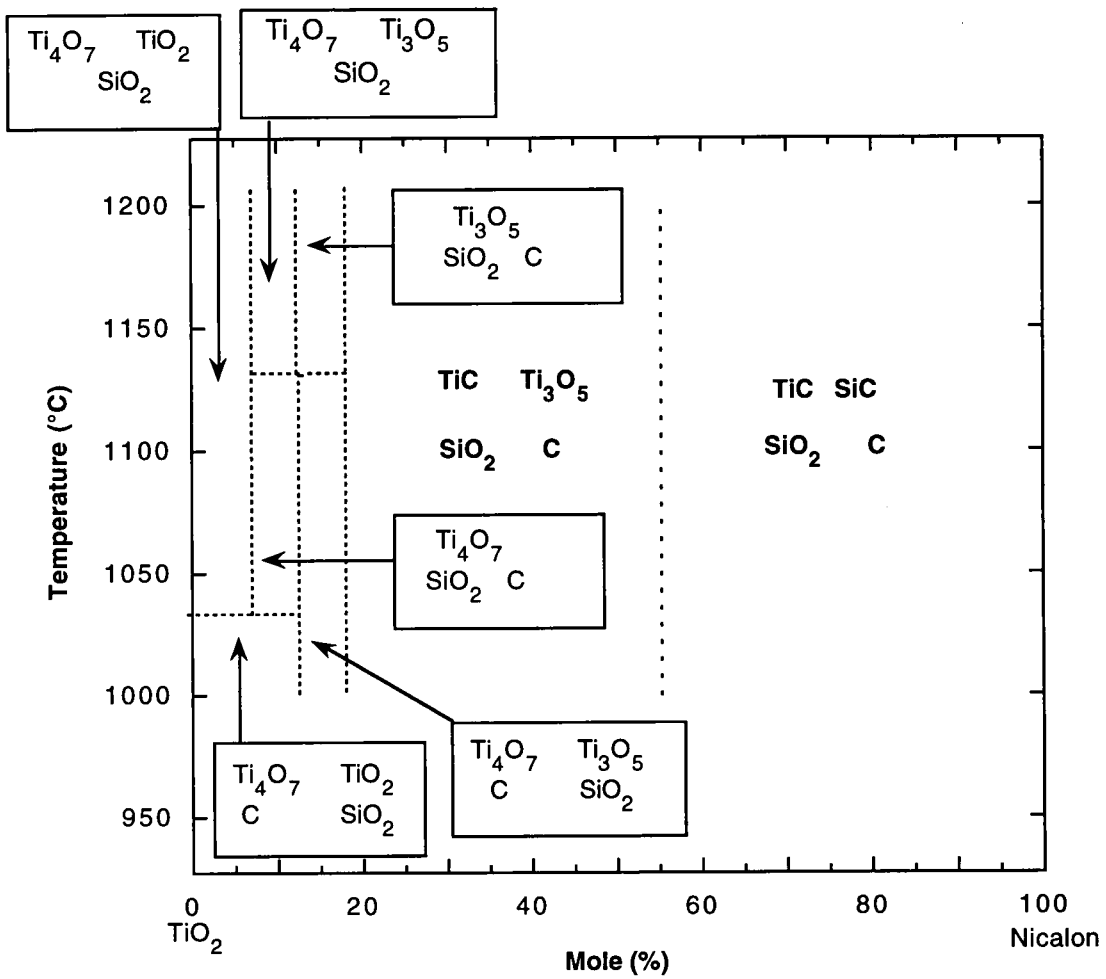


Fig. B.4.3. Computed TiO_2/Nicalon phase diagram for the temperature range of 1000-1200°C

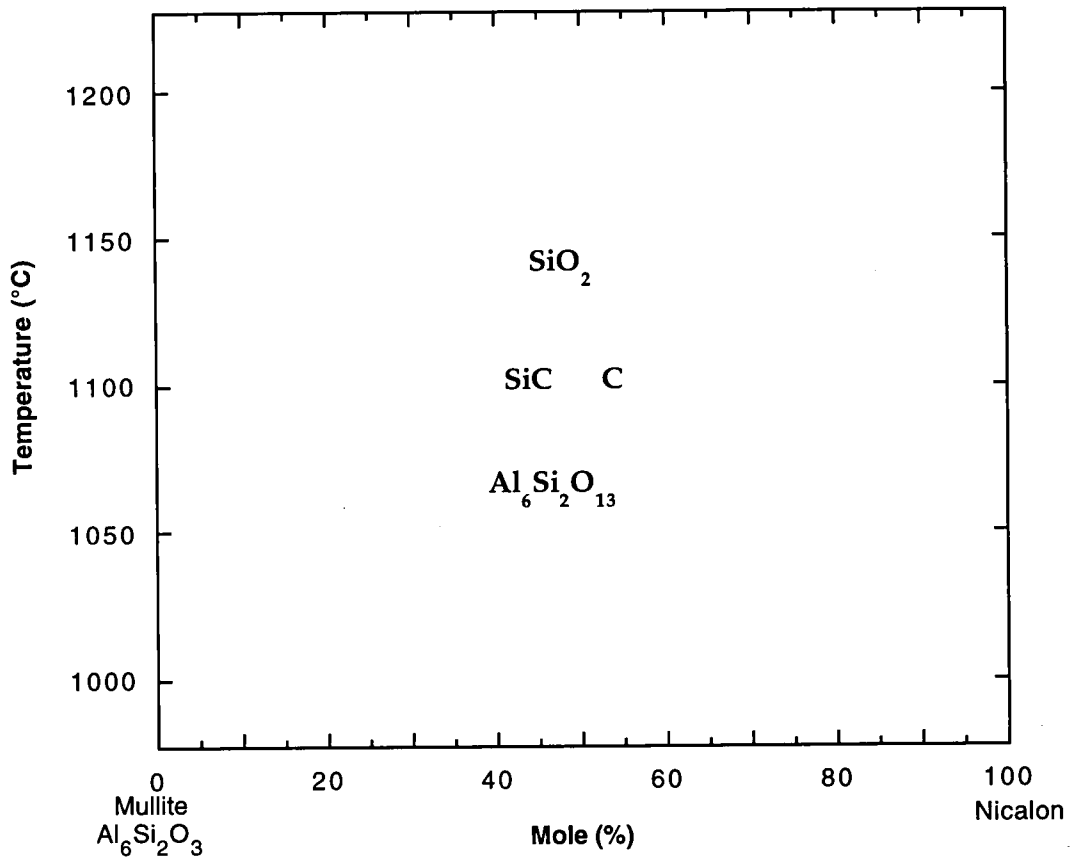


Fig. B.4.4. Computed mullite/Nicalon phase diagram for the temperature range of 1000-1200°C

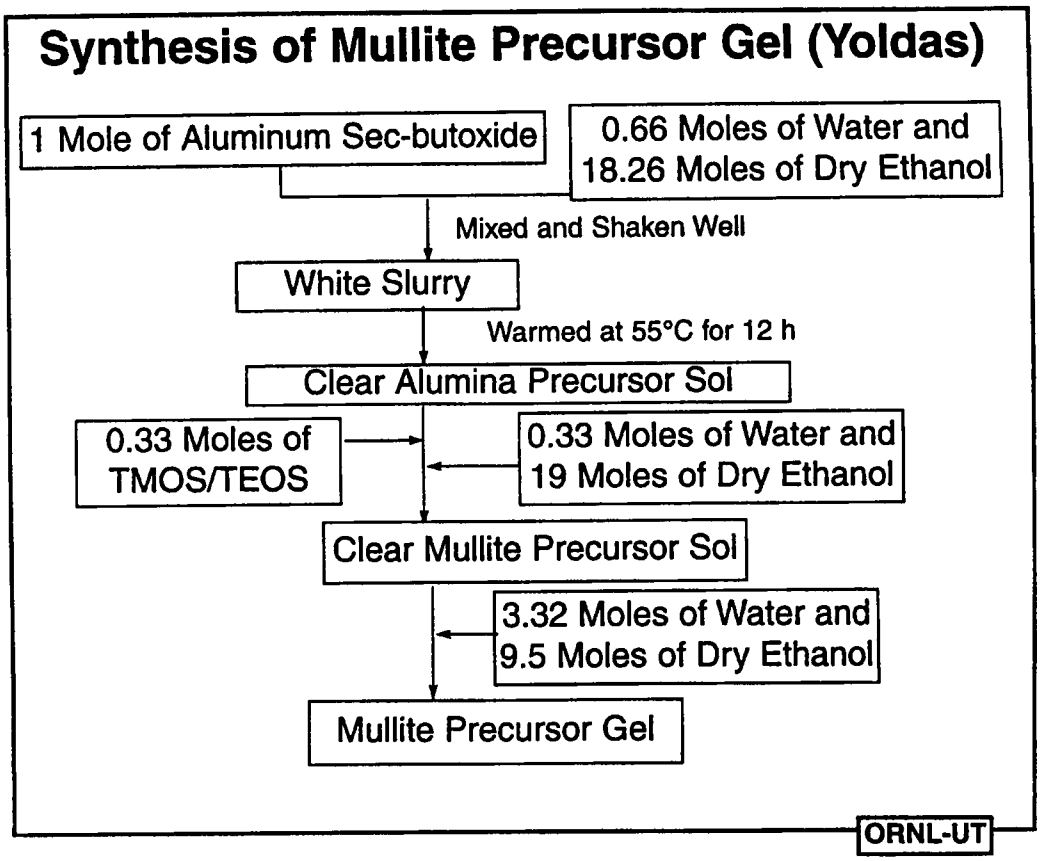


Fig. B.5.1. Flow diagram of the synthesis of mullite precursor gel using Yoldas' method

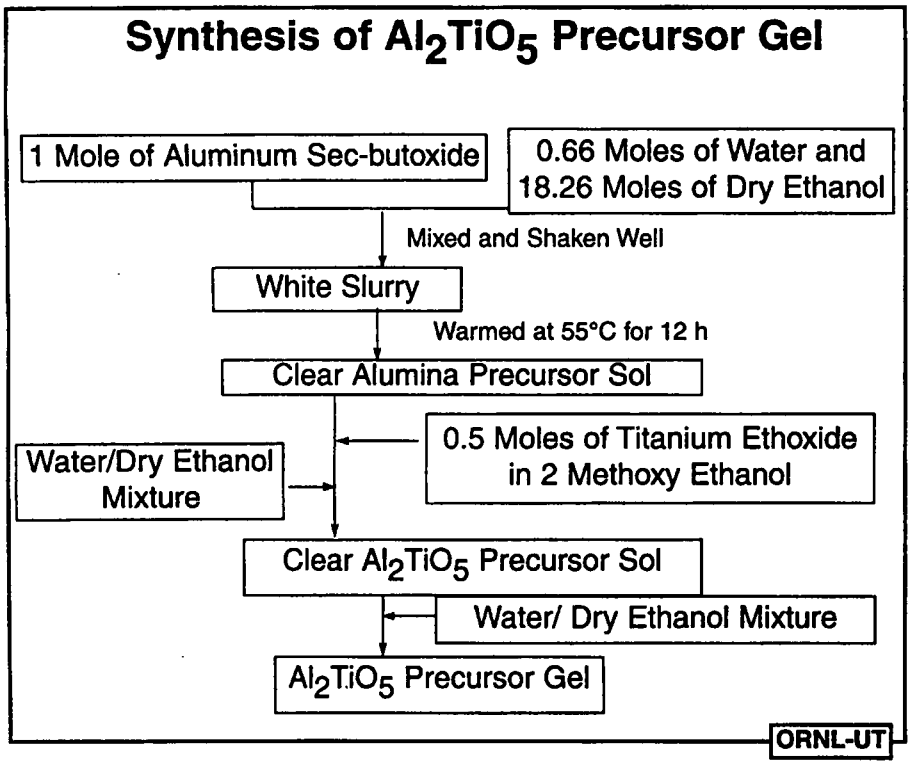


Fig. B.5.2. Flow diagram of the synthesis of an aluminum titanate precursor gel

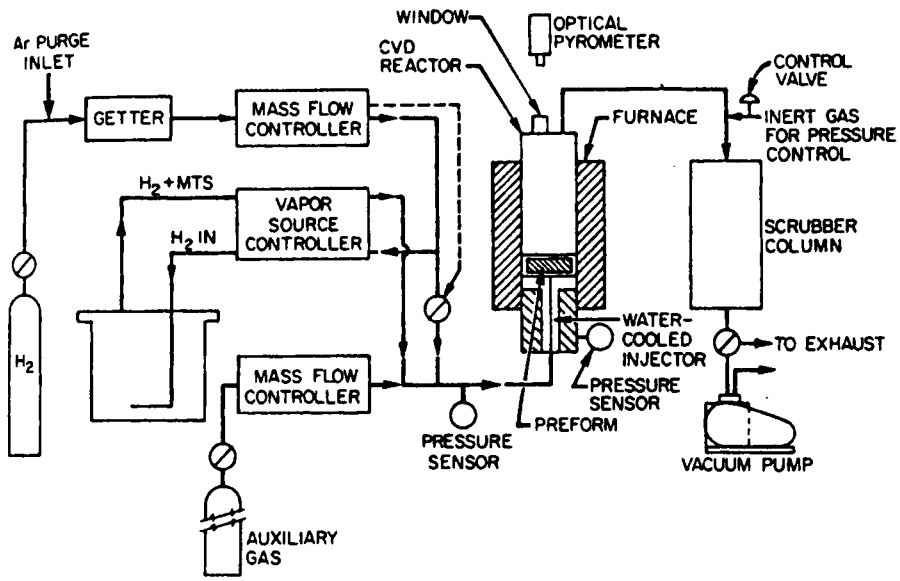


Fig. B.5.3. Schematic of a FCVI system

SOURCE R. A. Lowden, T. M. Besmann, and D. P. Stinton, "Ceramic Matrix Composites Fabrication and Processing: Chemical Vapor Infiltration," pp. 205-268 in Handbook on Continuous Fiber-Reinforced Ceramic Matrix Composites, Edited by R. L. Lehman, S. K. El-Rahaiby, and J. B. Wachtman, The American Ceramic Society, Ohio, December 1995.

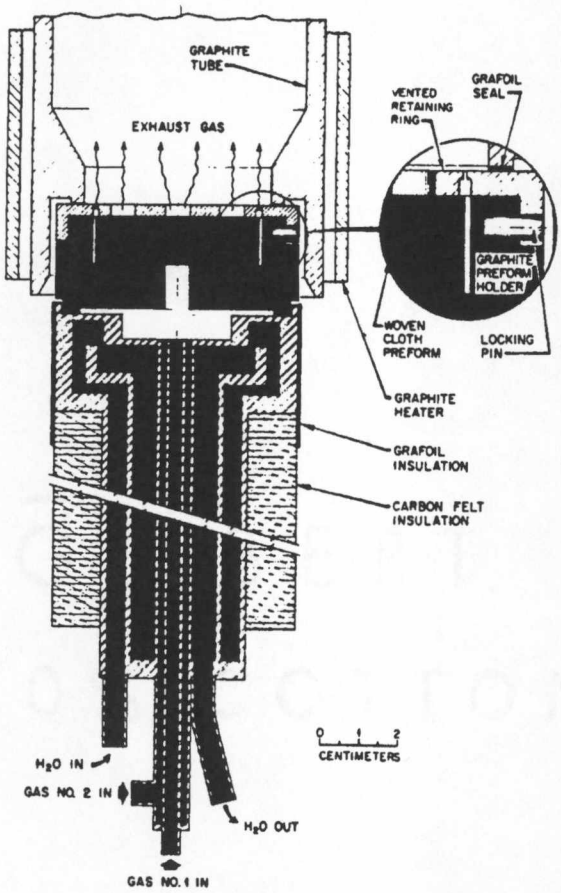


Fig. B.5.4. Schematic of the furnace used to densify fibrous preforms by the FCVI process

SOURCE R. A. Lowden, T. M. Besmann, and D. P. Stinton, "Ceramic Matrix Composites Fabrication and Processing: Chemical Vapor Infiltration," pp. 205-268 in Handbook on Continuous Fiber-Reinforced Ceramic Matrix Composites, Edited by R. L. Lehman, S. K. El-Rahaiby, and J. B. Wachtman, The American Ceramic Society, Ohio, December 1995.

Density of the fiber = rf
Density of carbon = rc
Density of oxide = ro

Diameter of the fiber = df
Diameter of the fiber + inner carbon coating = dc
Diameter of the fiber + inner carbon coating + oxide coating = do
Diameter of the fiber + inner carbon coating + oxide coating + outer carbon coating = dc2

Weight of the graphite holder = W1
Weight of the graphite holder + fiber preform = W2
(The fiber preform loses some weight during carbon coating due to removal of the sizing from the fiber)
W2 + weight of the inner carbon coating = W3
W3 + weight of the oxide coating after heat treament at 1050°C = W4
W4 + weight of the outer carbon coating = W5
Weight of the oxide coating = W6 = W4 - W3
Weight of the outer carbon coating = W7 = W5 - W4
Assume weight of the inner carbon coating = W8 = Weight of the outer carbon coating
Actual weight of the fiber preform = W9 = W3 - W8

Length of the fiber (cm) = $l = W9*4/(3.14*rf*df^2*10^{-8})$
$dc = \{[W8*4*108/(3.14*l*rc)] + df^2\}^{0.5}$
Inner carbon coating thickness = (dc-df)/2
$do = \{[W6*4*108/(3.14*l*ro)] + dc^2\}^{0.5}$
Oxide coating thickness = (do-dc)/2
$dc2 = \{[W7*4*108/(3.14*l*rc)] + do^2\}^{0.5}$
Outer carbon coating thickness = (dc-do)/2

Fig. B.5.5. Procedure for calculating the interface coating thickness

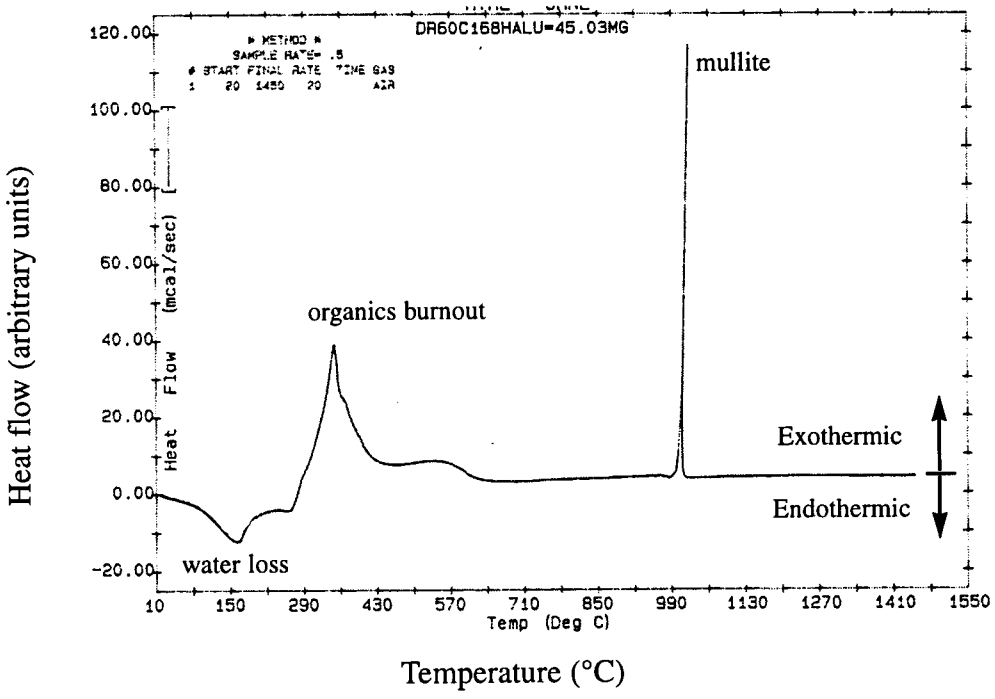


Fig. B.6.1. DSC curve of the powder obtained from the mullite precursor gel (MI) using the ASB-TMOS combination showing a mullite crystallization event around 990°C

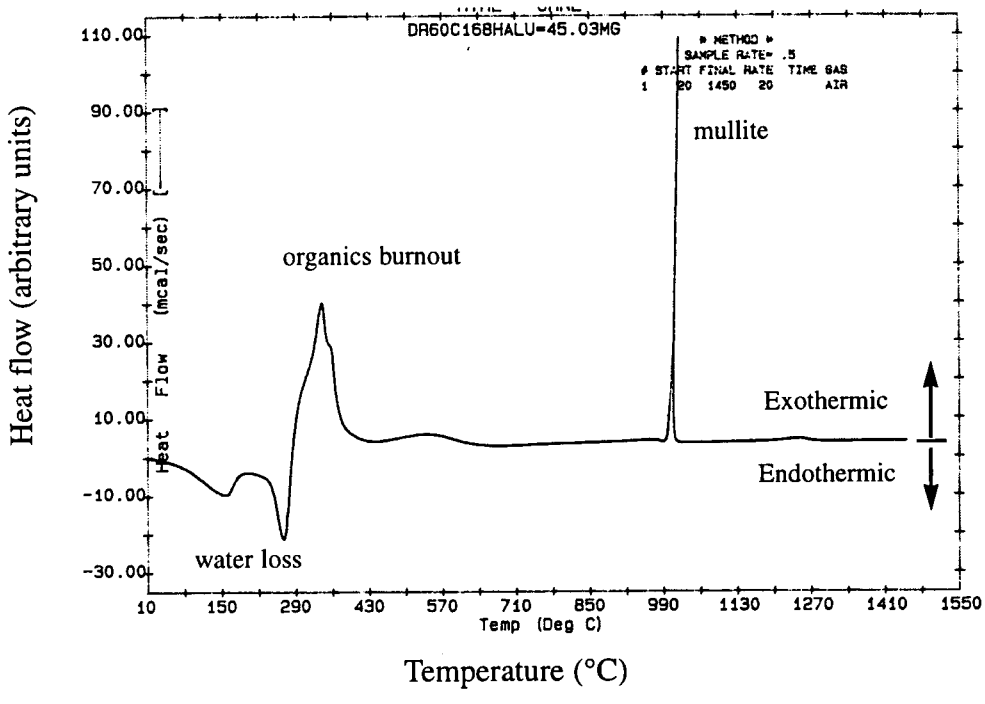


Fig. B.6.2. DSC curve of the powder obtained from the mullite precursor gel (MII) using the ASB-TEOS combination showing a mullite crystallization event around 990°C

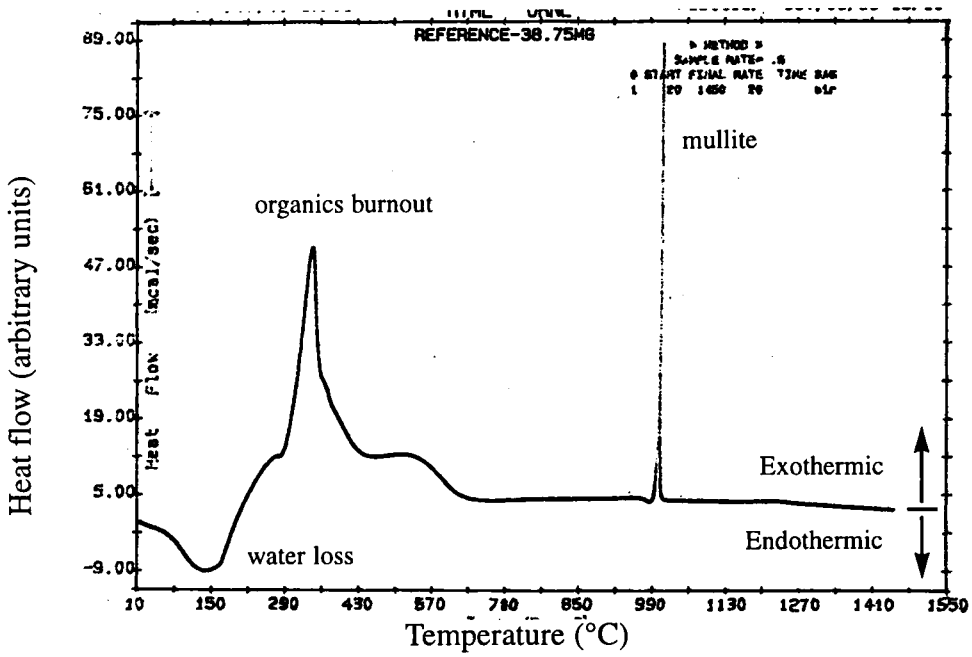


Fig. B.6.3. DSC curve of the powder obtained from the EI mullite precursor gel showing a sharp exothermic event around 990°C suggesting mullite crystallization

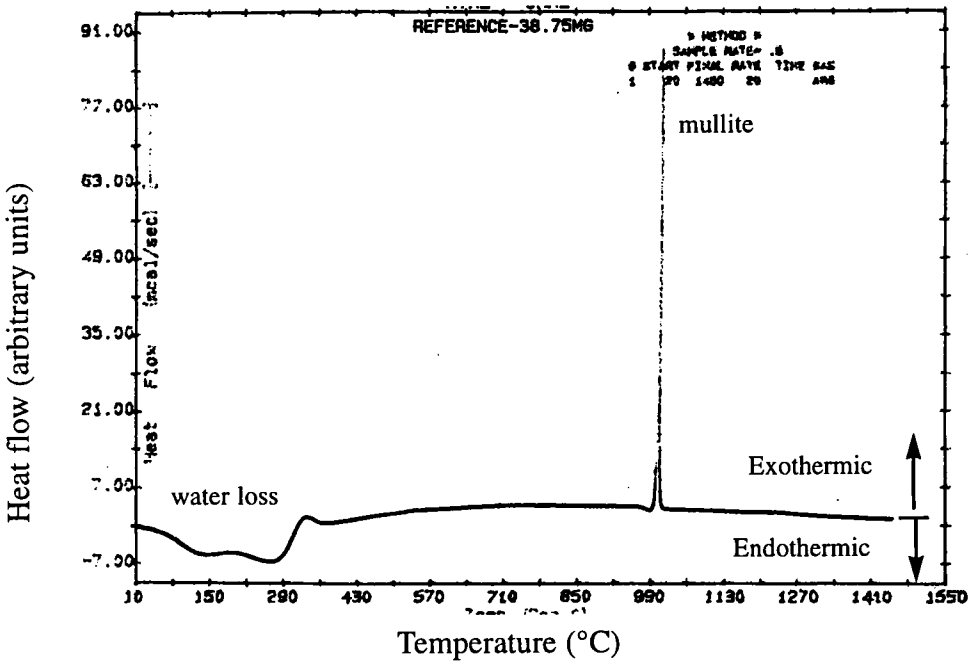


Fig. B.6.4. DSC curve of the powder obtained from the EI mullite precursor gel in argon showing a sharp exothermic peak around 990°C indicating mullite crystallization

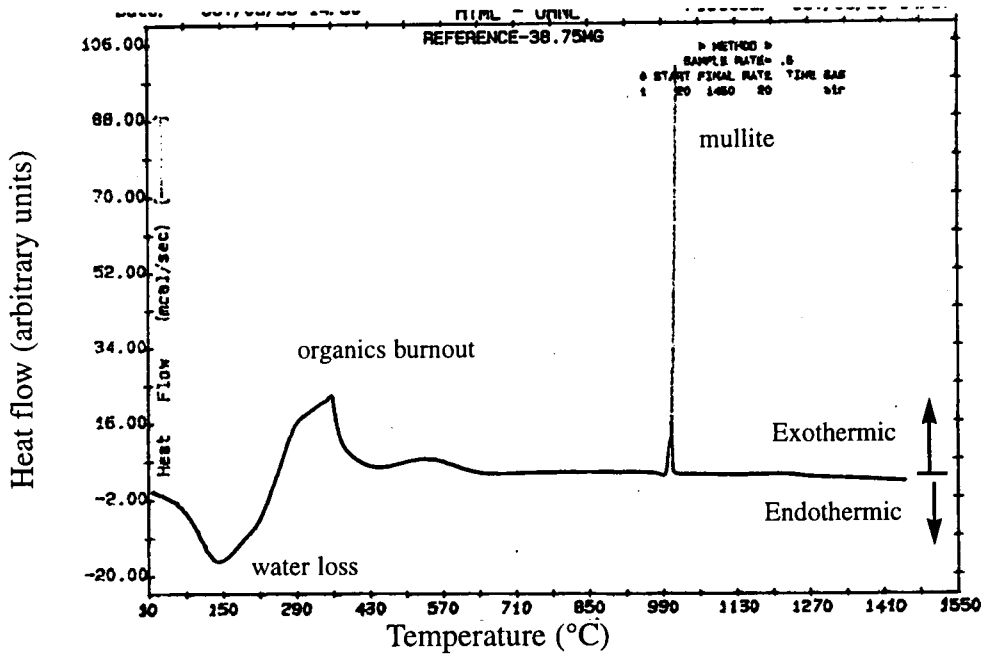


Fig. B.6.5. DSC curve of the powder obtained from the MEI mullite precursor gel in air showing a sharp exothermic event around 990°C indicating mullite crystallization

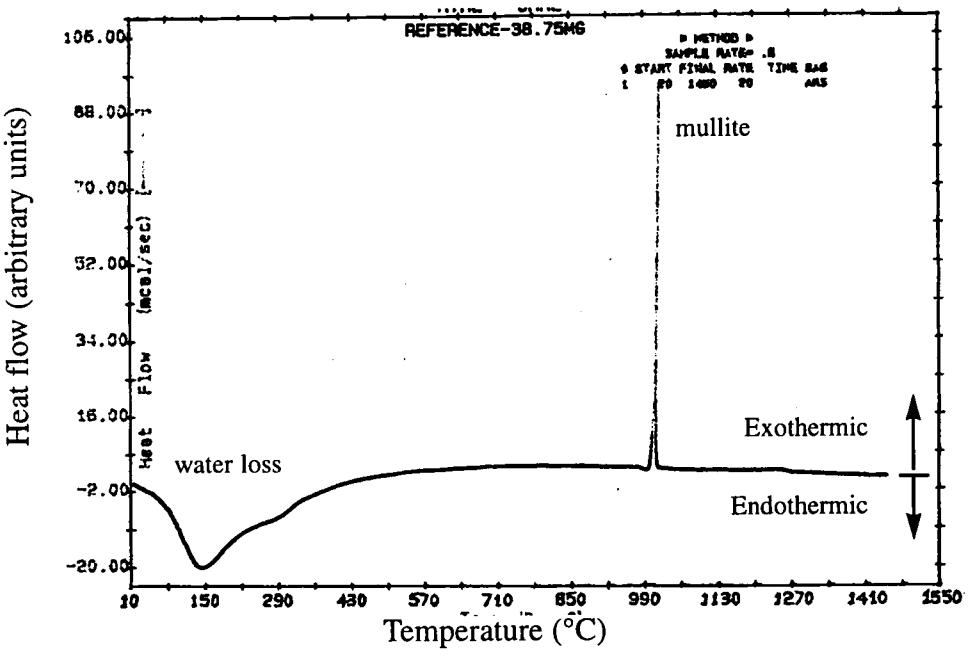


Fig. B.6.6. DSC curve of the powder obtained from the MEI mullite precursor gel in argon showing an exothermic peak around 990°C suggesting mullite crystallization

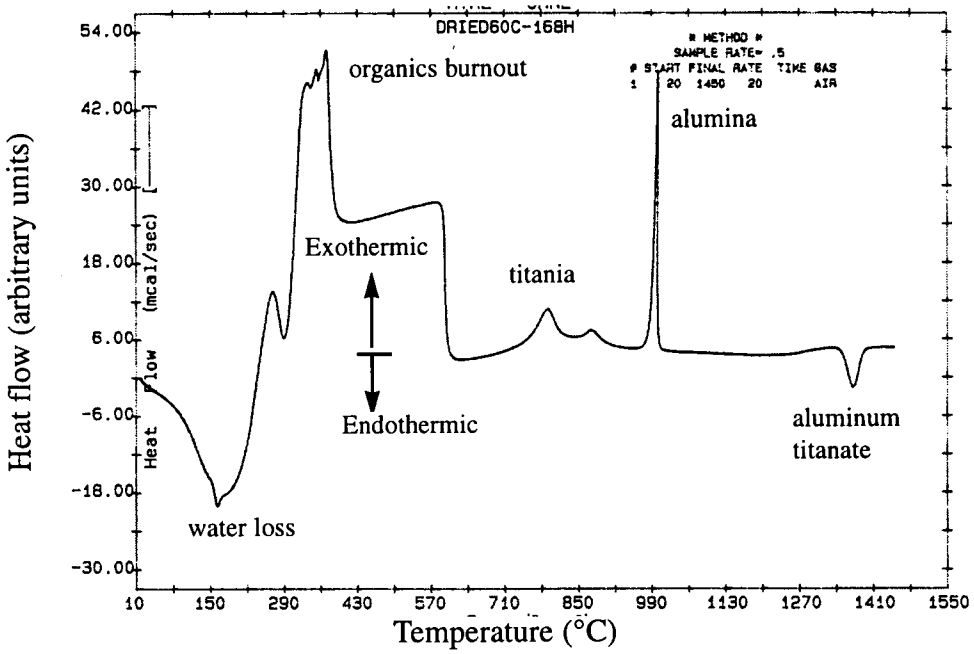


Fig. B.6.7. DSC curve of ATI aluminum titanate precursor gel derived powder indicating aluminum titanate formation around 1360°C

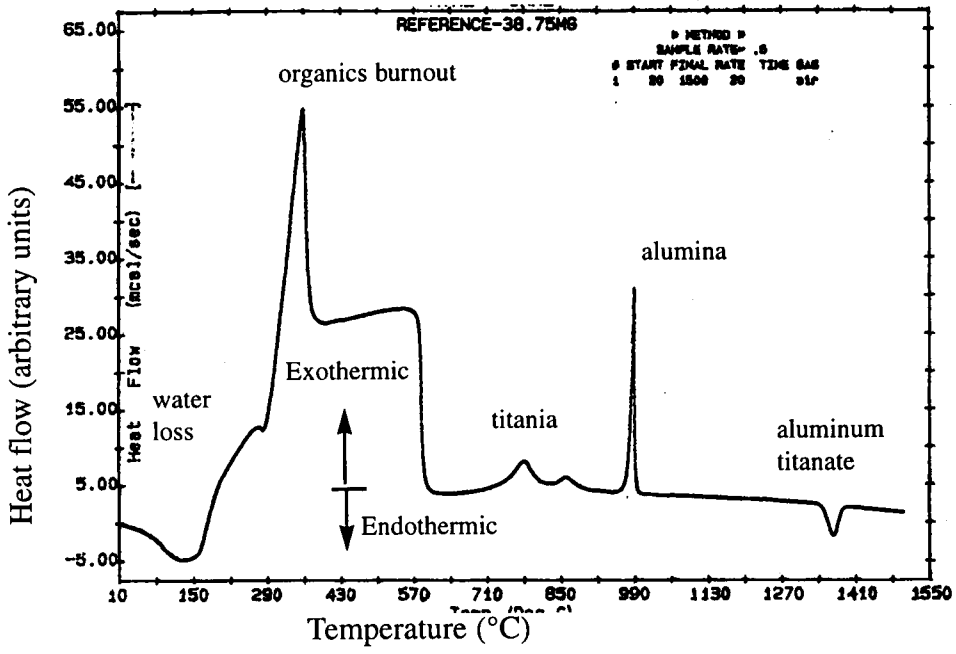


Fig. B.6.8. DSC curve of ATII aluminum titanate precursor gel derived powder in air indicating the aluminum titanate formation event occurring around 1370°C

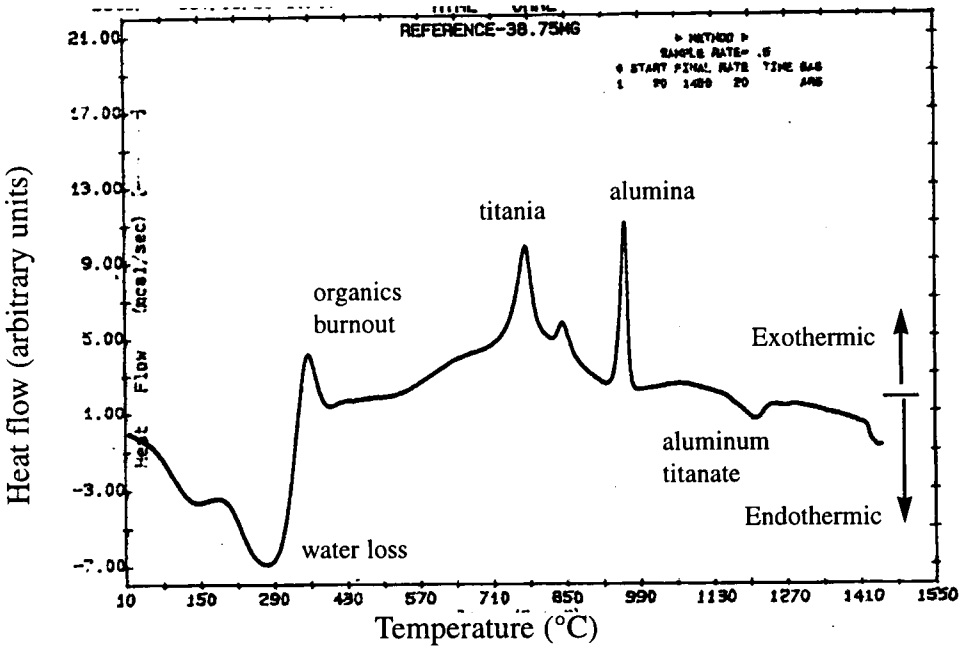
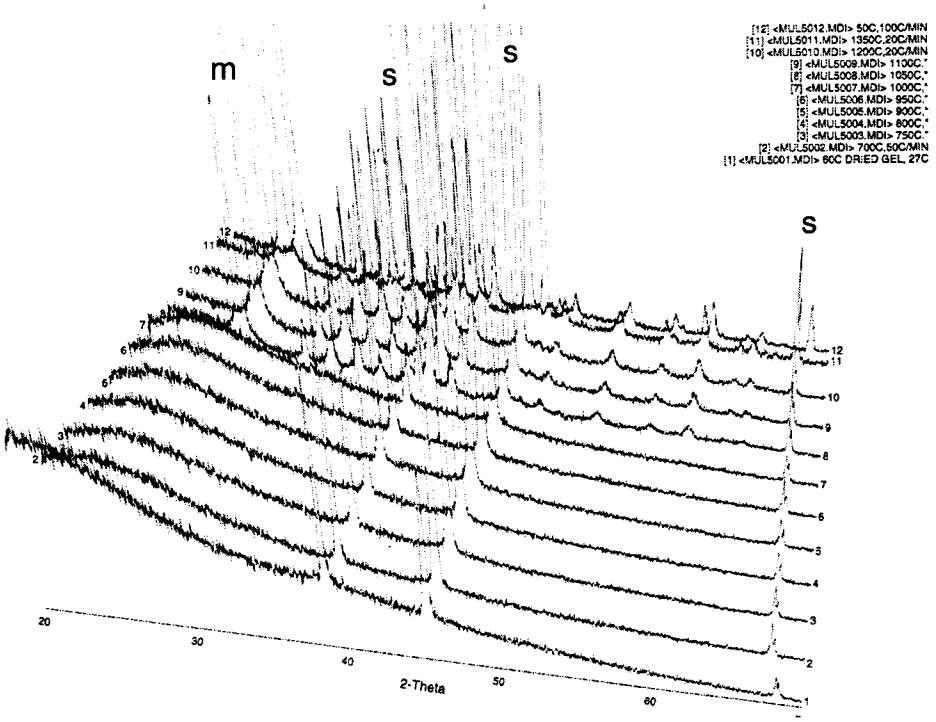
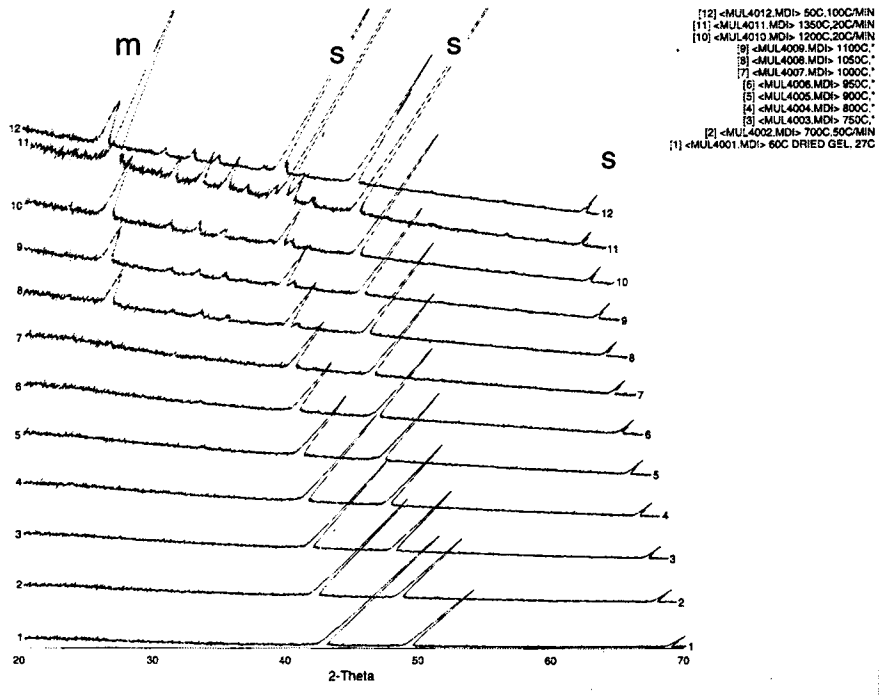


Fig. B.6.9. DSC curve of ATII aluminum titanate precursor gel derived powder in argon indicating the aluminum titanate formation event taking place around 1200°C



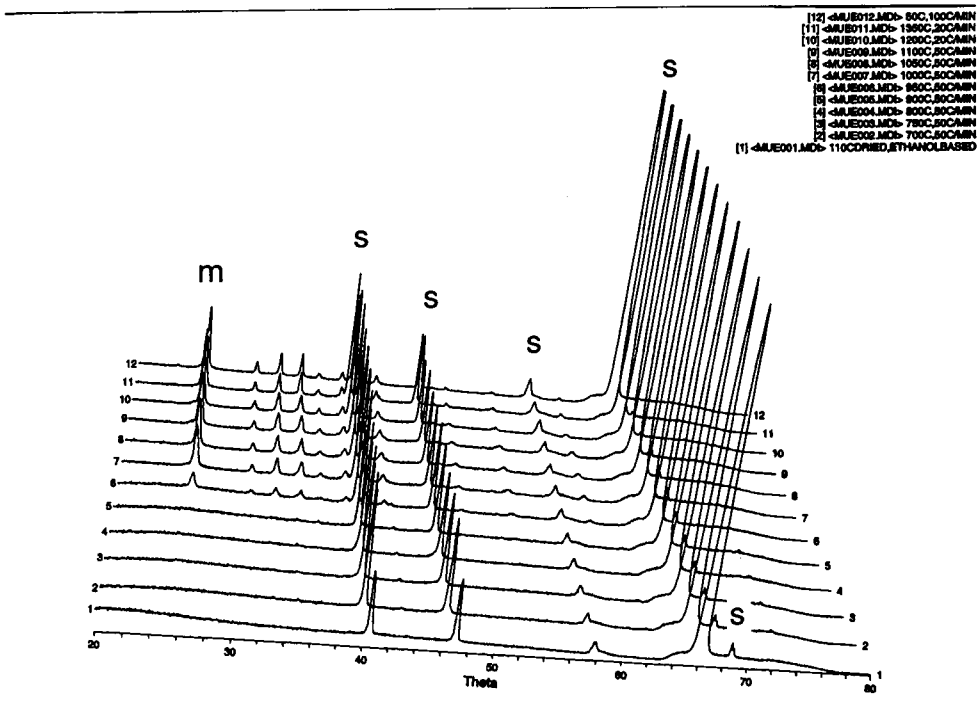
s - substrate peaks
m - mullite major peak

Fig. B.6.10. High temperature XRD patterns indicating that mullite crystallization occurrs at 1050°C from the MI mullite precursor gel derived powder



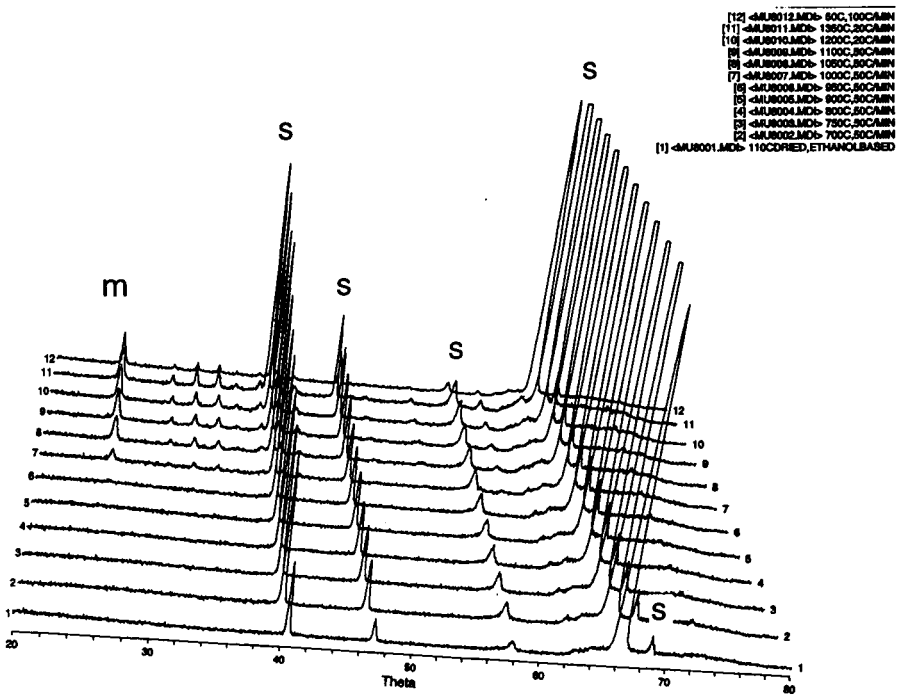
s - substrate peaks
m - mullite major peak

Fig. B.6.11. High temperature XRD patterns showing that mullite crystallization takes place at 1050°C from the MII mullite precursor gel



s - substrate peaks
m - mullite major peak

Fig. B.6.12 High temperature XRD patterns in air showing that mullite crystallization takes place at 950°C from the EI mullite precursor gel derived powder



s - substrate peaks
m - mullite major peak

Fig. B.6.13. High temperature XRD patterns indicating that mullite crystallization occurs at 1000°C in argon from the EI mullite precursor gel derived powder

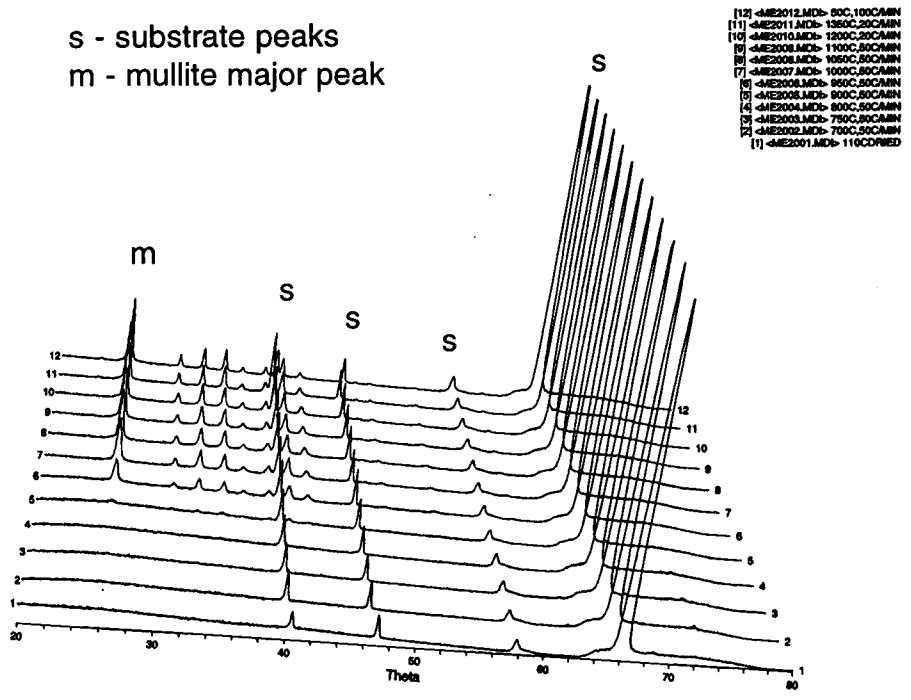


Fig. B.6.14. High temperature XRD patterns in air obtained from MEI mullite precursor gel derived powder showing that mullite crystallization occurs at 950°C

s - substrate peaks
m - mullite major peak

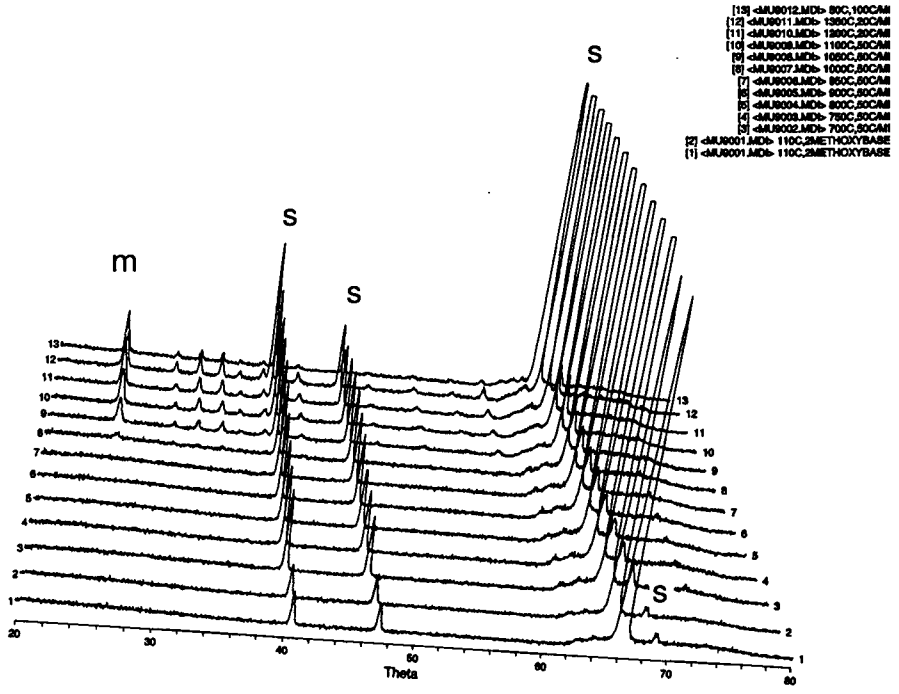


Fig. B.6.15. High temperature XRD patterns obtained in argon from MEI mullite precursor gel derived powder suggesting that mullite crystallization takes place at 1000°C

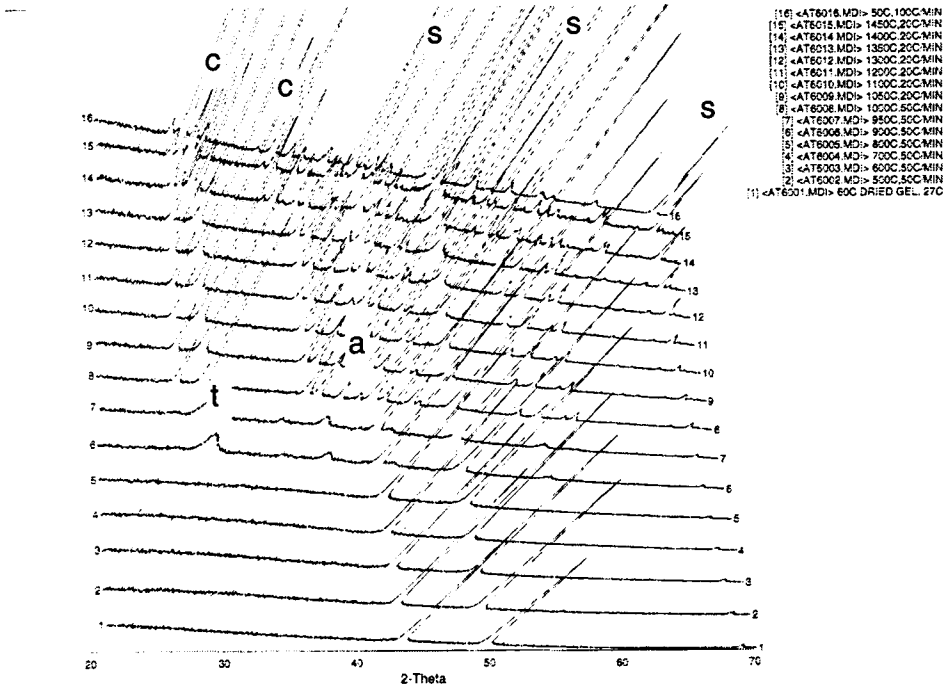
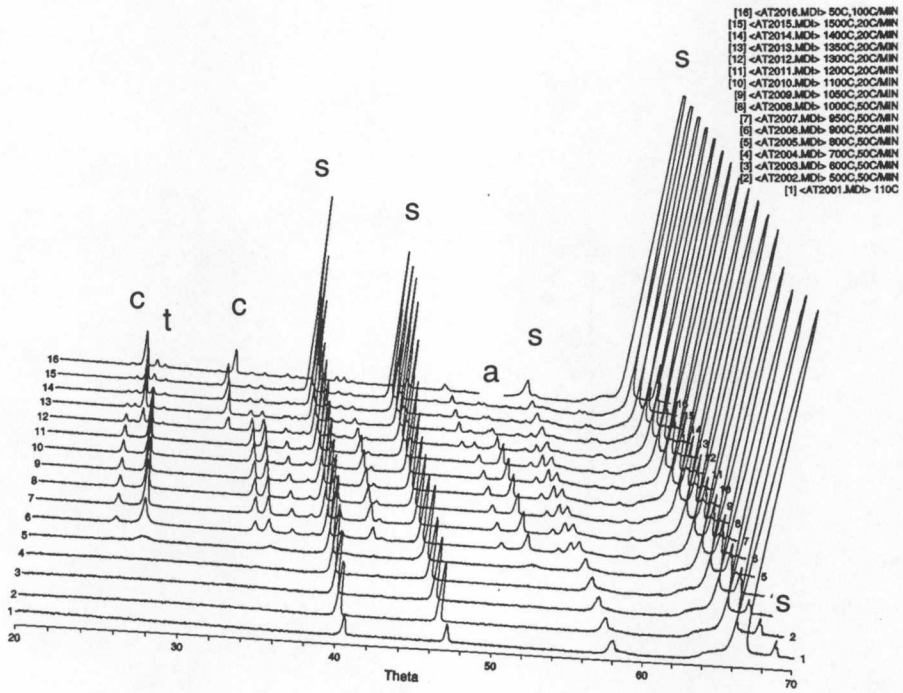


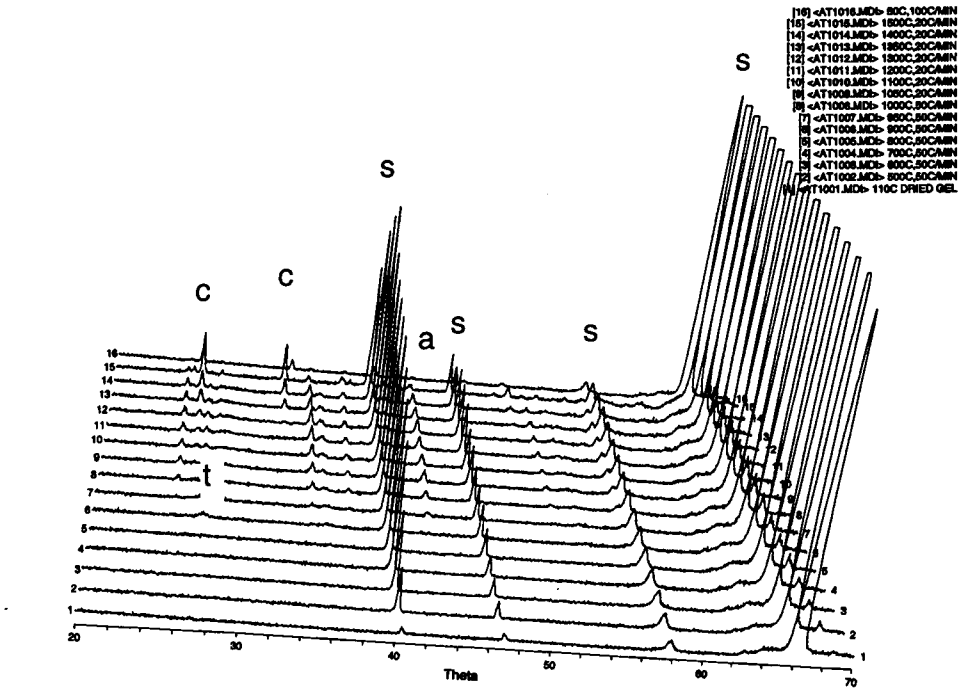
Fig. B.6.16. High temperature XRD patterns obtained in air from the ATI aluminum titanate precursor gel derived powder indicating that aluminum titanate forms at 1400°C



s - substrate peaks
Few selected peaks of
a - alumina
t - titania
c - aluminum titanate

Fig. B.6.17 High temperature XRD patterns obtained in air from the ATII aluminum titanate precursor gel derived powder indicating that aluminum titanate forms at 1300°C

100% COTTON



s - substrate peaks
Few selected peaks of
a - alumina
t - titania
c - aluminum titanate

Fig. B.6.18. High temperature XRD patterns obtained in argon from the ATII aluminum titanate precursor gel derived powder suggesting that aluminum titanate forms at 1200°C

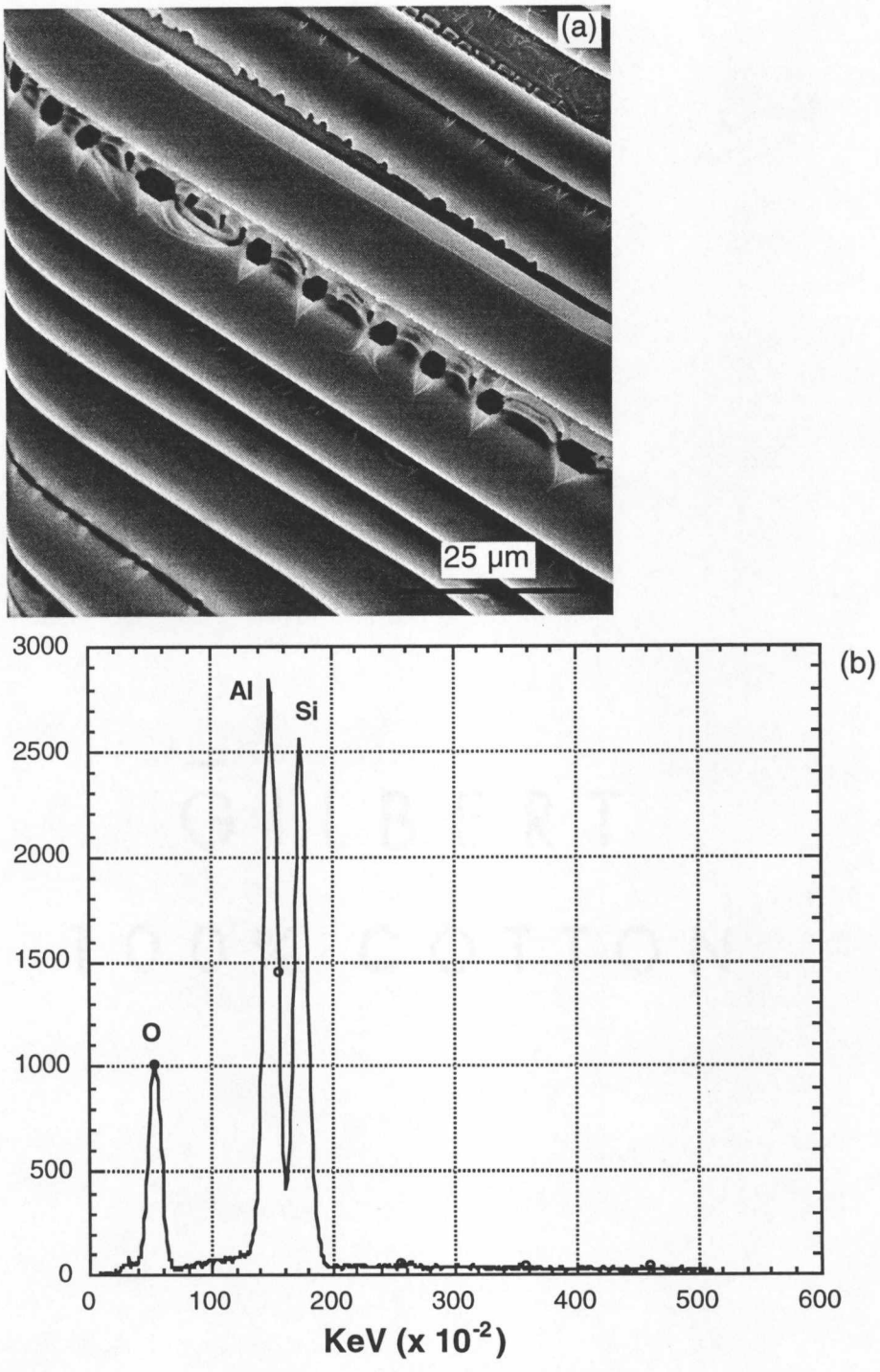


Fig. B.6.19. Mullite coating on a Nicalon tow heat-treated at 1000°C in air (a) A secondary electron image and (b) An EDX spectrum

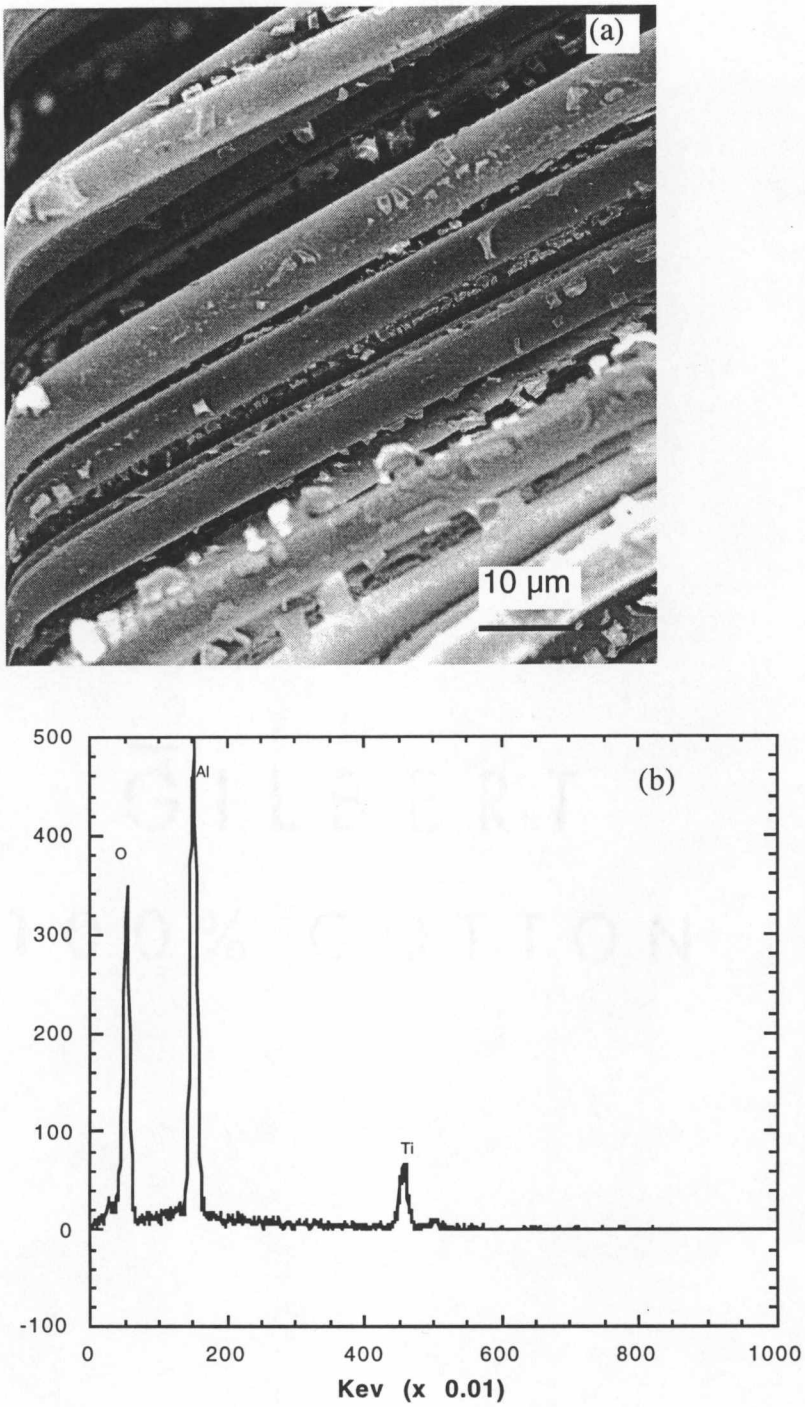


Fig. B.6.20. Alumina-titania coating on a Nicalon tow heat-treated at 1000°C (a) A secondary electron image and (b) An EDX spectrum

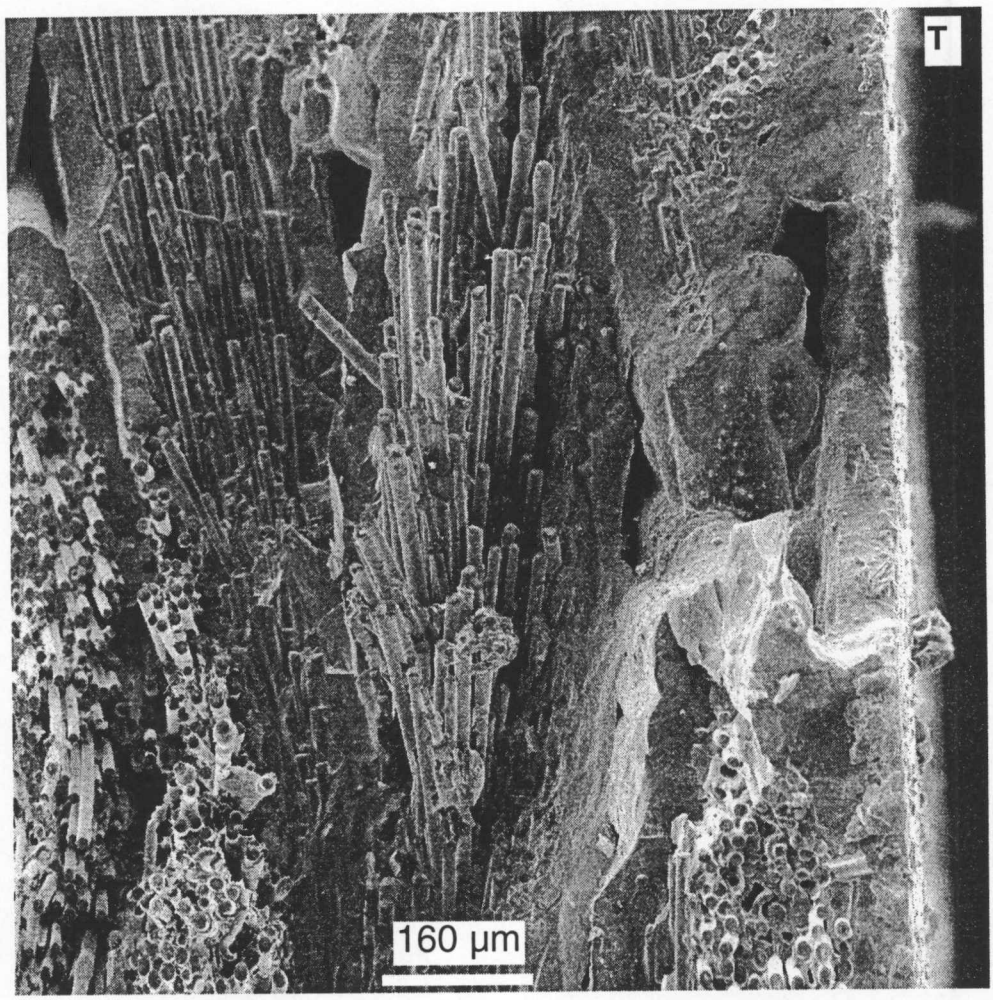


Fig. B.6.21 Tensile region of the fracture surface of a CVI 1077 composite (C interface) showing fiber pullout of the order of 300 µm in the as-processed condition

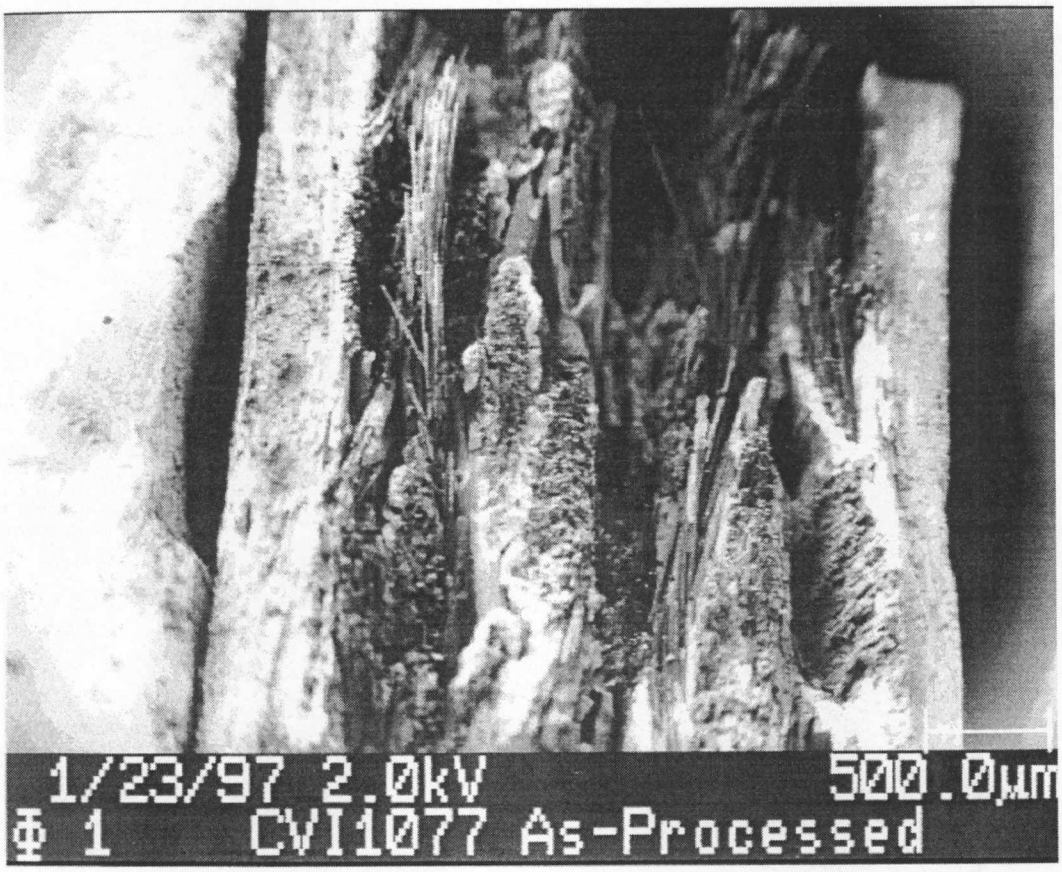


Fig. B.6.22. Fracture surface of an in-situ broken CVI 1077 composite in the as-processed condition

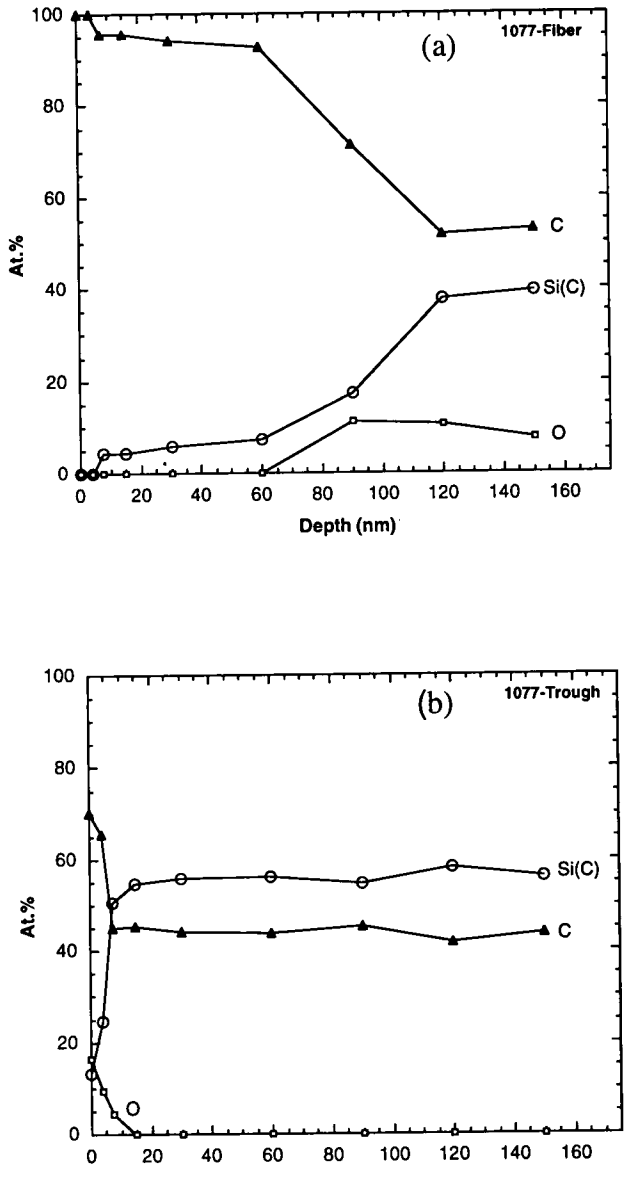


Fig. B.6.23. Compositional depth profiles obtained on a CVI 1077 composite in the as-processed condition (a) Fiber and (b) Trough

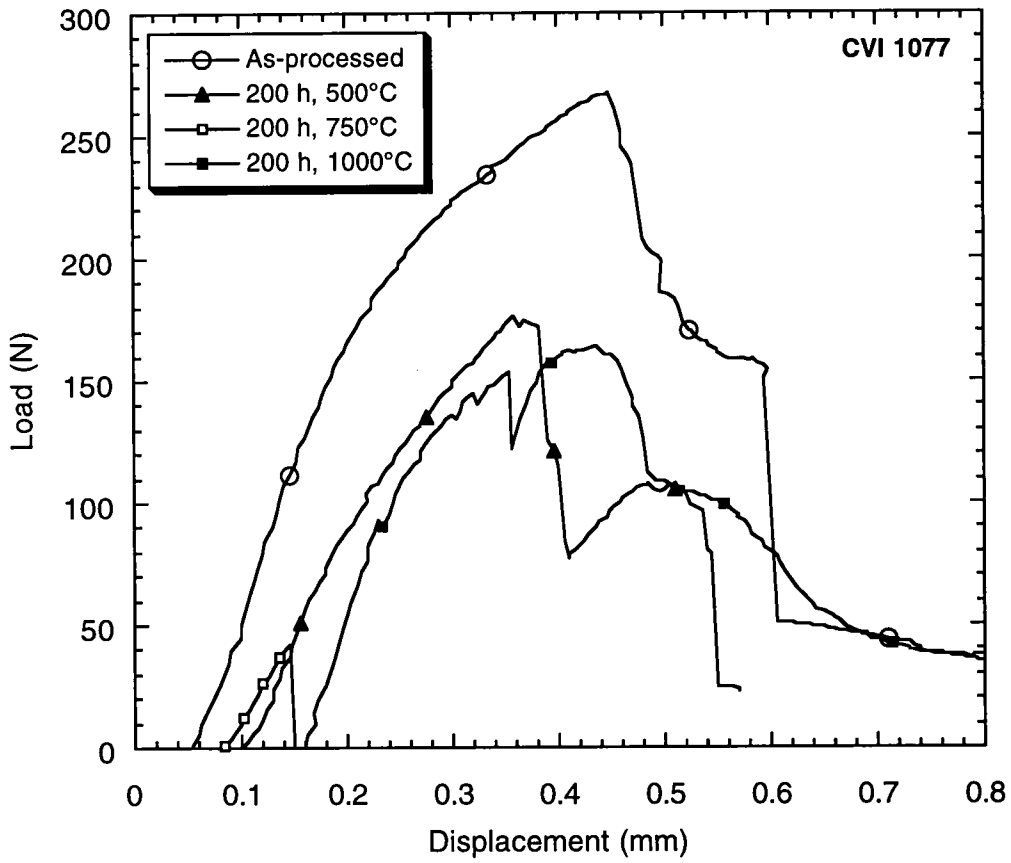


Fig. B.6.24. Representative load vs displacement curves for a CVI 1077 composite in the as-processed and oxidized conditions

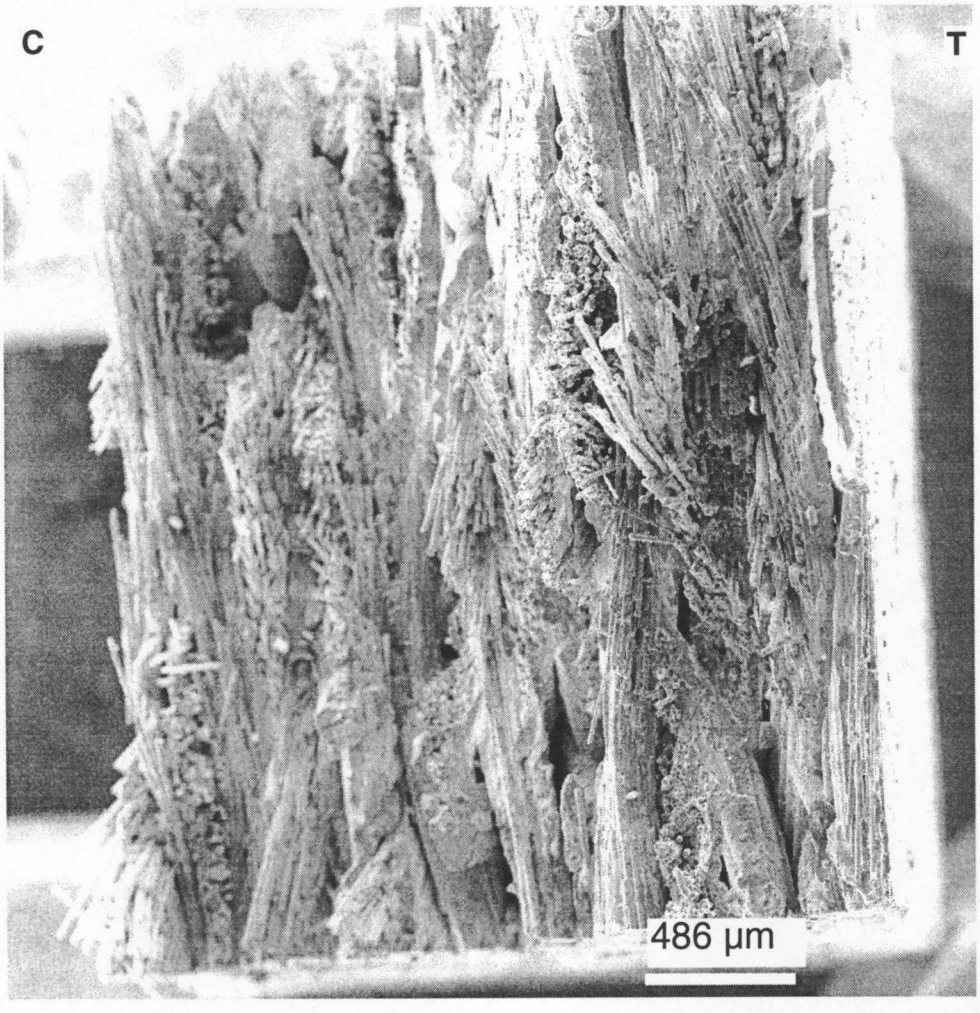


Fig. B.6.25. Fracture surface of a CVI 1077 composite after 200 h oxidation at 750°C

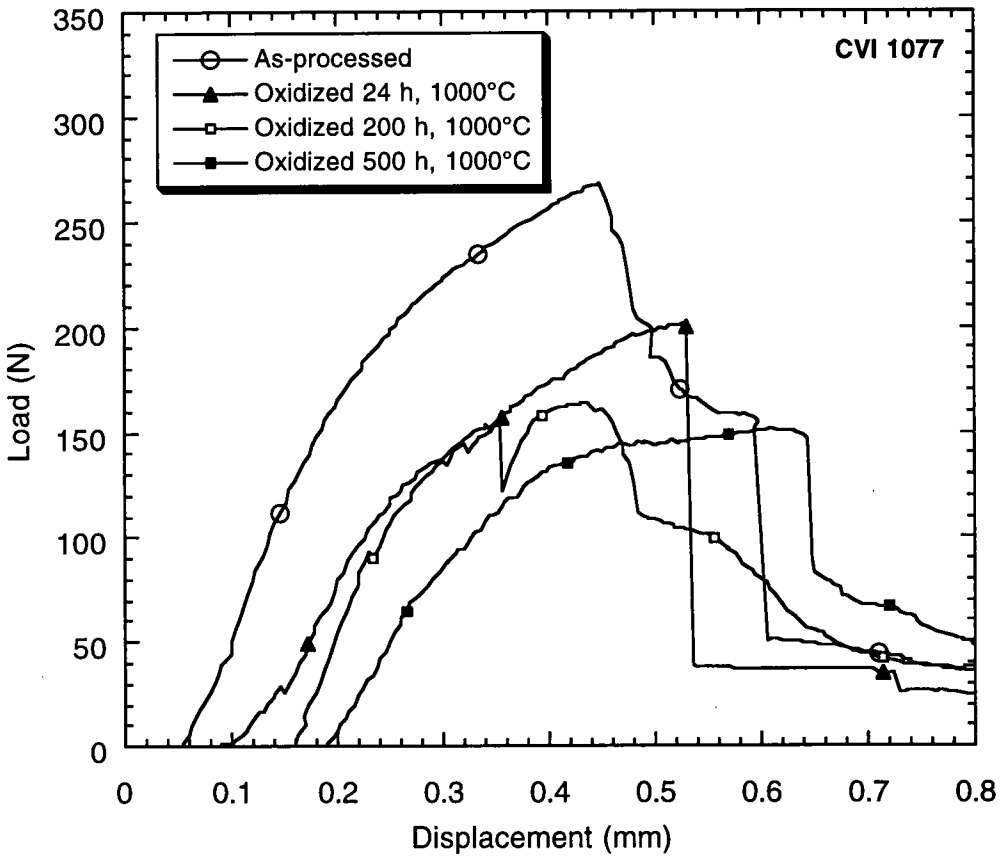


Fig. B.6.26. Representative load vs displacement curves of a CVI 1077 composite in the as-processed condition and after oxidation for up to 500 h at 1000°C

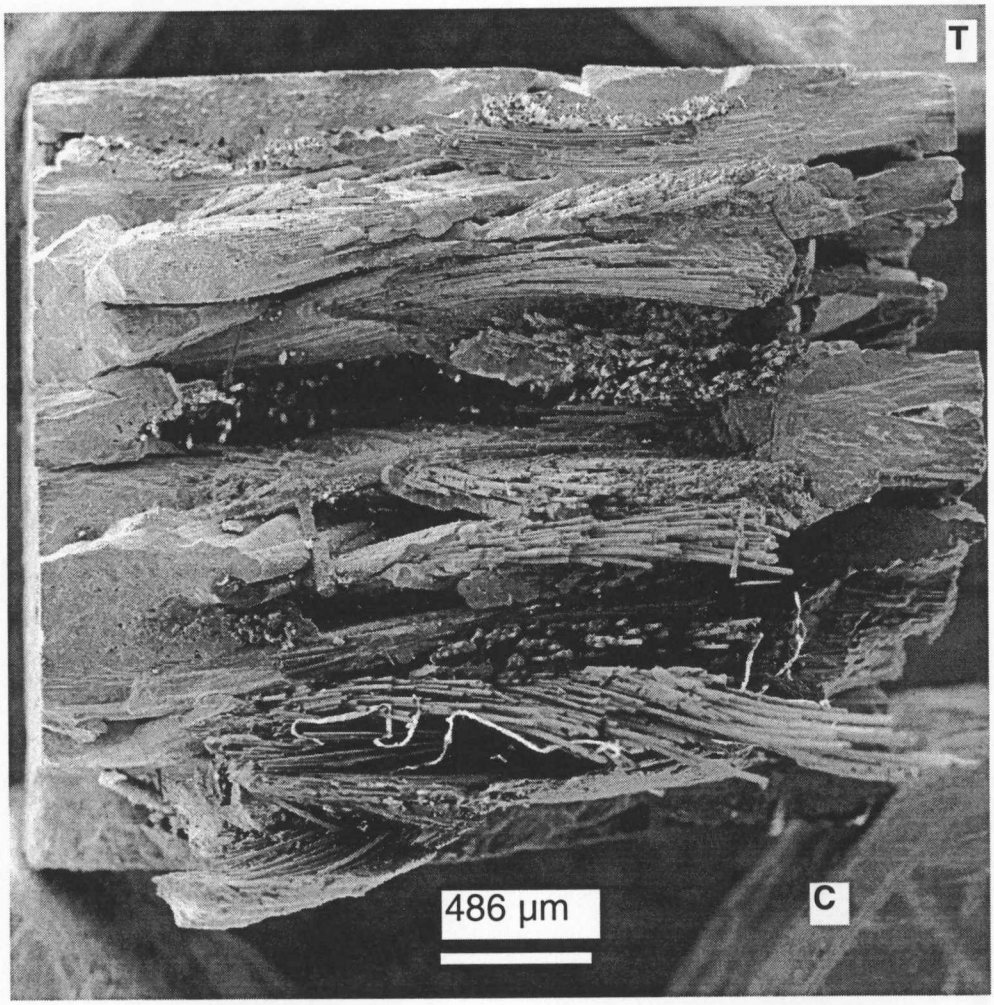


Fig. B.6.27. Fracture surface of a CVI 1077 composite after 500 h oxidation at 1000°C

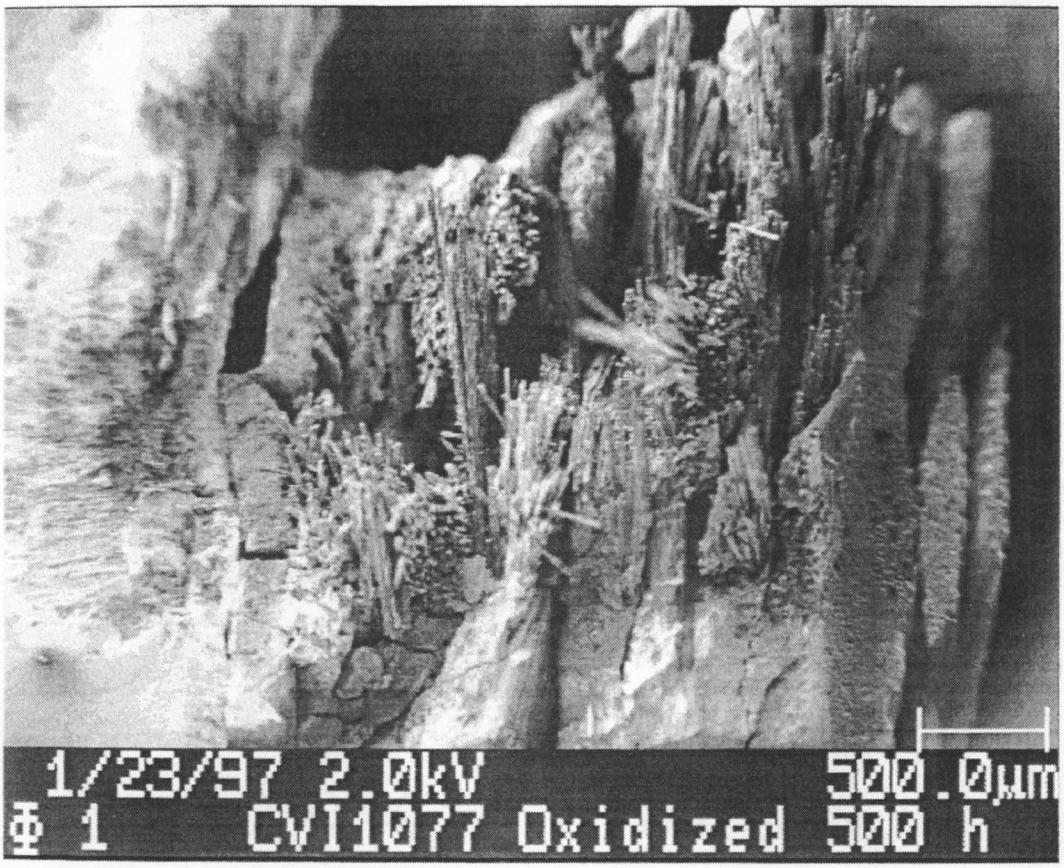


Fig. B.6.28. Fracture surface of an in-situ broken CVI 1077 sample oxidized for 500 h at 1000°C

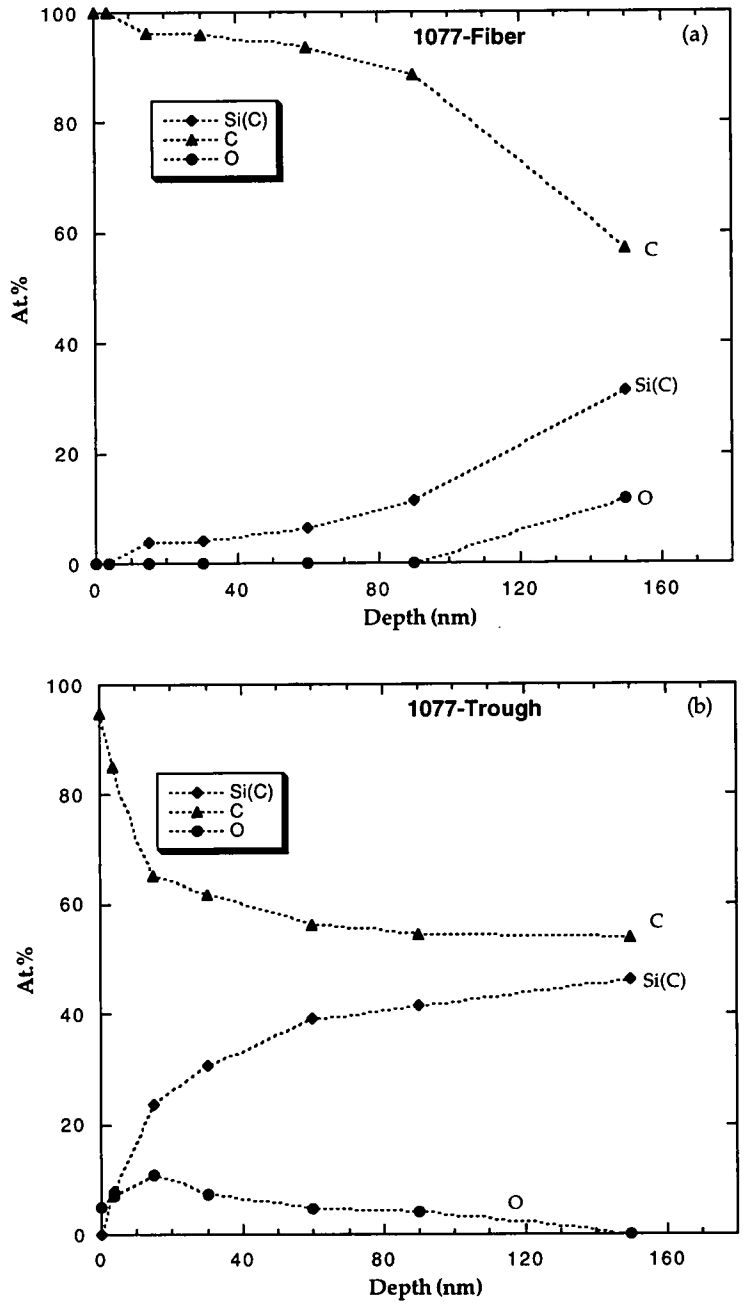


Fig. B.6.29. Compositional depth profiles obtained on a CVI 1077 composite after 500 h oxidation at 1000°C (a) Fiber and (b) Trough

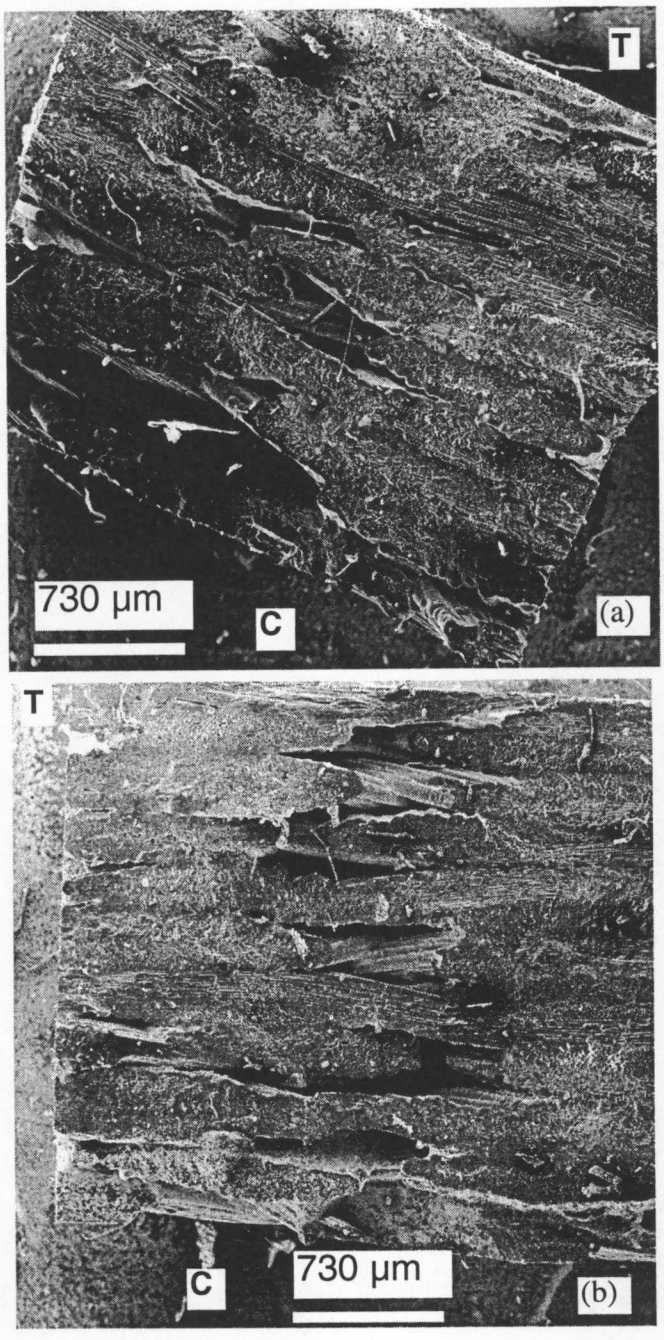


Fig. B.6.30. Fracture surface of a CVI 982 composite (mullite/C interface) (a) As-processed condition and (b) After 24 h oxidation at 1000°C

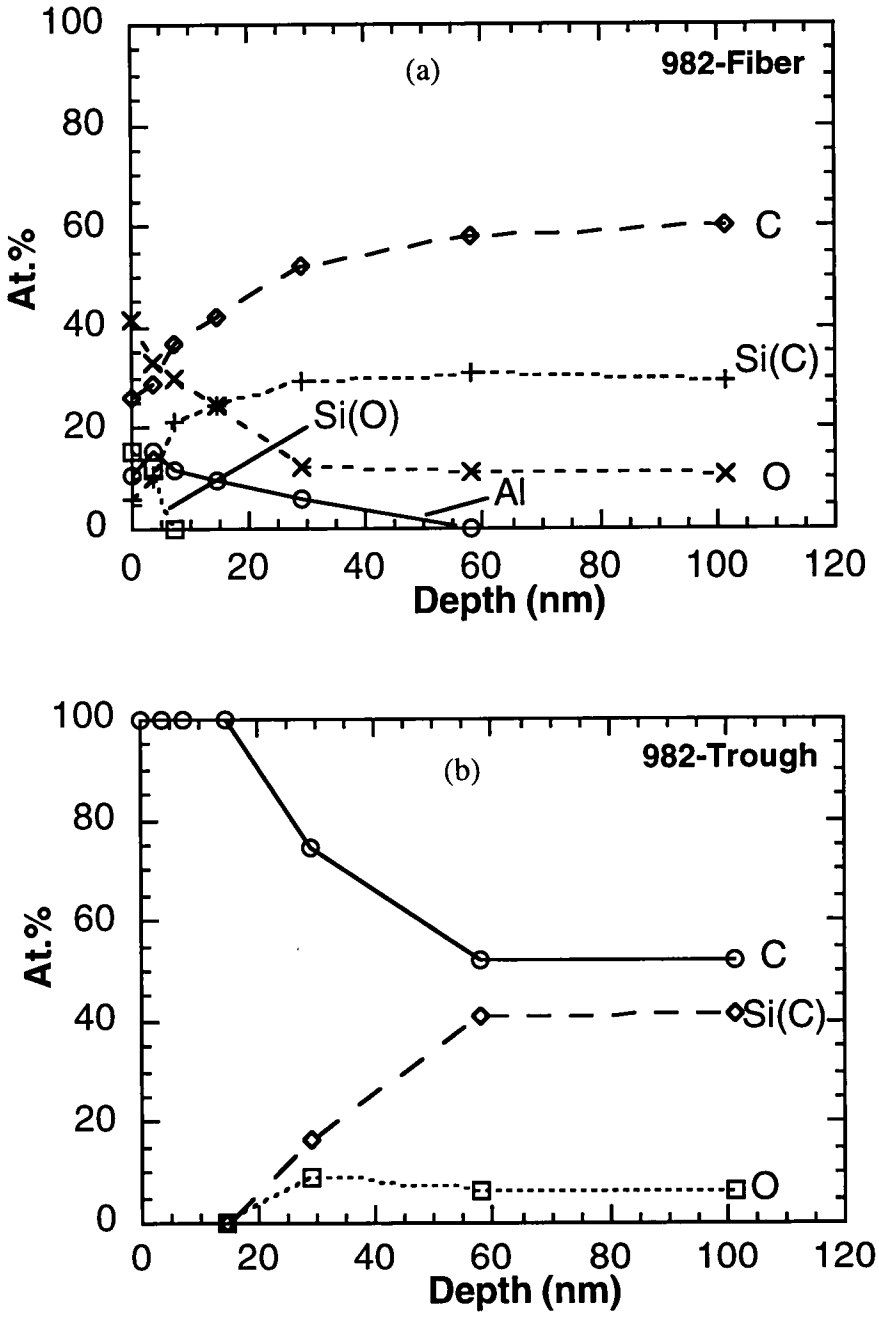


Fig. B.6.31. Compositional depth profiles obtained on a CVI 982 composite in the as-processed condition (a) Fiber and (b) Trough

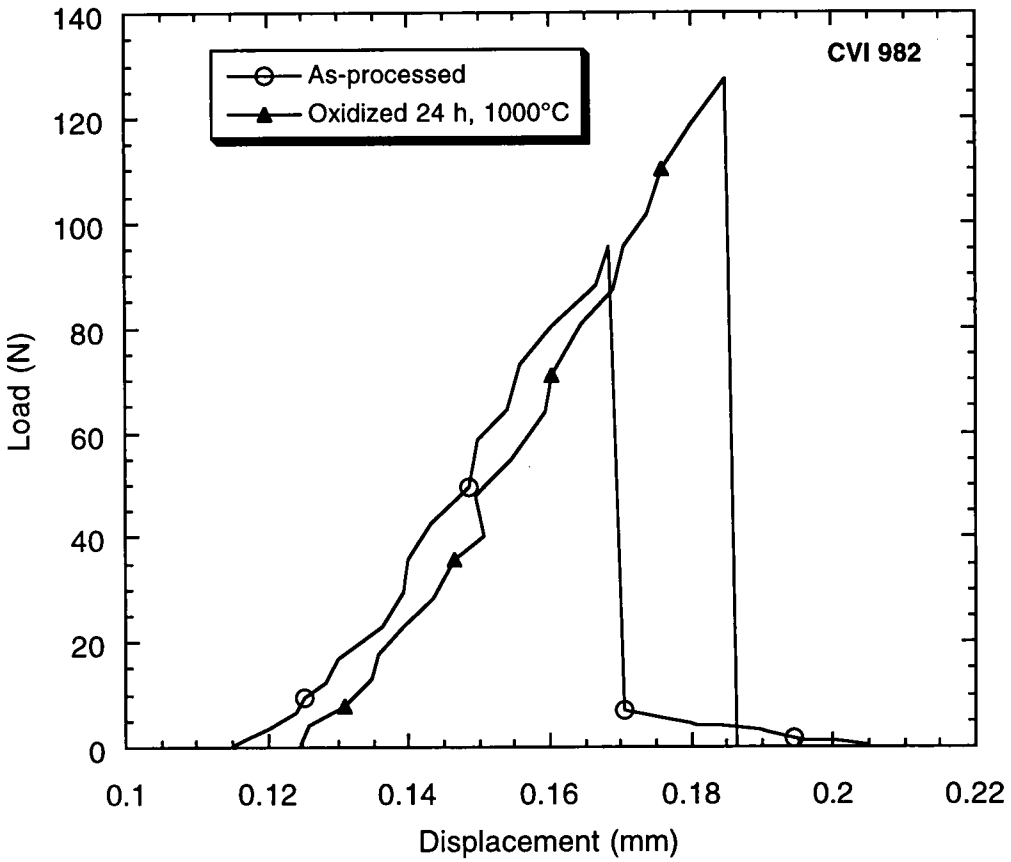


Fig. B.6.32. Representative load vs displacement curves of a CVI 982 composite in the as-processed and oxidized conditions

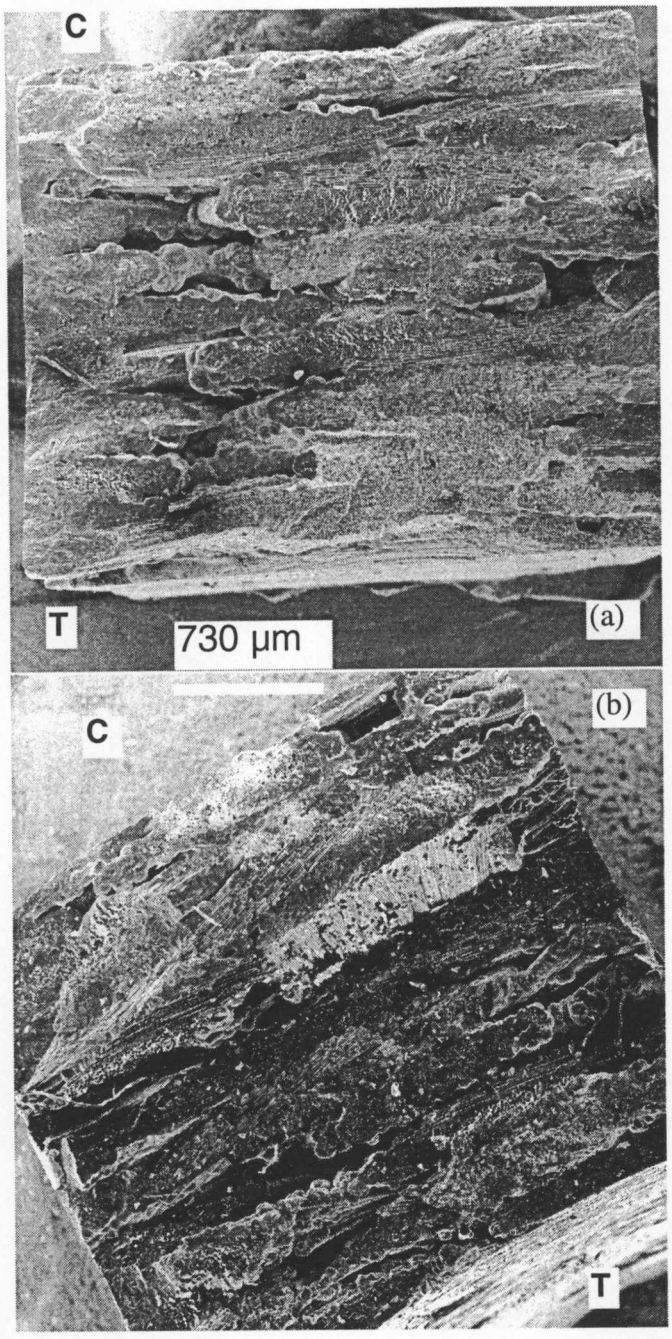


Fig. B.6.33. Fracture surface of a CVI 985 composite (Al_2O_3-TiO_2/C interface) (a) As-processed condition and (b) After 24 h oxidation at 1000°C

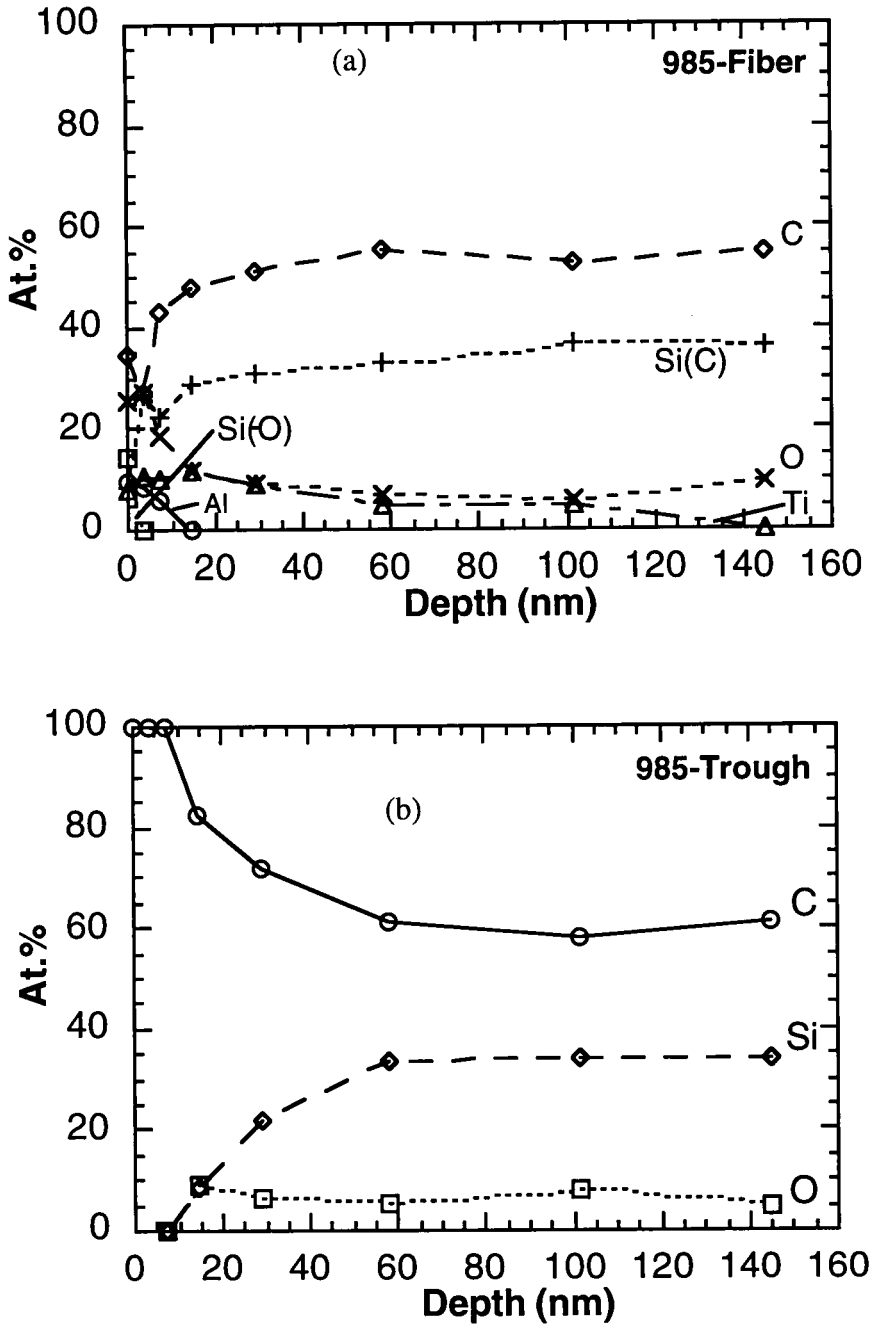


Fig. B.6.34. Compositional depth profiles obtained on a CVI 985 composite in the as-processed condition (a) Fiber and (b) Trough

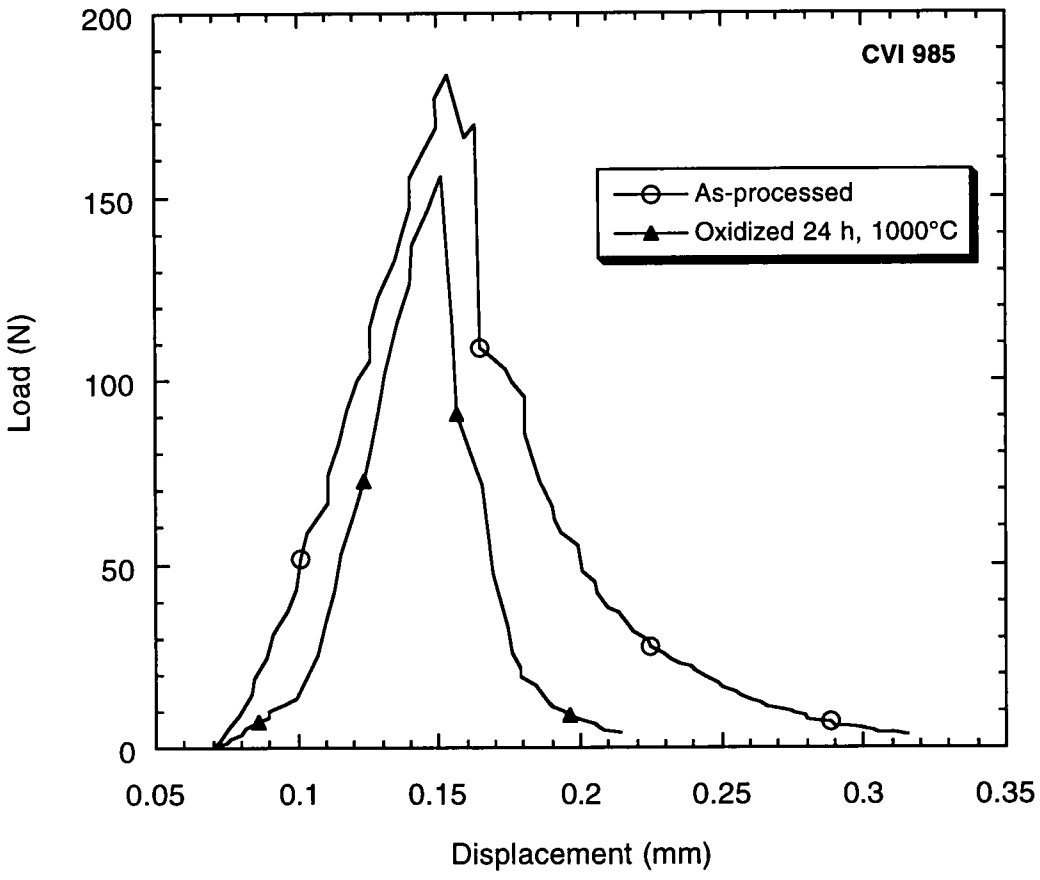


Fig. B.6.35. Representative load vs displacement curves of a CVI 985 composite in the as-processed and oxidized conditions

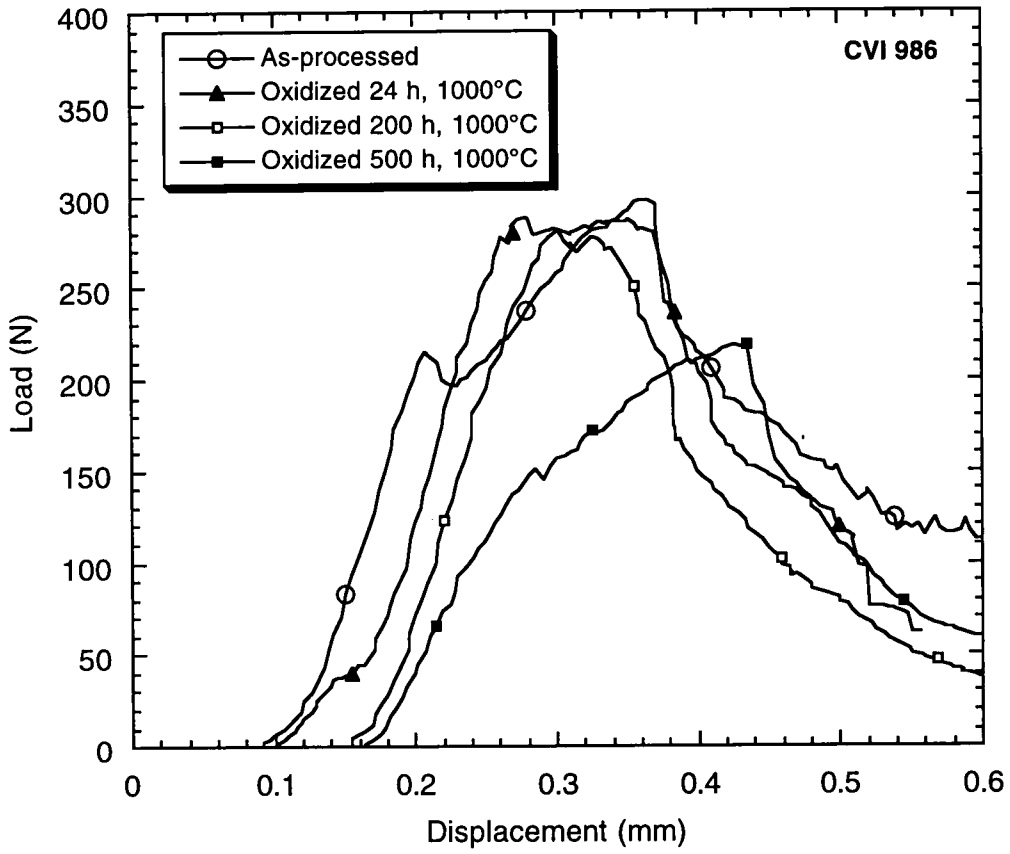


Fig. B.6.36. Representative load vs displacement curves of a CVI 986 composite (C/mullite/C interface) in the as-processed condition and after oxidation at 1000°C for up to 500 h

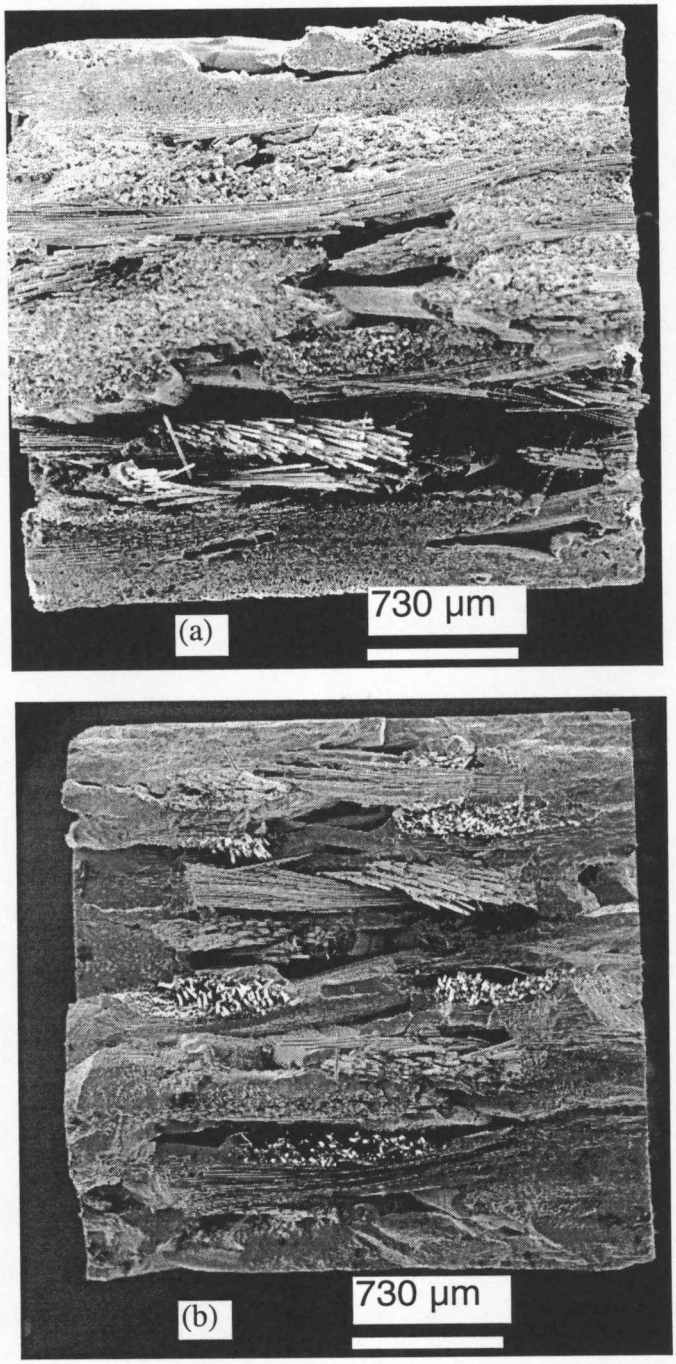


Fig. B.6.37. Fracture surface of a CVI 986 composite broken in-situ (a) As-processed condition and (b) After 500 h oxidation at 1000°C

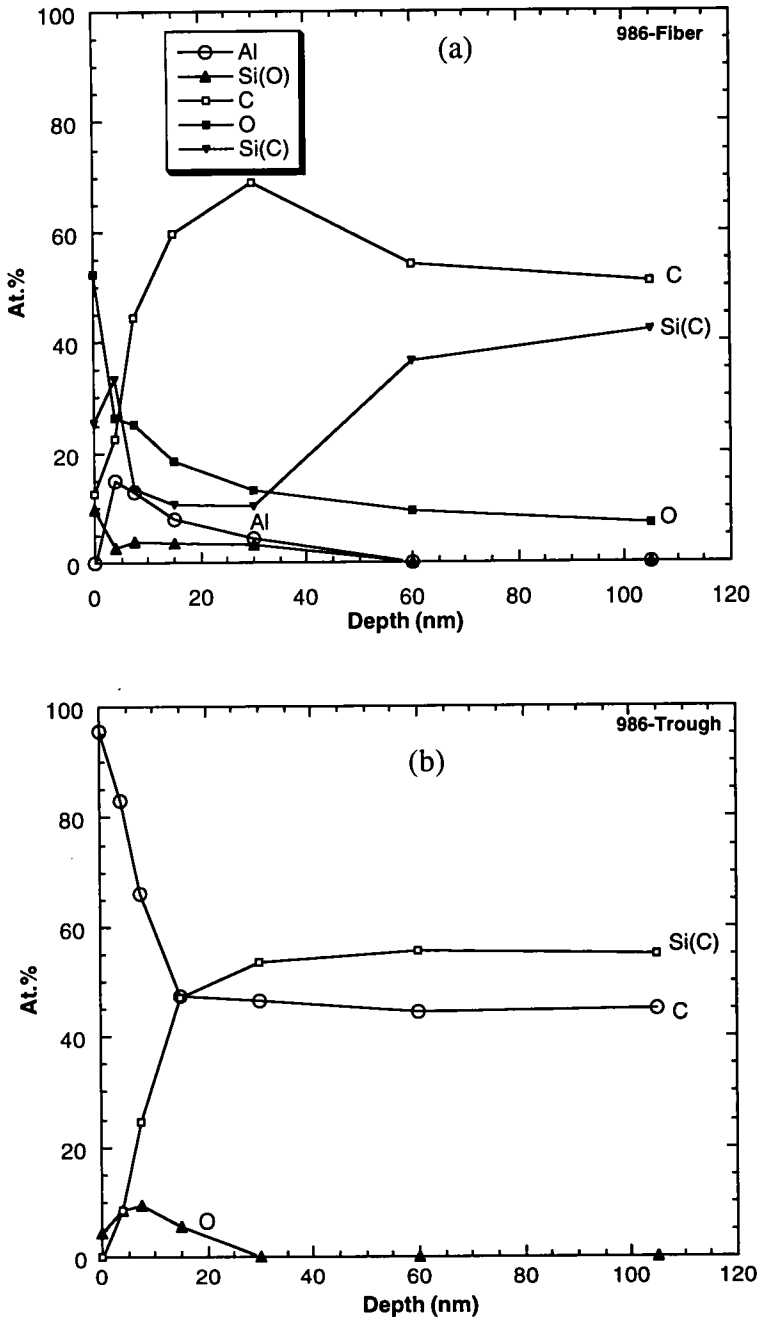


Fig. B.6.38. Compositional depth profiles obtained on a CVI 986 composite in the as-processed condition (a) Fiber and (b) Trough

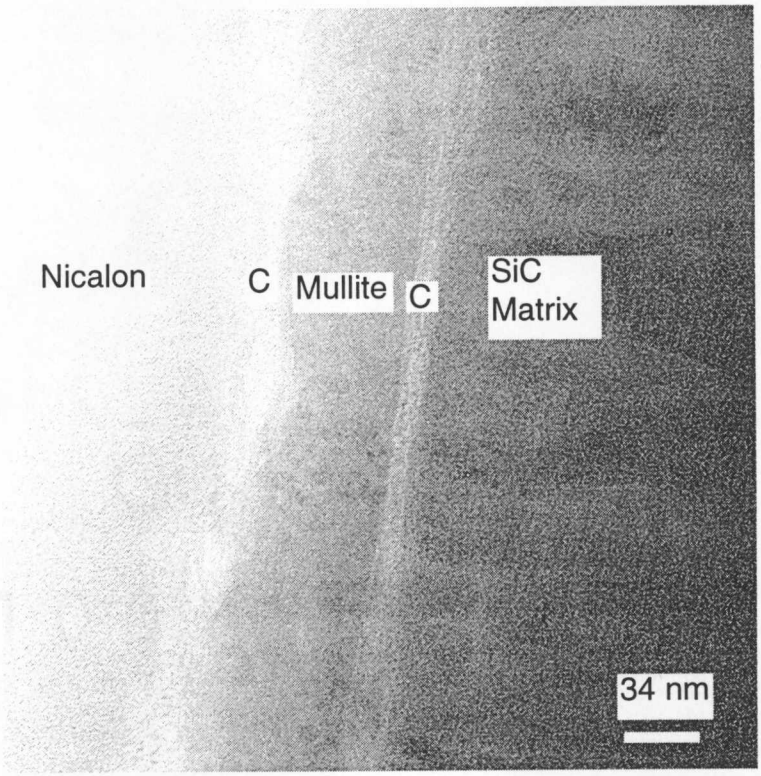


Fig. B.6.39. TEM image of a C/mullite/C interface in the CVI 986 composite. The mullite layer is microcrystalline and is ~ 70 nm thick, while the inner and outer carbon layers are each ~ 20 nm thick

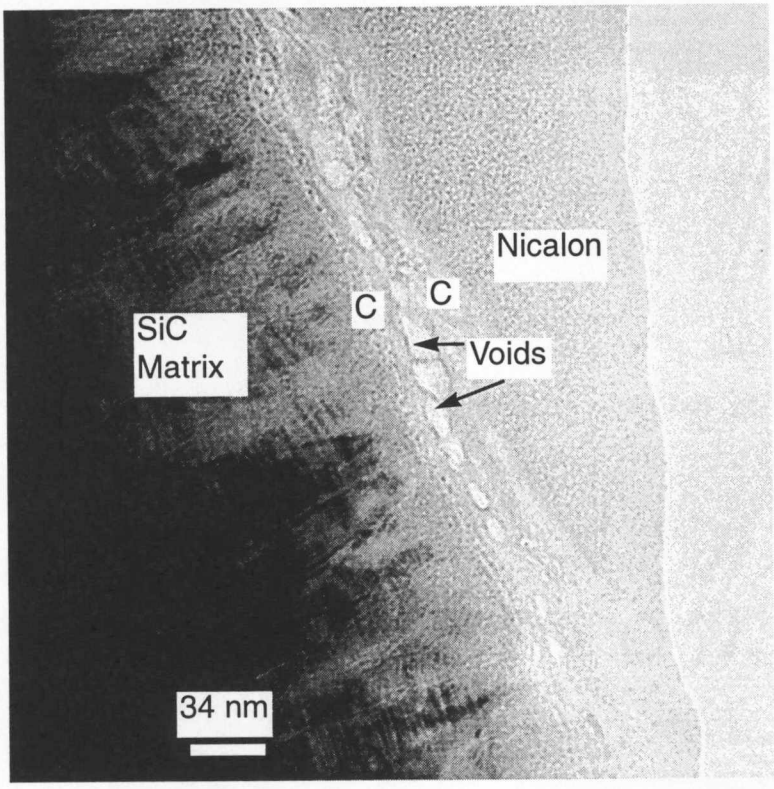


Fig. B.6.40. TEM image of a CVI 986 composite showing the absence of a mullite layer in the C/mullite/C interface. Instead of mullite, only voids are observed in between the C layers

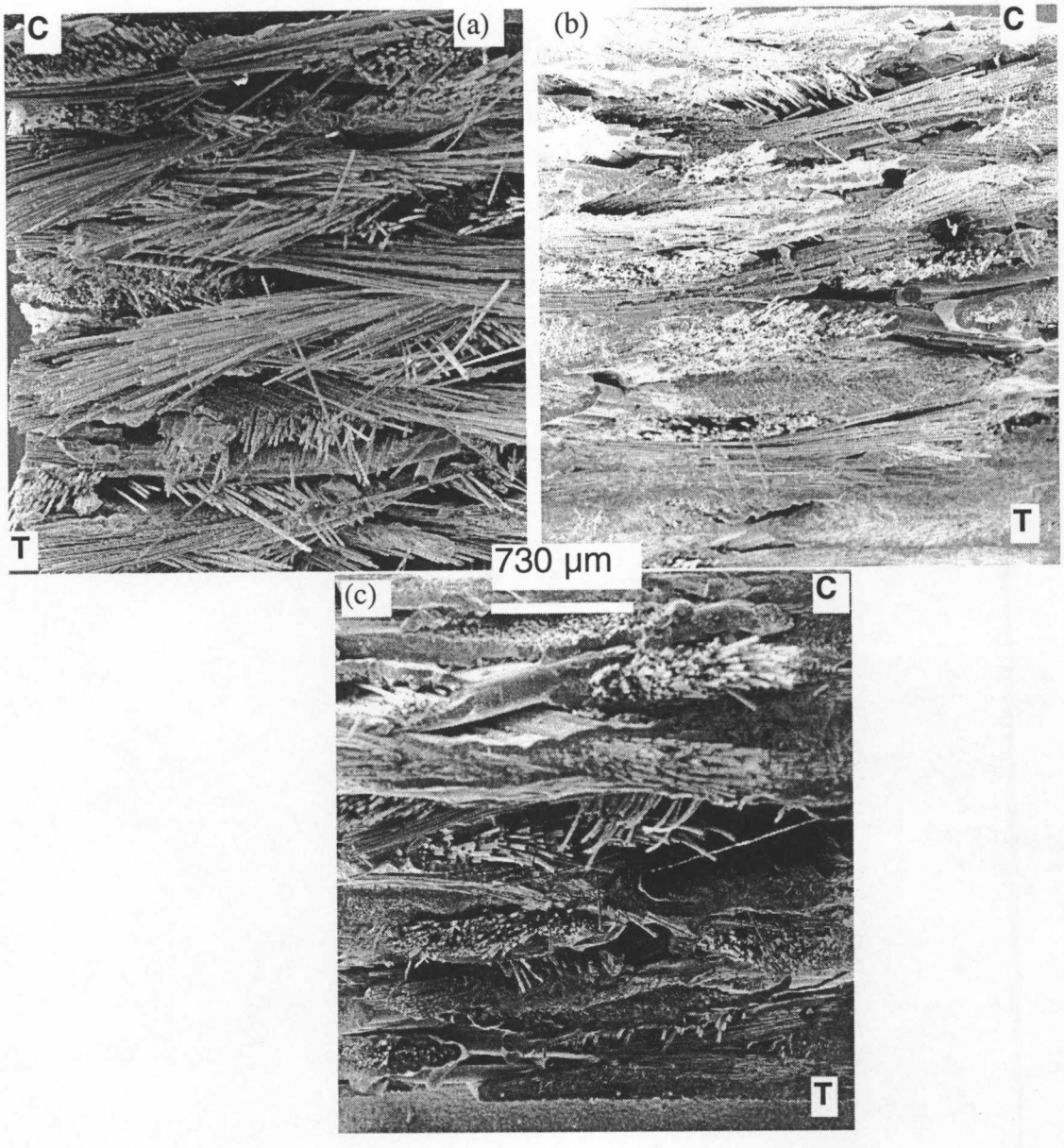


Fig. B.6.41. Fracture surface of a CVI 986 composite (a) As-processed condition (b) After 24 h oxidation at 1000°C and (c) After 500 h oxidation at 1000°C

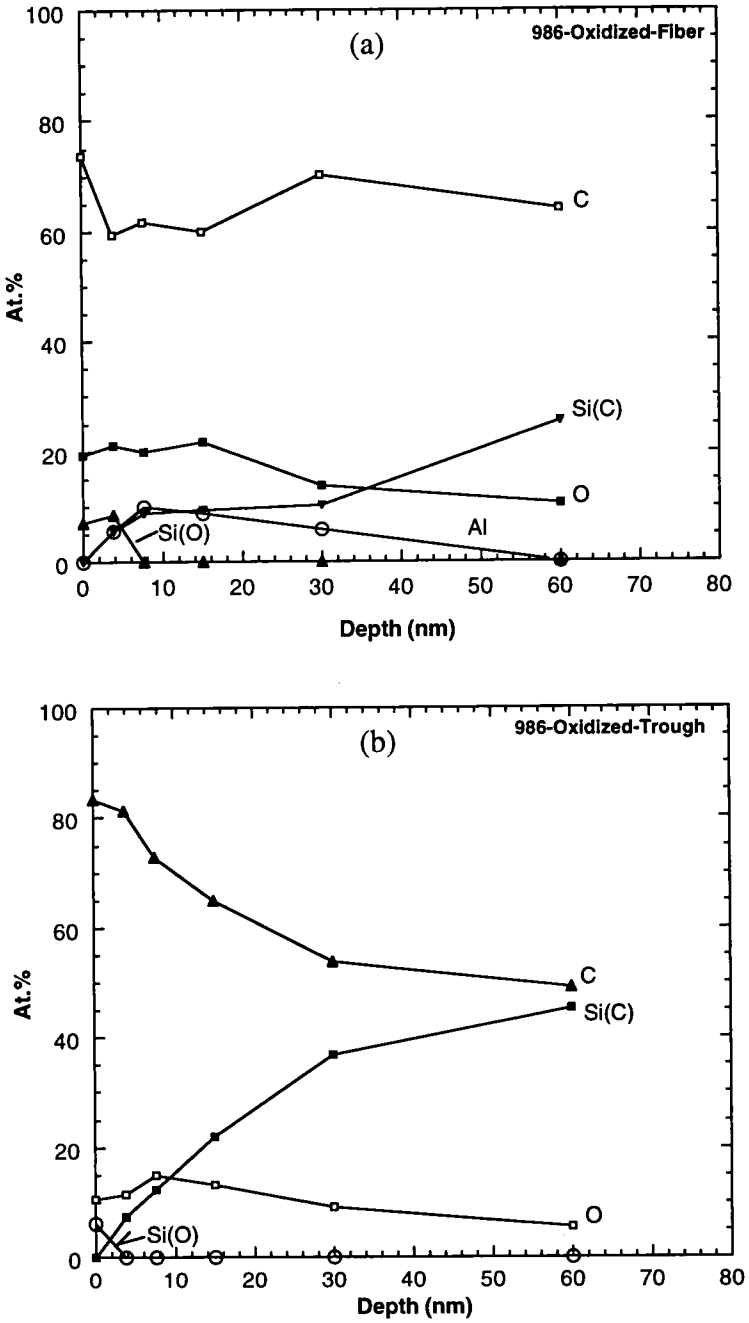


Fig. B.6.42. Compositional depth profiles obtained on a CVI 986 composite after 500 h oxidation at 1000°C (a) Fiber and (b) Trough

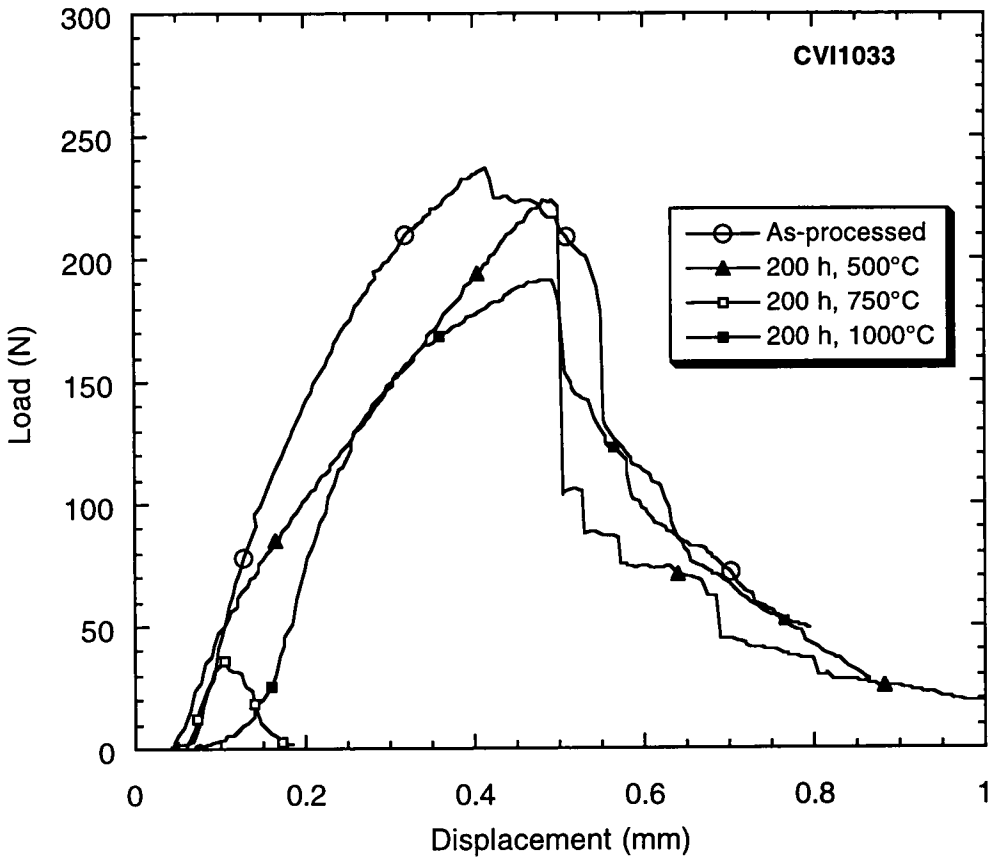


Fig. B.6.43. Representative load vs displacement curves of a CVI 1033 composite (C/mullite/C interface) in the as-processed as well as oxidized conditions

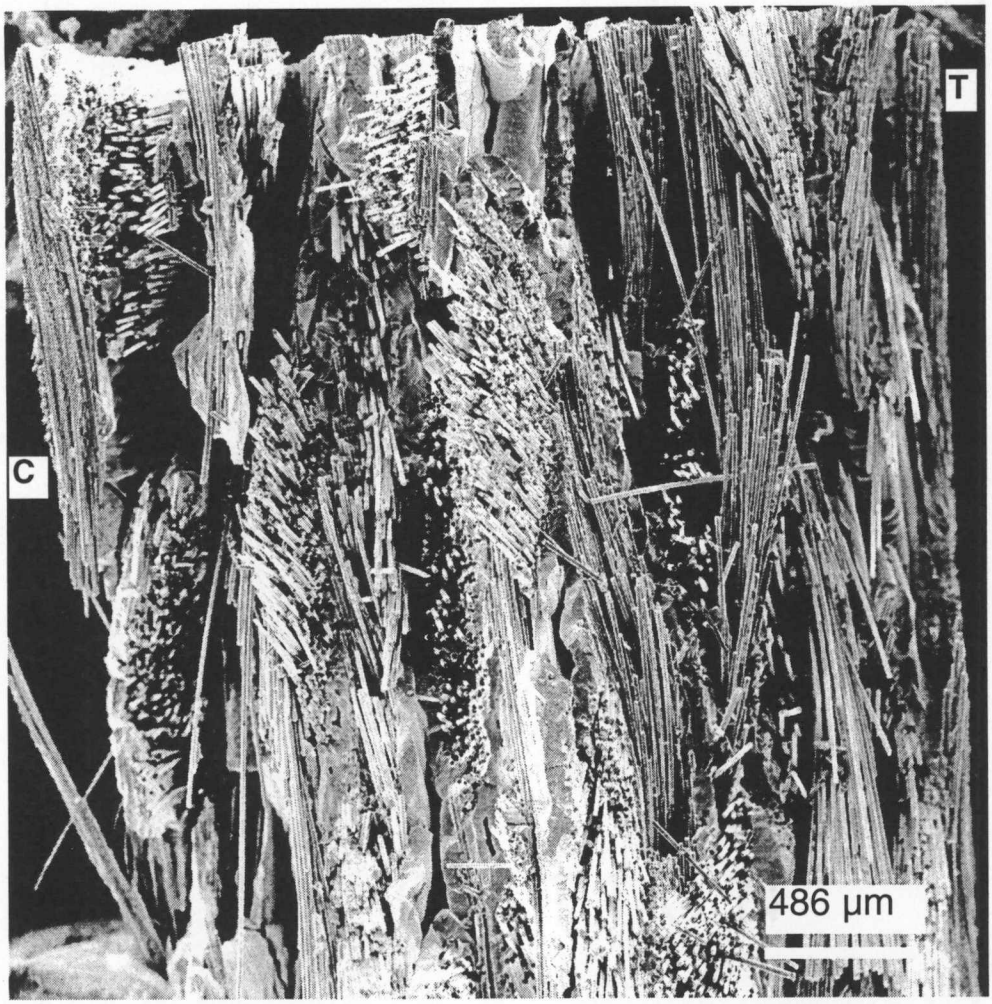


Fig. B.6.44. Fracture surface of a CVI 1033 composite showing a considerable amount of fiber pullout in the as-processed condition

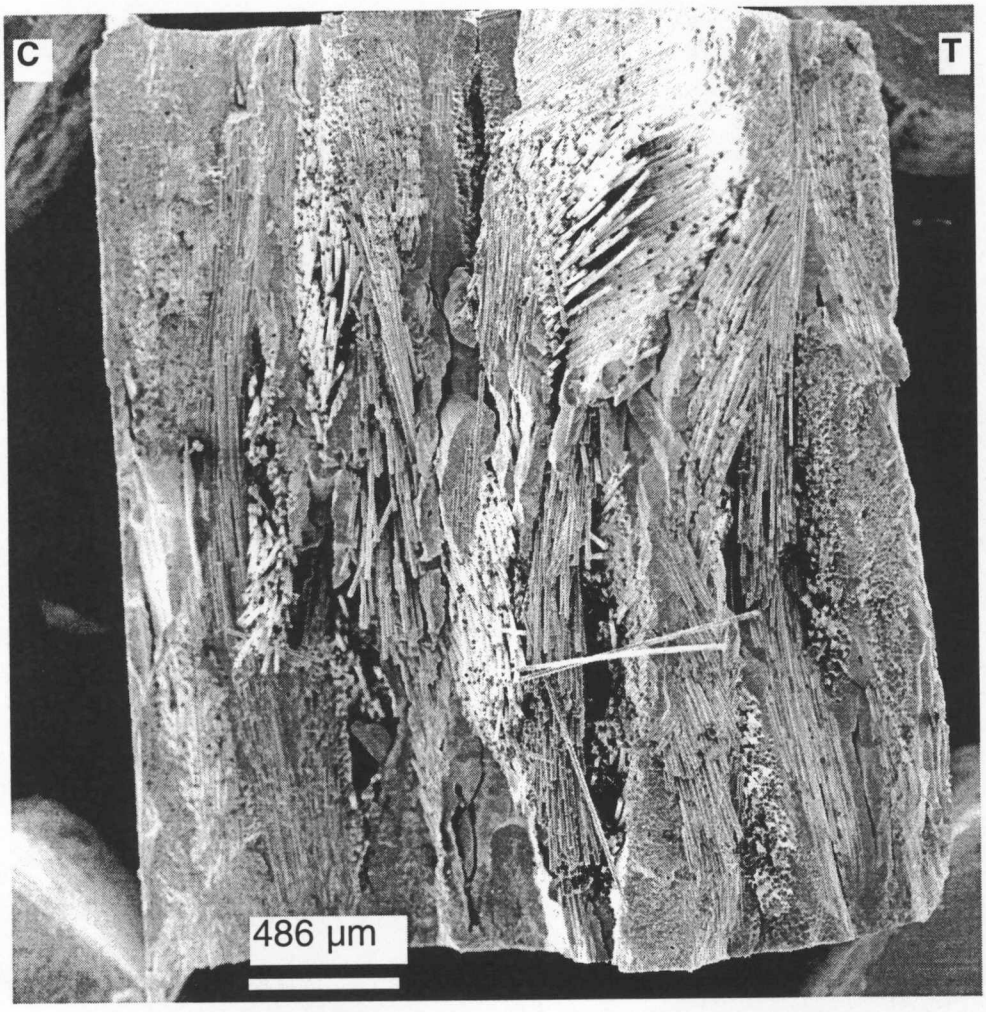


Fig. B.6.45. After 200 h oxidation at 1000°C, CVI 1033 composite fracture surface showing that the fiber pullout is confined to the interior of the sample

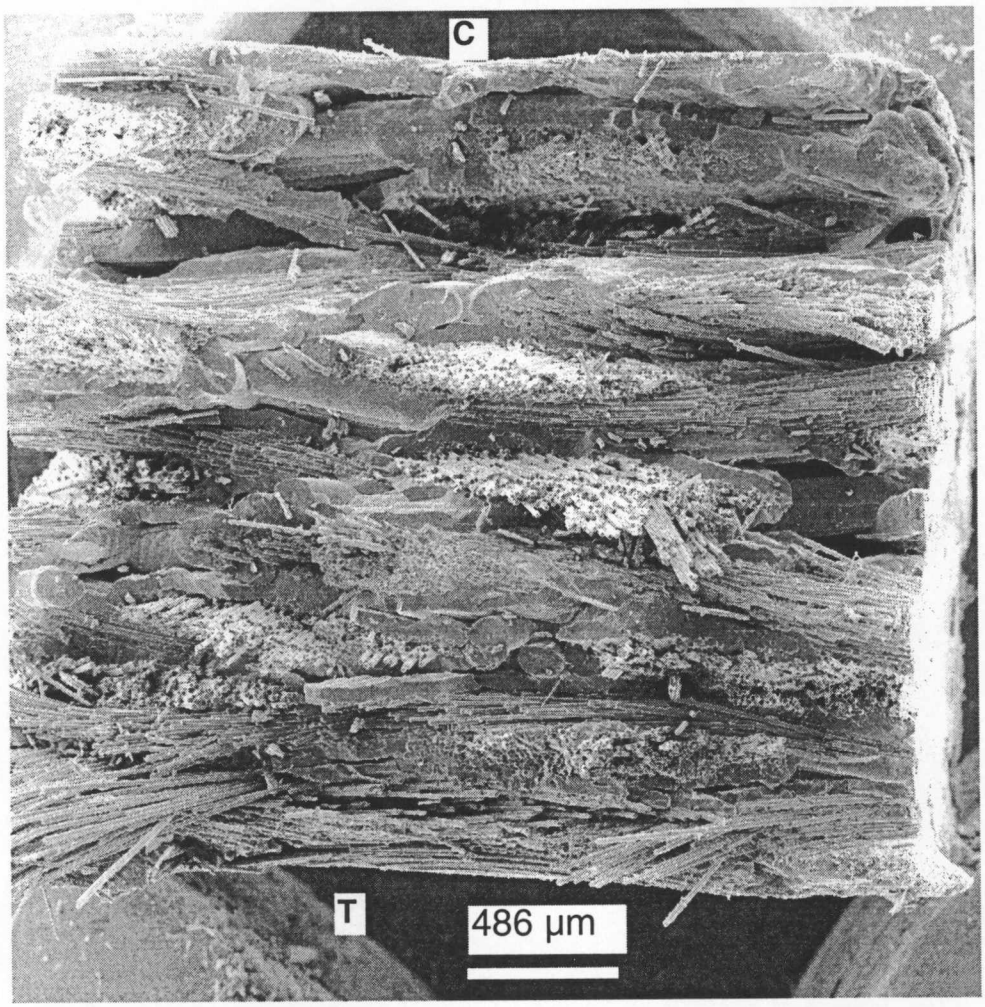


Fig. B.6.46. CVI 1033 composite fracture surface after 200 h oxidation at 500°C showing good fiber pullout

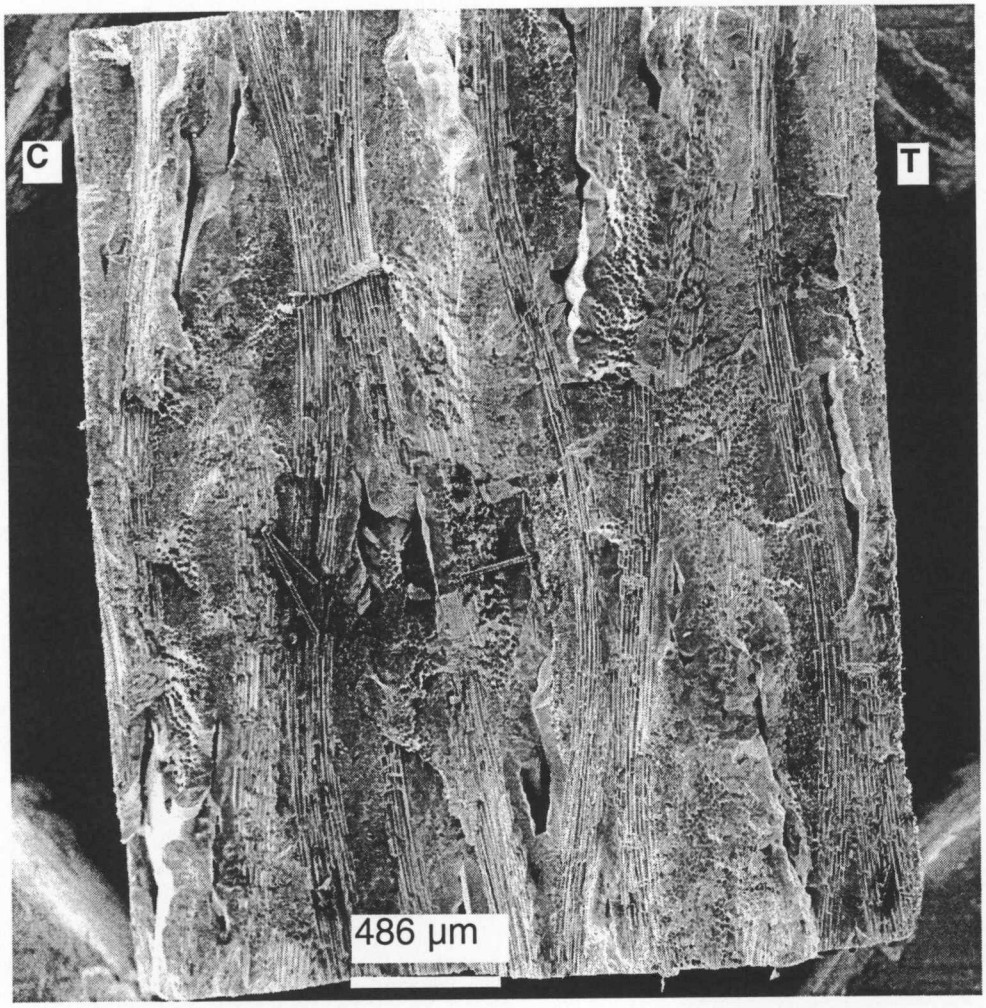


Fig. B.6.47 Fracture surface of a CVI 1033 composite after 200 h oxidation at 750°C showing brittle fracture

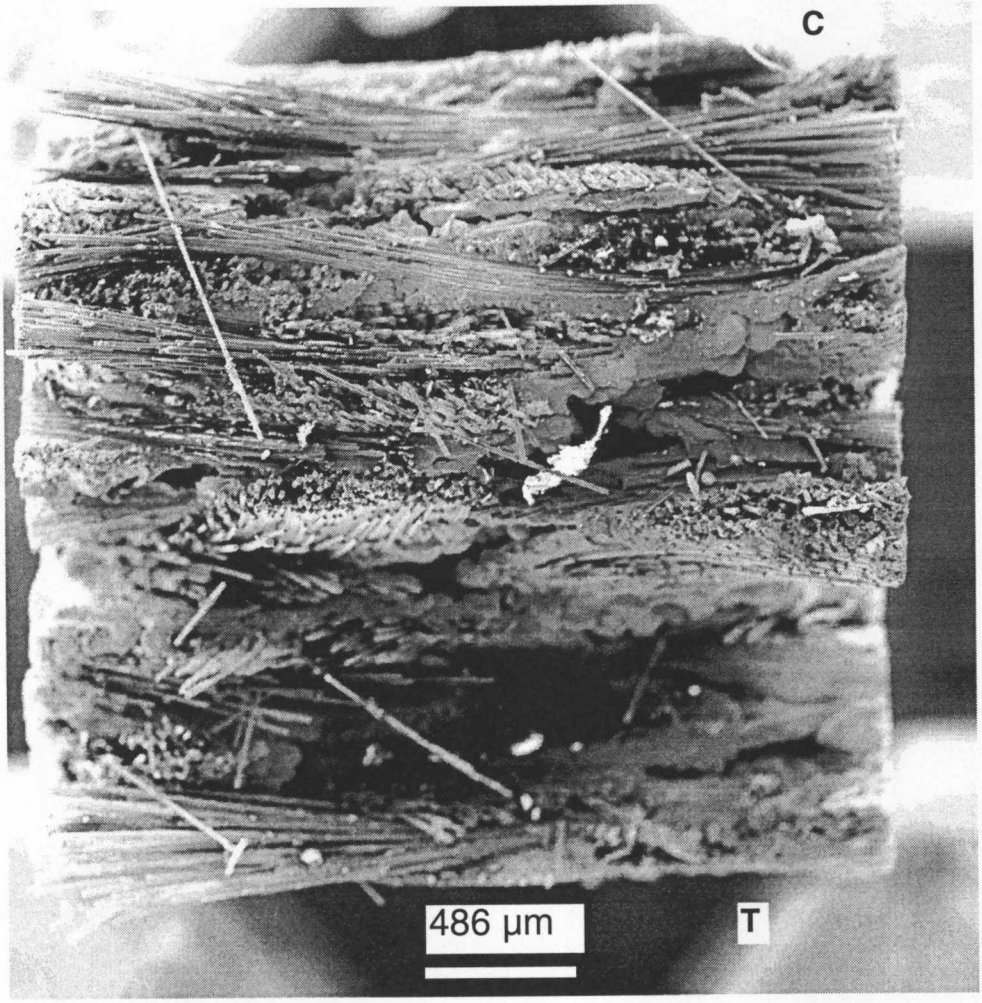


Fig. B.6.48. CVI 1080 composite fracture surface showing good amount of fiber pullout in the as-processed condition

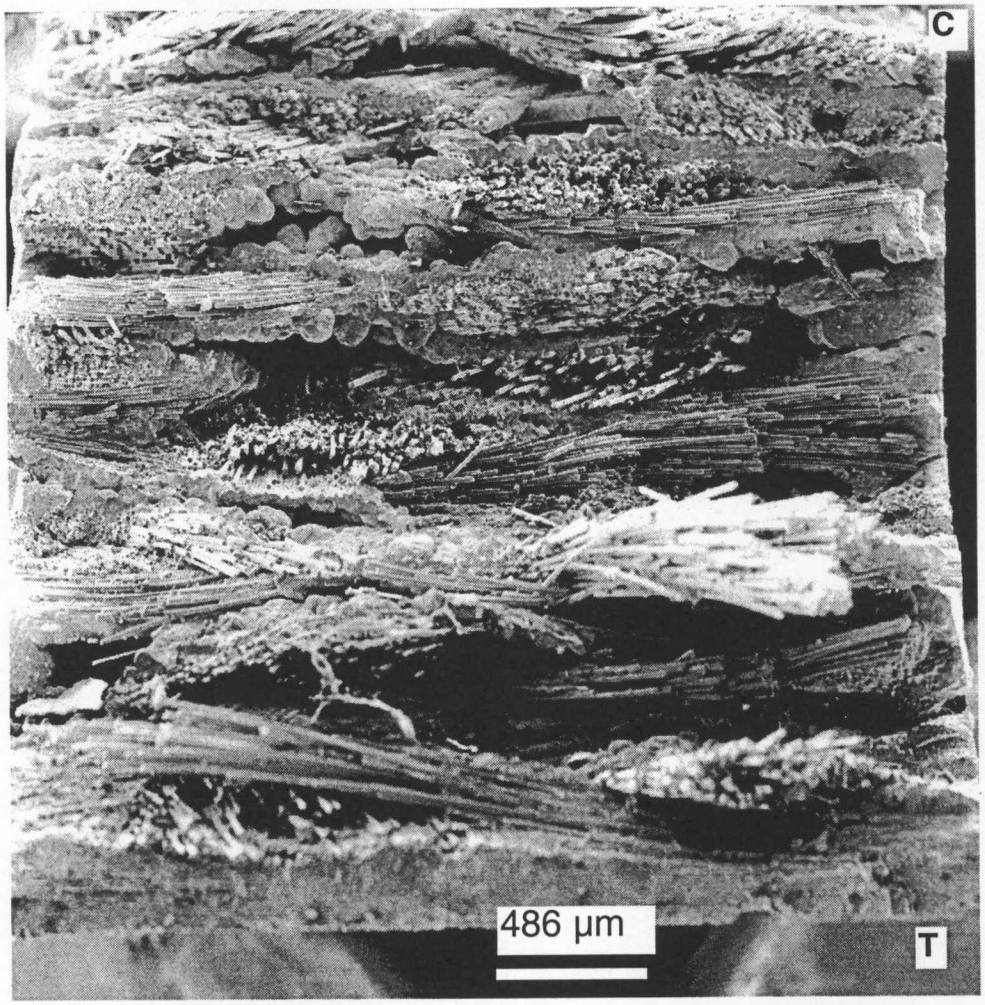


Fig. B.6.49. Fracture surface of a CVI 1080 composite after 24 h oxidation at 1000°C showing good amount of fiber pullout

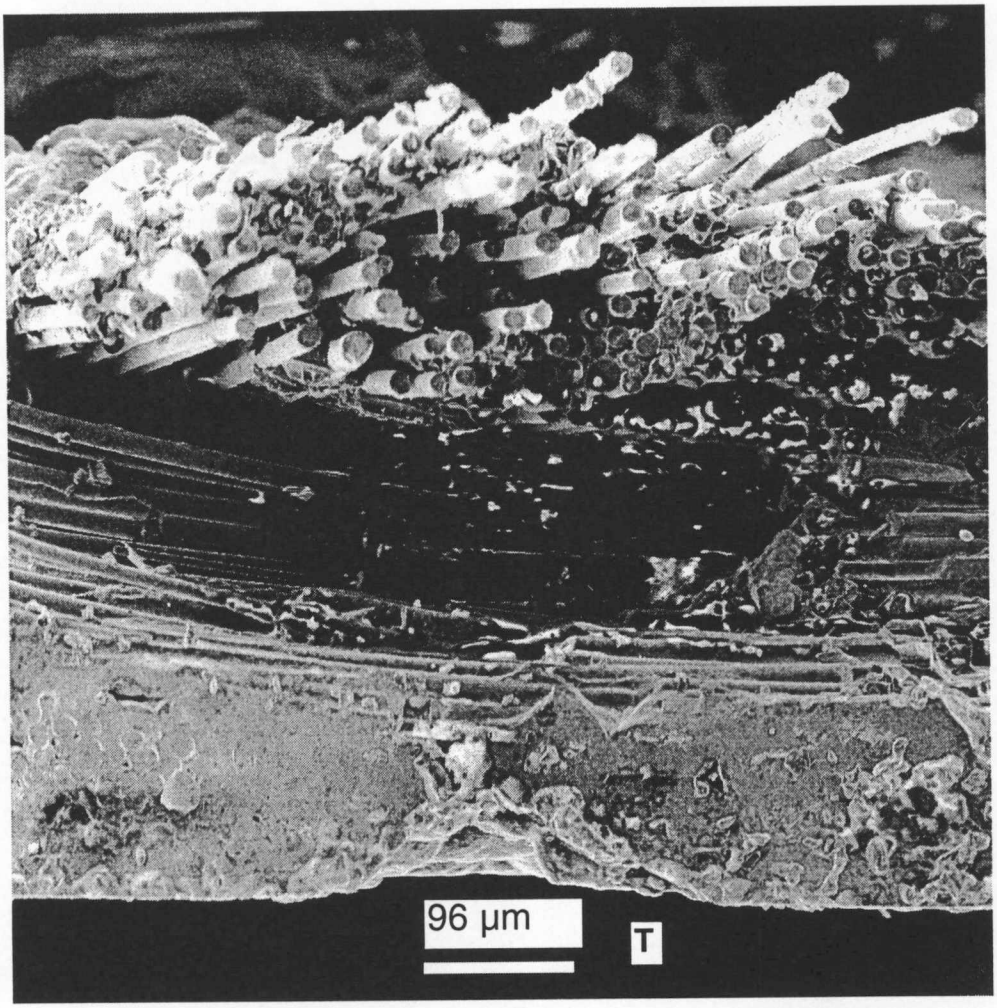


Fig. B.6.50. The tensile edge of the fracture surface of a CVI 1080 composite after 24 h oxidation at 1000°C. Note that the embrittlement zone extends ~ 200 µm

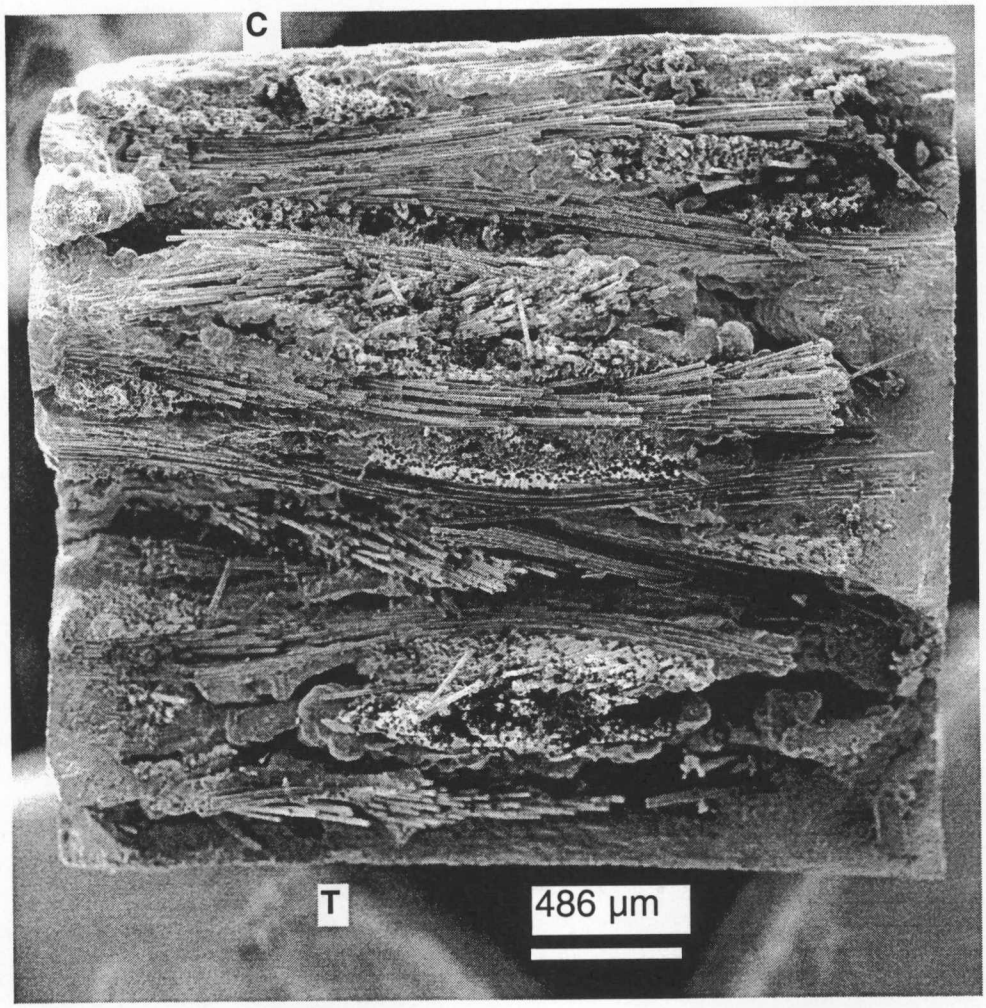


Fig. B.6.51. Fracture surface of a CVI 1080 composite after 200 h oxidation at 1000°C showing embrittlement near the sample edges

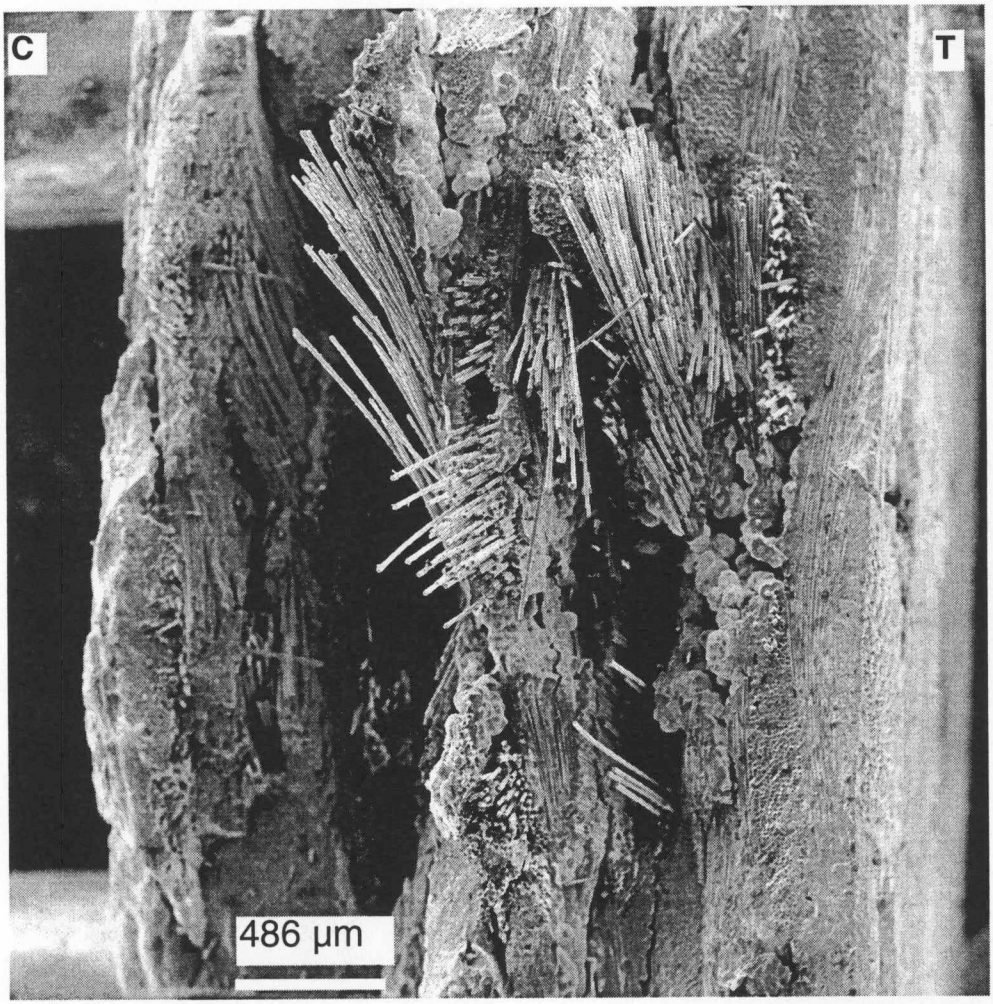


Fig. B.6.52. After 500 h oxidation at 1000°C, fracture surface of a CVI 1080 composite showing that the fiber pullout is seen only in the composite interior

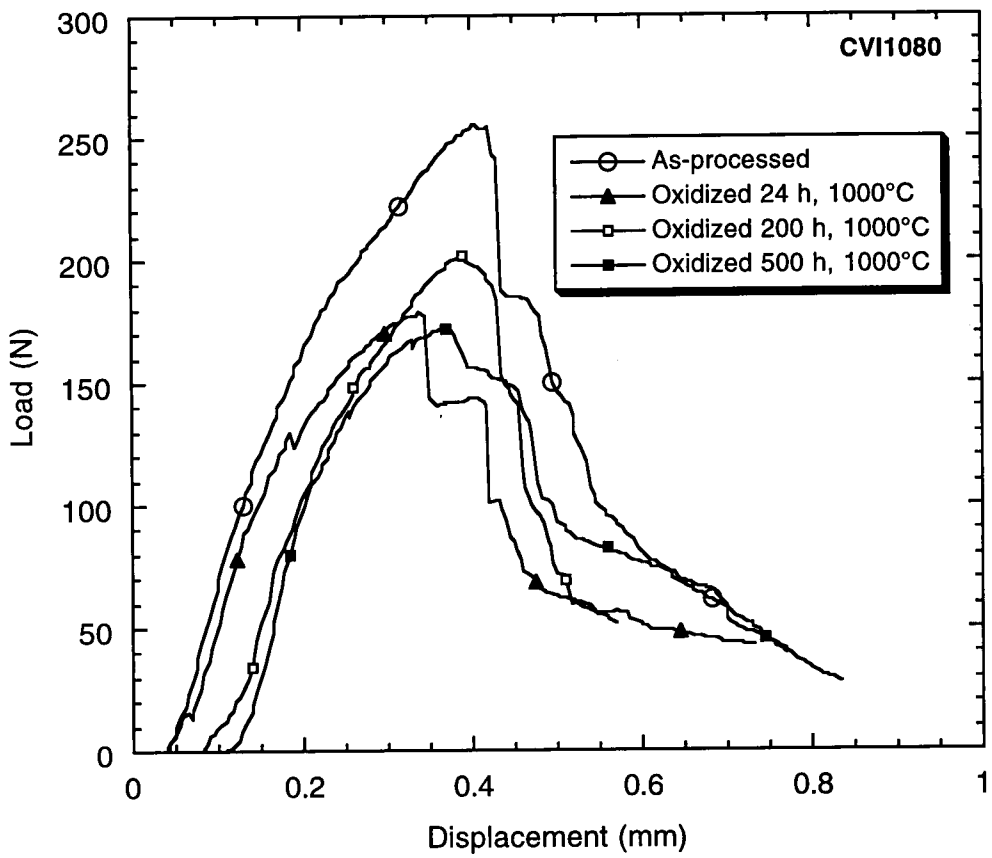


Fig. B.6.53. Representative load vs displacement curves of a CVI 1080 composite in the as-processed condition and after oxidation for up to 500 h at 1000°C

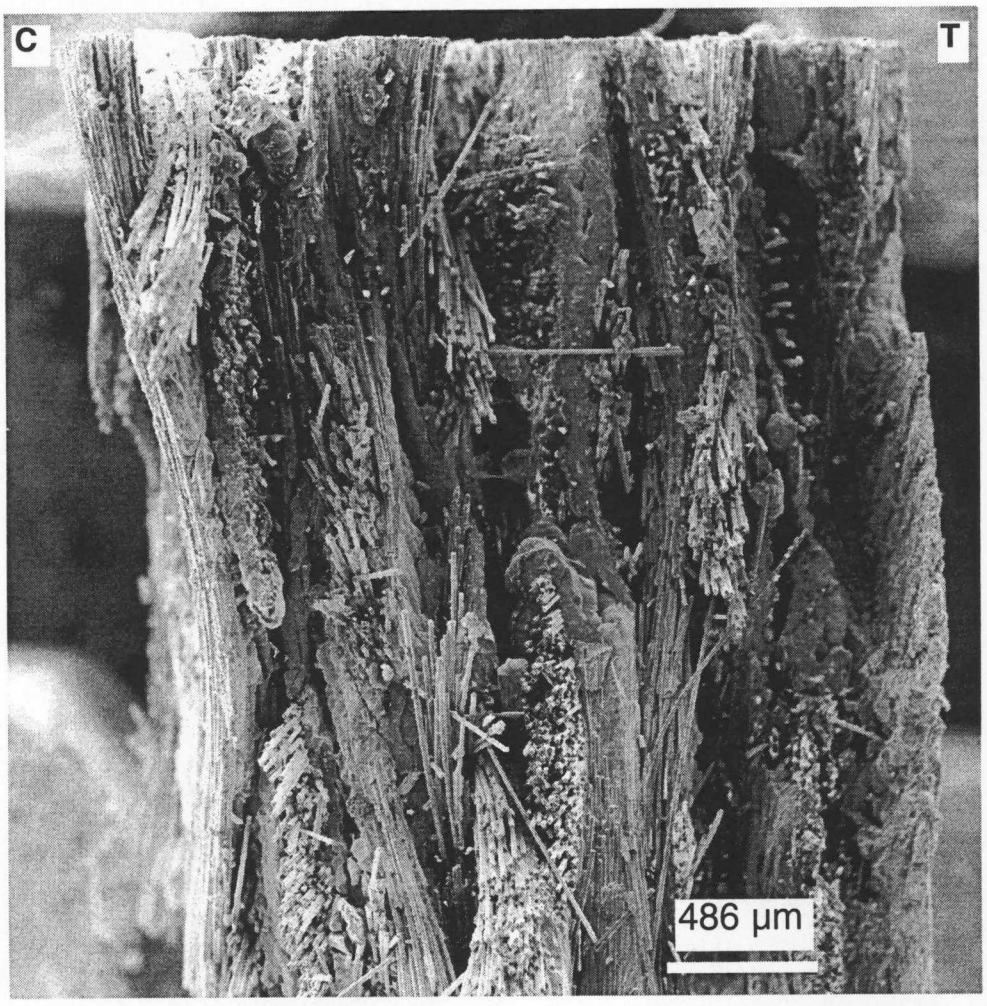


Fig. B.6.54. Fracture surface of a CVI 1081 composite (C/mullite/C interface) showing good amount of fiber pullout in the as-processed condition

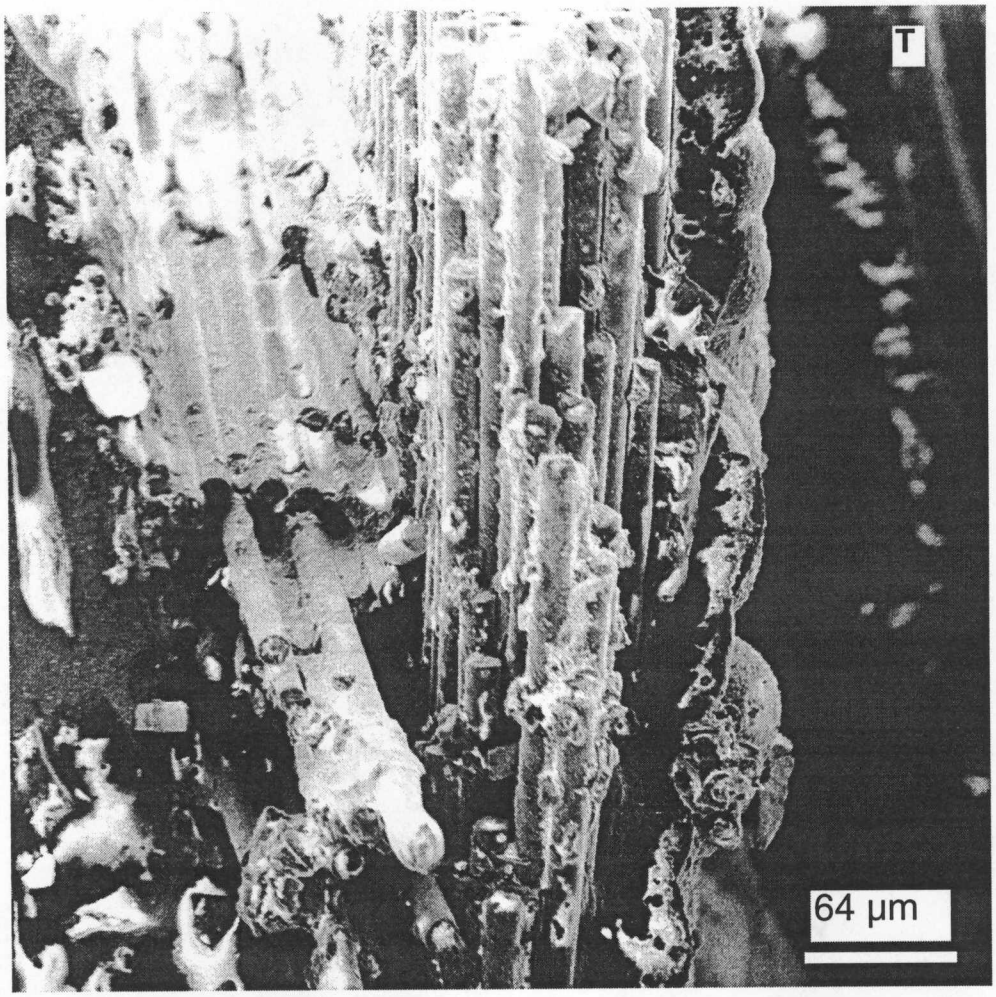


Fig. B.6.55. Near the tensile region of the CVI 1081 composite fracture surface, fiber pullout of the order of 200 µm is observed

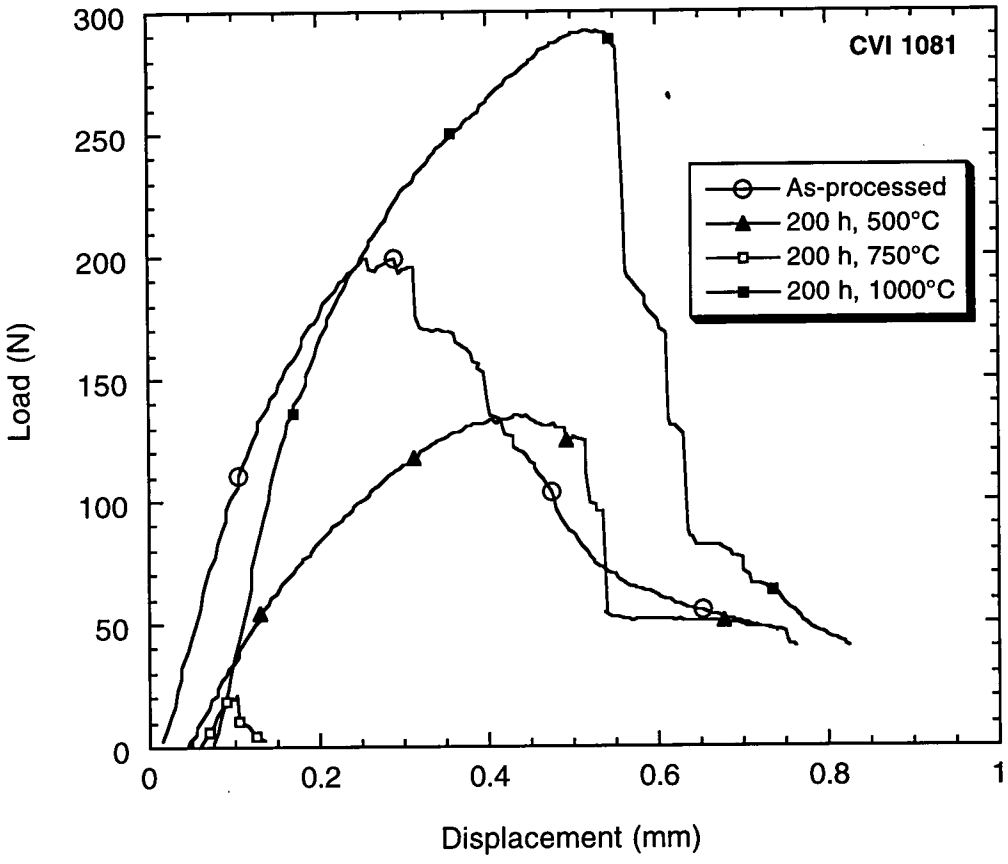


Fig. B.6.56. Load vs displacement curve for a CVI 1081 composite in the as-processed and oxidized conditions

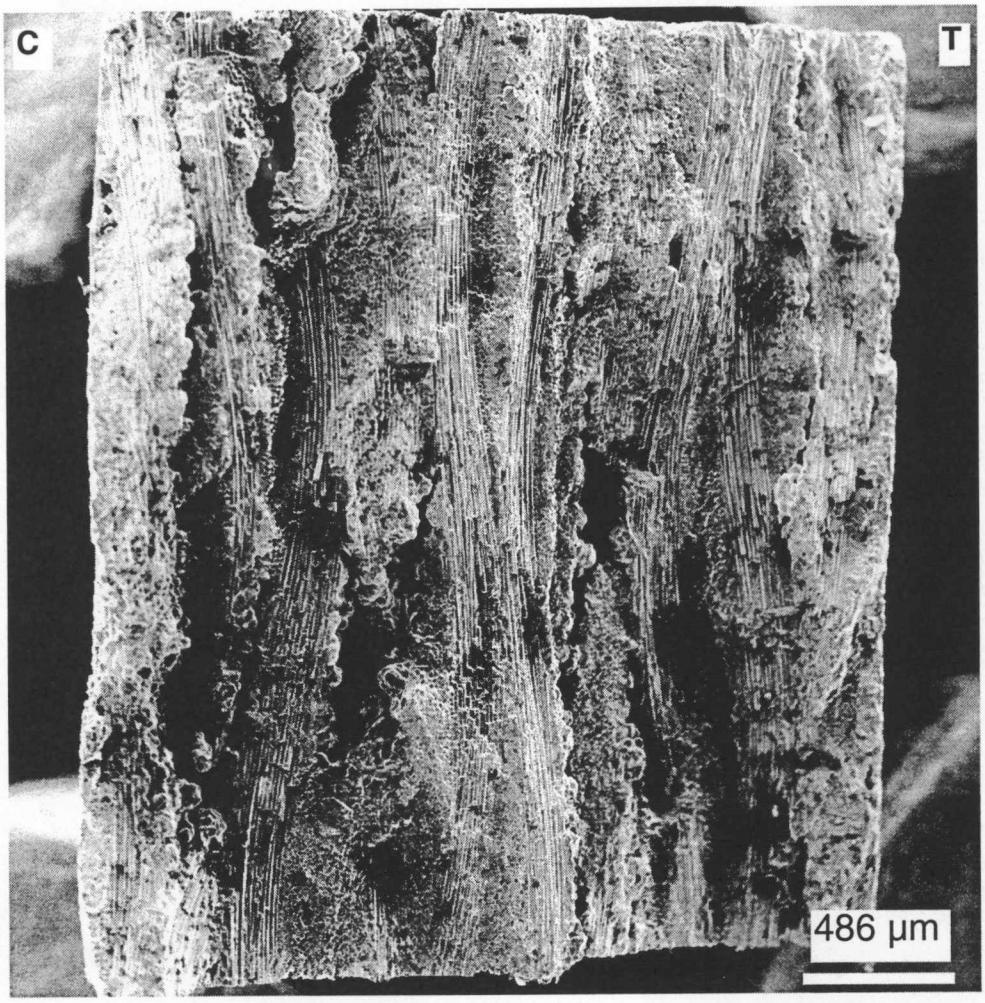


Fig. B.6.57. Fracture surface of a CVI 1081 composite exhibiting brittle fracture after oxidation at 750°C for 200 h in air

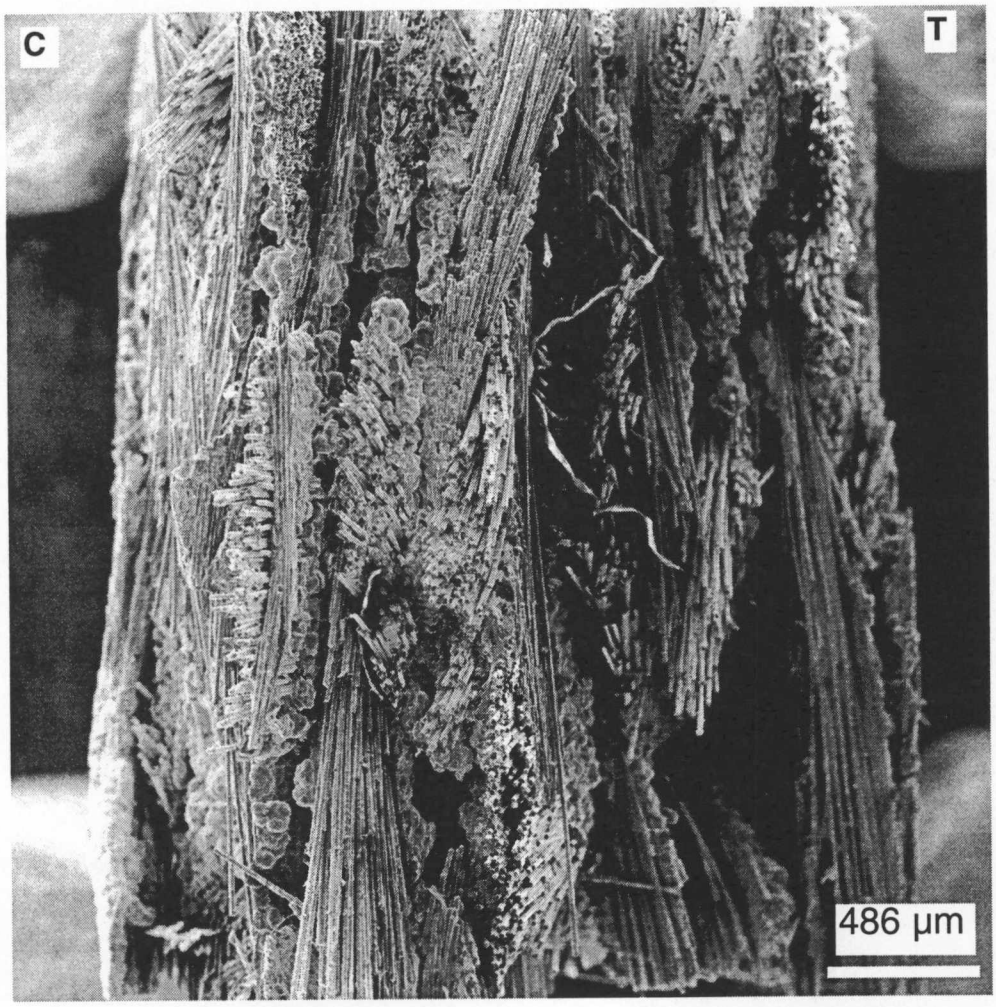


Fig. B.6.58. Fracture surface of a CVI 1081 composite showing a good amount of fiber pullout even after 200 h oxidation at 500°C in air

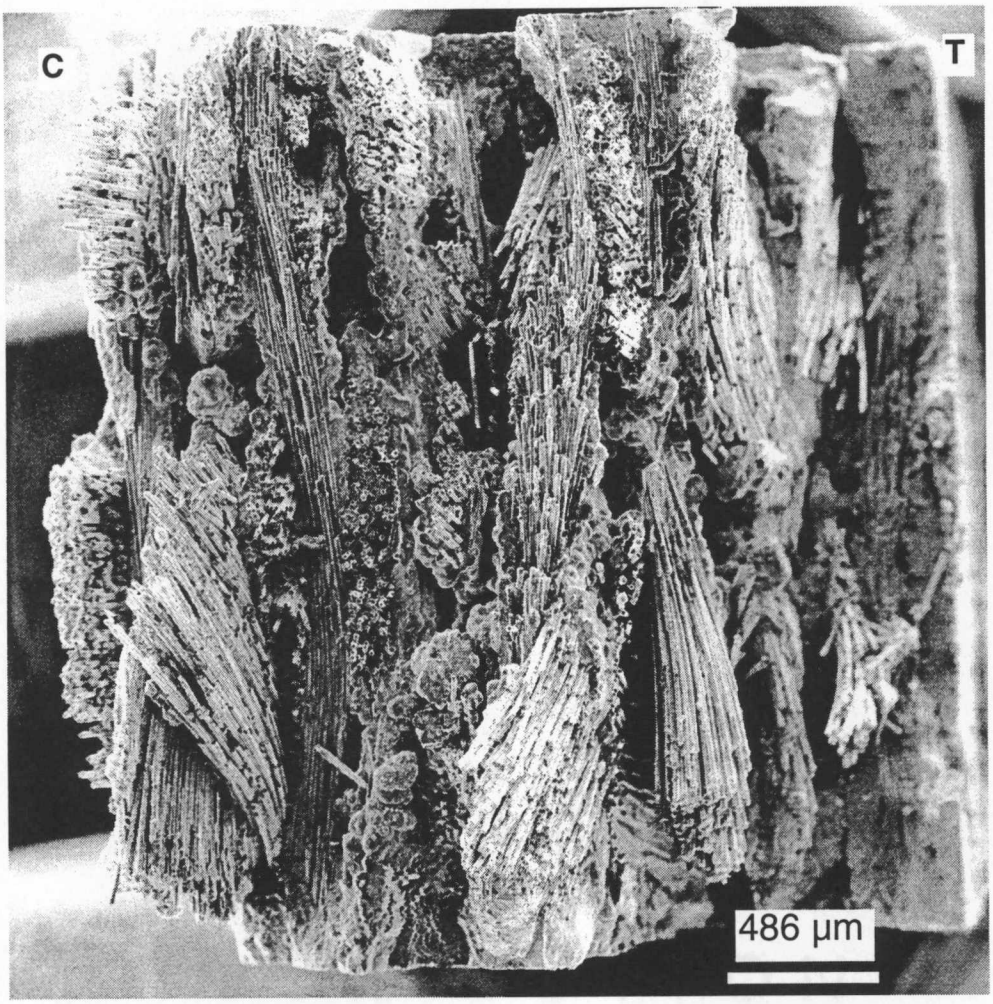


Fig. B.6.59. CVI 1081 composite exhibiting a fibrous fracture surface with a good amount of fiber pullout even after 200 h oxidation at 1000°C in air

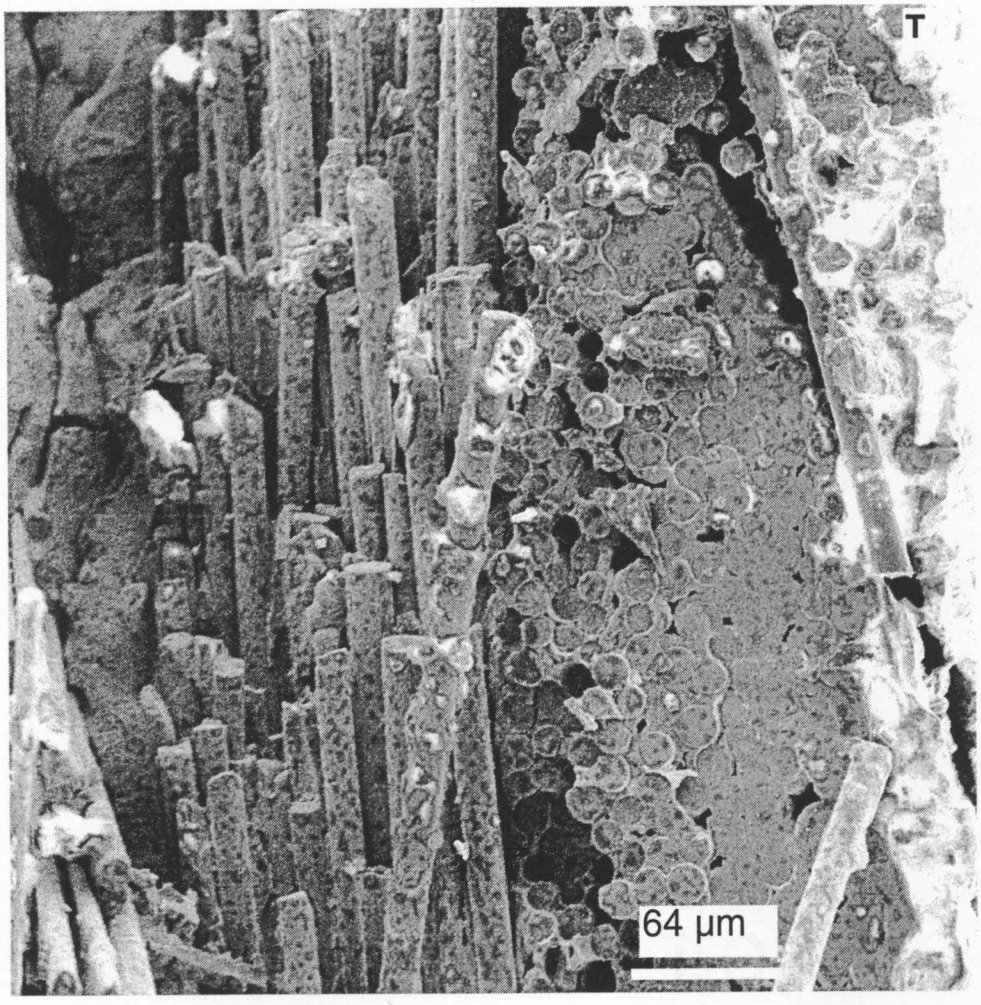


Fig. B.6.60. Embrittlement (~200 μm width) occurring near the tensile region in the CVI 1081 composite after oxidation for 200 h at 1000°C in air

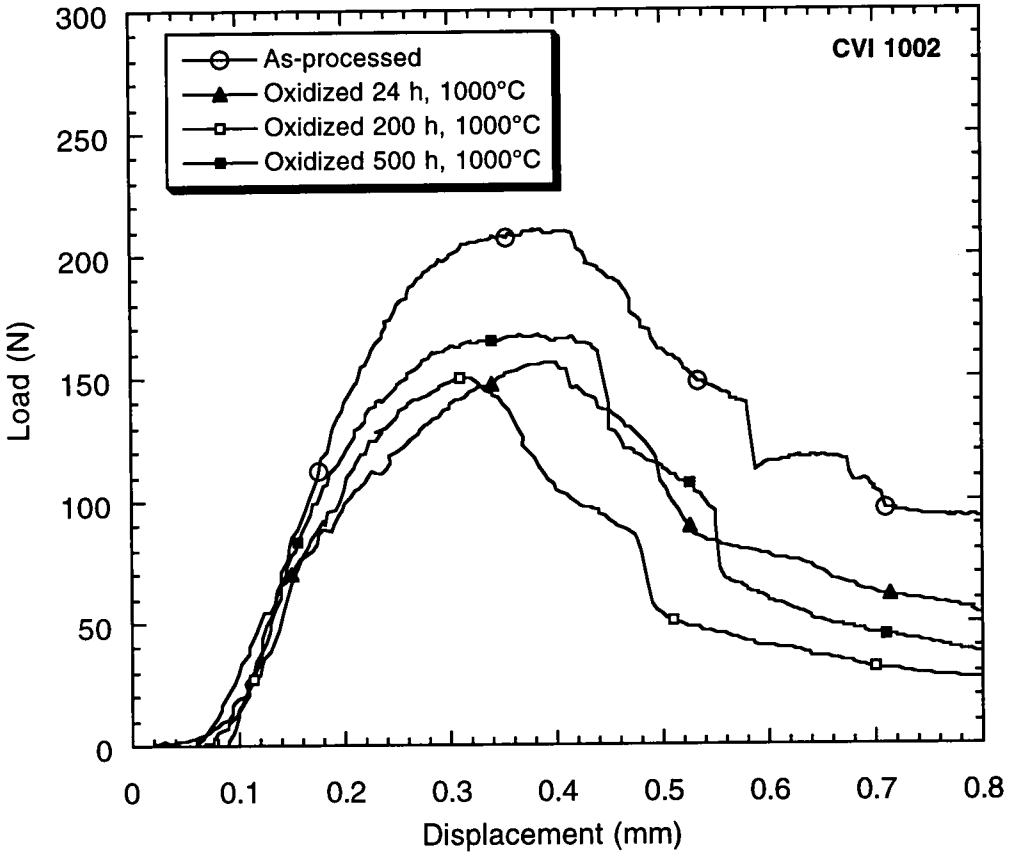


Fig. B.6.61. Representative load vs displacement curves of the CVI 1002 composite (C/Al_2O_3-TiO_2/C interface) in the as-processed condition and after oxidation for up to 500 h showing graceful failure

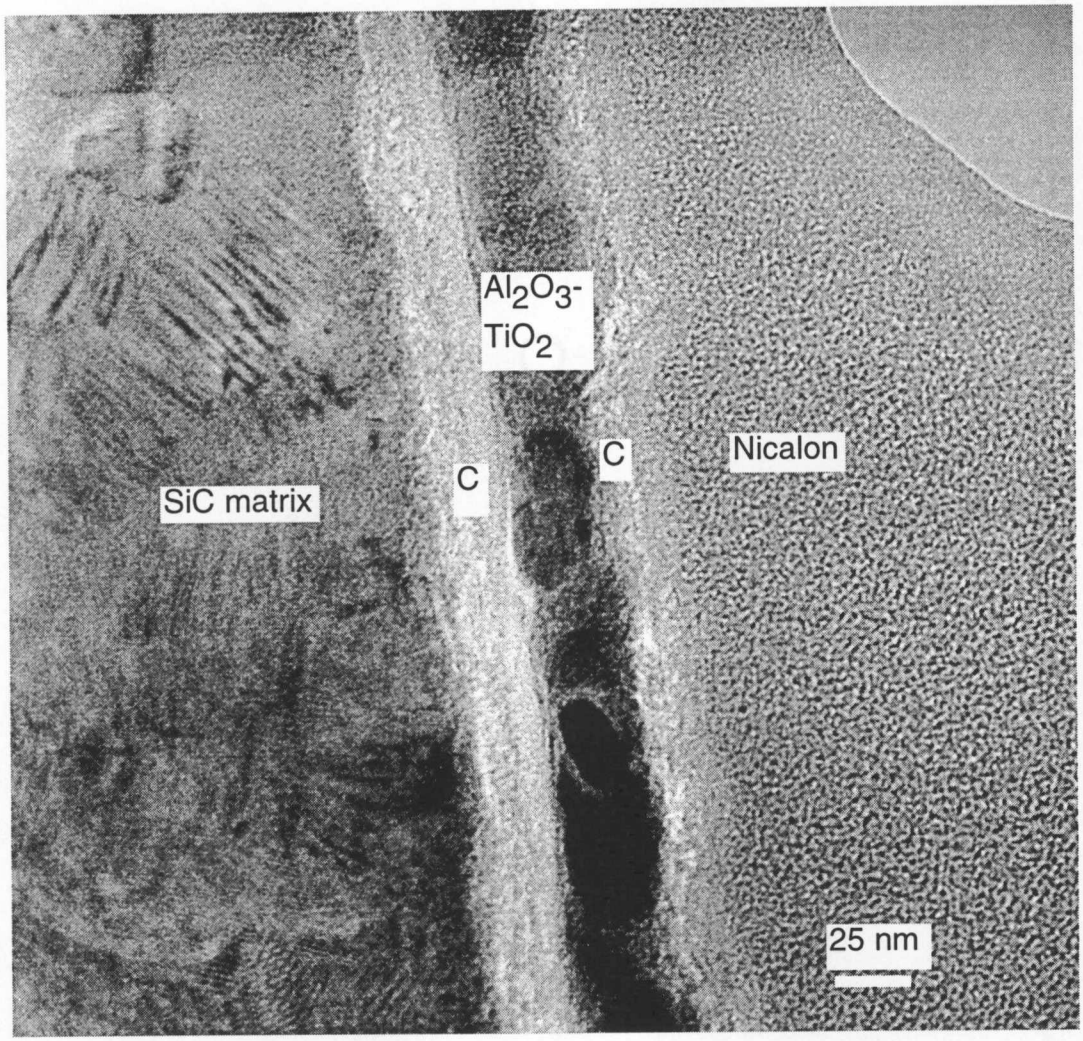


Fig. B.6.62. TEM image of the CVI 1002 composite showing that the Al_2O_3-TiO_2 layer (~30-50 μm thick) is bounded by C layers

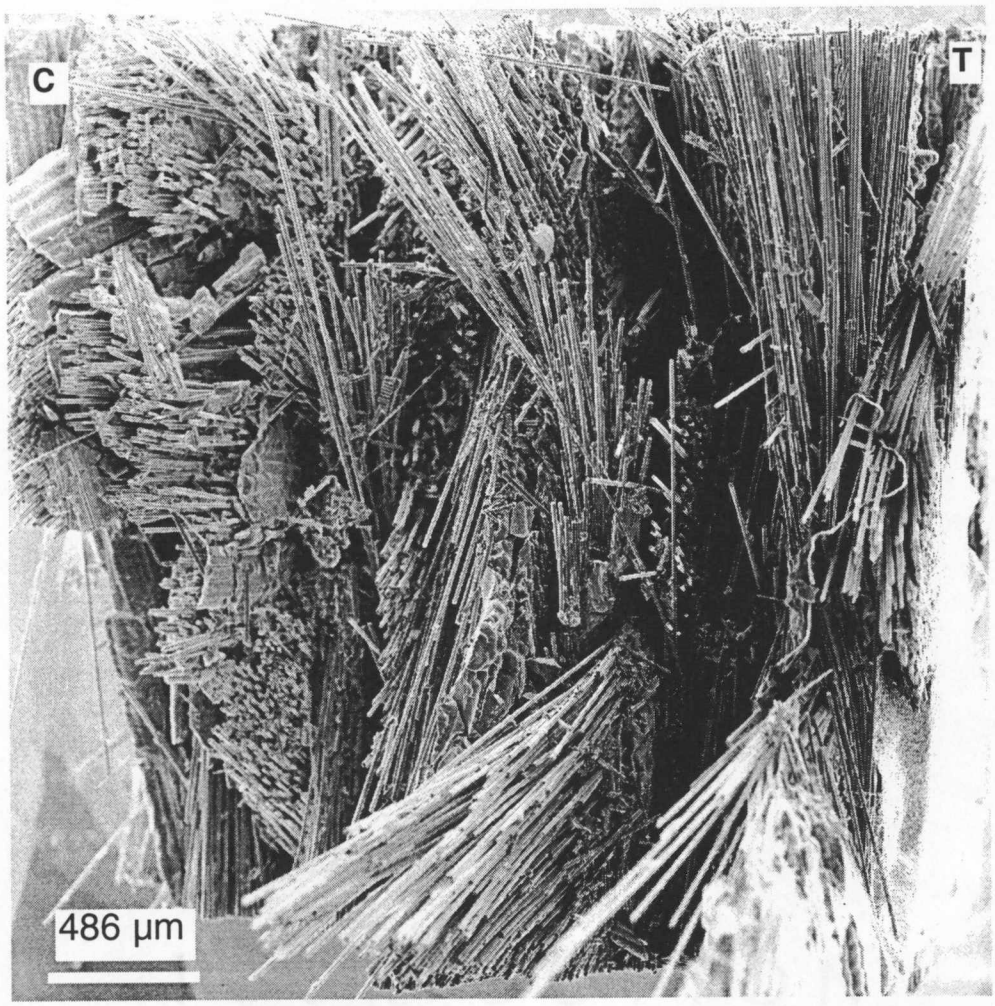


Fig. B.6.63. The CVI 1002 composite displaying a considerable amount of fiber pullout, with pullout lengths typically > 500 µm, in the as-processed condition

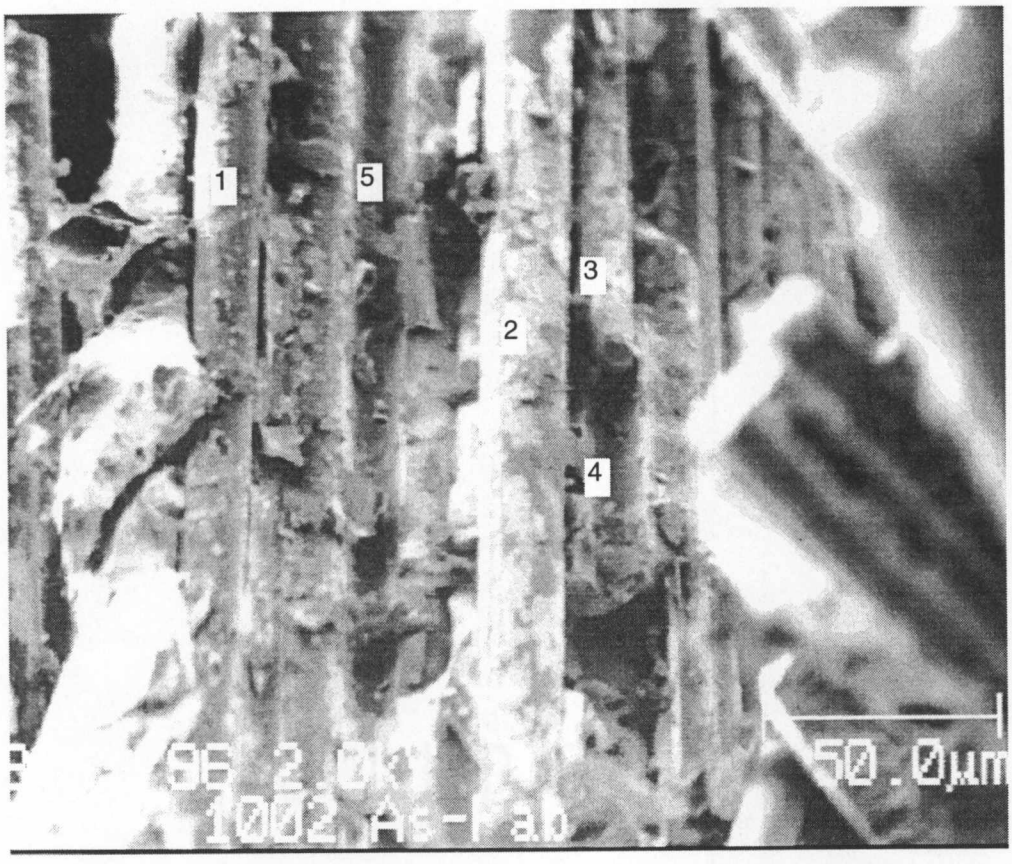


Fig. B.6.64. Micrograph showing three fibers (1, 2, 3) and two troughs (4, 5) selected for AES analyses in the CVI 1002 composite

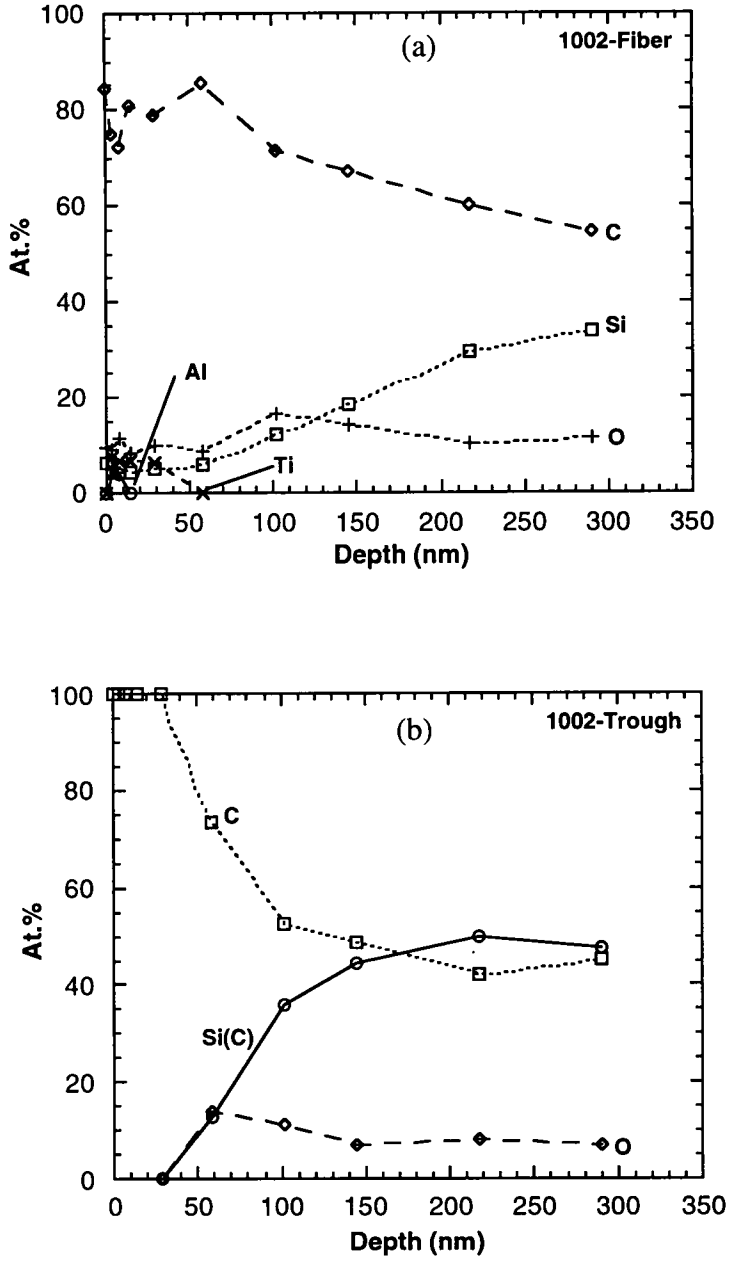


Fig. B.6.65. Compositional depth profiles obtained on the CVI 1002 composite in the as-processed condition (a) Fiber and (b) Trough

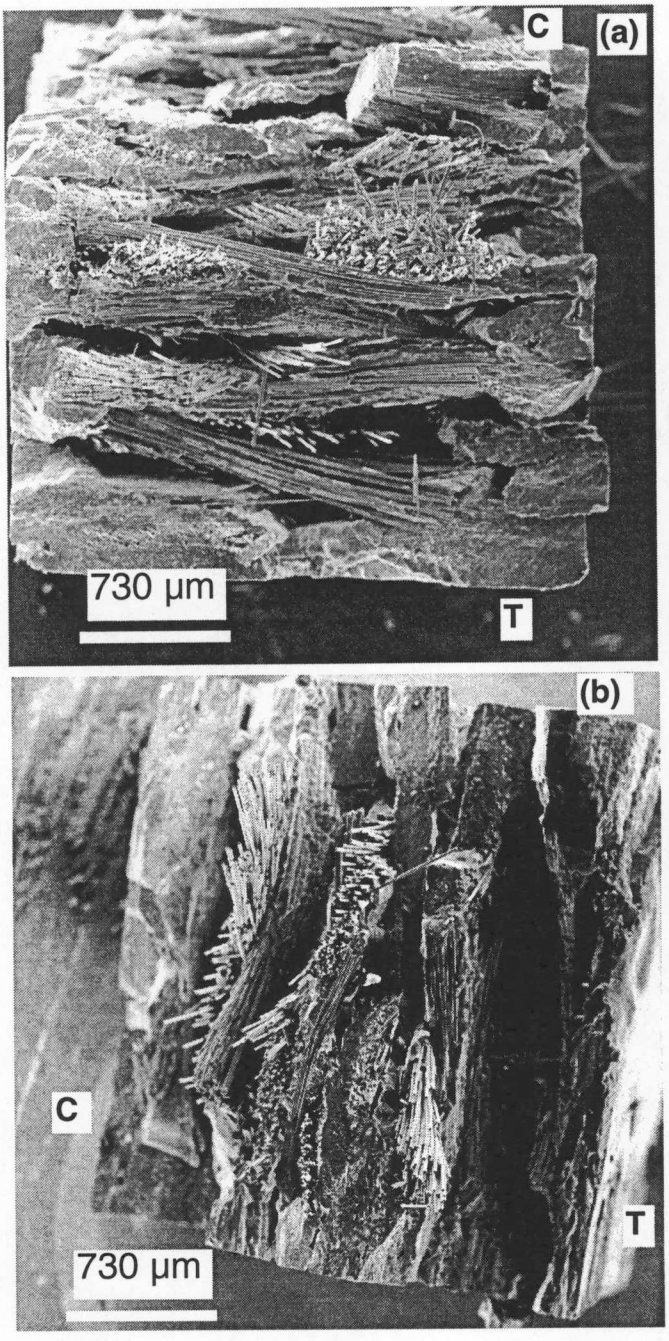


Fig. B.6.66. CVI 1002 fracture surface after oxidation at 1000°C in air (a) 200 h exposure and (b) 500 h exposure. Note that with increasing exposure time at 1000°C, the fiber pullout is confined to the interior of the composite, and the regions adjacent to the tensile edge exhibit brittle fracture

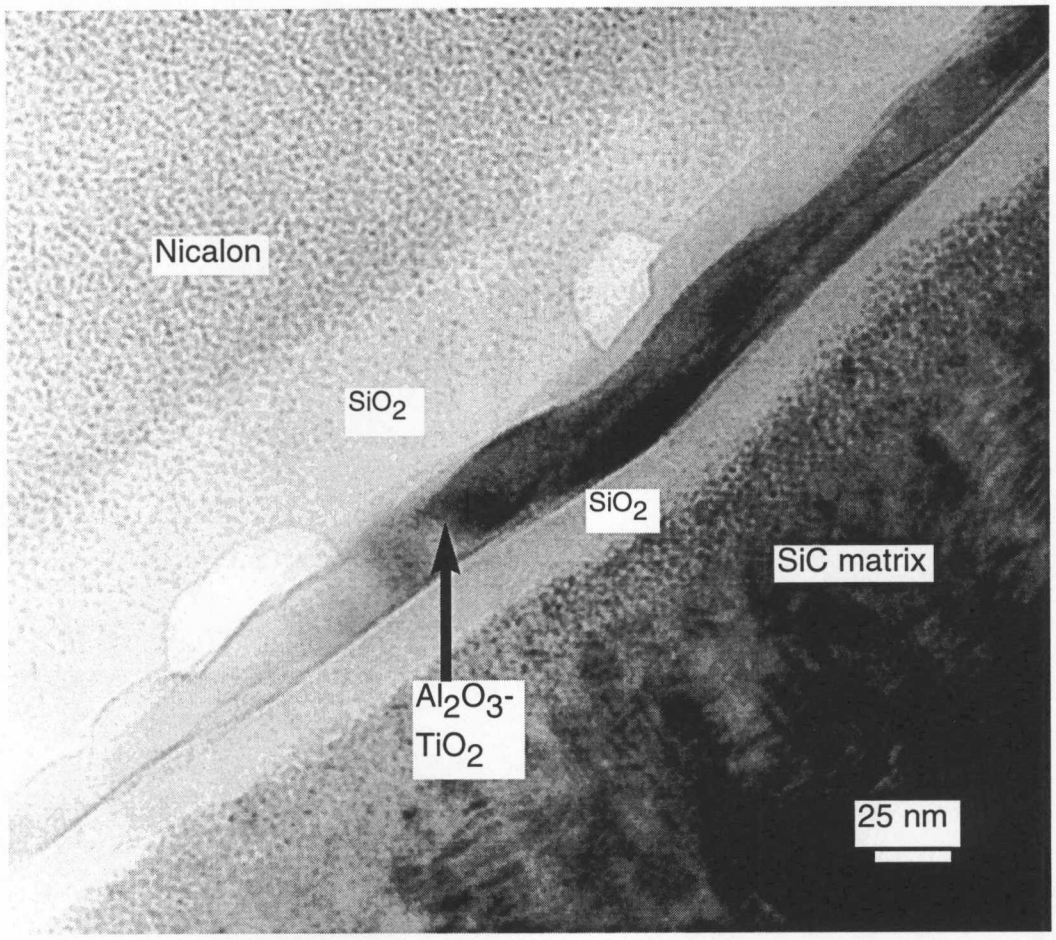


Fig. B.6.67. After oxidation for 500 h at 1000°C in air, a TEM image showing that C layers are replaced by SiO_2 along with the degradation of the Nicalon fiber surface. However, the Al_2O_3-TiO_2 layer (~30-50 μm thick) is intact

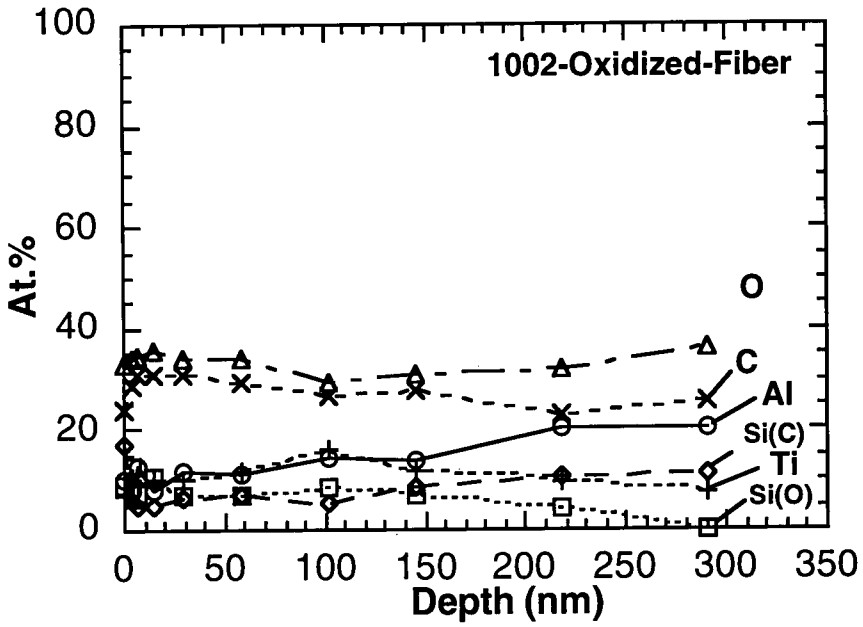


Fig. B.6.68. Al_2O_3-TiO_2 layer persisting even after 20 min of Ar sputtering on one fiber in the CVI 1002 composite oxidized for 500 h at 1000°C

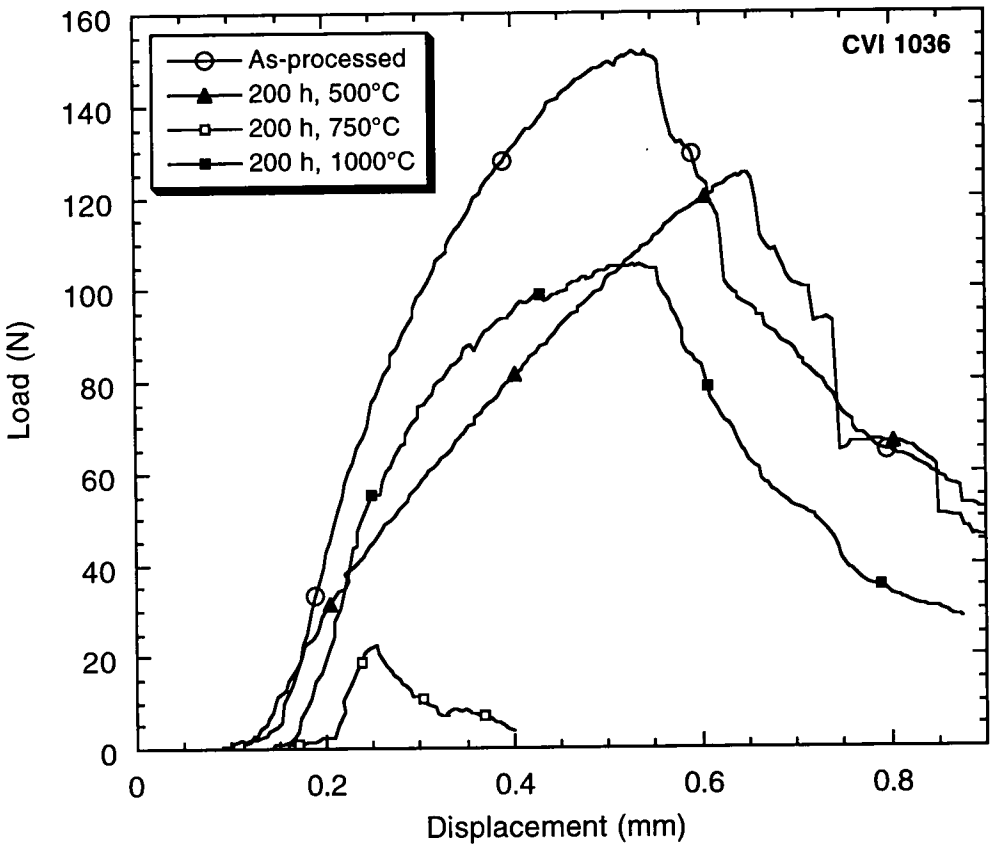


Fig. B.6.69. CVI 1036 composite (C/Al_2O_3-TiO_2/C interface) exhibiting good load bearing capacity and graceful failure in the as-processed condition as well as after oxidation for 200 h each at 500°C and 1000°C. Note that the flexure bars exposed to 750°C, however, undergo drastic reduction (79%) in strength

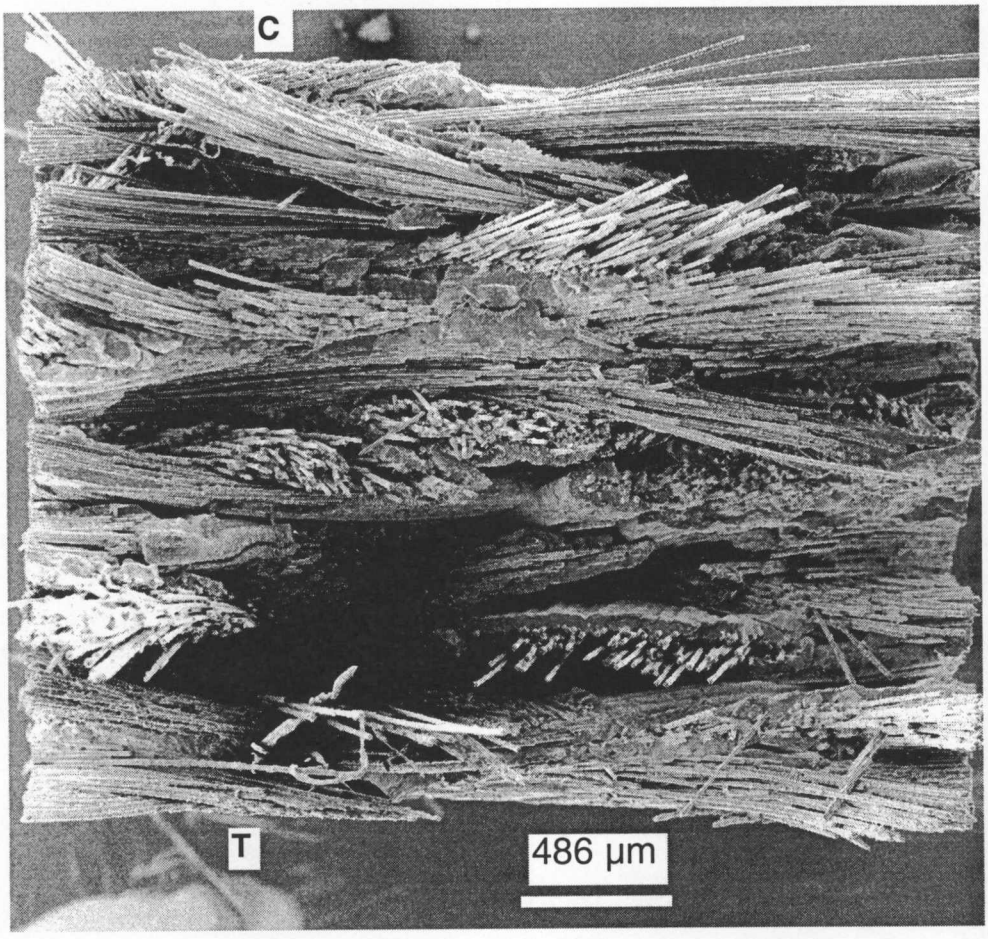


Fig. B.6.70. Fracture surface of a CVI 1036 composite in the as-processed condition showing considerable amount of fiber pullout

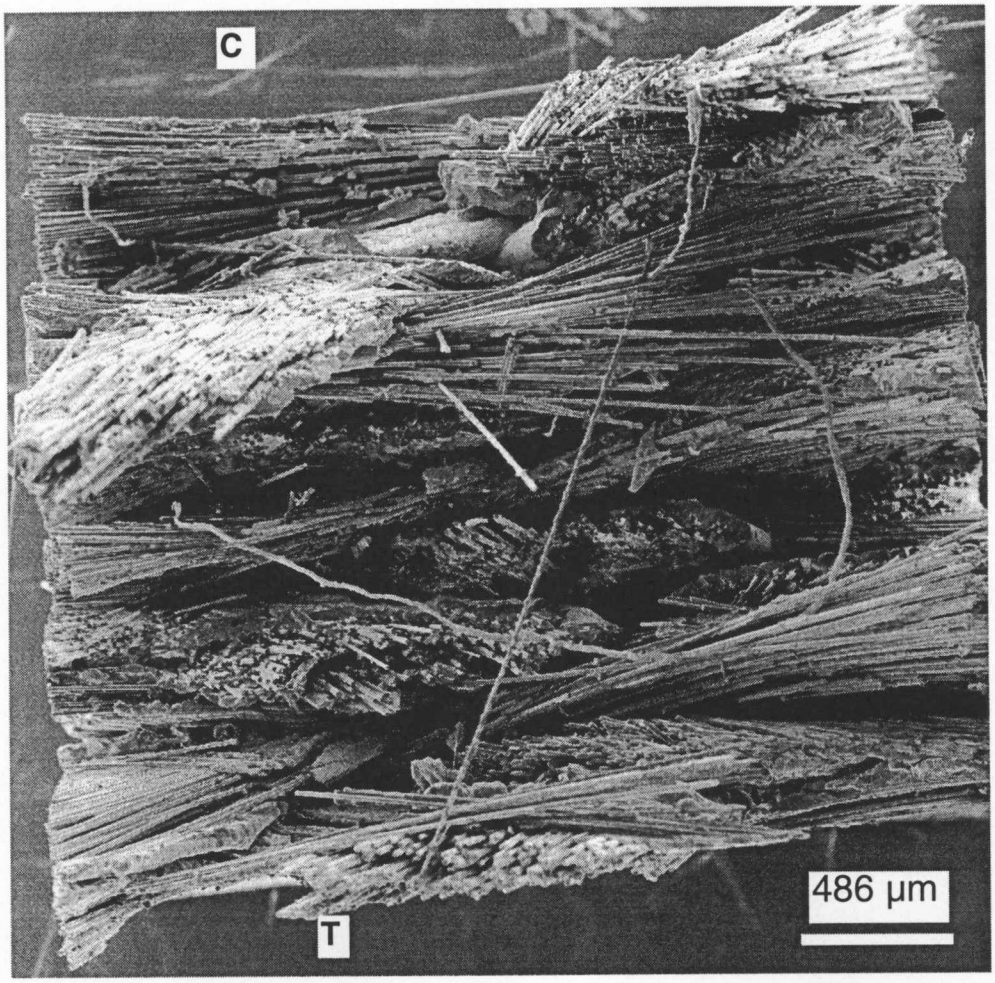


Fig. B.6.71. CVI 1036 composite showing considerable amount of fiber pullout even after 200 h exposure at 500°C in air

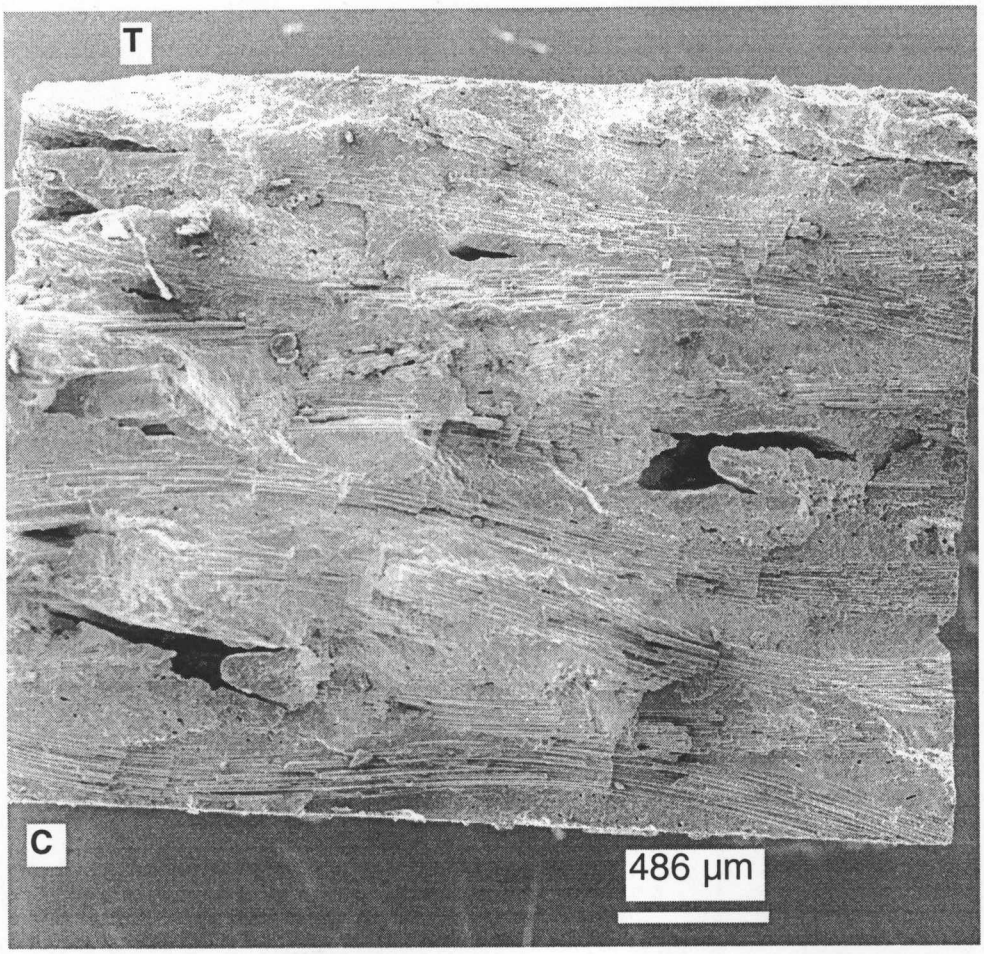


Fig. B.6.72. After oxidation at 750°C for 200 h in air, the CVI 1036 composite fracture surface showing brittle fracture

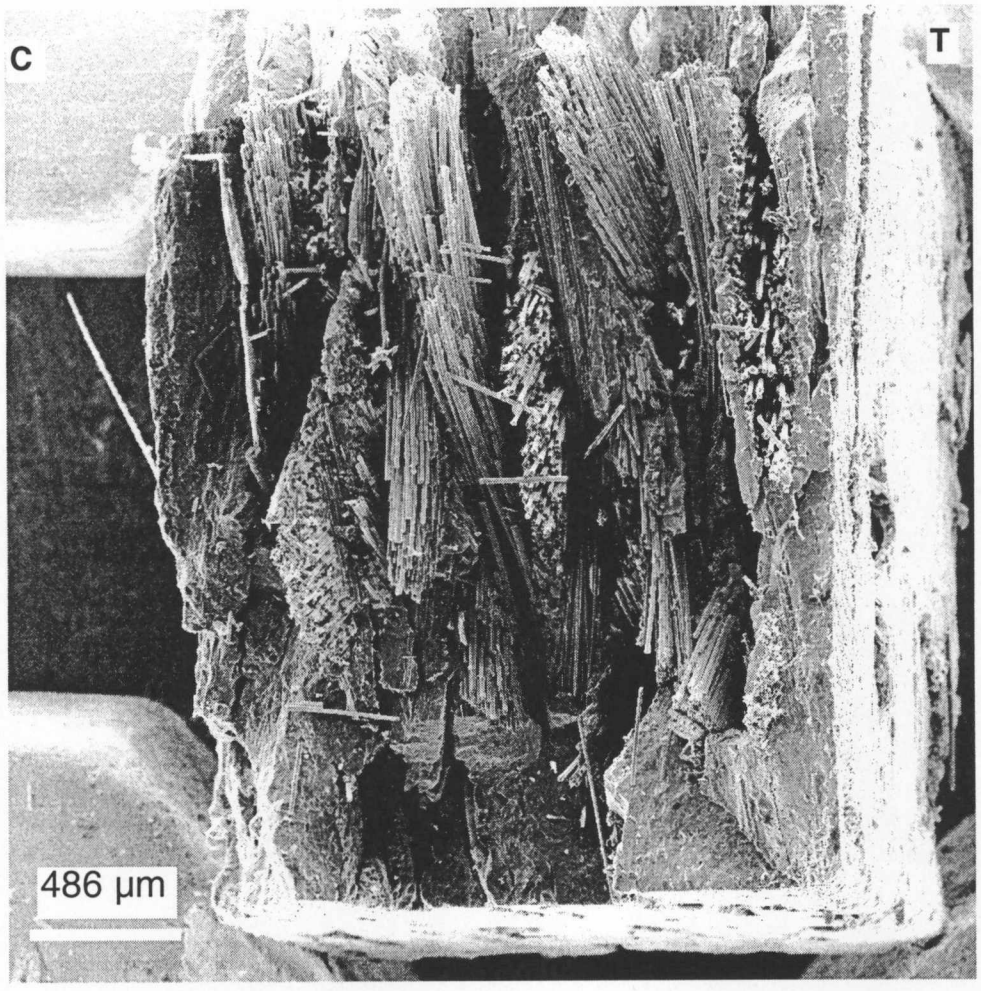


Fig. B.6.73. CVI 1036 composite fracture surface displaying reduced amount of fiber pullout after 200 h oxidation at 1000°C in air. Note that near the edges of the sample, only brittle fracture is observed

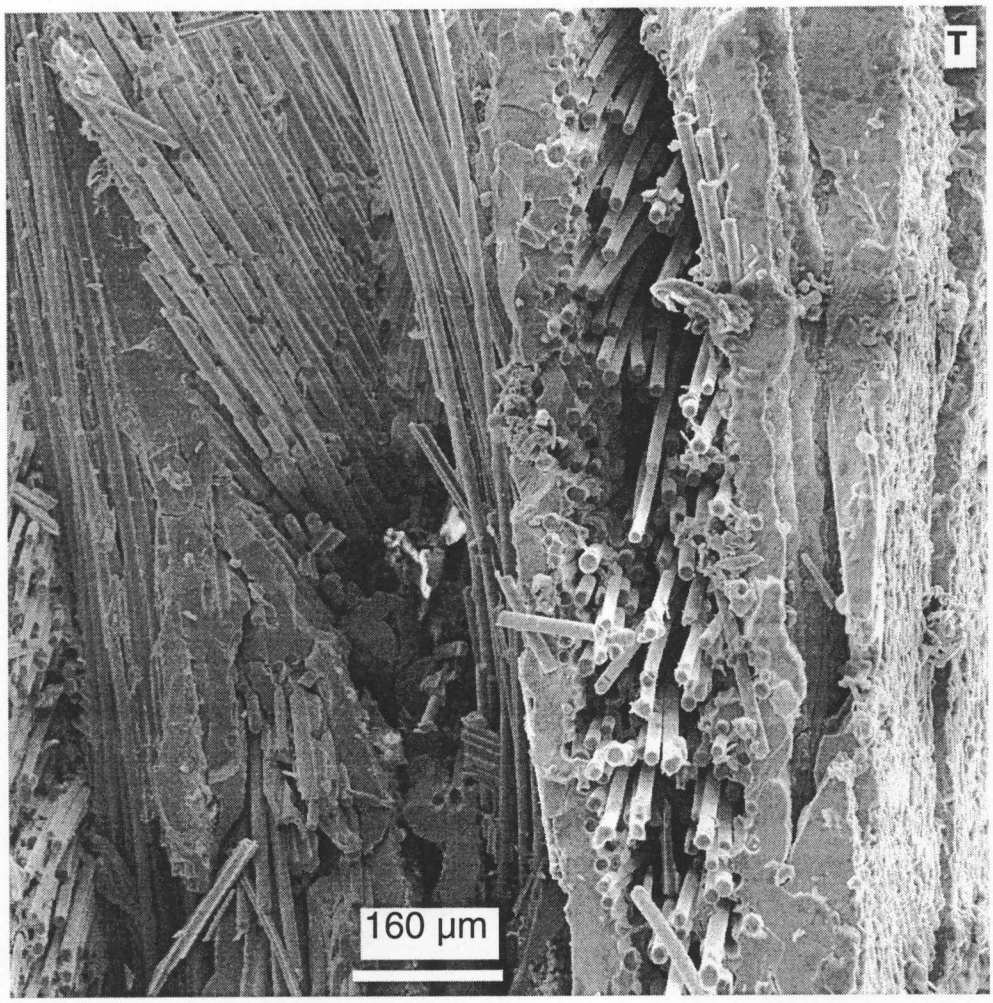


Fig. B.6.74. Fracture surface showing the embrittlement zone near the tensile edge (~300 µm) in the CVI 1036 composite after 200 h oxidation at 1000°C



Fig. B.6.75. CVI 1066 composite (C/Al_2O_3-TiO_2/C interface) fracture surface in the as-processed condition showing good amount of fiber pullout

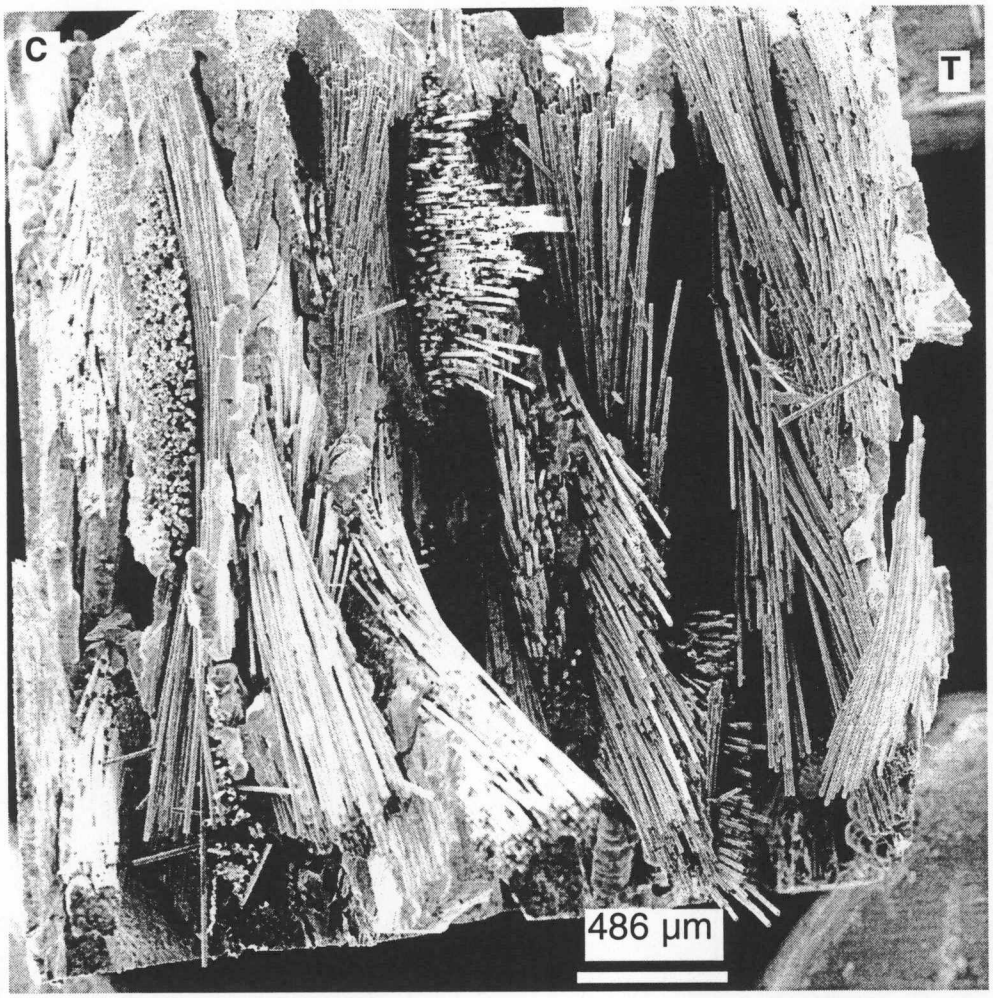


Fig. B.6.76. Fracture surface of a CVI 1066 composite showing good amount of fiber pullout even after oxidation for 24 h at 1000°C

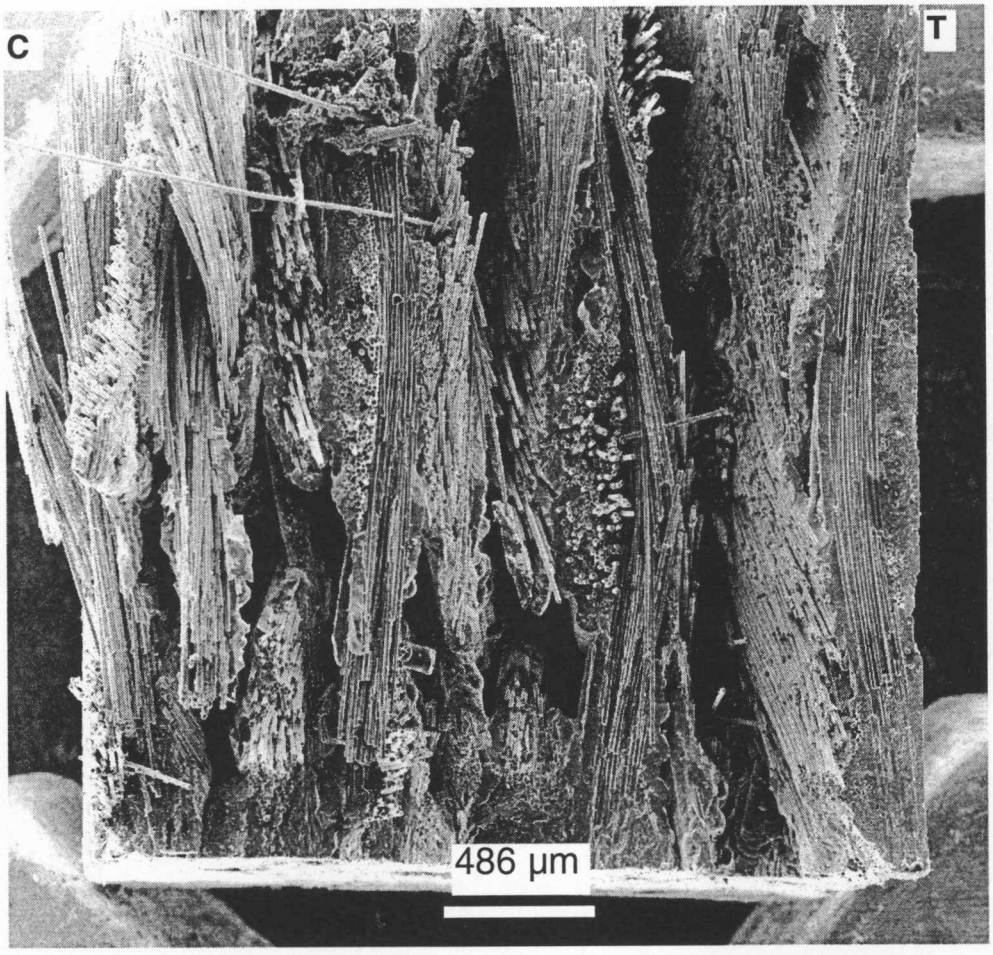


Fig. B.6.77. CVI 1066 fracture surface after 200 h oxidation at 1000°C showing good amount of fiber pullout. Note that the composite underwent only 14% strength reduction compared to the as-processed condition

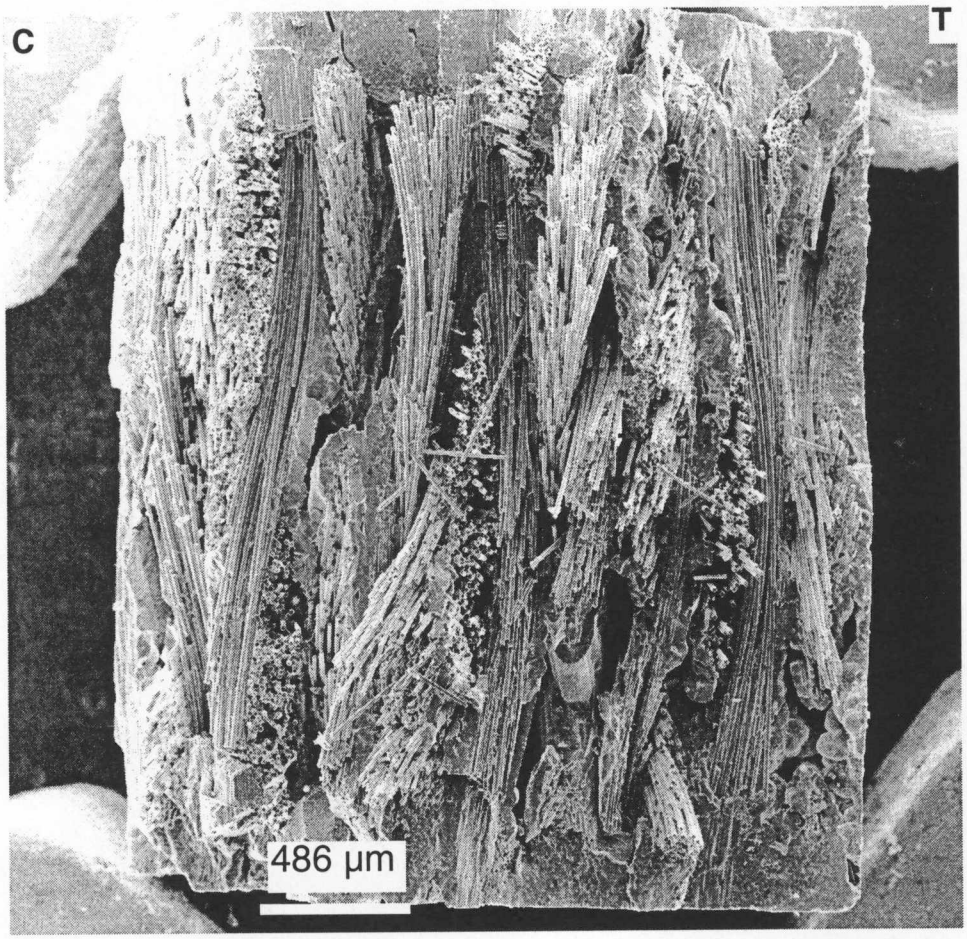


Fig. B.6.78. Fracture surface of a CVI 1066 composite, after 200 h oxidation at 1000°C followed by 200 h oxidation at 750°C in air, showing a good amount of fiber pullout

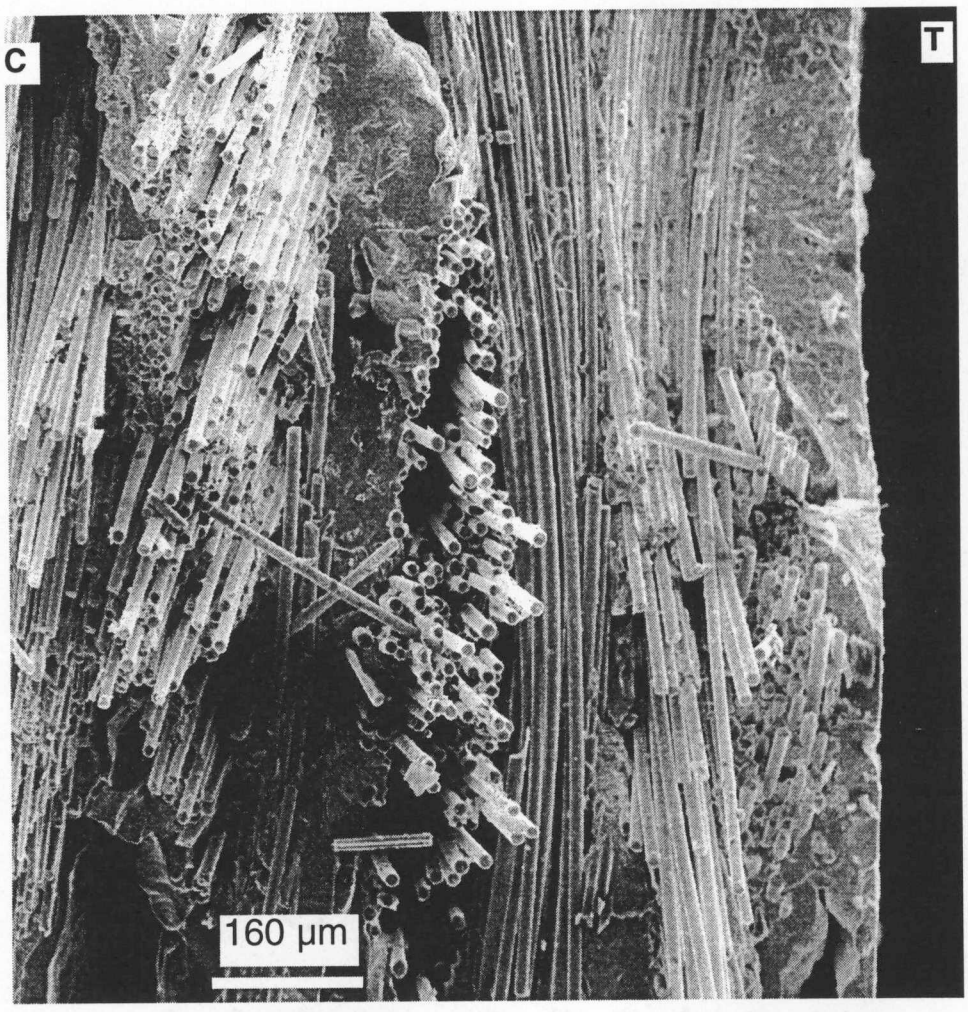


Fig. B.6.79. Fracture surface of a CVI 1066 composite (exposed at 750°C for 200 h following 200 h exposure at 1000°C in air) exhibiting an embrittlement zone ~250 µm width near the tensile edge

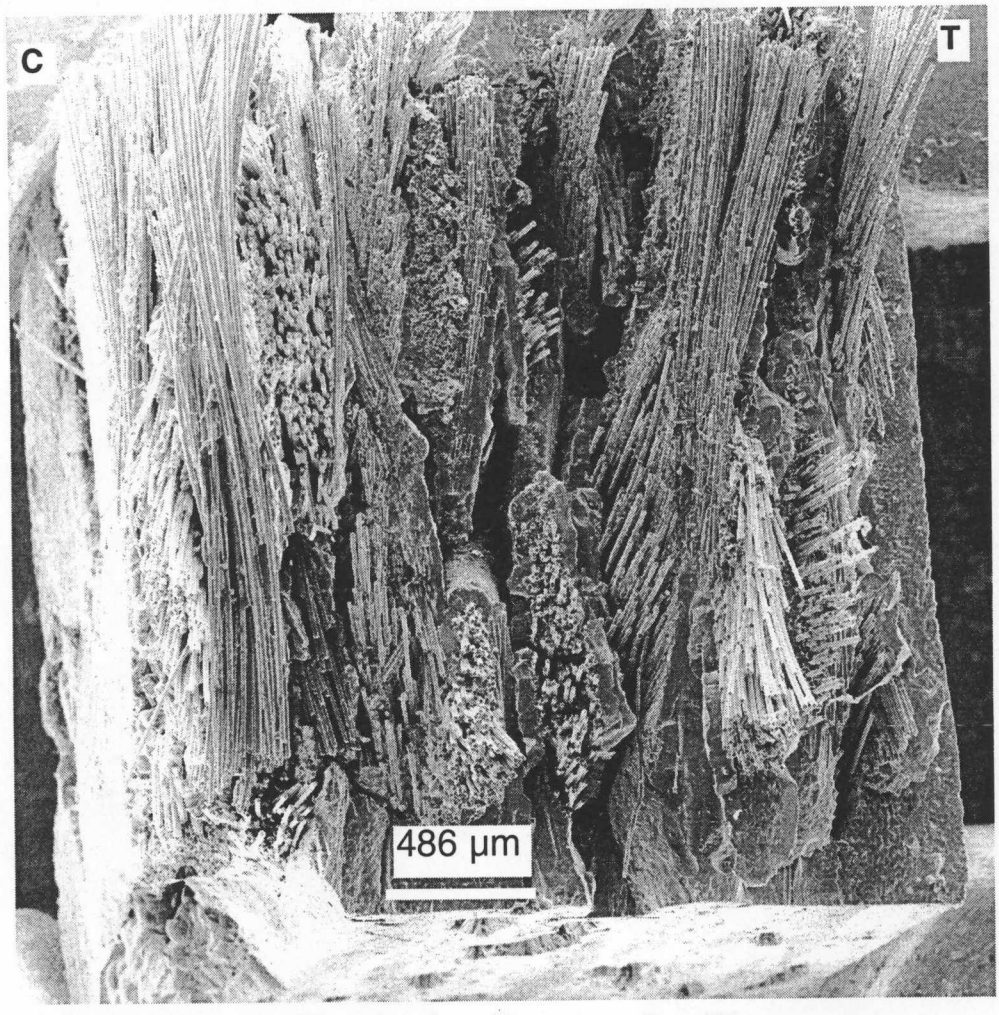


Fig. B.6.80. CVI 1066 composite fracture surface exhibiting a considerable amount of fiber pullout in the interior even after 500 h oxidation at 1000°C in air. However, brittle fracture is occurring near the edges of the sample

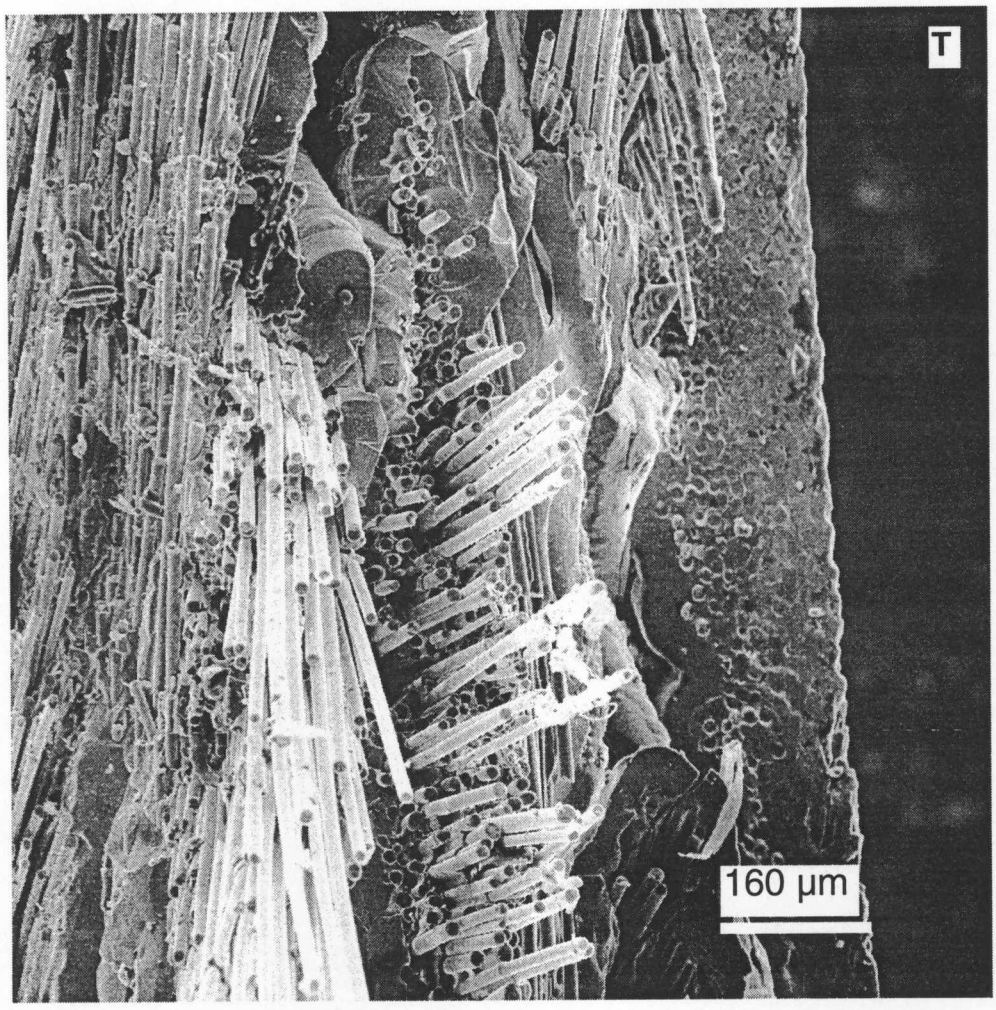


Fig. B.6.81. CVI 1066 composite fracture surface showing the embrittlement zone near the tensile edge (~ 300 µm wide) after 500 h oxidation at 1000°C in air

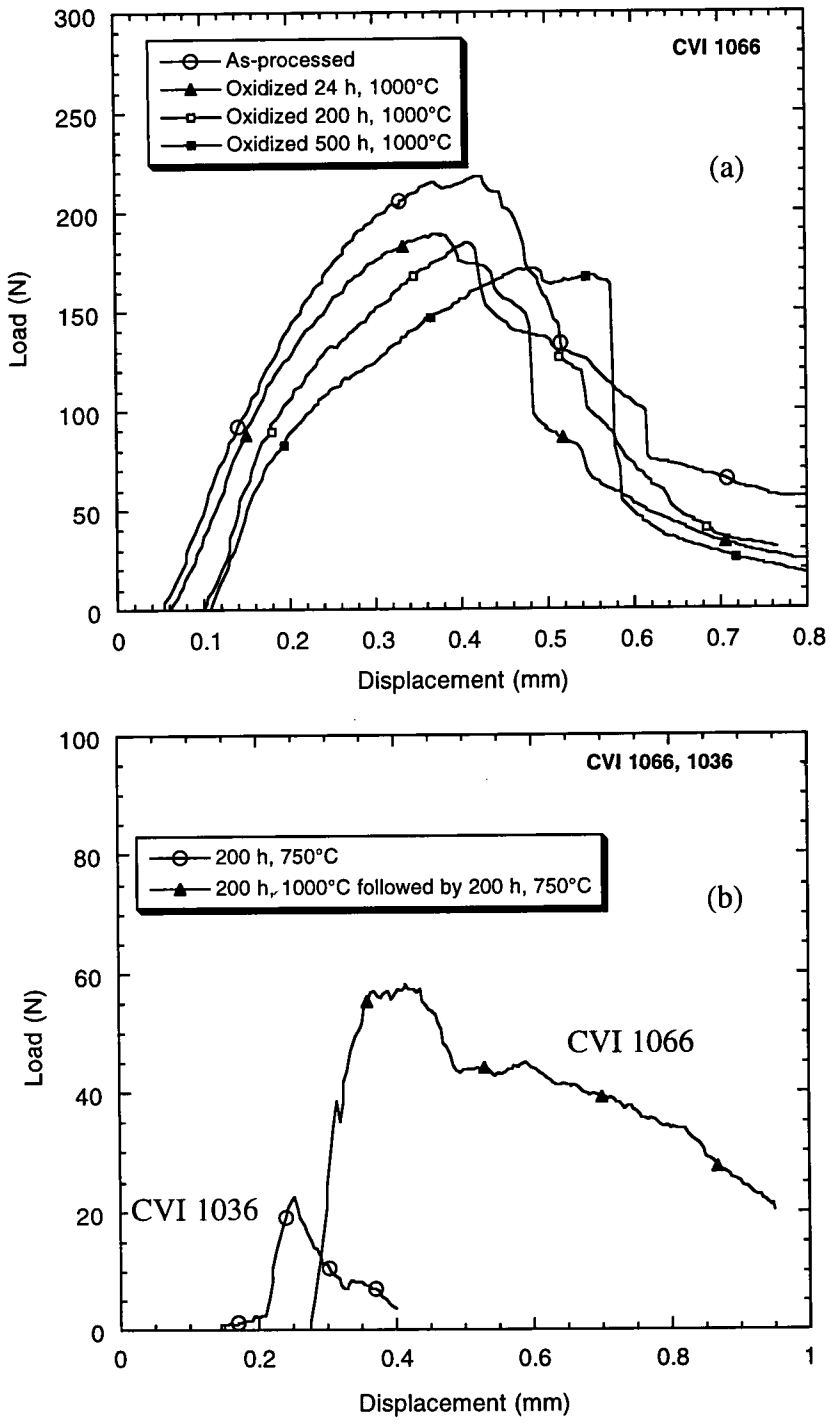


Fig. B.6.82 (a) Representative load vs displacement curves of a CVI 1066 composite in the as-processed and after oxidation at 1000°C for up to 500 h in air and (b) Comparison of CVI 1066 and CVI 1036 load vs displacement curve after oxidation at 750°C for 200 h in air. Prior to 750°C oxidation, the CVI 1066 sample was exposed for 200 h at 1000°C in air

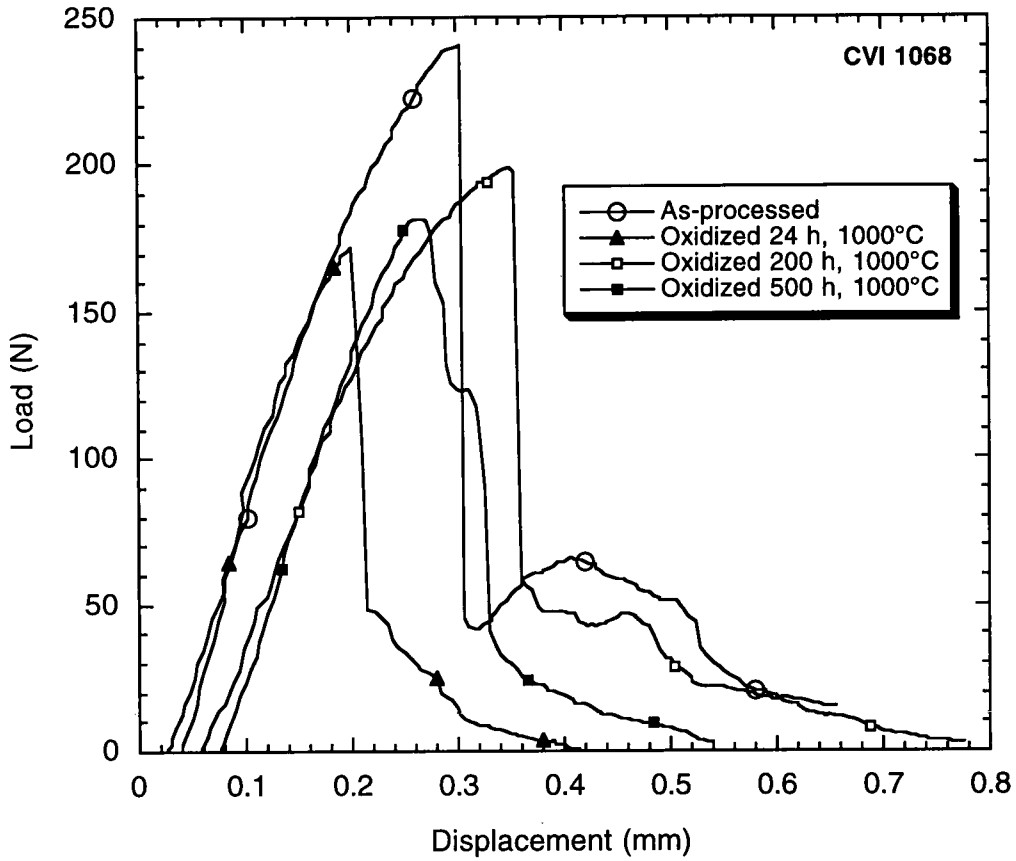


Fig. B.6.83. Representative load vs displacement curves of a CVI 1068 composite (BN interface) in the as-processed condition and after oxidation at 1000°C for up to 500 h in air



Fig. B.6.84. In the as-processed condition, the fracture surface of a CVI 1068 composite showing very little fiber pullout



Fig. B.6.85. CVI 1068 composite fracture surface exhibiting predominantly brittle fracture after oxidation at 1000°C for 24 h

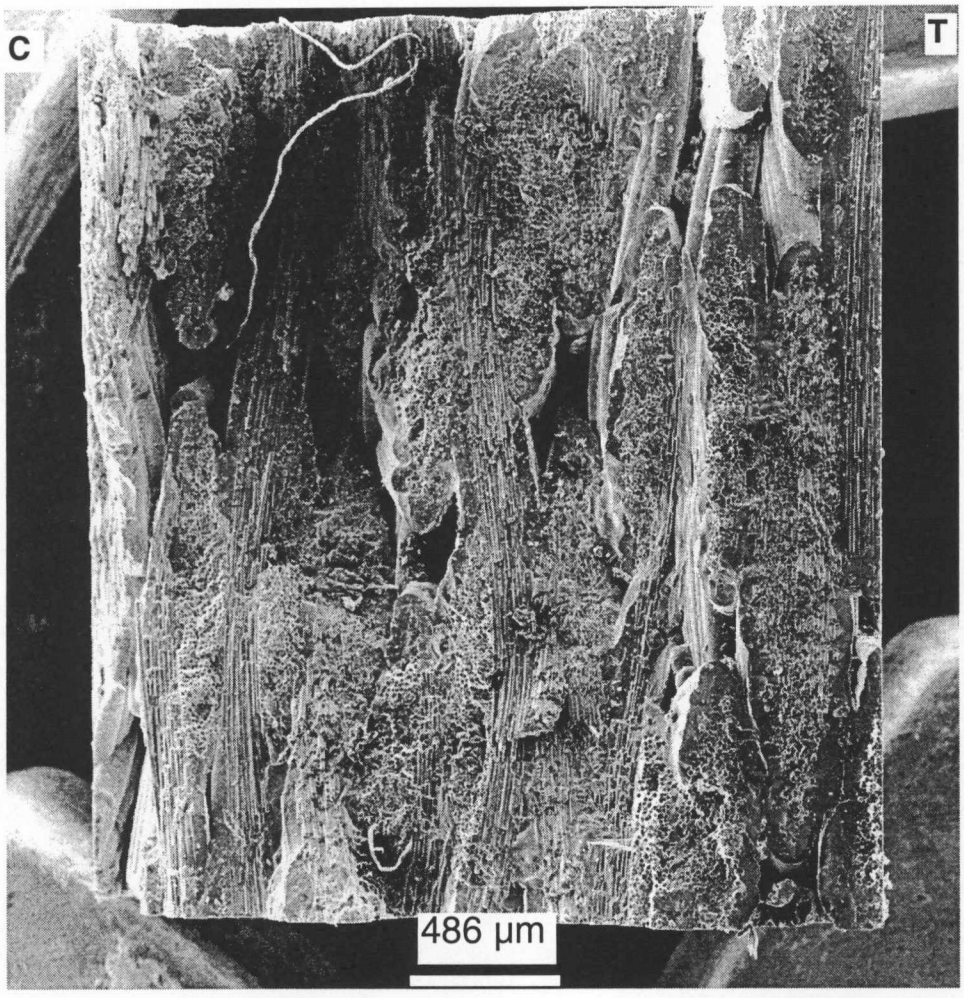


Fig. B.6.86. Fracture surface of a CVI 1068 composite after 200 h oxidation at 1000°C in air showing brittle fracture

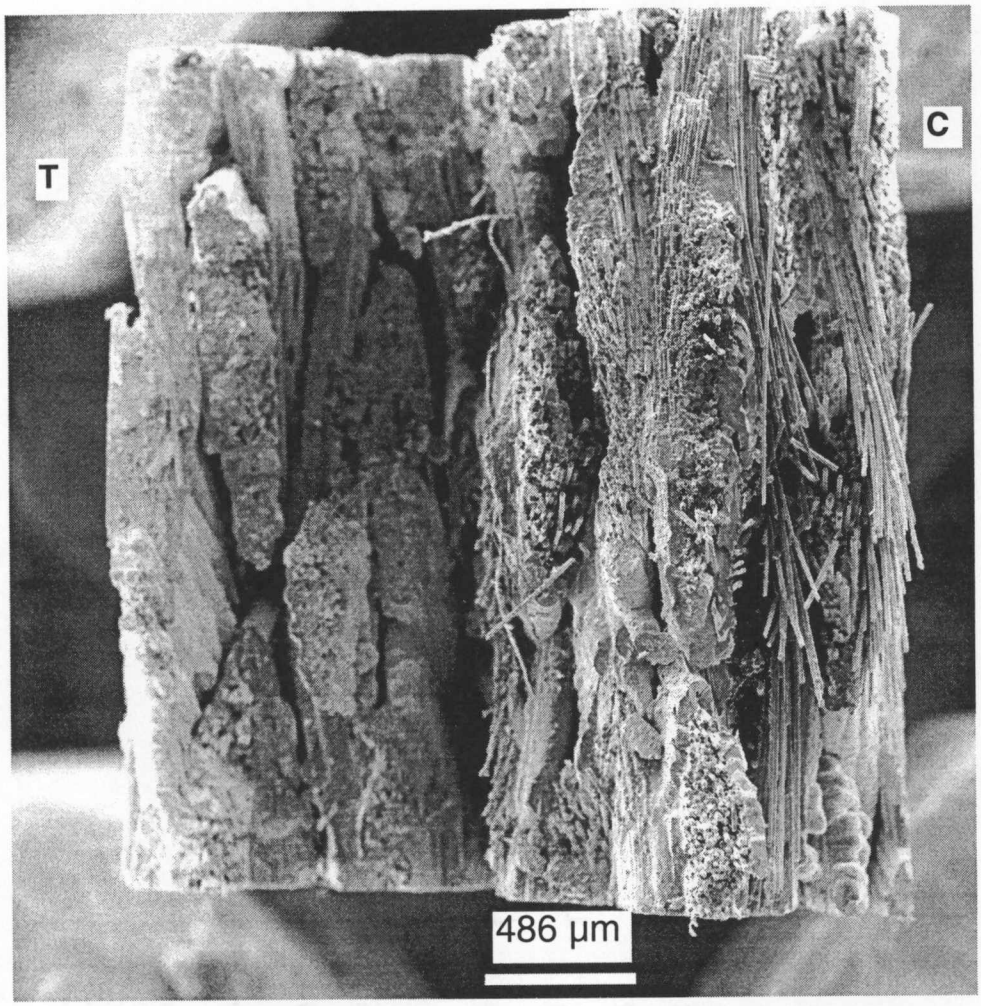


Fig. B.6.87. After 500 h oxidation at 1000°C, the fracture surface of a CVI 1068 composite showing brittle fracture in the tensile region

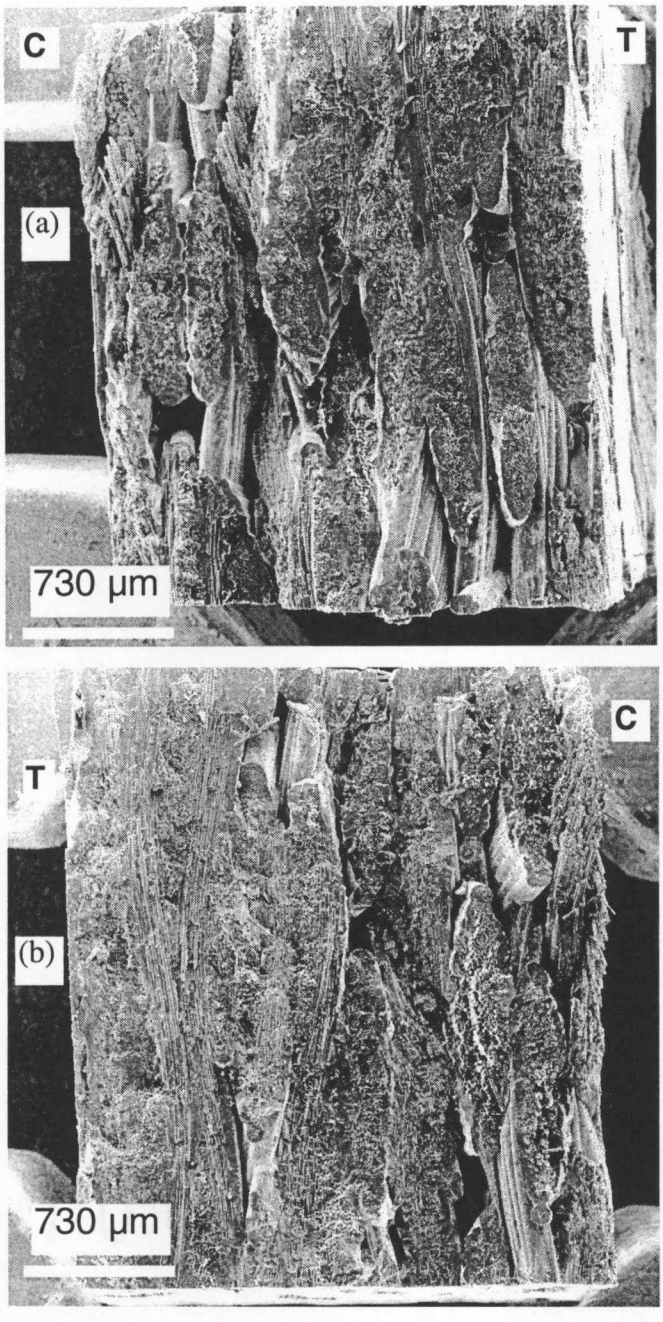


Fig. B.6.88. Fracture surface of theCVI 1068 composite after oxidation for 200 h at (a) 500°C and (b) 750°C

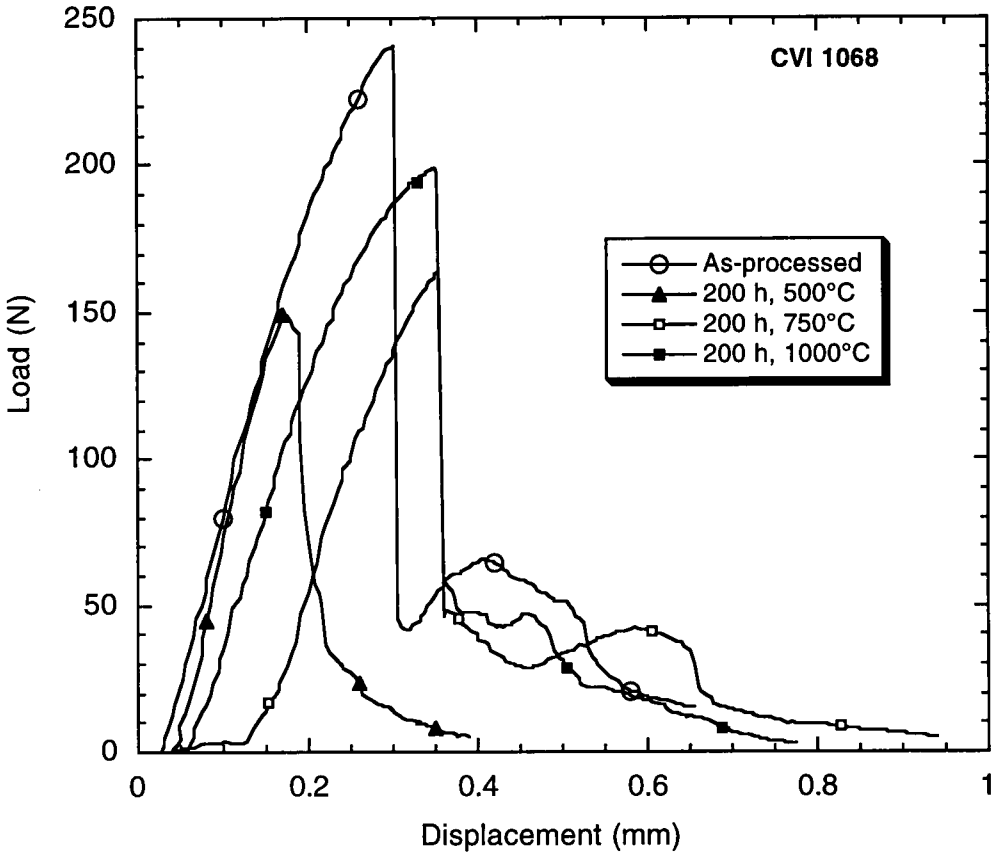


Fig. B.6.89. Representative load vs displacement curves of a composite with a BN interface in the as-processed and after oxidation conditions

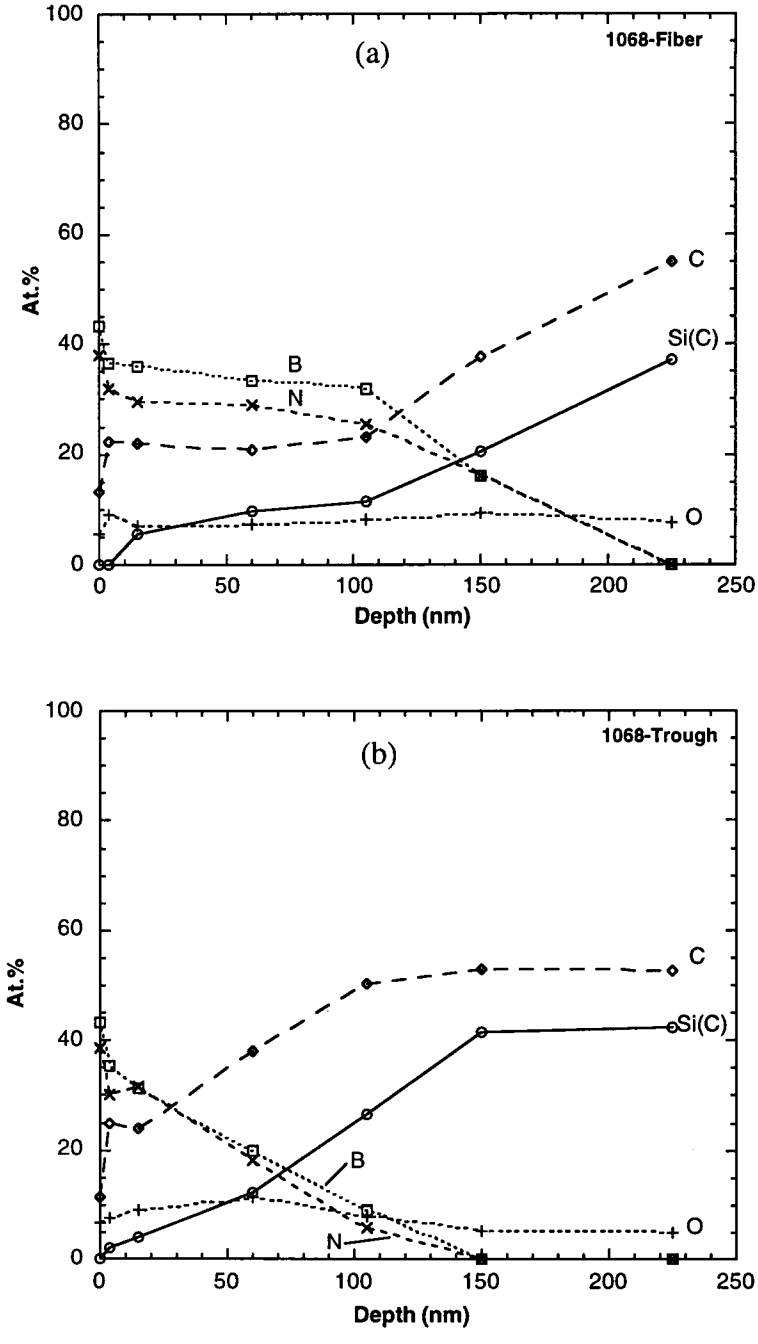


Fig. B.6.90. Compositional depth profile of a composite with a BN interface in the as-processed condition (a) Fiber and (b) Trough

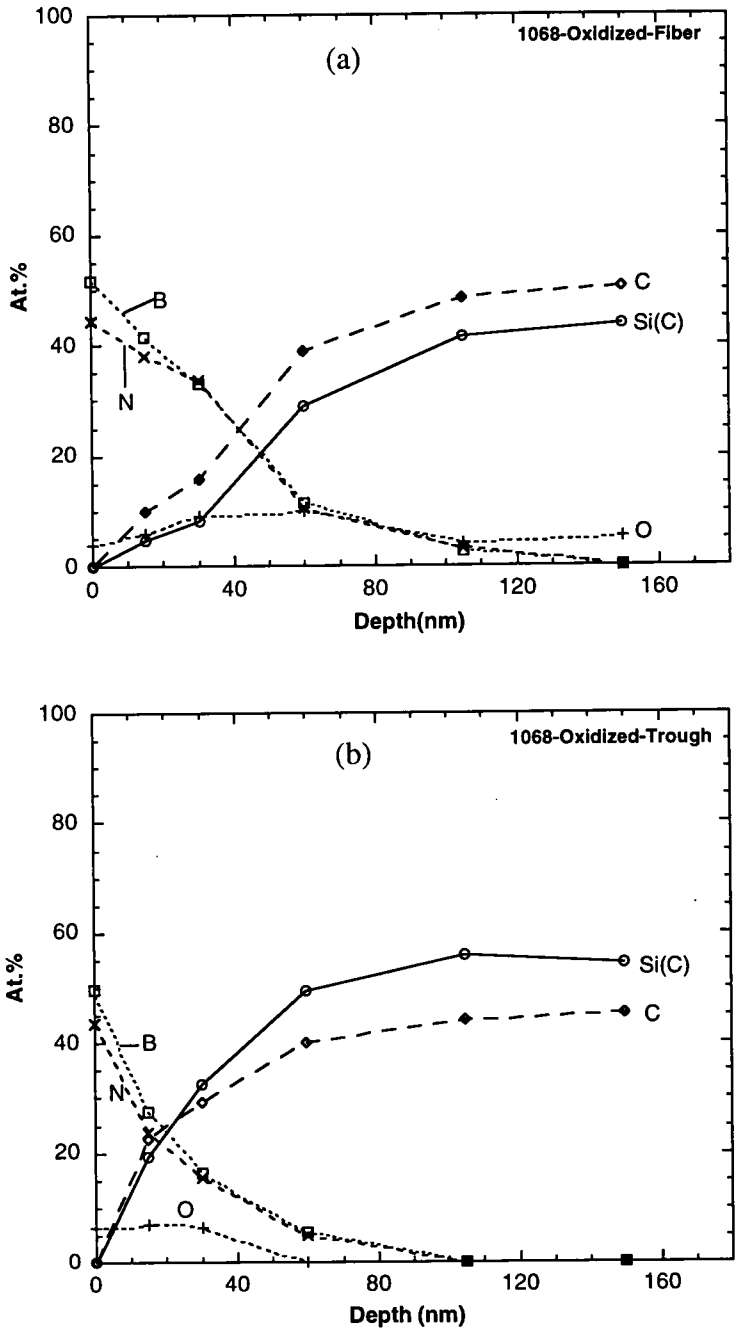


Fig. B.6.91. Compositional depth profiles obtained on a composite with a BN interface after oxidation at 1000°C for 500 h (a) Fiber and (b) Trough

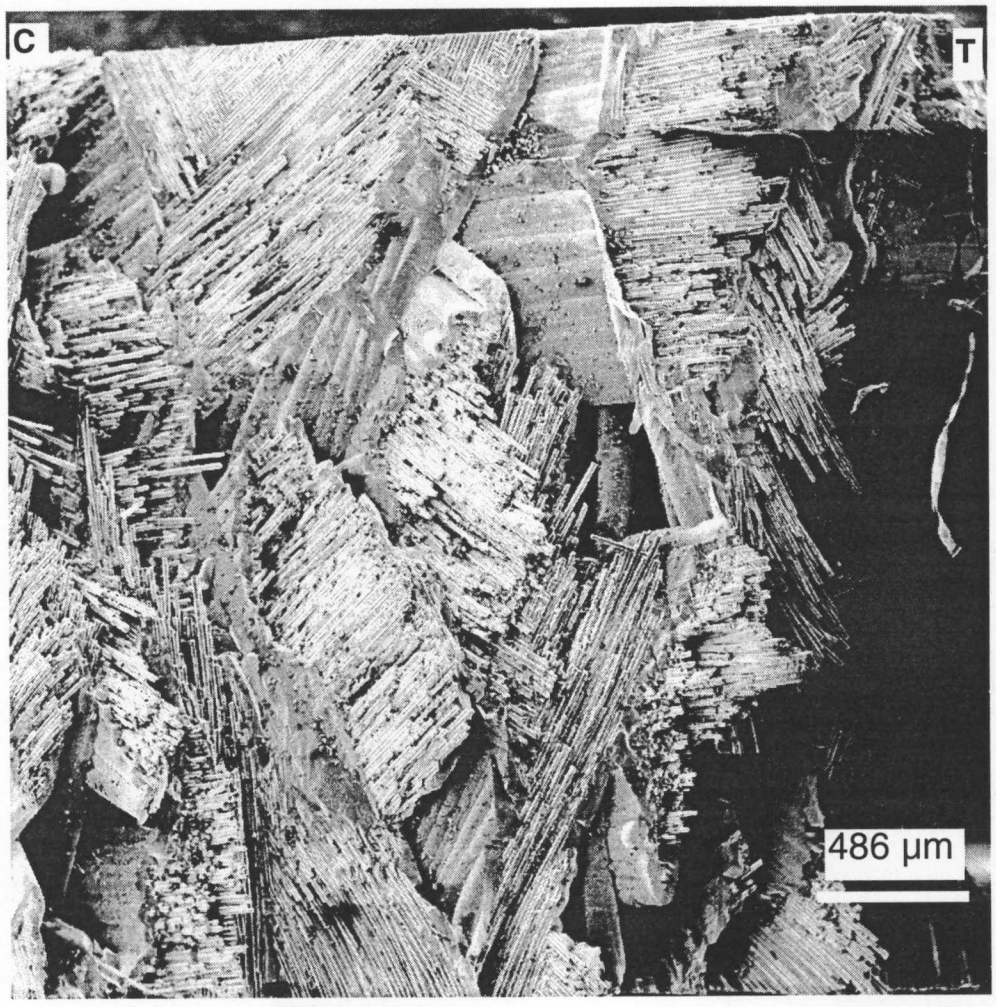


Fig. B.6.92. In the as-processed condition, the fracture surface of a composite with a BN/Al_2O_3-TiO_2/BN interface (CVI 1073) showing good amount of fiber pullout

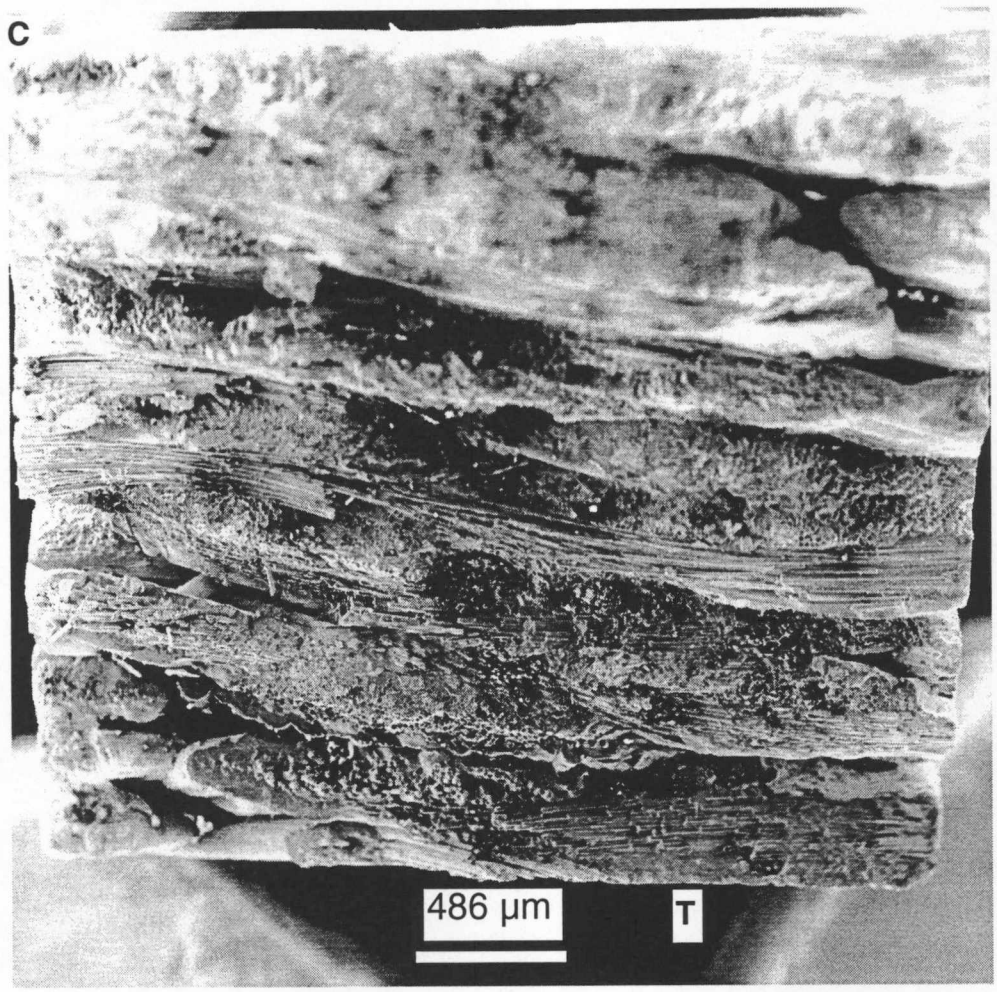


Fig. B.6.93. Fracture surface of a CVI 1073 composite after oxidation at 1000°C for 24 h showing brittle fracture with very little fiber pullout

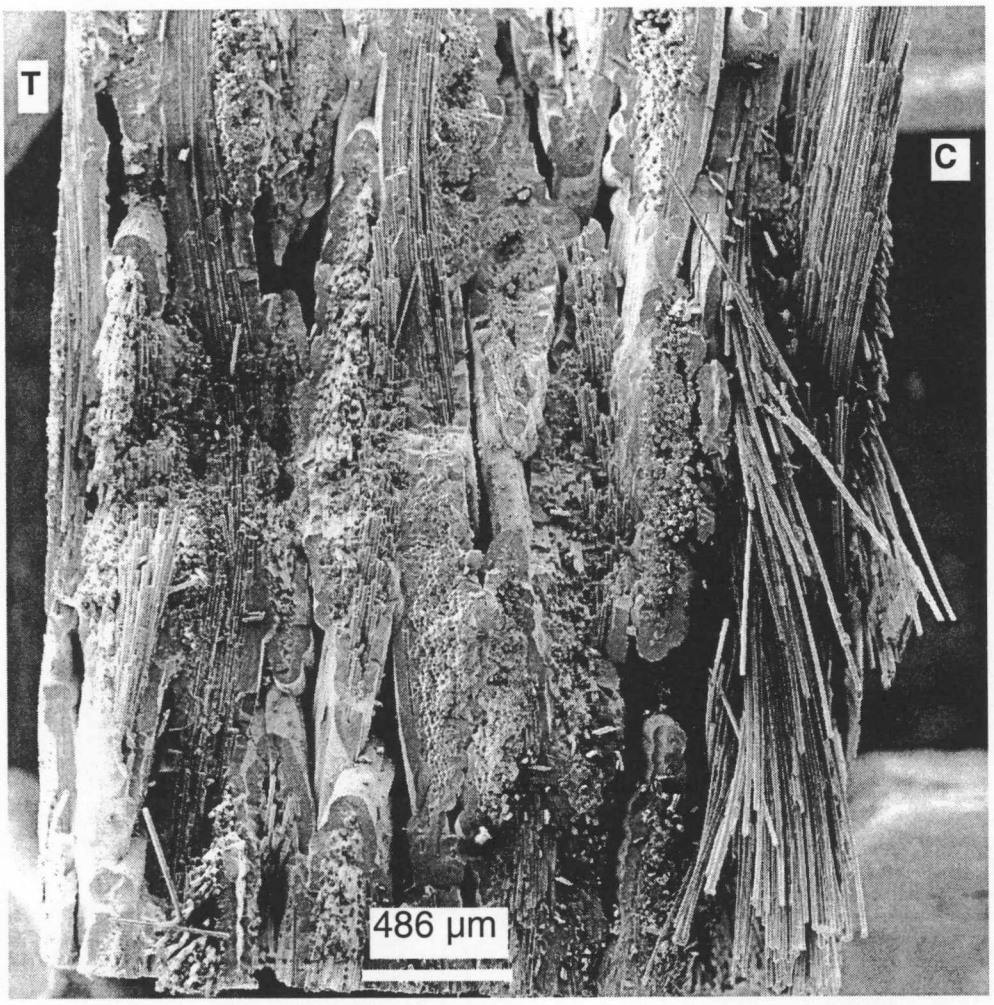


Fig. B.6.94. Fracture surface of a CVI 1073 composite after oxidation for 500 h at 1000°C showing good fiber pullout in the compressive region

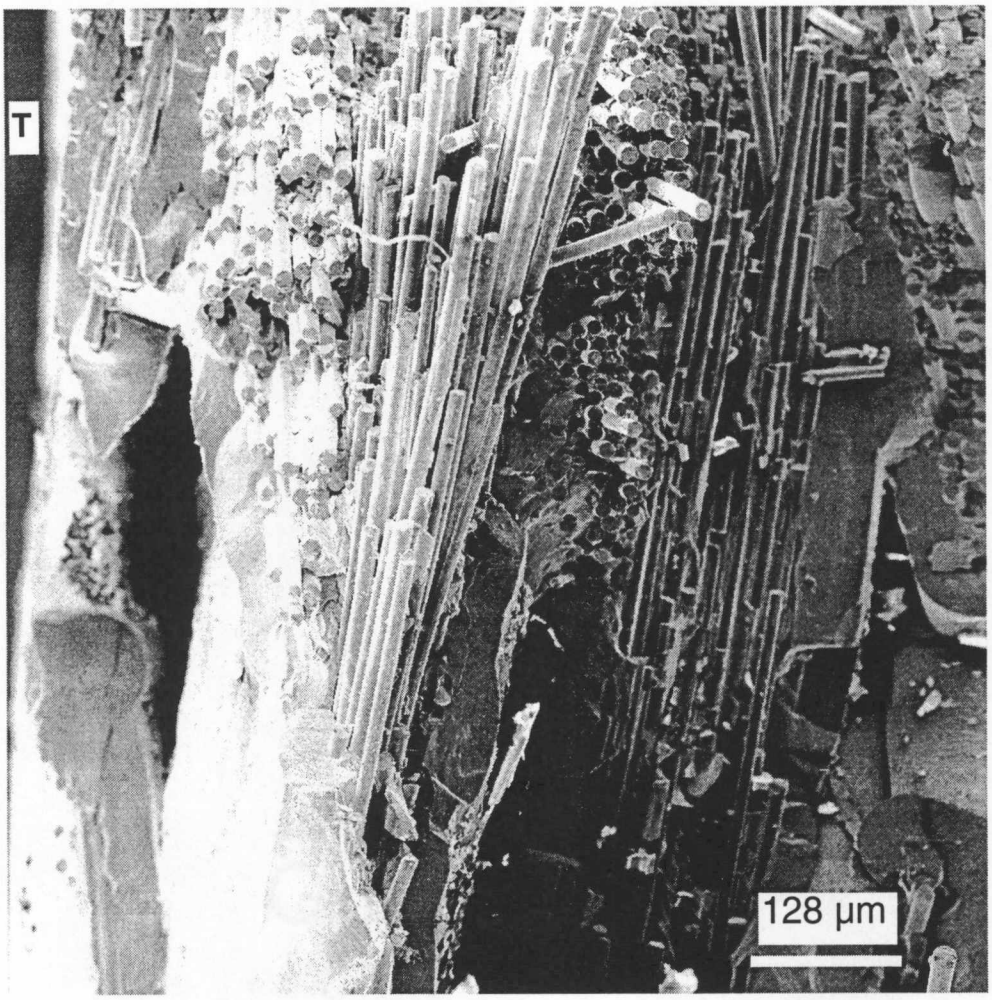


Fig. B.6.95. The tensile region of the fracture surface of a CVI 1073 composite after 500 h oxidation at 1000°C showing fiber pullout

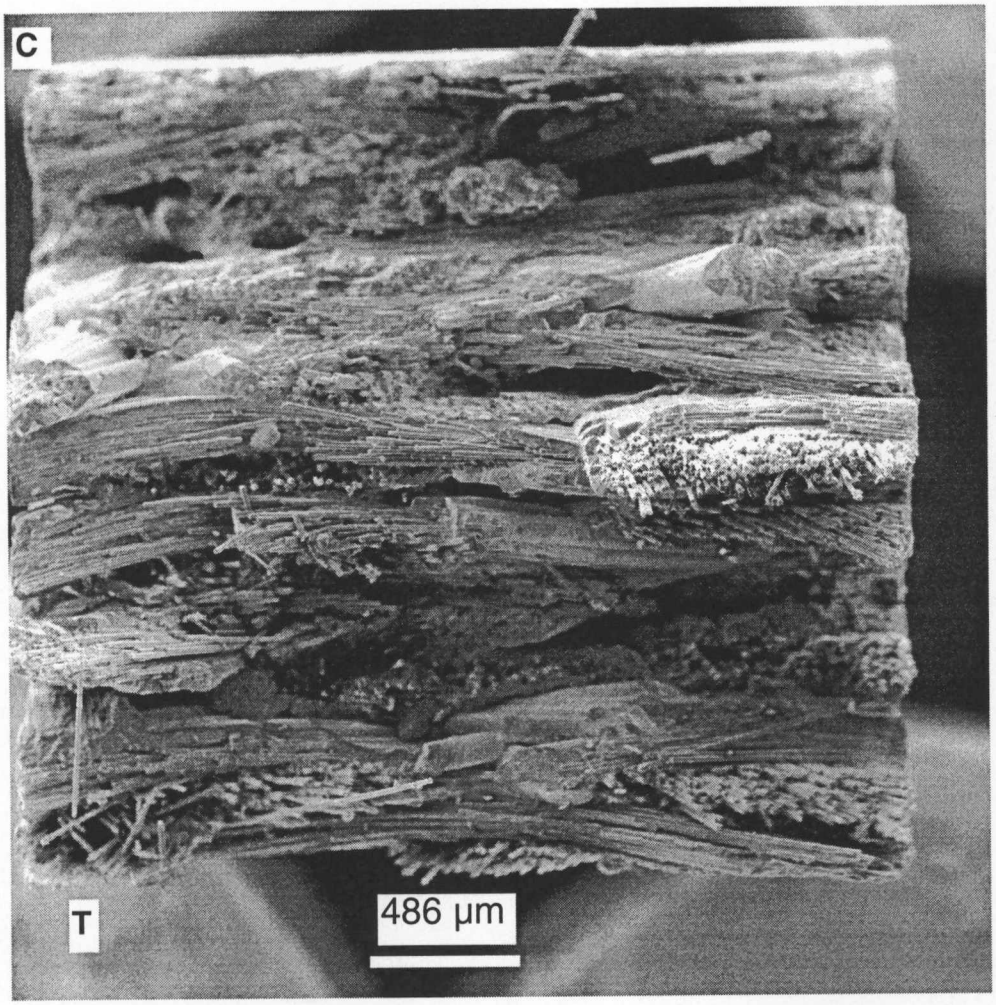


Fig. B.6.96. Fracture surface of a CVI 1073 composite after oxidation at 500°C for 200 h

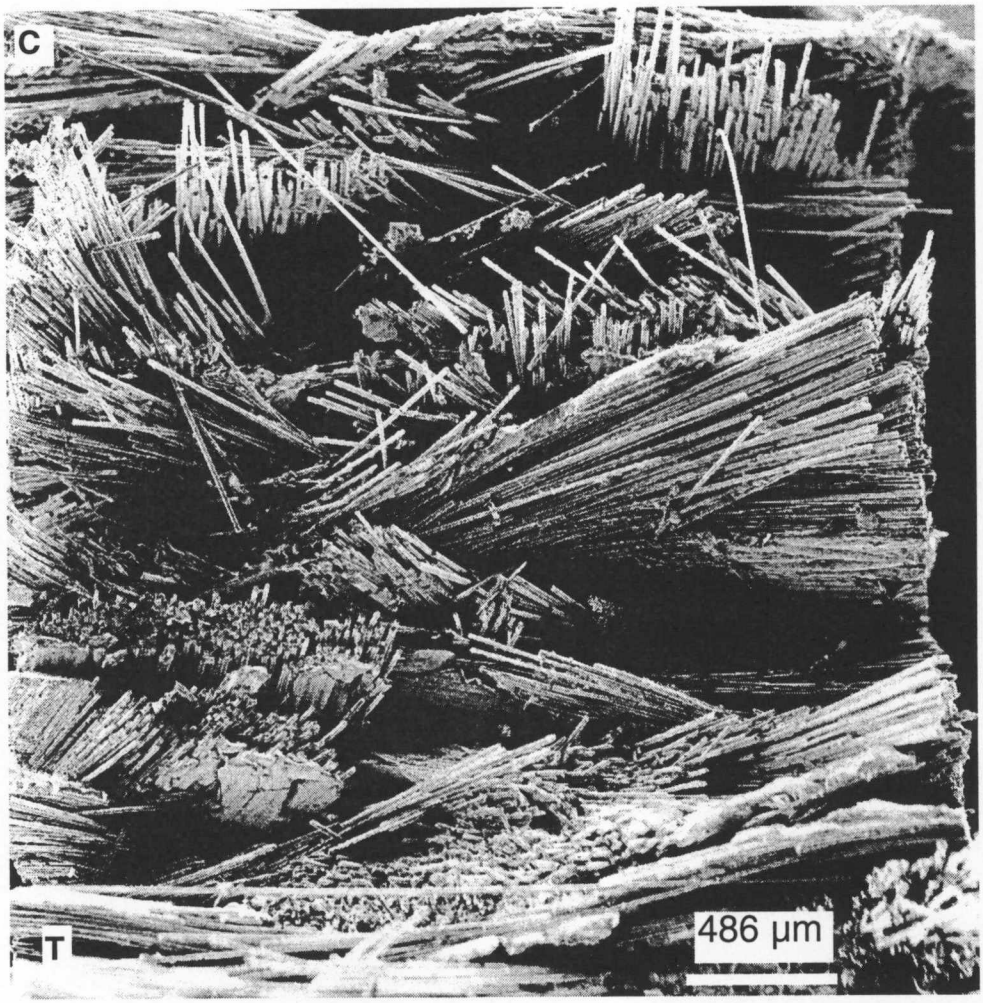


Fig. B.6.97. Fracture surface of a CVI 1073 composite after oxidation at 750°C for 200 h

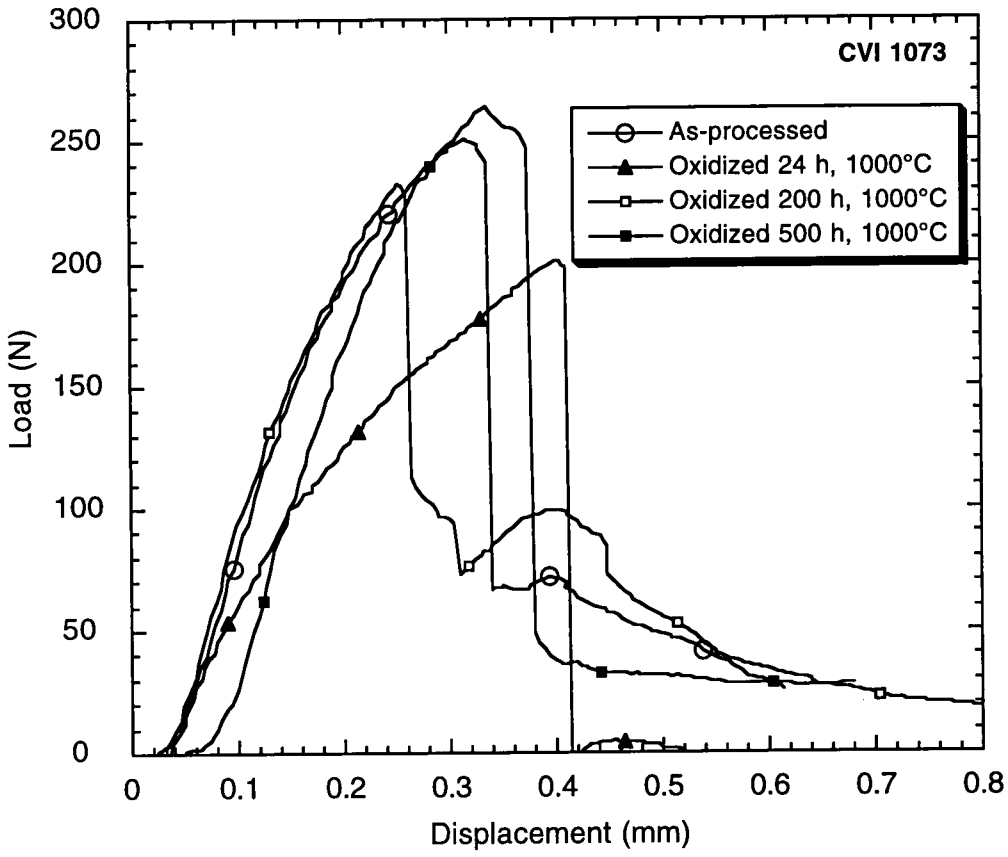


Fig. B.6.98. Representative load vs displacement curves of a composite with a BN/Al_2O_3-TiO_2/BN interface in the as-processed condition and after oxidation at 1000°C for up to 500 h

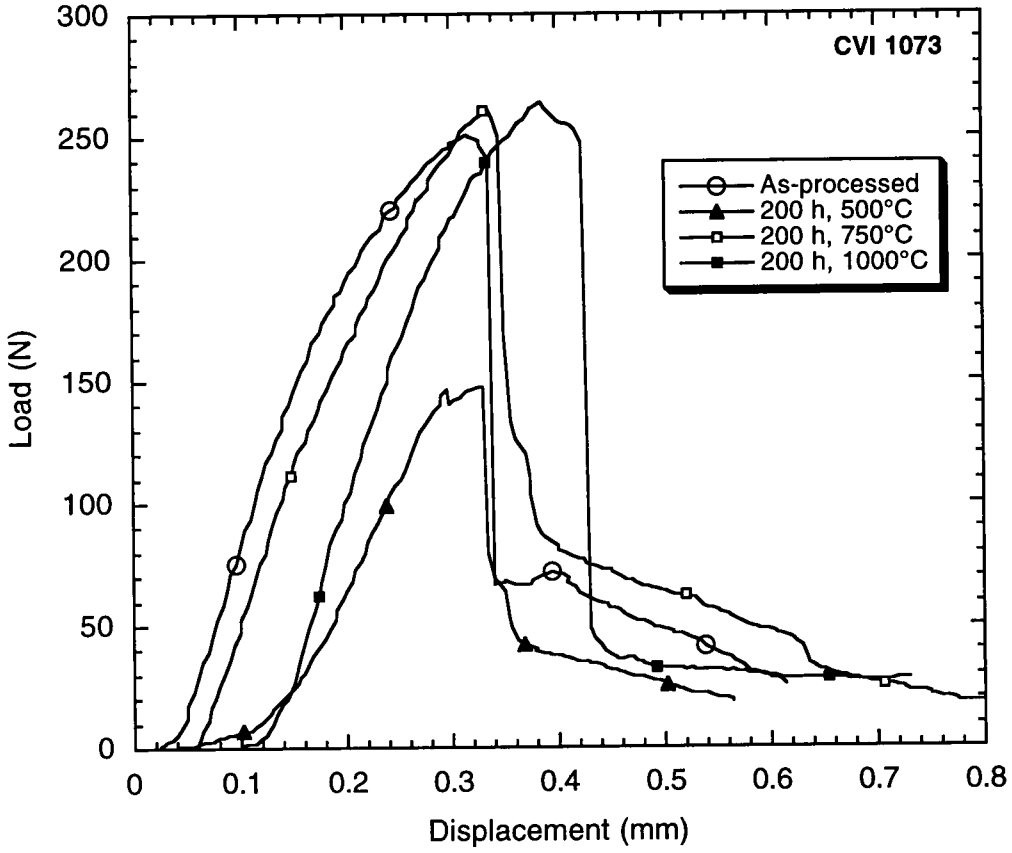


Fig. B.6.99. Representative load vs displacement curves of a composite with a BN/Al_2O_3-TiO_2/BN interface in the as-processed condition and after oxidation for 200 h each at 500°C, 750°C, and 1000°C

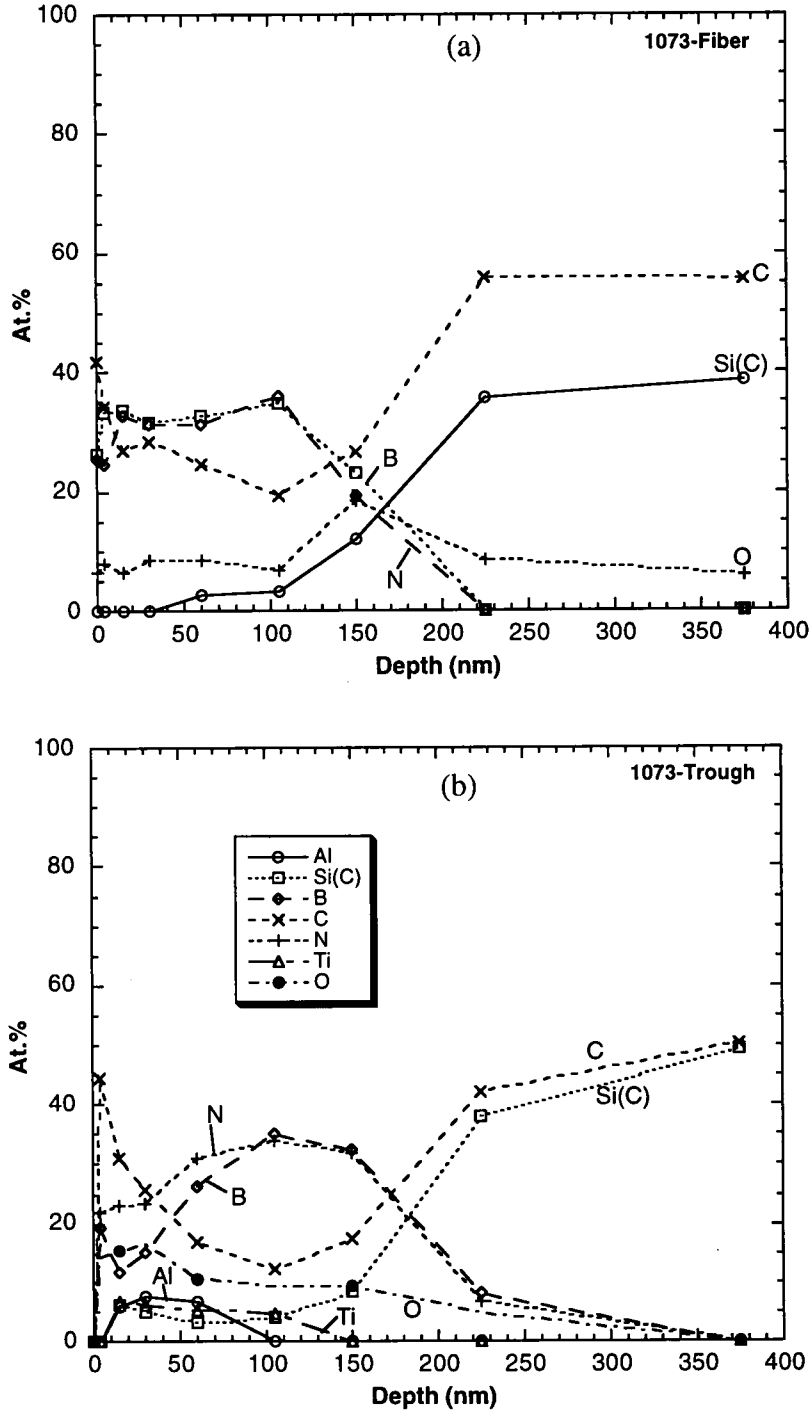


Fig. B.6.100. Compositional depth profiles on a composite with a BN/Al_2O_3-TiO_2/BN interface in the as-processed condition (a) Fiber and (b) Trough

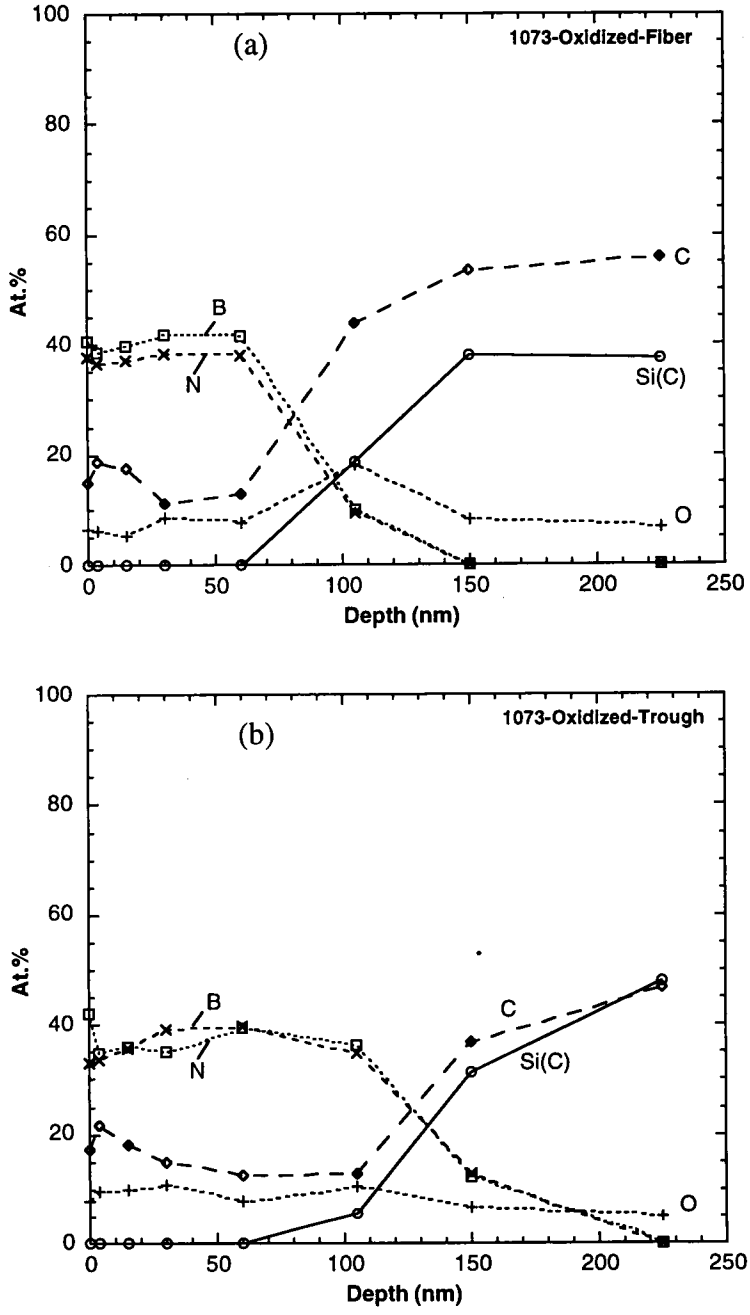


Fig. B.6.101. Compositional depth profiles on a composite with a BN/Al_2O_3-TiO_2/BN interface after 500 h oxidation at 1000°C (a) Fiber and (b) Trough

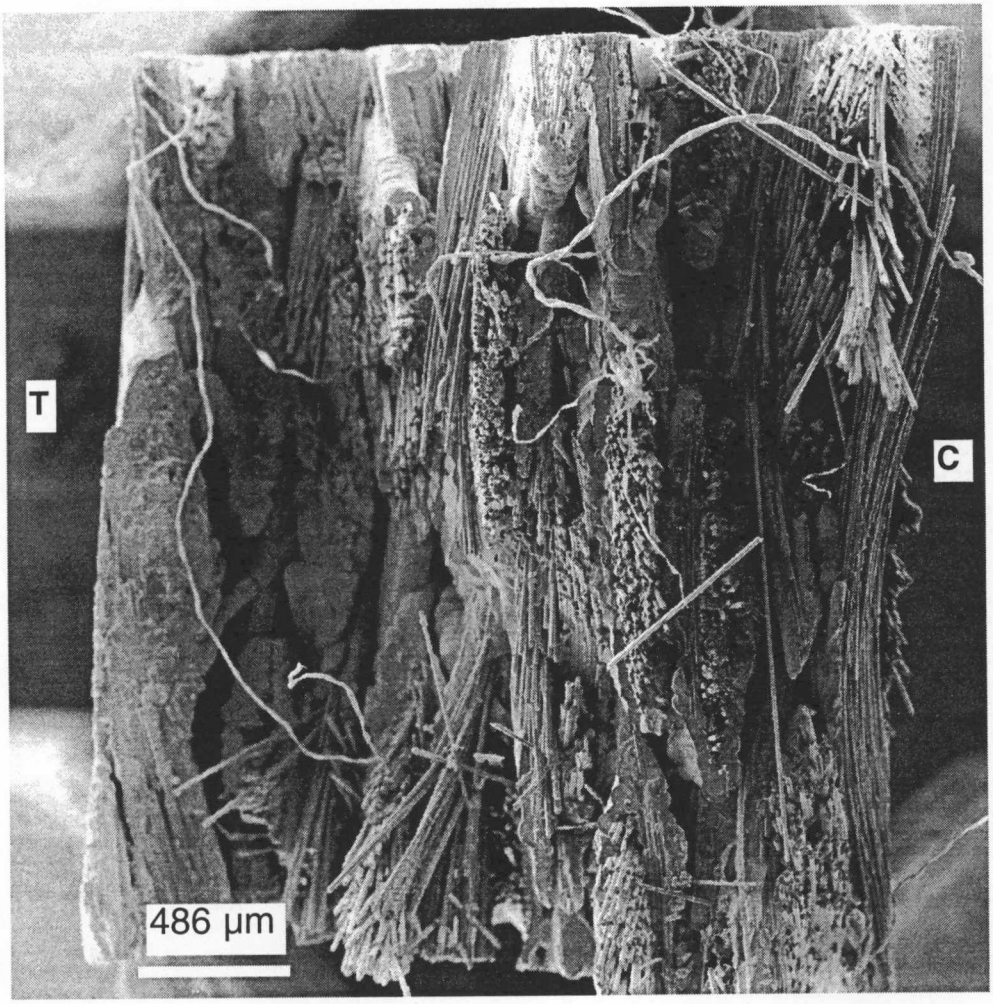


Fig. B.6.102. Fracture surface of a CVI 1054 composite (BN/mullite/BN interface) in the as-processed condition

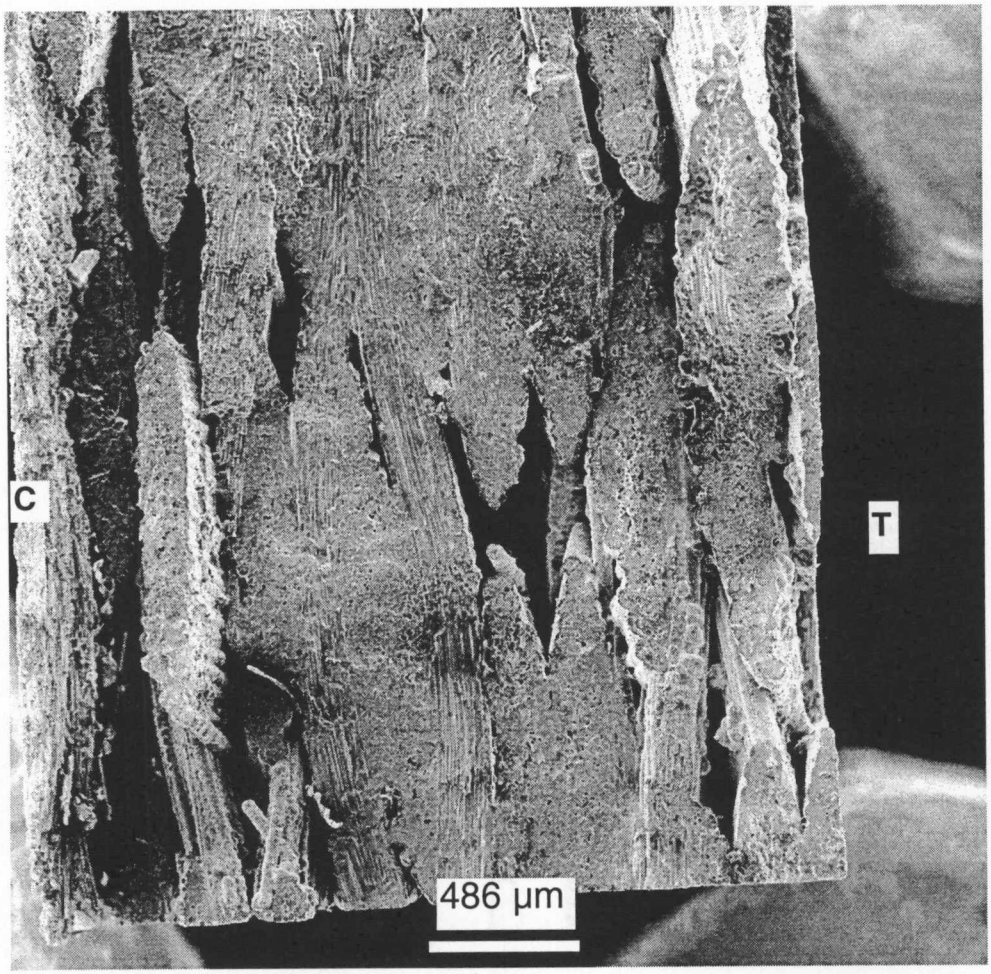


Fig. B.6.103. Fracture surface of a CVI 1054 composite exhibiting brittle fracture after 24 h oxidation at 1000°C

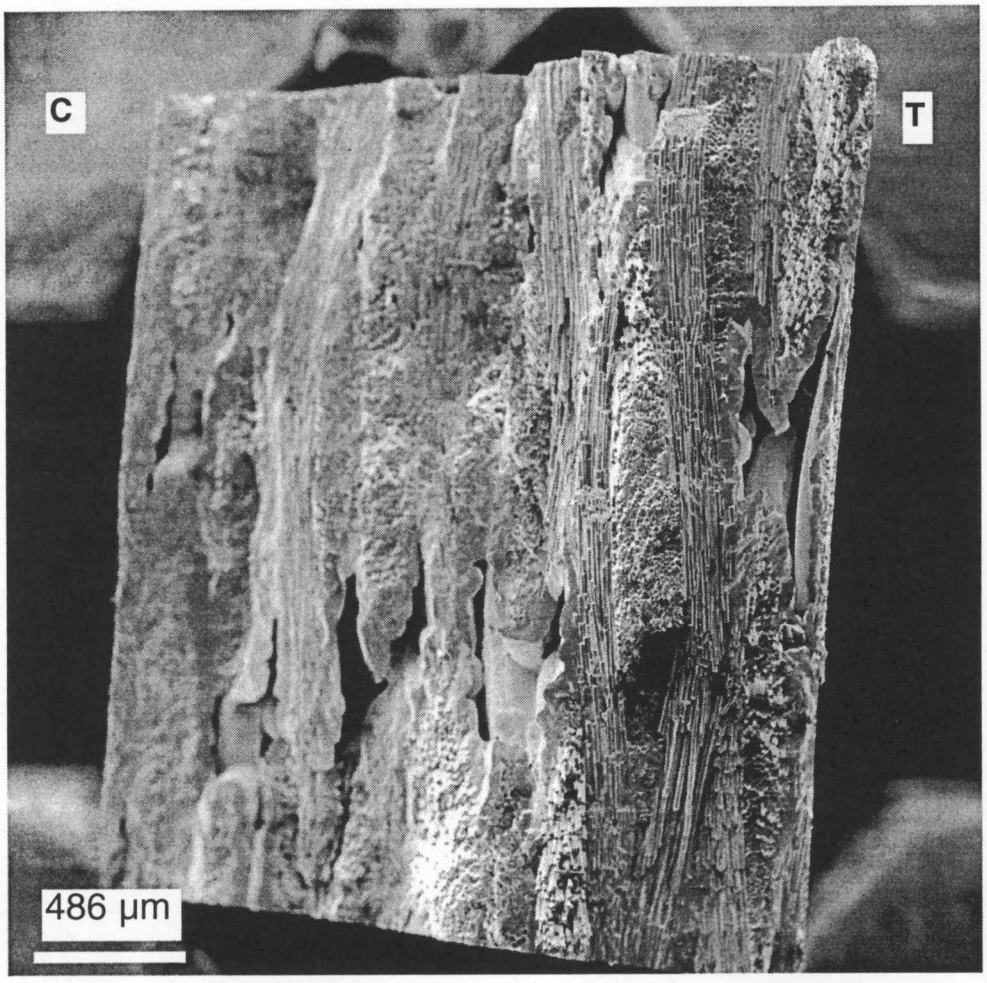


Fig. B.6.104. Fracture surface of a CVI 1054 composite after oxidation at 1000°C for 200 h

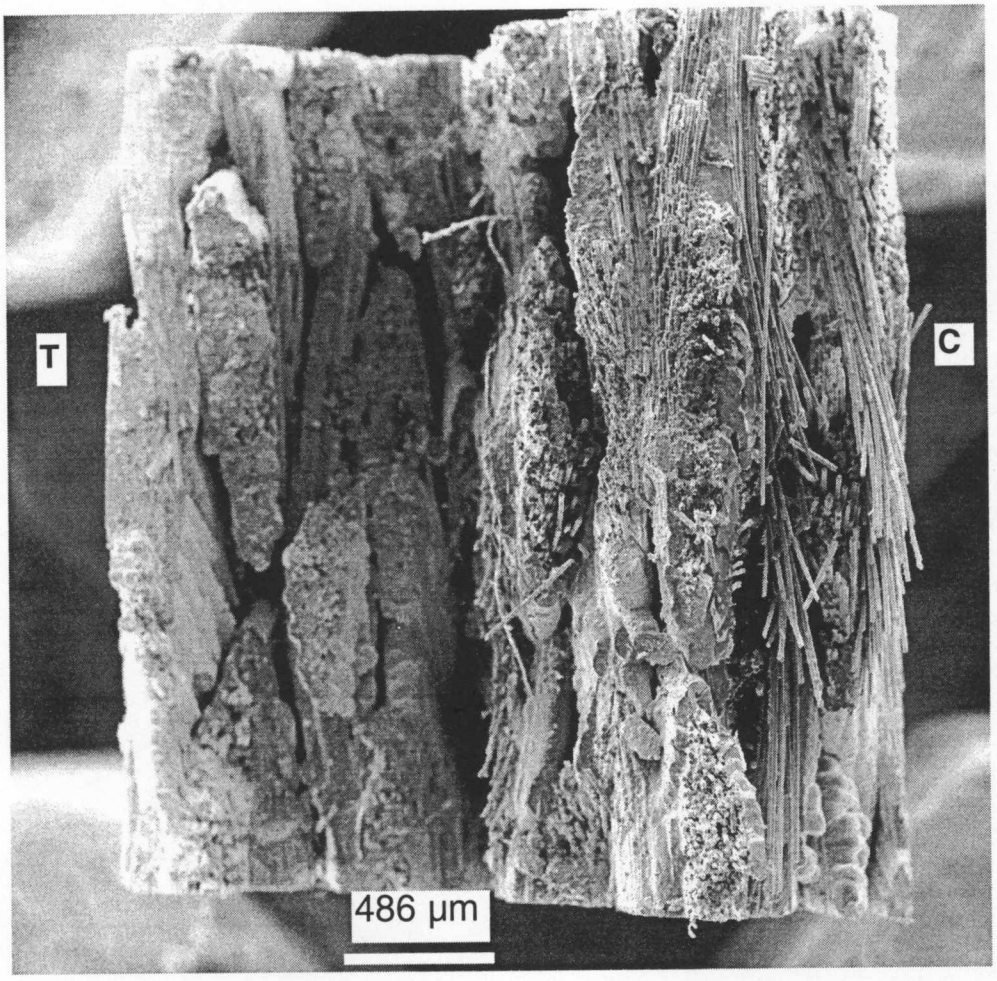


Fig. B.6.105. Fracture surface of a CVI 1054 composite after 500 h oxidation at 1000°C

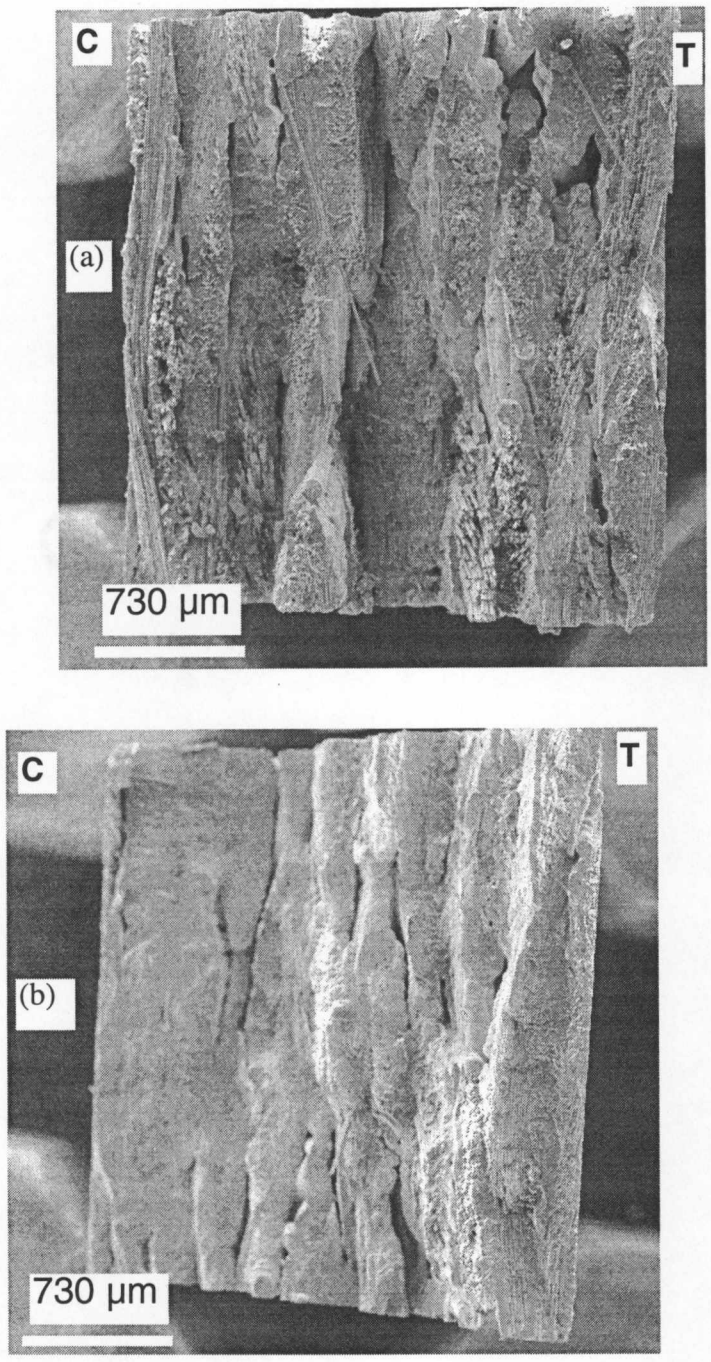


Fig. B.6.106. Fracture surface of a CVI 1054 composite after oxidation for 200 h at (a) 500°C and (b) 750°C

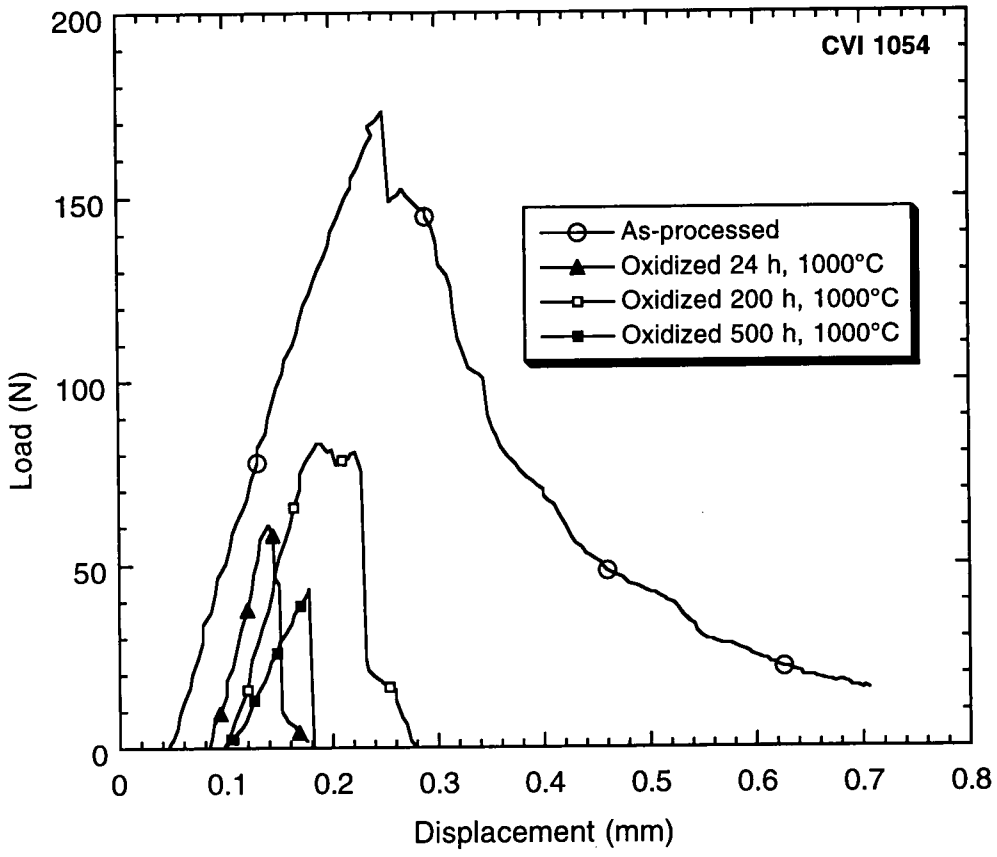


Fig. B.6.107. Representative load vs displacement curves of a composite with a BN/mullite/BN interface in the as-processed condition and after oxidation for up to 500 h at 1000°C

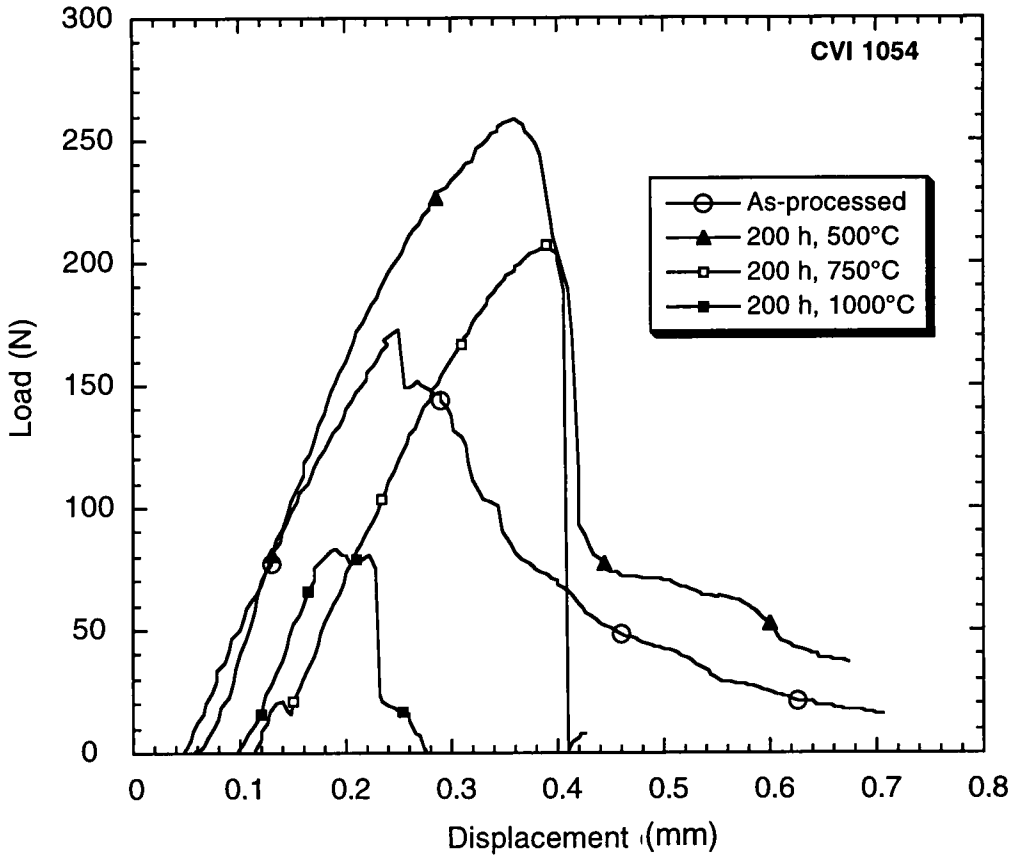


Fig. B.6.108. Representative load vs displacement curves of a composite with a BN/mullite/BN interface in the as-processed and oxidized conditions

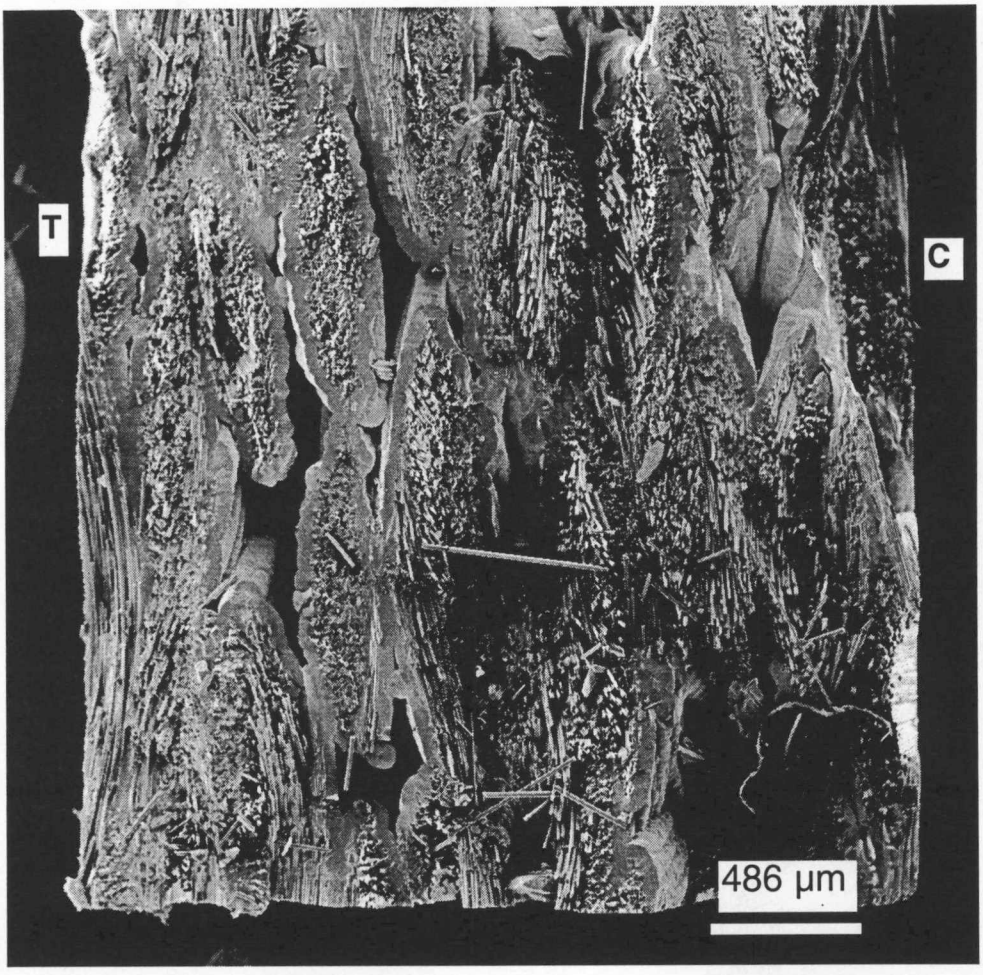


Fig. B.6.109. Fracture surface of a Nextel/SiC composite with a mullite/C interface (CVI 997) in the as-processed condition

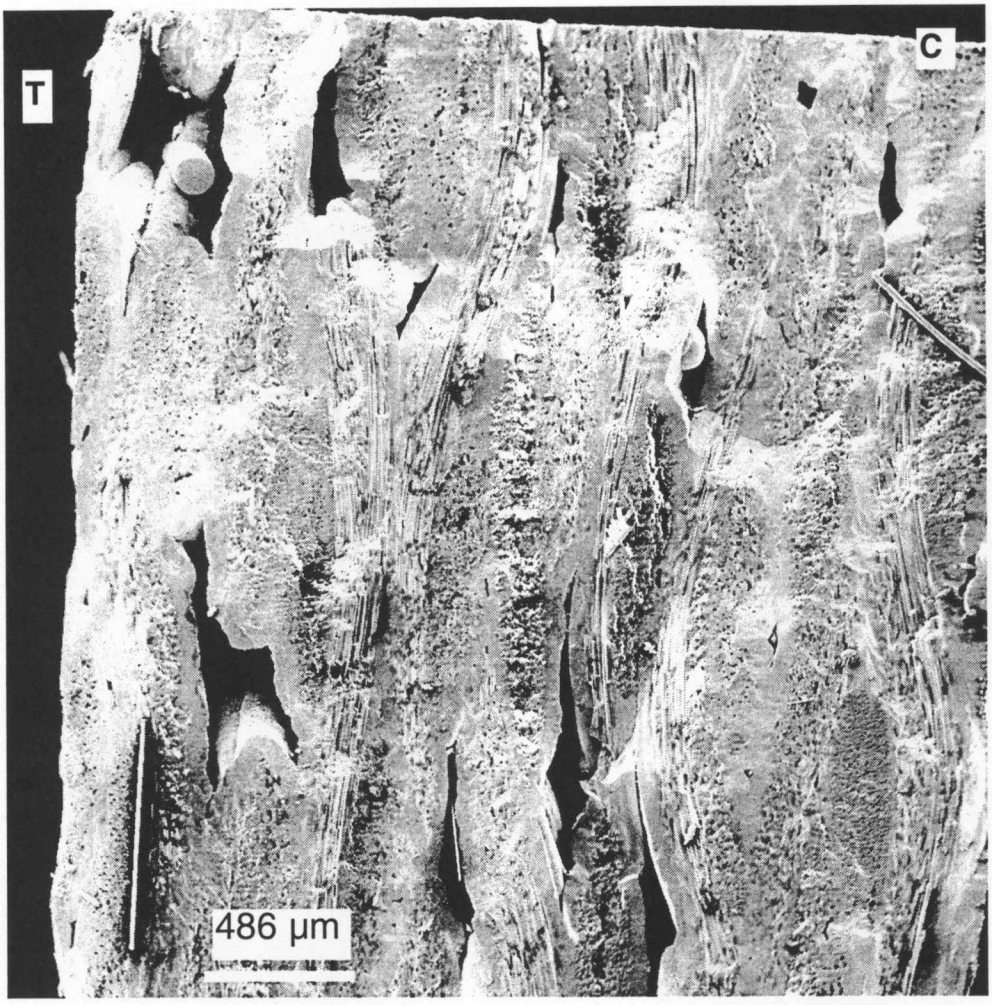


Fig. B.6.110. Fracture surface of a CVI 997 composite after oxidation at 1000°C for 24 h

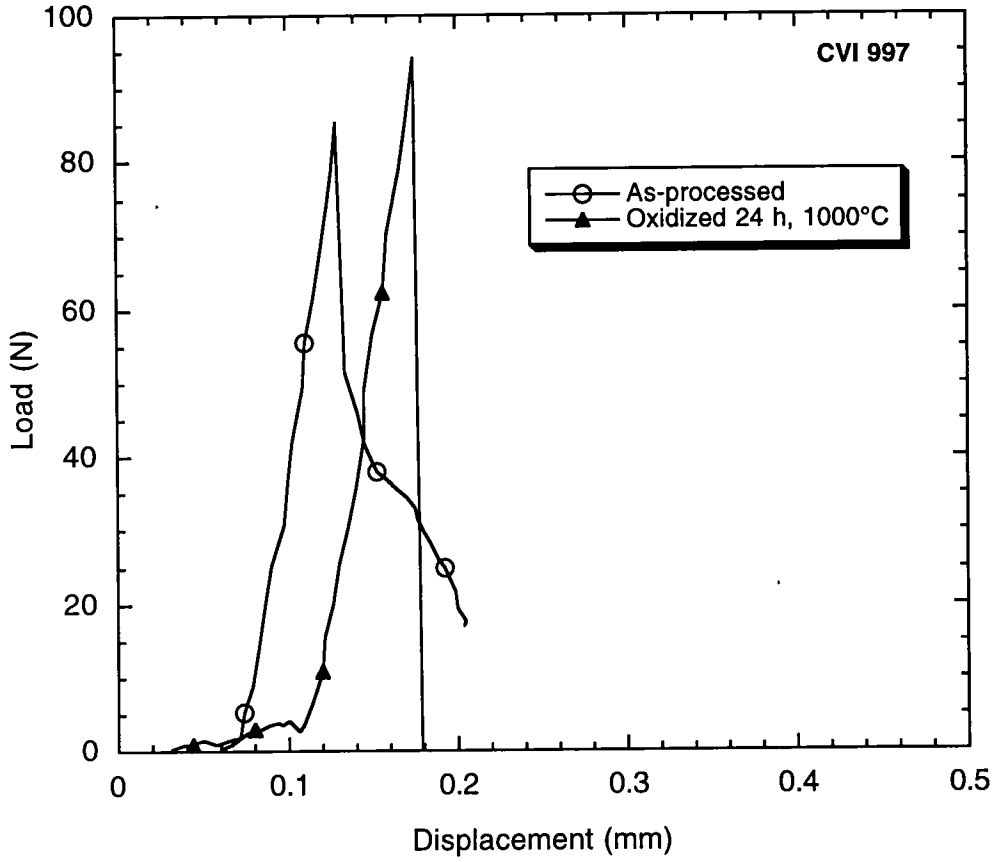


Fig. B.6.111. Representative load vs displacement curve of a Nextel/SiC composite with a mullite/C interface

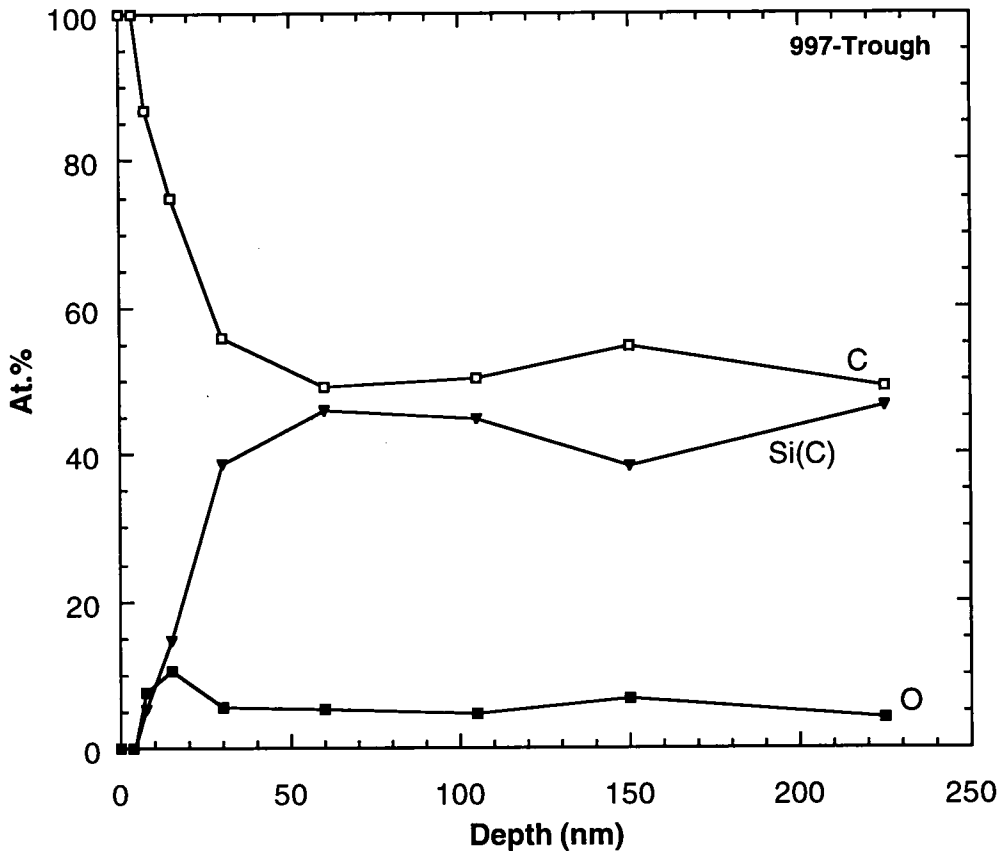


Fig. B.6.112. Compositional depth profile obtained on a trough in a Nextel/SiC composite with a mullite/C interface

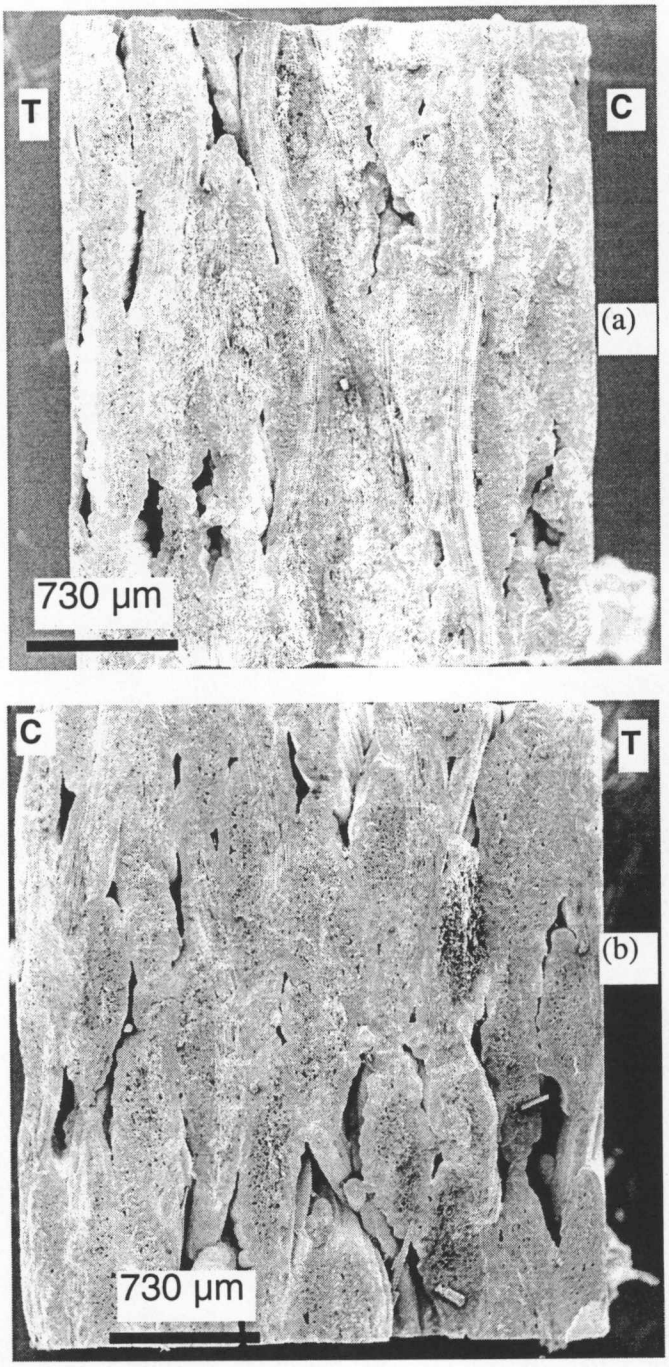


Fig. B.6.113. Fracture surface of a Nextel/SiC composite with an Al_2O_3-TiO_2/C interface (CVI 998) (a) As-processed condition and (b) After oxidation at 1000°C for 24 h

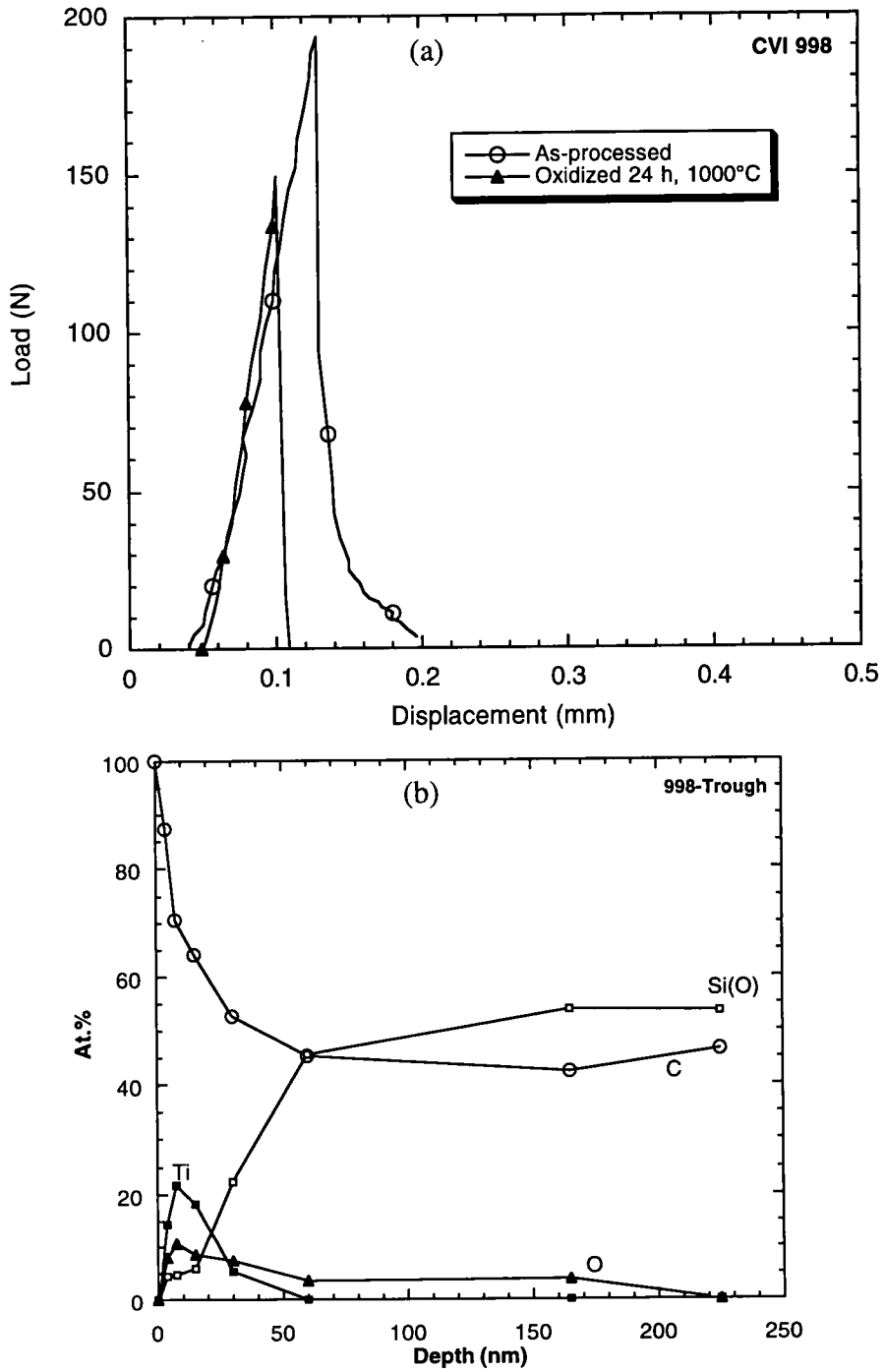


Fig. B.6.114. Nextel/SiC composite with an Al_2O_3-TiO_2/C interface
(a) Load vs displacement curve and (b) Compositional depth profile on a trough

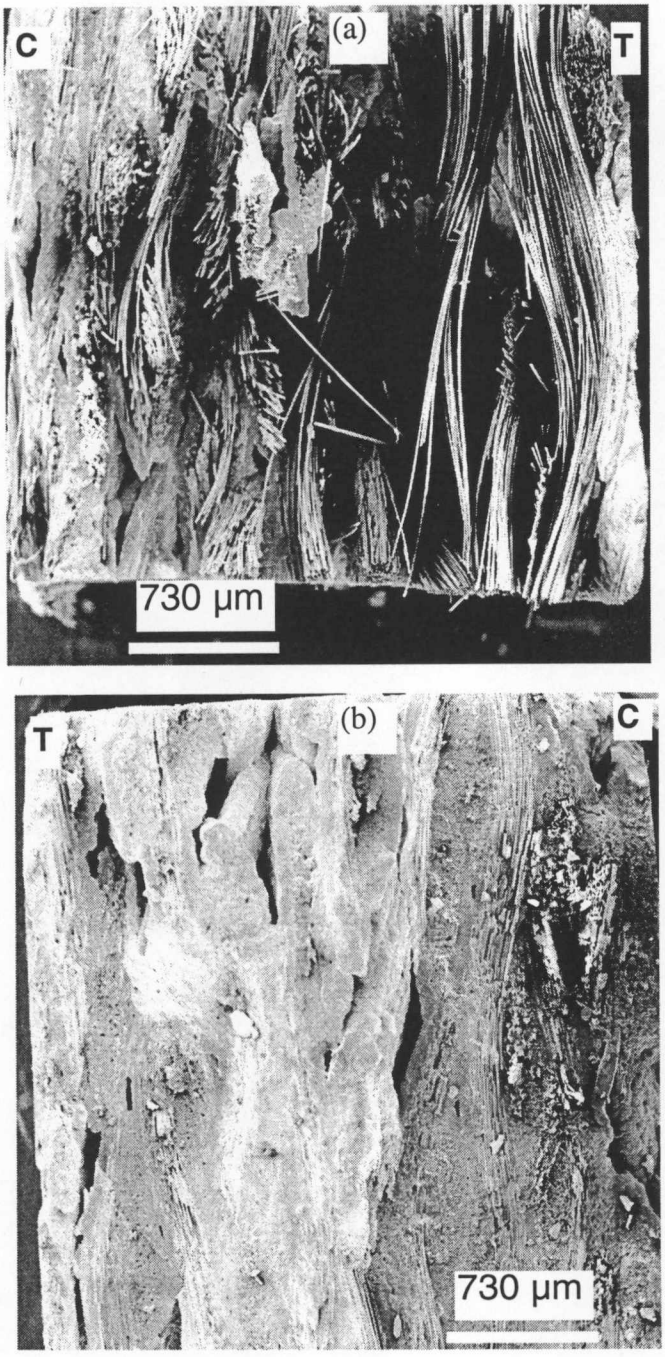


Fig. B.6.115. Fracture surface of a Nextel/SiC composite with a C/mullite/C interface (CVI 999) (a) As-processed condition and (b) After 24 h oxidation at 1000°C

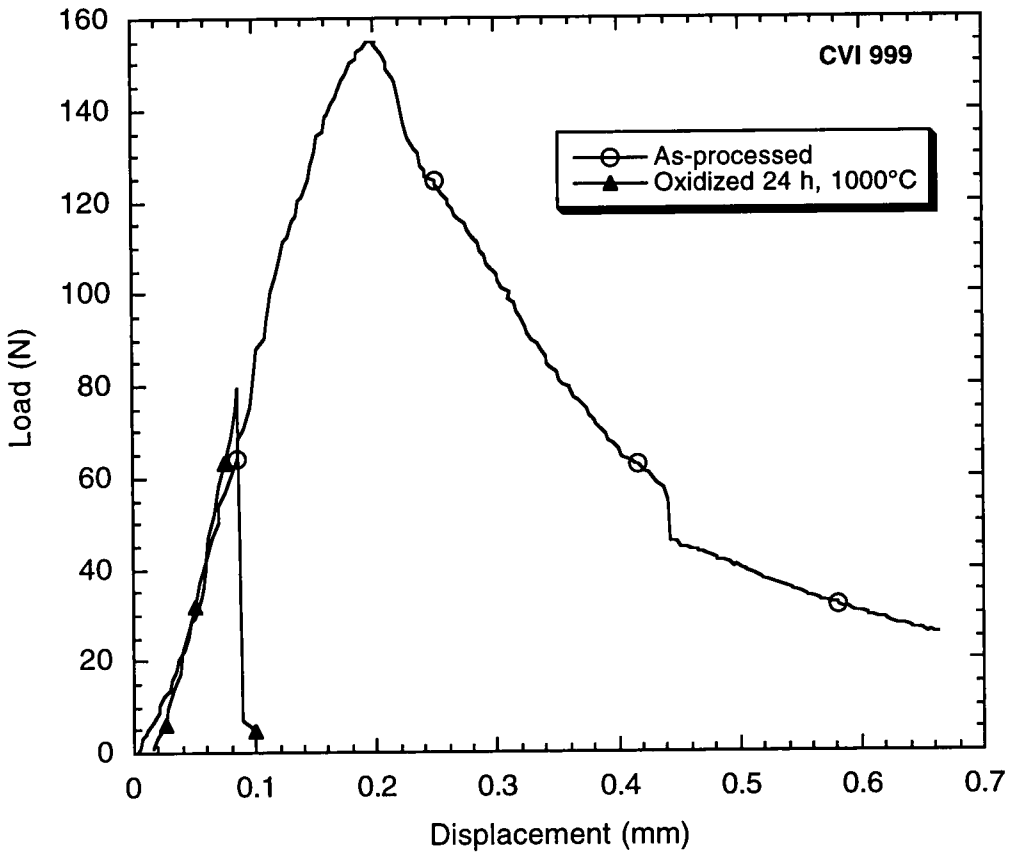


Fig. B.6.116. Representative load vs displacement curves of a CVI 999 composite

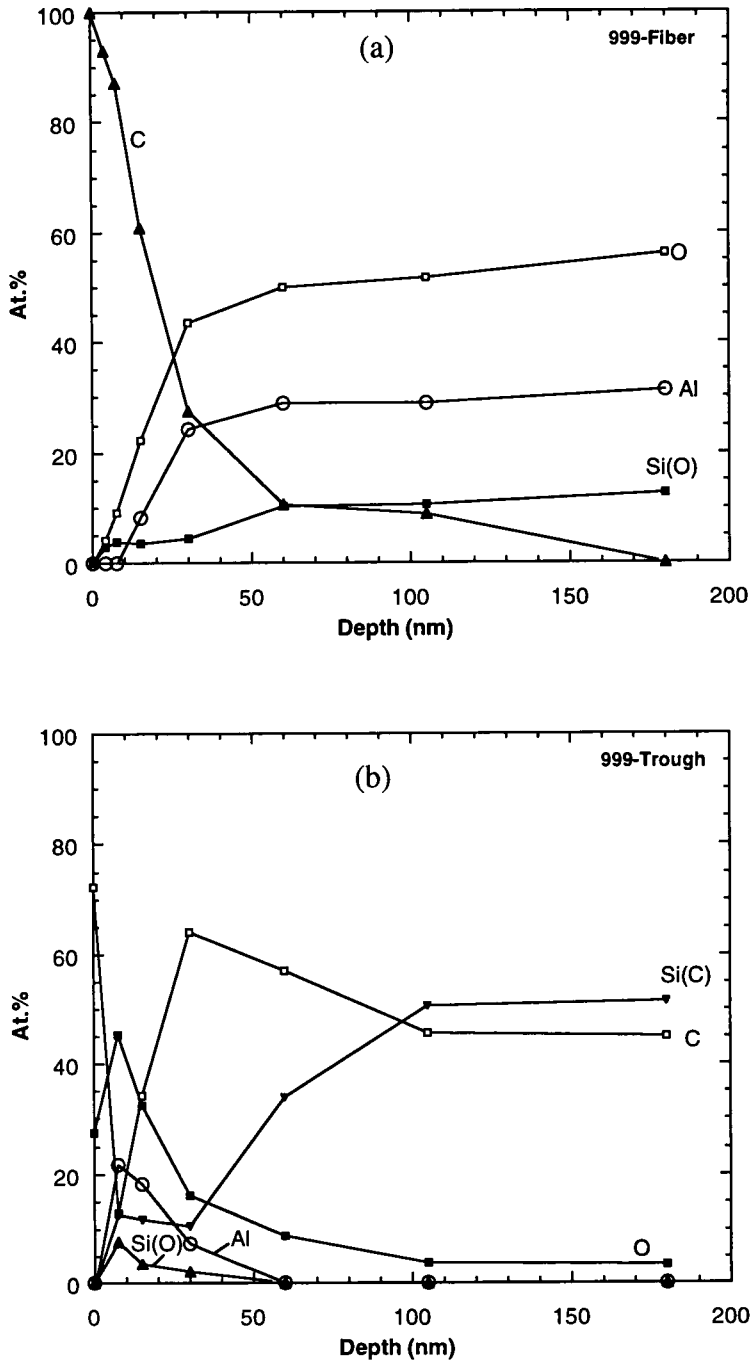


Fig. B.6.117. Compositional depth profiles obtained on a CVI 999 composite (a) Fiber and (b) Trough

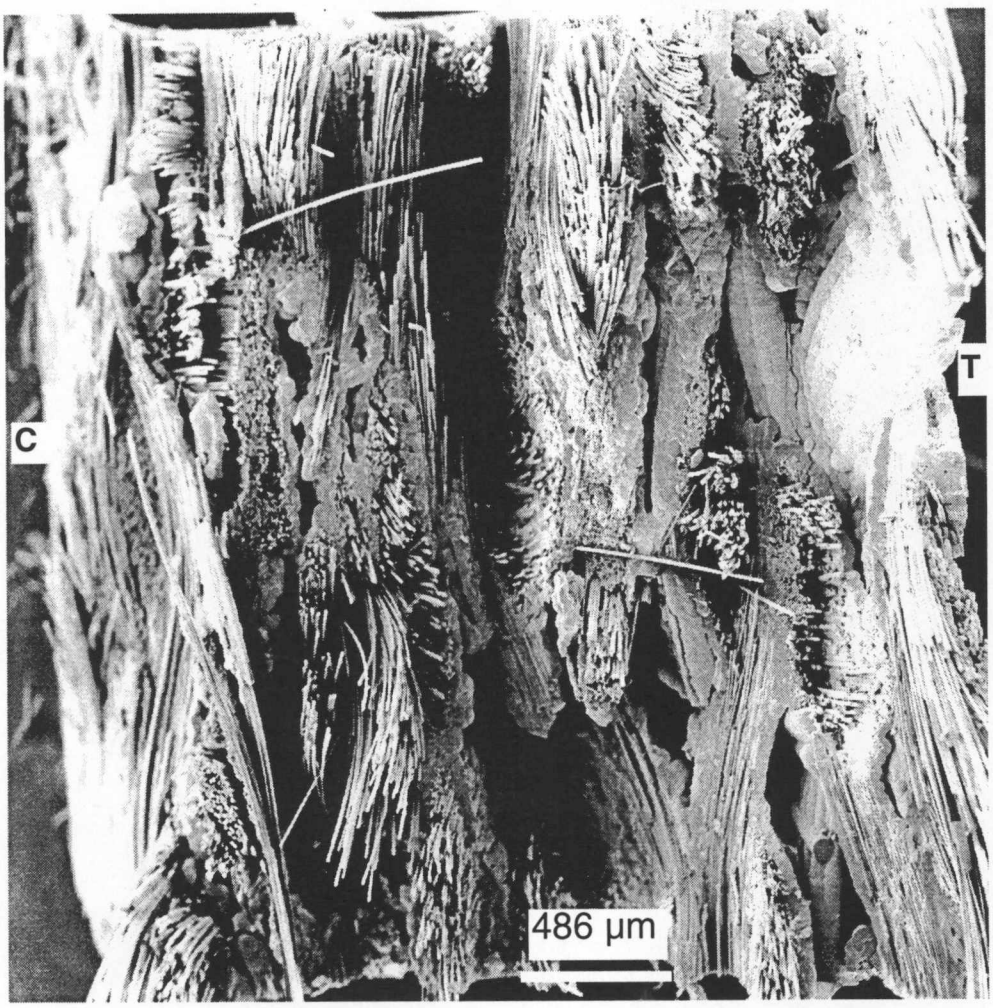


Fig. B.6.118. Fracture surface of a Nextel/SiC composite with a C/Al_2O_3-TiO_2/C interface (CVI 1000) in the as-processed condition

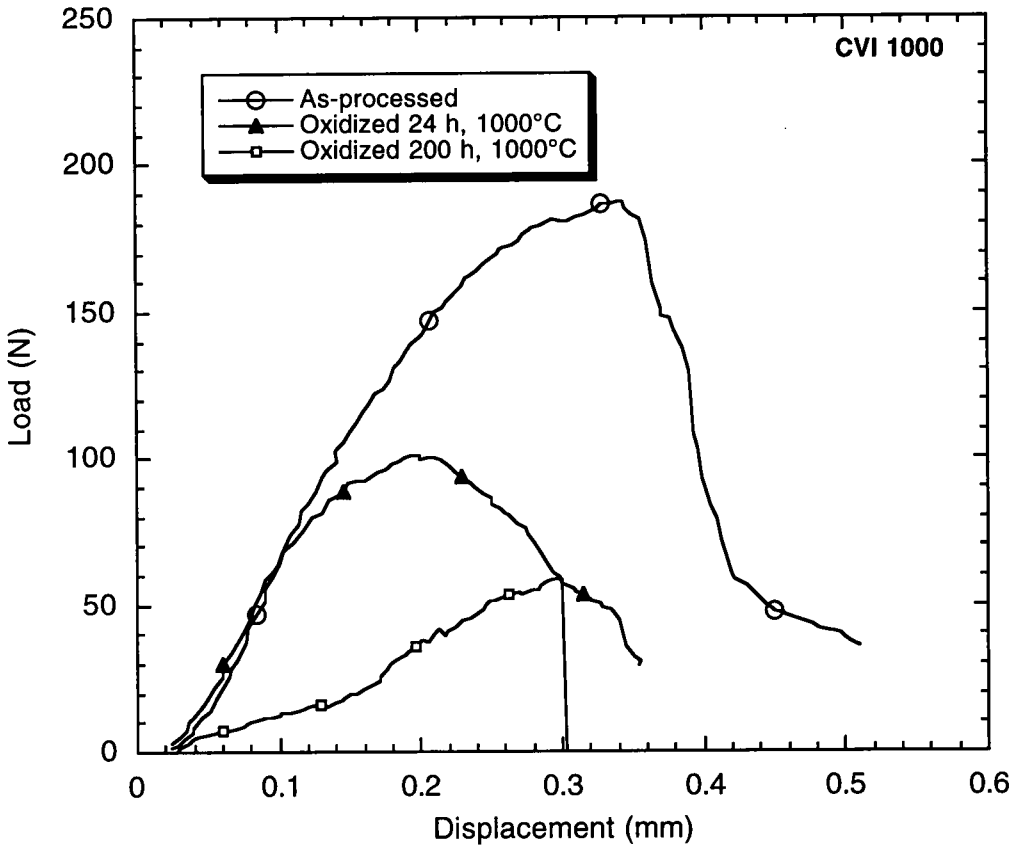


Fig. B.6.119. Representative load vs displacement curves of a composite with a C/Al_2O_3-TiO_2/C interface in the as-processed and oxidized conditions

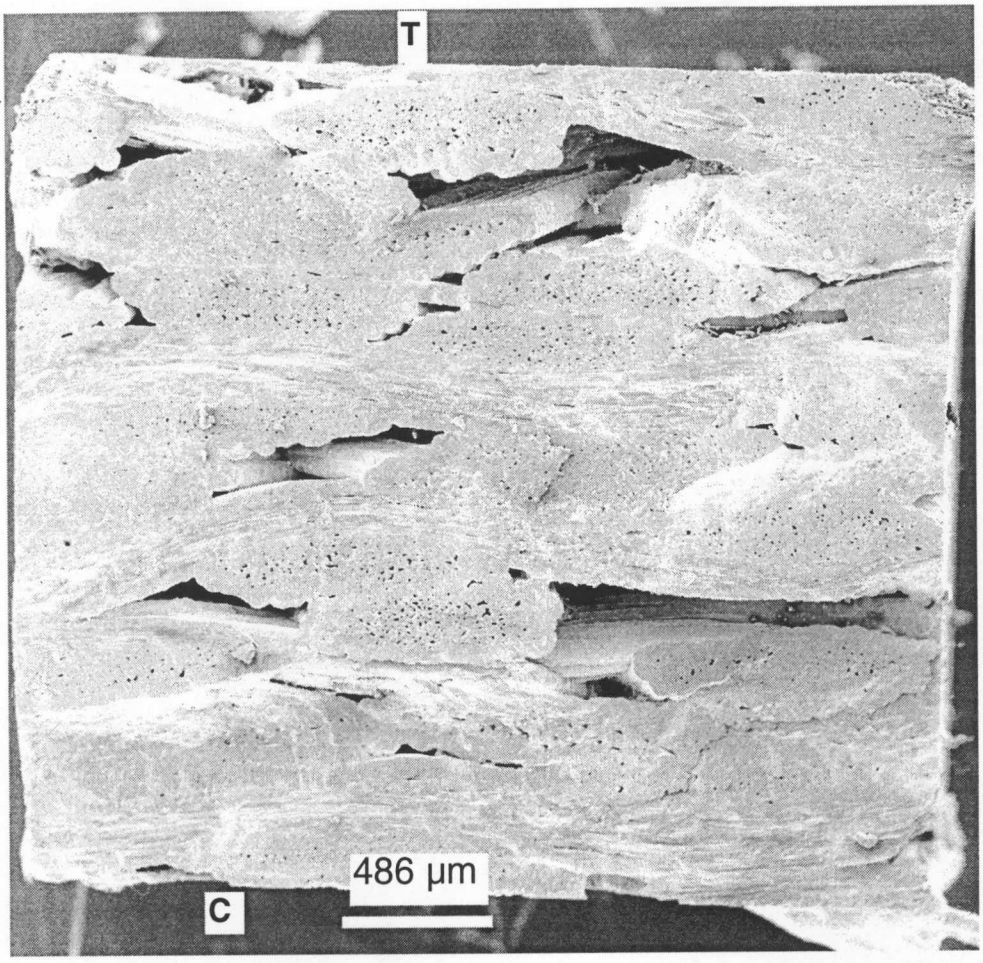


Fig. B.6.120. Fracture surface of a CVI 1000 composite showing brittle fracture after oxidation for 200 h at 1000°C

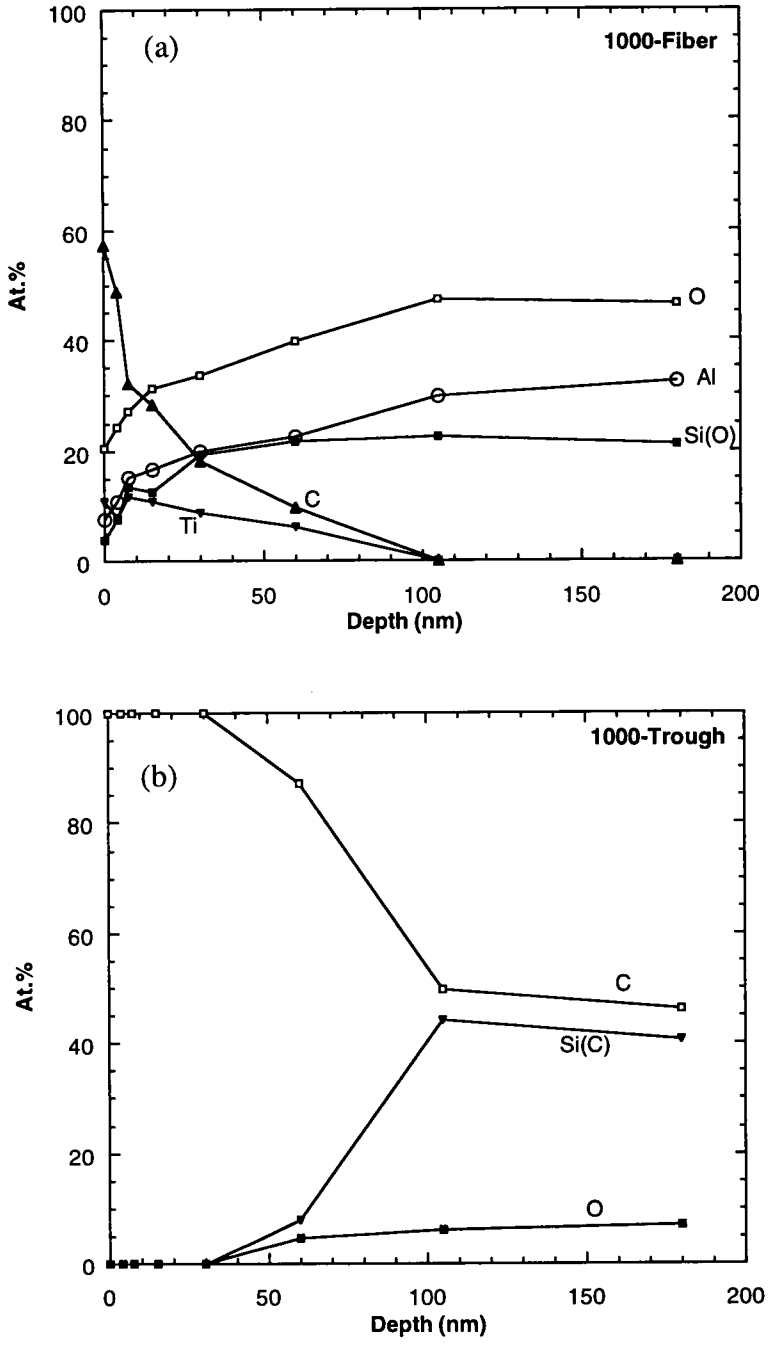


Fig. B.6.121. Compositional depth profiles obtained on a CVI 1000 composite in the as-processed condition (a) Fiber and (b) Trough

APPENDIX C

The thermal residual radial stresses, developed during cooling from processing to room temperature, derived by Hsueh et al. [21] are presented here. The stress at the fiber-interface region, σ_a, is given by

$$\sigma_a = \{ (1+\nu_f)(\alpha_m-\alpha_f) + \{[a^2+b^2(1-2\nu_f)/(2b^2(1-\nu_f)] + b^2-a^2/b^2 * (1+\nu_m)E_f/((2(1-\nu_f^2)E_m\} * [(1+\nu_f)\alpha_f + (\nu_w-\nu_f)\alpha_m - (1+\nu_w)\alpha_w] \} * \Delta T / \{-2a^2(1-\nu_f^2)/(b^2-a^2)E_f + [(a^2+b^2(1-2\nu_f)/2b^2(1-\nu_f) + b^2-a^2(1+\nu_m)E_f/(b^2(2(1-\nu_f^2)E_m] * [(1+\nu_w)(1-2\nu_w)/E_w + \{a^2(1-2\nu_f) + b^2\}/(b^2-a^2) * (1+\nu_f)/E_f] \}$$

while the stress at the interface-matrix region, σ_b, is given by

$$\sigma_b = \{(1+\nu_f)\alpha_f + (\nu_w-\nu_f)\alpha_m - (1+\nu_w)\alpha_w + (b^2-a^2)/2a^2 * E_f(\alpha_m-\alpha_f)*1/(1-\nu_f) * [(1+\nu_w)(1-2\nu_w) * 1/E_w + \{a^2 * (1-2\nu_f)+b^2) * (1+\nu_f)/(E_f*(b^2-a^2))\}] \} * \Delta T / \{ -2b^2(1-\nu_f^2)/(E_f(b^2-a^2) + [(a^2+b^2 * (1-2\nu_f)/(2a^2*(1-\nu_f) + (b^2-a^2)/a^2 * (1+\nu_m)*E_f/(2* (1-\nu_f^2) *E_m)] * [(1+\nu_w)(1-2\nu_w)/E_w + (a^2*(1-2\nu_f) + b^2)/(b^2-a^2) * (1+\nu_f)/E_f] \}$$

where the subscripts w,f, and m denote the fiber, interface, and matrix, respectively, and E is the Young's modulus, ν is the Poisson's ratio, and α is the coefficient of thermal expansion.

APPENDIX D

Effect of Two Film Layers on Residual Thermal Stresses in Ceramic Matrix Composites

Abstract

Compressive clamping stresses are present at the fiber/matrix interface in composites on cooling from processing to room temperature, when the fiber has a lower thermal expansion than the matrix. If the stresses are high enough, it could result in composites exhibiting brittle behavior. Consequently, the effects of two film layers between the fiber and the matrix on the residual stresses are evaluated using a derived elastic stress solution for thermal stresses in composites with two film layers. Analysis of the thermomechanical properties of two film layers indicate that the residual stresses are reduced in the presence of film layers with low Young's modulus.

1. Introduction

Thermal expansion mismatch between materials in a system inevitably causes residual thermal stresses as they are cooled from processing to room temperature. Poritsky[1] derived the expressions for thermal stresses in long cylindrical glass-metal seals, and since then several analytical models have been proposed.[2-5] Thermal stresses also exist in whisker or fiber reinforced materials such as metal matrix or ceramic matrix composites (CMCs). Aveston's flexure testing study of hot-pressed samples of cordierite glass reinforced with SiC fibers highlighted the importance of residual thermal stresses.[6] Since the cordierite glass matrix has a thermal expansion coefficient higher than that of the SiC fiber, the matrix clamped the fibers during cooling and resulted in a brittle composite. On the other hand, when the cordierite glass was heat treated to form a low-expansion coefficient crystalline matrix, the resulting composite exhibited extensive fiber pullout in the tensile region. The behavior was due to the SiC fibers contracting away from the matrix on cooling and resulting in the reduction of thermal stresses.

Borom and Johnson[7] utilized a biceramic dilatometry technique and studied the thermomechanical relationship in a mullite/lithium aluminosilicate (LAS) system. Due to the reactivity of LAS with SiC, they were unable to make SiC/LAS samples for their study. However, they noted that the results obtained for mullite/LAS system would be applicable to SiC/LAS composites since mullite and SiC possess similar thermal expansion properties. They observed that the crystallized LAS exhibited a viscoelastic behavior on combining with mullite and a stress reversal temperature also existed in the above system. Based on this result, they inferred that the SiC/LAS composites

exhibited brittle behavior at elevated temperatures due to the matrix clamping on the fibers between the stress reversal temperature and the set point temperature. Earlier, Luh and Evans[8] and Mah et al. [9] observed that the fracture mode of SiC/LAS composites changed from tough, fibrous pullout behavior at room temperature to brittle behavior at 900°C and 1000°C in air.

In fiber-reinforced CMCs, the toughening mechanisms, such as fiber debonding and pullout, mandate relatively low interfacial stresses to enable extensive fiber pullout.[10] Earlier, Outwater[11] noted that the presence of compressive clamping stresses will increase the shear stress required for fiber pullout and would prohibit the interface debonding. Hsueh et al.[12] summarized that composites which display extensive fiber pullout are confined to fiber/matrix combinations having negligible radial compressive (clamping) or even tensile stresses imposed on fibers and hence have low interfacial shear stresses. These arguments are applicable even to whisker-reinforced composites where whisker pullout, whisker debonding and bridging contribute to toughness.

It is widely accepted that the film layer (interface) between the fiber and the matrix plays a key role in determining the properties of CMCs.[13-16] In Nicalon/SiC composites, the presence of C or BN film layers (interfaces) have promoted good toughness.[15,16] Lowden[16] measured interfacial shear stresses in Nicalon/SiC composites using an indentation method and observed that the interfacial shear stress was inversely proportional to the carbon interface thickness. Higher the carbon coating thickness, the interface shear stresses were lower and the composites exhibited good strength and higher fiber pullout. Earlier, Hsueh et al.[12] presented an elastic stress solution for the thermal stresses and studied the effect of one film layer on the thermal stresses in

fiber/whisker-reinforced composites with low fiber volume fractions. Lowden[16] utilized Hsueh et al.'s model[12] and observed that the normalized compressive stresses decreased with increasing carbon coating thickness and this could possibly explain the interfacial shear strength decrease with increasing carbon coating thickness.

The objective of the present paper is to provide an elastic stress solution for thermal stresses in CMCs with two film layers with a low fiber volume fraction. The effect of thermomechanical properties of the film layers on the residual thermal stresses will also be discussed.

2. Derivation of Thermal Stresses

The following assumptions are made about the composite system considered in the current study: (1) dilute fiber concentration in the matrix (2) no chemical interaction between the fiber, matrix and the film layers (3) the effect of surrounding fibers are not considered and (4) stresses due to processing are completely relaxed at elevated temperatures. The different thermal stresses are determined by first permitting the constituents to undergo an unconstrained differential shrinkage during cooling from a temperature at which the system is completely stress relaxed. In order to restore displacement continuity at the interfaces, the radial components, σ_a (fiber/film layer 1 interface), σ_c (film layer 1/film layer 2 interface), and σ_d (film layer 2/matrix interface), and axial components, $\sigma_{z(w)}$, $\sigma_{z(c)}$, $\sigma_{z(d)}$, and $\sigma_{z(m)}$, of the tractions are then placed on the composite (Fig. 1). The paranthesized subscripts of the axial stresses denote the fiber (w), film layer 1 (c), film layer 2 (d), and matrix (m) in the system. Since there is no external force on the composite under consideration, the axial tractions are contingent to

the requirement that the resultant axial force is zero. For the case of a single fiber in an infinite matrix, the matrix axial stress $\sigma_{z(m)} = 0$.

Based on the above conditions, the thermal stresses of the fiber and interfaces (film layer 1 and film layer 2) can be evaluated. Based on Timoshenko and Goodier[17] and Hsueh et al.[12], the radial and tangential stresses in the film layers subjected to the three interface tractions, σ_a, σ_c, and σ_d, are obtained:

$$\sigma_{r(c)} = \frac{a^2c^2(\sigma_a - \sigma_c)}{(c^2 - a^2)r^2} - \frac{a^2\sigma_a - c^2\sigma_c}{c^2 - a^2} \tag{1a}$$

$$\sigma_{\theta(c)} = \frac{a^2c^2(\sigma_c - \sigma_a)}{(c^2 - a^2)r^2} - \frac{a^2\sigma_a - c^2\sigma_c}{c^2 - a^2} \tag{1b}$$

$$\sigma_{r(d)} = \frac{c^2d^2(\sigma_c - \sigma_d)}{(d^2 - c^2)r^2} - \frac{c^2\sigma_c - d^2\sigma_d}{d^2 - c^2} \tag{1c}$$

$$\sigma_{\theta(d)} = \frac{c^2d^2(\sigma_d - \sigma_c)}{(d^2 - c^2)r^2} - \frac{c^2\sigma_c - d^2\sigma_d}{d^2 - c^2} \tag{1d}$$

where a is the radius of the fiber or the inner radius of film layer 1, c is the outer radius of the film layer 1, d is the outer radius of the film layer 2, and r is the distance from the axis of symmetry (Fig. 1). The corresponding stresses in the fiber and the matrix are given by[12,17]

$$\sigma_{r(w)} = \sigma_{\theta(w)} = \sigma_a \tag{2}$$

$$\sigma_{r(m)} = -\sigma_{\theta(m)} = \sigma_d\left(\frac{d}{r}\right)^2 \tag{3}$$

The present analysis is applicable only to the stress components within the central region of the length of the fiber (away from the fiber ends). This is because the planes which are perpendicular to the fiber axis remains planar even after thermal contraction in the central portion. The stress distributions in the composite are dependent upon the solutions of the surface tractions (σ_a, σ_c, σ_d, $\sigma_{z(w)}$, $\sigma_{z(c)}$, and $\sigma_{z(d)}$) and these tractions are governed by the continuity conditions at the interfaces.

When the composite is cooled from the processing temperature to room temperature, there are two strain components (elastic and thermal) with the total tangential and axial strains given by[12,17]

$$\varepsilon_\theta = \frac{1}{E}\left[\sigma_\theta - \upsilon(\sigma_r + \sigma_z)\right] + \alpha\Delta T \qquad (4a)$$

$$\varepsilon_z = \frac{1}{E}\left[\sigma_z - \upsilon(\sigma_r + \sigma_\theta)\right] + \alpha\Delta T \qquad (4b)$$

where E, υ, α, and ΔT represent the Young's modulus, Poisson ratio, coefficient of thermal expansion (CTE), and the temperature differential (negative for cooling), respectively. The strains in the fiber, film layers, and the matrix can then be computed by substituting in equation 4, the appropriate radial and tangential stresses (given by equations (1), (2), and (3)), axial stresses, Poisson ratios, Young's moduli, and thermal expansion coefficients.

By imposing the requirement of continuity at the interfaces, the radial and axial stresses in the fiber, film layers, and matrix can then be determined from the strains:

$$\varepsilon_{\theta(w)} = \varepsilon_{\theta(c)} \qquad \text{(at r = a)} \qquad (5a)$$

$$\varepsilon_{\theta(c)} = \varepsilon_{\theta(d)} \qquad \text{(at r = c)} \qquad (5b)$$

$$\varepsilon_{\theta(d)} = \varepsilon_{\theta(m)} \qquad \text{(at r = d)} \qquad \text{(5c)}$$

$$\varepsilon_{z(w)} = \varepsilon_{z(c)} = \varepsilon_{z(d)} = \varepsilon_{z(m)} \qquad \text{(5d)}$$

The thermal stresses, σ_a, σ_c, σ_d, $\sigma_{z(w)}$, $\sigma_{z(c)}$, and $\sigma_{z(d)}$, derived using the combinations of equations (1) to (5) are given below:

$$\sigma_a = \frac{\Delta T[Z - RB + SD]}{RA - SC - F} \qquad \text{(6a)}$$

where Z, R, B, S, A, F, C, and D represent:

$$Z = \upsilon_c(\alpha_m - \alpha_c) + (\alpha_d - \alpha_c) - \upsilon_d(\alpha_m - \alpha_d)$$

$$R = \frac{(1+\upsilon_c)}{(c^2 - a^2)E_c}\left[a^2 + c^2(1-2\upsilon_c)\right] + \frac{(1+\upsilon_d)}{(d^2 - c^2)E_d}\left[d^2 + c^2(1-2\upsilon_d)\right]$$

$$B = \frac{(c^2 - a^2)E_c}{2c^2(1-\upsilon_c^2)}\left[\alpha_m(\upsilon_c - \upsilon_w) + \alpha_w(1+\upsilon_w) - \alpha_c(1+\upsilon_c)\right]$$

$$S = \frac{2d^2(1-\upsilon_d^2)}{(d^2 - c^2)E_d}$$

$$A = \frac{(c^2 - a^2)}{2c^2(1-\upsilon_c^2)}\left[\frac{(1+\upsilon_c)\left\{a^2(1-2\upsilon_c) + c^2\right\}}{(c^2 - a^2)} + \frac{E_c(1-2\upsilon_w)(1+\upsilon_w)}{E_w}\right]$$

$$F = \frac{2a^2(1-\upsilon_c^2)}{(c^2 - a^2)E_c}$$

C is given by

$$C = \frac{JA}{L}$$

where J and L represent

$$J = \frac{2c^2(1-\upsilon_d^2)}{E_d(d^2-c^2)} \quad \text{and}$$

$$L = \frac{(1+\upsilon_d)[c^2+d^2(1-2\upsilon_d)]}{E_d(d^2-c^2)} + \frac{1+\upsilon_m}{E_m}$$

and D is given by

$$D = \frac{JB+P}{L}$$

where P is given by

$$P = (\alpha_m - \alpha_d)(1+\upsilon_d)$$

$$\sigma_c = A\sigma_a + B\Delta T \tag{6b}$$

$$\sigma_d = C\sigma_a + D\Delta T \tag{6c}$$

$$\sigma_{z(w)} = E_w(\alpha_m - \alpha_w)\Delta T + 2\sigma_a\upsilon_w \tag{6d}$$

$$\sigma_{z(c)} = E_c(\alpha_m - \alpha_c)\Delta T + 2\upsilon_c\frac{(c^2\sigma_c - a^2\sigma_a)}{c^2-a^2} \tag{6e}$$

$$\sigma_{z(d)} = E_d(\alpha_m - \alpha_d)\Delta T + 2\upsilon_d\frac{(d^2\sigma_d - c^2\sigma_d)}{d^2-c^2} \tag{6f}$$

If there were no film layers present, then the interfacial radial stress, σ_{a0}, and the axial stress in the fiber, σ_{z0}, can be deduced from equation (6) by making a = c = d, $E_w = E_c = E_d$, $\upsilon_w = \upsilon_c = \upsilon_d$, and $\alpha_w = \alpha_c = \alpha_d$:

$$\sigma_{a0} = \frac{(\alpha_m - \alpha_w)\Delta T}{\frac{(1-2\upsilon_w)}{E_w} + \frac{1+\upsilon_m}{(1+\upsilon_w)E_m}} \tag{7a}$$

$$\sigma_{z0} = E_w(\alpha_m - \alpha_w)\Delta T + 2\sigma_{a0}\upsilon_w \tag{7b}$$

Equations (7a) and (7b) are identical to the thermal stresses derived by Hsueh and Evans[18] for a metal cylinder embedded in an infinite ceramic matrix.

If there was only one layer present, the interfacial radial stresses, σ_{a1} (fiber/film interface) and σ_{d1} (film/matrix interface), and the axial stresses, $\sigma_{z(w1)}$ (fiber) and $\sigma_{z(d1)}$ (film layer 1) can be deduced from equation (6) by making c = a, and thermomechanical properties of the fiber and film layer 1 to be the same (i.e., $E_c = E_w$, $\upsilon_c = \upsilon_w$, and $\alpha_c = \alpha_w$). The equations, thus, derived are identical with the thermal stresses solution given by Hsueh et al.[12] for a composite with a fiber, matrix, and one film layer.

3. Modeling

The thermal stresses solution derived in equation (6) is applicable to two systems:

SYSTEM 1: A fiber surrounded by two film layers followed by an infinite matrix (as in Fig. 1) and is pertinent to a composite where the fiber volume fraction is low.

SYSTEM 2: A fiber surrounded by one film layer bounded by a finite matrix (the second film layer acts as a matrix) and then an infinite matrix. Such a solution is applicable even to a composite with a high fiber volume fraction.

Although the developed model is applicable to two systems, only system 1 is considered in the present study. Table 1 summarizes the thermal and mechanical properties of the fiber, matrix and films considered. The fiber is Nicalon (7.5 μm radius) and the matrix is SiC. The fiber has a lower CTE than that of the SiC matrix, and hence a radial compressive stress will develop during cooling from processing to room temperature. The film type in Table 1 is designated by A followed by three digits. The first digit denotes the Young's modulus. The second digit represents the Poissons

ratio and is denoted by 1 in all cases since υ=0.3 for all the film types. The third digit represents the CTE (α) and is denoted by: 1 if α = 1 x 10^{-6}°/C; 2 if α = 5.5 x 10^{-6}°/C; and 3 if α = 10 x 10^{-6}°/C. Each film type has 2 film layers: film layer 1 (0.25 μm thick) and film layer 2 (0.25 μm thick). The film layer 1 is adjacent to the fiber and the film layer 2 is between the film layer 1 and the matrix. In the film types A1**, A2**, and A3**, film layer 1 and the film layer 2 have identical thermomechanical properties. In the film types A413, A513, A613, and A713, only the Young's modulus of the film layer 1 and film layer 2 are different but the other properties are identical. The thermal stresses are calculated based on a temperature differential (ΔT) of 1000°C between the processing and room temperature.

In the composite cases considered in Fig. 2, film layer 1 and film layer 2 have identical properties. Figure 2 shows the effect of modulus and CTE of the film layers on the compressive radial stresses developed at the fiber-film layer 1, film layer 1-film layer 2, and the film layer 2-matrix interfaces. In the absence of any film layer(s), a compressive radial stress of 232 MPa is developed at the fiber-matrix interface in a composite. It should be noted that whenever comparisons are made in the subsequent paragraphs, it is always with reference to the thermal stresses in a composite with no film layer (unless it is specifically mentioned).

When the film layers have low CTE (α = 1 x 10^{-6}°/C; A111, A211, and A311 in Fig. 2), the compressive stress at the three interfaces (fiber-film layer 1, film layer 1-film layer 2 and film layer 2-matrix interface) are either increased or only slightly reduced compared to composites where no film layers are present. For composites with

A211 and A311 films, the thermal stresses are >280 MPa at both the film layer 1-film layer 2, and the film layer 2-matrix interface.

When the film layers have moderate CTE similar to that of the matrix (α = 5.5 x 10^{-6}°/C; A112, A212, and A312 in Fig. 2), the thermal stresses at all the interfaces (fiber-film layer 1, film layer 1-film layer 2, and film layer 2-matrix interface) are lowest for the material with the lowest Young's modulus (A112). For composites with moderate CTE films, the thermal stresses are reduced (< 220 MPa) in both film layer 1-film layer 2 and film layer 2-matrix interfaces compared to composites with low CTE films.

When the film layers have high CTE (α = 10 x 10^{-6}°/C; A113, A213, and A313 in Fig. 2), the thermal stresses developed at the composite interfaces are lower than those of composites with moderate or low CTE film layers. For the above case, even when the composite has a high modulus film (E = 400 GPa; A313) the thermal stresses at the film layer 1-film layer 2 and film layer 2-matrix interfaces are at least 40% lower than that of the composite with no film layer. The thermal stresses are reduced by almost equal amounts at the three interfaces for the composite with a film layer having the lowest E and the highest CTE (A113). Based on the above discussion, it could be summarized that the thermal stresses in the various interfaces are reduced in the presence of film layers with low Young's modulus. When comparing composites having film layers with similar modulus, the thermal stresses are more effectively reduced in the composite where the film layer has a higher CTE. Earlier, Hsueh et al.[12] made similar observation for a composite with only one film layer.

Next, we will consider the effect of combining film layers having high CTE but different modulus in composites (A413, A513, A613, and A713). In addition, we would include the following composites as reference: the composite with no interface and composite with film A113. Figure 3 shows the thermal radial stresses developed at the various interfaces for the films considered, and the stresses are lowered at least 20% in all the three interfaces when compared to a composite with no film layer. When comparing composites having film layer 1 with a similar low modulus (A413, A613, and A113), the radial stresses at the fiber-film layer 1 interface is lowest in the presence of a film layer 2 with the lowest Young's modulus (A113) while at the film layer 2-matrix interface, the film layer 2 with the highest modulus (A413) has the lowest radial stresses. In comparing composites having film layer 2 with a similar low modulus (A513, A713, and A113), the radial stresses at the film layer 1-film layer 2 and film layer 2-matrix interfaces are the lowest and the fiber-film layer 1 is the highest when a film layer 1 with a highest Young's modulus is present (A513). Based on the above discussion, we can summarize that the radial stresses can be lowered at least 20% by utilizing film layers with high CTE and even a high modulus film layer adjacent to the fiber followed by a low modulus film layer can be used in combination to effectively reduce the stresses in at least 2 interfaces.

4. Conclusions

An elastic stress solution for thermal stresses in ceramic matrix composites with two film layers was derived. This model serves as a guideline for selecting film layers with thermomechanical properties to minimize the thermal residual stresses in fiber-

reinforced materials. The thermal stresses in composite interfaces are reduced in the presence of film layers with low Young's modulus. When comparing composites having film layers with similar modulus, the thermal stresses are more effectively reduced in the composite where the film layer has a higher CTE. The radial stresses can be lowered at least 20% by utilizing film layers with high CTE, and even a high modulus film layer adjacent to the fiber followed by a low modulus film layer can be combined effectively to minimize the stresses in at least 2 interfaces.

References

[1] H. Poritsky, "Analysis of Thermal Stresses in Sealed Cylinders and the Effect of Viscous Flow During Anneal," Physics (N. Y.), 5 [12], 406-141 (1934).

[2] A. W. Hull and E. E. Burger, "Glass-to-Metal Seals," Physics (N.Y.), 5 [12], 384-405 (1934).

[3] G. D. Redston and E. Stanworth, "Glass-to-Metal Seals," J. Soc. Glass Technol., 29 [132], 48-76T (1945).

[4] A. K. Varshneya and J. E. Marra, "Stresses in Dumet-Glass Seals," J. Am. Ceram. Soc., 68 [3], 127-130 (1985).

[5] S. M. Rekhson and G. W. Scherer, "Viscoelastic-Elastic Composites: III, Bead Seal," J. Am. Ceram. Soc., 65 [9], 419- 425 (1982).

[6] J. Aveston, "Strength and Toughness in Fibre Reinforced Ceramics,"; Proceedings of National Physical Laboratory Conference on the Properties of the Fibre Composites, Middlesex, England, Paper No. 5, 1971.

[7] M. P. Borom and C. A. Johnson, "Thermomechanical Mismatch in Ceramic-Fiber-Reinforced Glass-Ceramic Composites," J. Am. Ceram. Soc., 70 [1], 1-8 (1987).

[8] E. Y. Luh and A. G. Evans, "High-Temperature Failure of a SiC-Fiber-Reinforced Lithium Aluminosilicate Glass-Ceramic," Ceram. Eng. Sci. Proc., 6 [7-8], 608-11 (1985).

[9] T. Mah, M. G. Mendiratta, A. P. Katz, R. Ruh, and K. S. Mazdiyasni, "High Temperature Mechanical Behavior of Fiber-Reinforced Glass-Ceramic Matrix Composites," J. Am. Ceram. Soc., C248-C251 (1985).

[10] D. B. Marshall and A. G. Evans, "Failure Mechanisms in Ceramic-Fiber/Ceramic-Matrix Composites," J. Am. Ceram. Soc., 65 [5], 225-231 (1985).

[11] J. O. Outwater, Jr., "Mechanics of Plastics Reinforcement in Tension," Mod. Plast., 33 [7], 156-162 (1956).

[12] C-H. Hsueh, P. F. Becher, and P. Angelini, "Effects of Interfacial Films on Thermal Stresses in Whisker-Reinforced Ceramics," J. Am. Ceram. Soc., 71 [11], 929-933 (1988).

[13] S. Shanmugham, D. P. Stinton, F. Rebillat, A. Bleier, T. M. Besmann, E. Lara-Curzio, and P. K. Liaw, "Oxidation-Resistant Interfacial Coatings for Continuous Fiber Ceramic Composites," Ceram. Eng. Sci. Proc., 16 [4], 389-399 (1995).

[14] J. J. Brennan, "Interfacial Characteristics of Glass- Ceramic Matrix/SiC Fiber Composites," J. de Physique, Colloque C5 Suppl., 10 [49], 791-809 (1988).

[15] R. A. Lowden and D. P. Stinton, "Interface Modification in Nicalon/SiC Composites," Ceram. Eng. Sci. Proc., 9 [7-8], 705-722 (1988).

[16] R. A. Lowden, "Fiber Coatings and the Mechanical Properties of a Fiber-Reinforced Ceramic Composite," pp. 619-630 in Ceram. Trans., Vol. 19, Advanced Composite Materials, Edited by M. D. Sacks, The American Ceramic Society Inc., Westerville, Ohio, 1991.

[17] S. P. Timoshenko and J. N. Goodier, Theory of Elasticity; p. 70, McGraw-Hill, New York, 1951.

[18] C. H. Hsueh and A. G. Evans, "Residual Stresses and Cracking in Metal/Ceramic System for Microelectronics Packaging," J. Am. Ceram. Soc., 68 [3], 120-127 (1985).

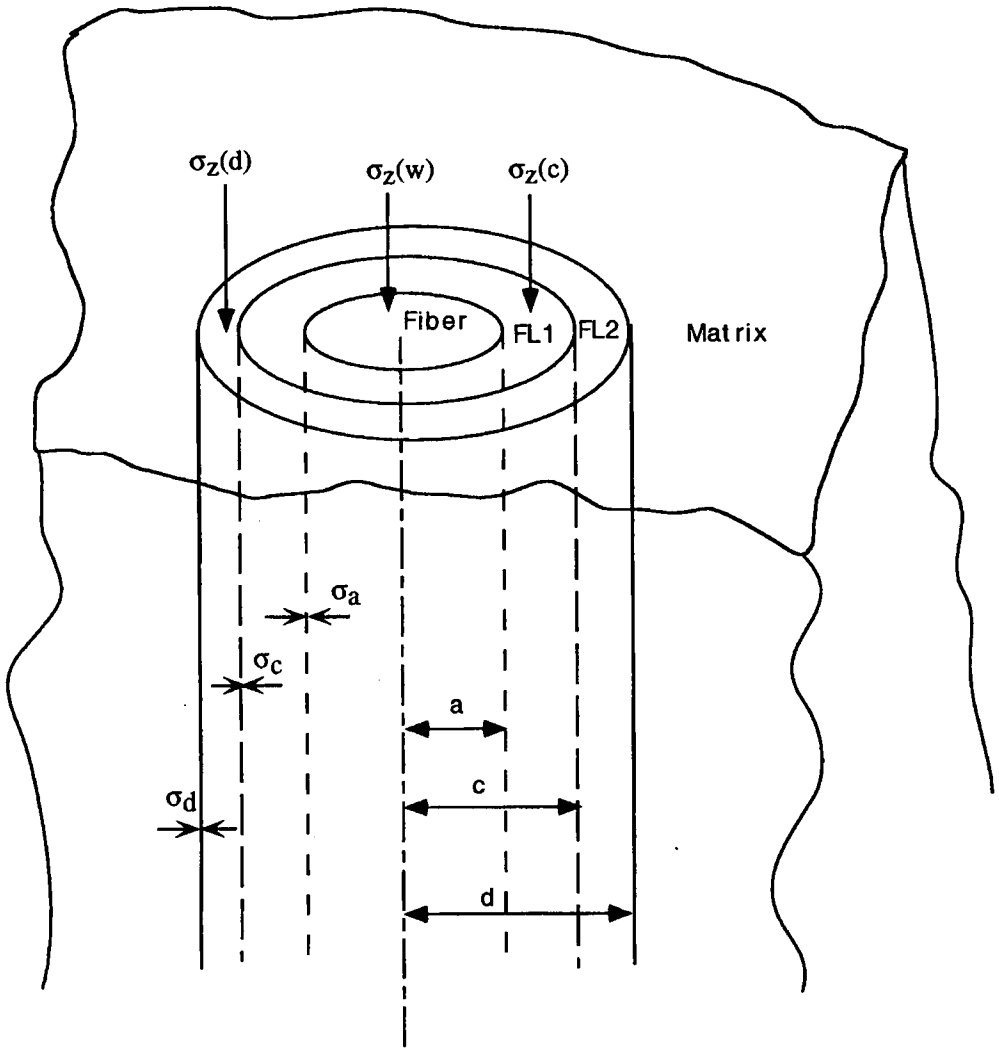


Fig. 1. Schematic of the fiber/film layer 1/film layer 2/matrix system along with the interfacial and axial tractions to maintain continuity at the interfaces during cooling from processing to room temperature

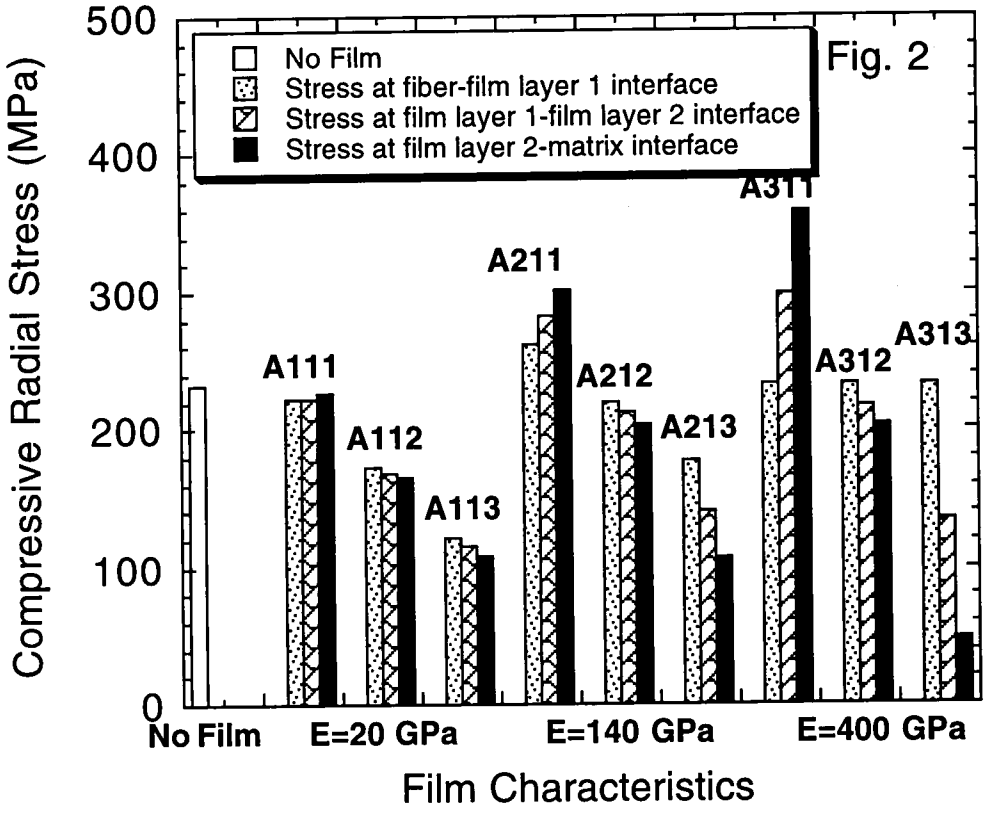


Fig. 2. The effect of thermomechanical properties of the film layers on the compressive radial stresses at the interfaces

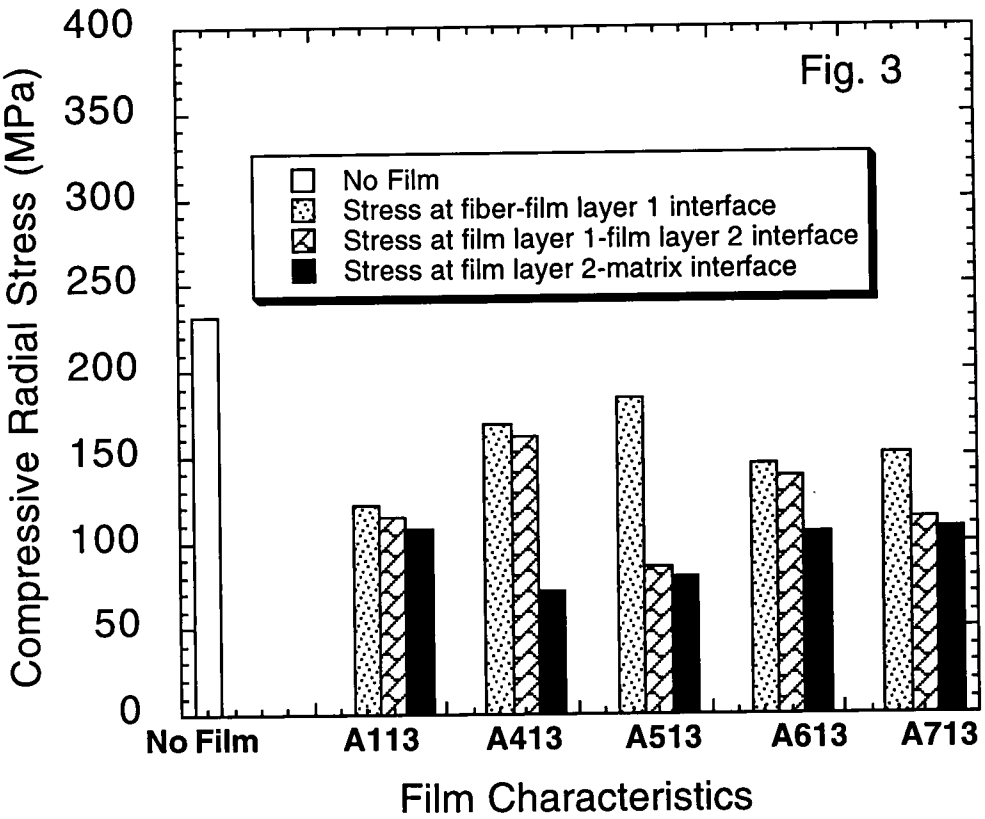


Fig. 3. The effect of combining film layers having high CTE but different modulus in composites on thermal residual radial stresses

Table 1. Mechanical and Thermal Properties of the Fiber, Matrix and Films

Film Type	Material	Young's Modulus, E (GPa)	Poissons Ratio, υ	CTE, α ($x10^{-6}$ /°C)
	Fiber (Nicalon)	190	0.12	3.9
	Matrix (SiC)	400	0.3	5.5
A111	Film layer 1	20	0.3	1
	Film layer 2	20	0.3	1
A112	Film layer 1	20	0.3	5.5
	Film layer 2	20	0.3	5.5
A113	Film layer 1	20	0.3	10
	Film layer 2	20	0.3	10
A211	Film layer 1	140	0.3	1
	Film layer 2	140	0.3	1
A212	Film layer 1	140	0.3	5.5
	Film layer 2	140	0.3	5.5
A213	Film layer 1	140	0.3	10
	Film layer 2	140	0.3	10
A311	Film layer 1	400	0.3	1
	Film layer 2	400	0.3	1
A312	Film layer 2	400	0.3	5.5
	Film layer 2	400	0.3	5.5
A313	Film layer 1	400	0.3	10
	Film layer 2	400	0.3	10
A413	Film layer 1	20	0.3	10
	Film layer 2	400	0.3	10
A513	Film layer 1	400	0.3	10
	Film layer 2	20	0.3	10
A613	Film layer 1	20	0.3	10
	Film layer 2	140	0.3	10
A713	Film layer 1	140	0.3	10
	Film layer 2	20	0.3	10

Note: Fiber is 7.5 μm in radius; Film 1 is 0.25 μm thick; Film 2 is 0.25 μm thick

Vita

Subramaniam Shanmugham was born in Chinnalapatti, Tamil Nadu, India on December 4, 1970. He grew up in Madras, India, and studied in P. S. Senior Secondary School and graduated with Distinction in March 1987. In August 1987, he enrolled in College of Engineering (Guindy), Anna University, Madras, India and received the Bachelor of Engineering degree in Mechanical Engineering in April 1991. During his stint in Anna University, he won several academic honors including the "Anna University Gold Medal" for standing first out of 120 students in the Department of Mechanical Engineering. In August 1991, he came to U.S. to pursue a M.S. degree in Metallurgical Engineering at the University of Tennessee, Knoxville, Tennessee. He did most of his thesis work (low expansion ceramics) at Oak Ridge National Laboratory, and graduated in August 1993. After graduation, he worked as a Research Associate in the Department of Materials Science and Engineering, University of Tennessee, Knoxville till April 1997. During this period, he was also enrolled in the Ph. D. program in Metallurgical Engineering. He received his doctoral degree in May 1997. He is presently employed as a Research Scientist at MicroCoating Technologies in Atlanta, Georgia.